Damage to DNA induced by low energy electrons and photons: mechanisms and analysis at the molecular level

Thesis

Damage to DNA Induced by Low Energy Electrons and Photons: Mechanisms and Analysis at the Molecular Level

by Małgorzata Śmiałek, M. Sc. Eng. Phys.

A thesis submitted for the degree of Doctor of Philosophy

The Open University

Department of Physics and Astronomy

Department of Chemistry and Analytical Sciences

The Open University

October 2007

DATE OF SUBMISSION: NOVEMBER 2007
DATE OF AWARD: 11 MARCH 2008

Abstract

In this thesis studies of interactions of both VUV light and low energy (below 20 eV) electrons with dry DNA films and DNA samples in aqueous solutions are reported. The damage induced by such radiation is quantified by monitoring both loss of supercoiled DNA and formation of single and double strand breaks using agarose gel electrophoresis. In addition VUV spectra of DNA were recorded and, for the first time, spectral signatures of both the structural water in DNA and individual contributions of separate DNA nucleotides were resolved.

Such investigations required the assembly and calibration of new apparatus. New protocols for the synthesis and purification of high quality samples of plasmid DNA were also developed. Alternative methods for analysis of DNA damage were explored, such as the atomic force microscopy technique, which allows for lesion imaging, and a new method, based on the ELISA assay was developed for labelling damage sites.

VUV irradiation experiments revealed enhanced damage upon irradiation with 170 nm photons that was shown, via VUV absorption experiments, to be due to the excitation of structural water leading to increased hydroxyl (OH) radical formation causing chemical damage to the plasmid DNA. In agreement with earlier work both single (SSBs) and double (DSBs) strand breaks were induced during by electron irradiation at 4.5 eV, 5 eV and 10 eV but only SSB were observed for electron irradiation at 1 eV.

'I only took the regular course.'

'What was that?' inquired Alice.

'Reeling and writhing, of course, to begin with', the Mock Turtle replied;

Lewis Carroll, *Alice's Adventures in Wonderland*

Abbreviations

AFM – atomic force microscope;

AGE – agarose gel electrophoresis;

AMP – ampicillin;

bp – base pairs

BrdUTP – bromodeoxyuridine triphosphate;

CAM – chloramphenicol;

DEA – dissociative electron attachment;

DNA – deoxyribonucleic acid;

DSBs – double strand breaks;

EDTA - ethylenediamine tetraacetic acid;

ELISA - enzyme-linked immunosorbent assay;

EtOH – ethanol, ethyl alcohol;

HRP - horseradish peroxidase;

LB medium – luria – bertani medium;

MDSBs – multiple double strand breaks

OD – optical density;

PAGE – polyacrylamide gel electrophoresis;

PBS - phosphate buffered saline;

PFGE - pulsed-field gel electrophoresis;

RNA - ribonucleic acid;

rpm – revolutions per minute;

SSBs – single strand breaks;

TBE – tris – borate – EDTA buffer;

TdT - terminal deoxynucleotidyl transferase;

TEM – trochoidal electron monochromator;

TET – tetracycline;

TMB - 3', 3', 5', 5'-tetramethylbenzidine;

TUNEL - terminal deoxynucleotide transferase duUTP nick end labelling;

UHP – ultra high purity;

UHV – ultra high vacuum

UV – ultraviolet;

VUV –vacuum ultraviolet.

Acknowledgements

Many people in one way or another took part in my journey that started three and a half years ago and therefore must be acknowledged here as without them it would not have been possible for me to complete it.

I would like to express my gratitude to my supervisors Professor Nicholas St. J. Braithwaite, Professor Nigel J. Mason and Professor David E. G. Shuker for their guidance, patience and confidence in me. Thanks to their great motivational skills and interest in my project I was able to complete it. Thanks to Nick for his enormous enthusiasm and optimism as well as useful comments on my work. Thanks to David for his knowledge and faith that even a physicist can understand a little bit of chemistry, as well as for caring about me. Special thanks goes to Nigel for taking a risk three and a half years ago and accepting me as his PhD student not knowing anything about me. Apart from providing great support and his engagement in my work, Nigel also gave me the opportunity to meet many great scientists, work with them and learn from them.

Completion of the project would have not been possible without the people that taught me everything I now know about biology, biochemistry and experimental physics. Many thanks to Professor Melvyn Folkard, Dr Kevin Prise and (hopefully Dr by now) Geoffrey Brand from the Gray Cancer Institute for their continual support. To my first lab-mates in chemistry who had to cope with somebody who didn't know how to use a pipette and who had to deal with me later: Dr Sharon Moore, Dr Patricia Ragazzon, Dr Antonio Codina-Barrios, Dr Chiara Da Pieve, David Smith and Patrick O'Connell. Special thanks go to the physics Post Docs: Dr Anita Dawes, Dr Phillip Holtom and Dr Paul Kendall for their help and useful comments.

I am extremely grateful to people that helped me with the experimental work that was done outside the Open University: Dr Søren Vrønning Hoffmann, Dr Nykola Jones from ISA, Denmark, and Dr David Shaw from Daresbury Laboratory, UK. Thanks to their great knowledge and experience I managed to collect the data presented in this thesis.

I consider myself lucky to have had the opportunity to work with and learn from Professor David Field from Åarhus University, Professor Janusz Rak from University of Gdańsk and Professor Hauke Clausen-Schaumann from Technische Universität München.

I am appreciative of all the help given me by the technical staff from both Chemistry and Physics Departments, Graham Jeffs, Pravin Patel, Martin Percy and Roger Bence, and laboratory managers from both departments Dr Jill Clarke and Sandra Mills for helping me so much by making everything ready 'for yesterday'. Sandra, if it wasn't for you I wouldn't be even half way to where I am now.

Sharing my office with Lindsey Shaw-Greening, Becky Enoch and Bhala Sivaraman was a joyful experience for me and definitely will not be forgotten. Many thanks to Linz and Becky for working hard on my English for the past three years.

I am especially grateful to people I consider my friends for making those years that were quite difficult for me rather enjoyable: Sharon Moore, Minaxi Vinodkumar, Allen Bowden, David Smith, Patrick O'Connell, Glyn and Marielle (soon both) Derrick, Nanda Frascione, Vincenzo Abbate, Rania Xeniou, Nyk Jones, Adam Ovens, Mike Davis and Debs Mairs, Anita and Darran Dawes, Phil Holtom, Chiara Da Pieve, Emily Unell, Liz Uttley (Drage), Maria Tynan, Robin Barnard, Phil Rosenberg, Silvia Bergamini, Kat Miljkovic, Stefano Caprasecca, Michal Piotrowicz and last but not least Sylwia Ptasinska.

More than anyone my parents, Mirosława and Piotr Śmiałek should be acknowledged for supporting my decisions at all times (even if they weren't truly

the best ones) and for making me who I am now. I would also like to thank Janusz, my fiancée, for letting me go when I felt I should go, supporting me and waiting patiently for me through all these years to come back.

Table of Contents

List of Figures

List of Tables

Chapter 1

Introduction

1.1 Radiation damage to DNA

Advances in cancer radiation therapy are most likely to arise through a deeper understanding of the mechanisms by which radiation interacts with cells, and the means by which such mechanisms can be manipulated. Furthermore, although it is well known that ionising radiation is a carcinogen, the risks associated with typical occupational and environmental exposures are still not well understood. As measurements of biological effects are difficult at low doses, much reliance is placed on the construction of 'damage' models to predict such effects, models that ultimately must allow legislation to be developed that will mediate any perceived risks. In order to develop models of the effects of ionising radiation a mechanistic model of radiation action is required that is based on sound experimental data. Since damage to DNA within the cell is the major cause of cell death and mutation we particularly need to investigate the effect of ionising radiations on DNA.

Ionising radiations, from natural background radiation or derived from diagnostic and therapeutic techniques, (e.g. X-rays, radiotherapy, positron emission tomography) can produce a range of structural and chemical modifications of the DNA helix. Of these, double strand breaks (DSB), where both strands of the helix are broken within a few base pairs, can lead to lasting damage via the production of chromosome aberrations, mutations and ultimately cell death. It is now known that the effectiveness of different ionising radiations is critically dependent on the *patterns of ionizations* they produce on a nanometre scale, comparable with the diameter of the DNA helix. Theoretical track structure modelling is being used

with increasing sophistication to simulate the distinctive patterns of ionizations produced by ionising radiation. Such models reveal that much of the radiation damage is *site specific* with penetrating primary radiations (i.e. energetic photons or ions) producing nanometre sized clusters of ionisations at the end of the radiation track. Hence in order to understand the mechanism of radiation damage it is essential to:

(i) understand the interaction of different types of radiation with the constituent cellular molecules (DNA itself and its complements the nucleotides, the nucleosides, phosphates, sugars and, of course, cellular water and

(ii) fully characterize the mechanisms by which different types of radiation damage DNA.

This will allow models to be formulated that can predict not just the patterns of ionizations, but also the spectra of damage complexity that different types of radiation can induce in DNA. Hence we require knowledge of the relationship between the amounts of energy deposited within a given region of the DNA helix and the type and severity of damage that is produced.

In this thesis the main focus was on exploring VUV irradiation to DNA samples in aqueous environment since there was some existing data with which to directly compare. The reproducibility of the results obtained and those of previous workers (Folkard et al., 2002) requires careful preparation of the DNA samples and a complete understanding of the methods by which DNA damage is analysed. Accordingly the establishing of the protocols for sample preparation and analysis that can be used in the future by the new members of the Open University (and other) research groups to ensure that the results are compatible was sought. We have also explored alternative methods for assessing DNA damage using atomic force microscopy and ELISA assay.

Preliminary results of electron interactions with DNA deposited on a surface to compare with the earlier work of (Boudaiffa et al) and estimate the cross sections for low energy electron impact induced DNA fragmentation are also presented.

This thesis is organised in 10 chapters in this first chapter we will describe some of the basic physical and chemical characteristics of DNA and review the current state of knowledge of the mechanisms by which radiation damages DNA.

1.2 Deoxyribonucleic acid

Deoxyribonucleic acid (DNA) is one of the most important biological molecules as it carries genetic information about living organisms. In eukaryotic organisms the most vulnerable target for radiation damage is the genomic DNA that is placed in the cell nucleus and is responsible for carrying the description of the organism in a form of base sequences known as genes. In case of prokaryotic organisms, such as bacteria, the genomic DNA is not restricted to the nucleus area (as there is none) but is suspended in the bacterium lumen. Additionally, some small DNA fragments, called plasmids, can be incorporated into the bacterium, changing its genetic properties.

The double helical form of DNA structure was proposed in 1953 by Watson and Crick (Watson and Crick, 1953). DNA consists of two helical chains each coiled round the same axis. Chains are made of bases (purines: adenine and guanine and pyrimidines: cytosine and thymine) connected to one another by pentose (sugar) - phosphate linkages. In the case of DNA the sugar is deoxyribose. There are additional linkages between those chains that stabilize the whole structure, namely hydrogen bounds between bases from two chains. Only specific pairs of bases can bond together: adenine can pair with thymine and guanine with cytosine. Figure 1-1 shows a scheme base pairing in the DNA double chain. Each strand of DNA is 2.2 to 2.6 nanometres wide and one nucleotide unit is 0.33 nanometres long.

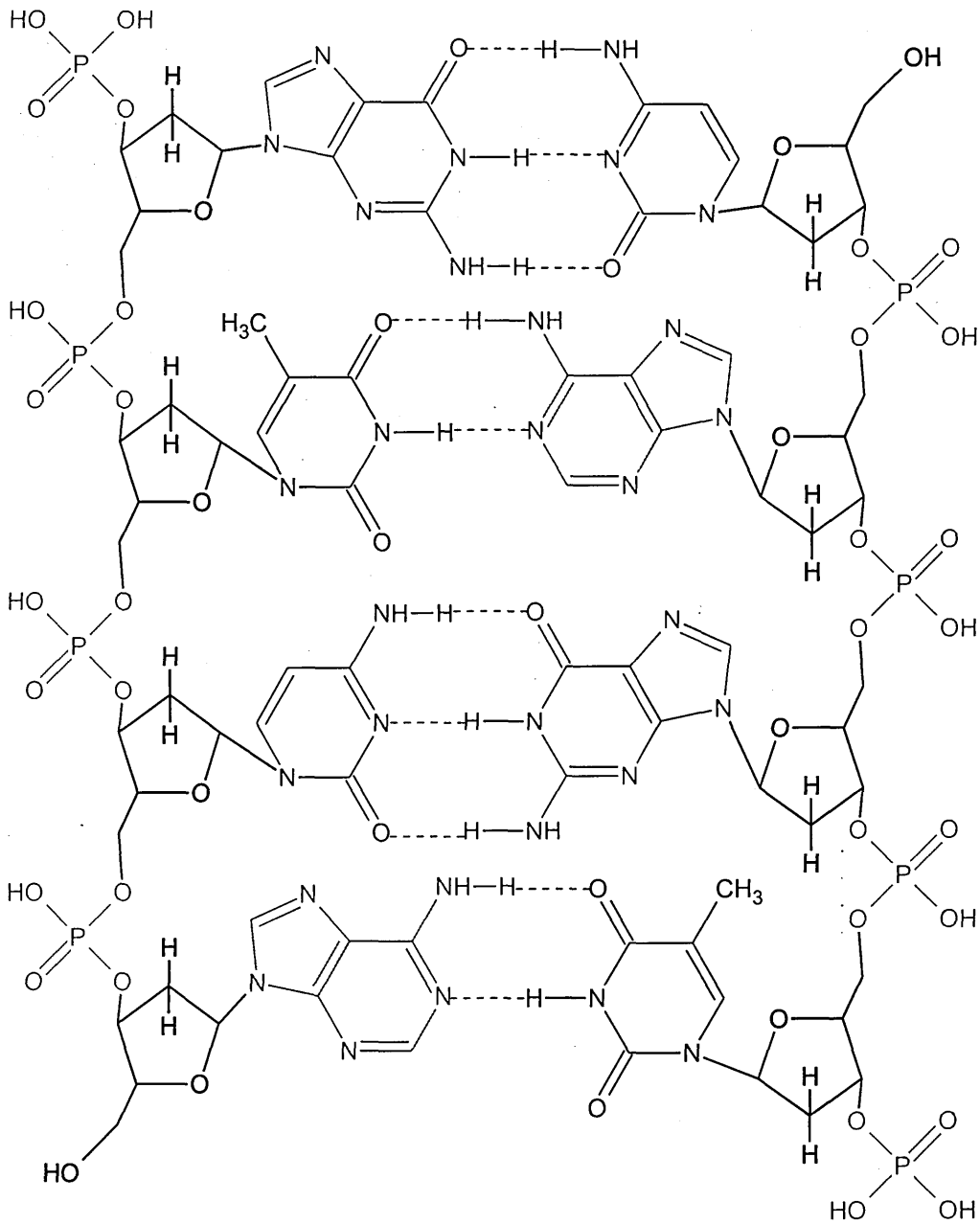

Figure 1-1. Diagrammatic scheme of the four base-pairs-in a DNA double chain: phosphate groups, deoxyribose, adenine, guanine, cytosine, thymine and hydrogen bonds.

The DNA base-sugar complex is known as nucleoside, whereas a DNA base-sugar-phosphate group complex is kown as nucleotide (mono-, di- or triphospate depending on the number of phosphate groups attached).

Although each individual repeating unit is very small, DNA chains can be enormous molecules containing millions of nucleotides (i.e. the largest human chromosome is 220 million base pairs long). The DNA double helix can also form three-dimentional structures, such as supercoils.

1.3 Plasmid DNA

Plasmid DNA is a small DNA molecule that is separated from the chromosomal DNA and is able to replicate independently (see Figure 1-2). Typically it is circular and double stranded and its size varies from 1 to 400 kbp. A cell, depending on its type, can contain either a single copy of a large plasmid or multiple ones of smaller molecules that are incorporated into the cell to change its genetic properties, such as the antibiotic resistance. Cells in which the plasmid replication process does not depend on the chromosomal DNA replication contain multiple copies of plasmid molecules, whereas cells in which the two processes are linked contain single copies. The number of plasmid molecules depends both on the plasmid copy number and its size.

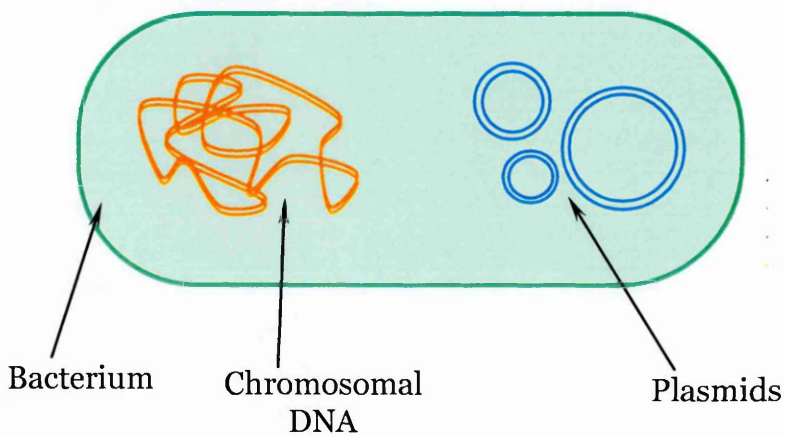

Figure 1-2. Bacterial cell with plasmid molecules inside.

In the irradiation studies discussed in the thesis, plasmid pBR322 was chosen as a form of DNA. The main reason for this decision was that it is one of the most well known *E. coli* cloning vectors (a molecule that can easily incorporate a fragment of foreign DNA for gene expression purposes) and both its sequence and the restriction sites (particular sequences of nucleotides that are recognized by enzymes as places to cut the DNA molecule) have been established. This plasmid is 4361 base pairs long (Watson, 1988) and occurs in 3 topoisomeric forms:

supercoiled, relaxed and linear (see Figure 1-3). Just one break in one of the strands of DNA double helix converts a supercoiled molecule into a relaxed one.

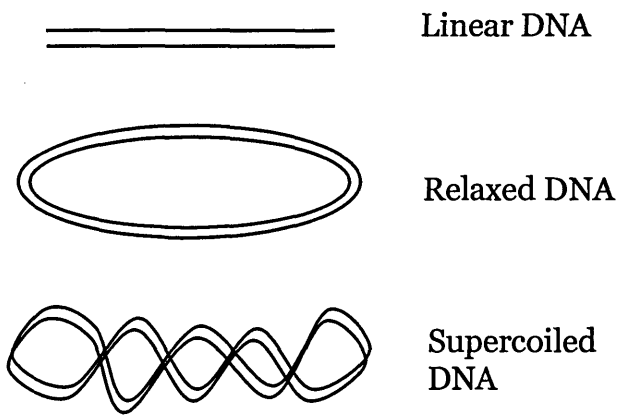

Figure 1-3. Topoisomeric forms of plasmid DNA.

The plasmid itself carries four genes (see Figure 1-4 for gene positions and the restriction sites): the replicon *rep* responsible for the replication of plasmid (source - plasmid pMB1); *rop* gene coding for the Rop protein, which promotes conversion of the unstable RNA I - RNA II complex to a stable complex and serves to decrease copy number (number of plasmid copies that can be made in a cell cycle; source - plasmid pMB1); *bla* gene, coding for beta-lactamase that gives resistance to ampicillin (source - transposon Tn3) and *tet* gene, encoding tetracycline resistance protein (source - plasmid pSC101). Such conformation allows for a choice of the selective antibiotic (antibiotic to which the bacteria carrying pBR322 will be resistant to) to be either ampicillin or tetracycline or both of them.

As pBR322 derives from plasmid pMB1 (which carries mutation that allows for more copies of plasmid to be produced if the proteins synthesis can be inhibited), it can be amplified upon bacteria culture incubation with another antibiotic, chloramphenicol. Chloramphenicol will inhibit new protein syntheses that are required for chromosomal DNA amplification. Also, repressor synthesis will be disrupted and therefore the copy number of the plasmid molecules will not be controlled. As plasmid pBR322 forms a relaxed complex with replication proteins,

it requires only a presence of stable bacterial replication proteins and thus its synthesis will not be disrupted.

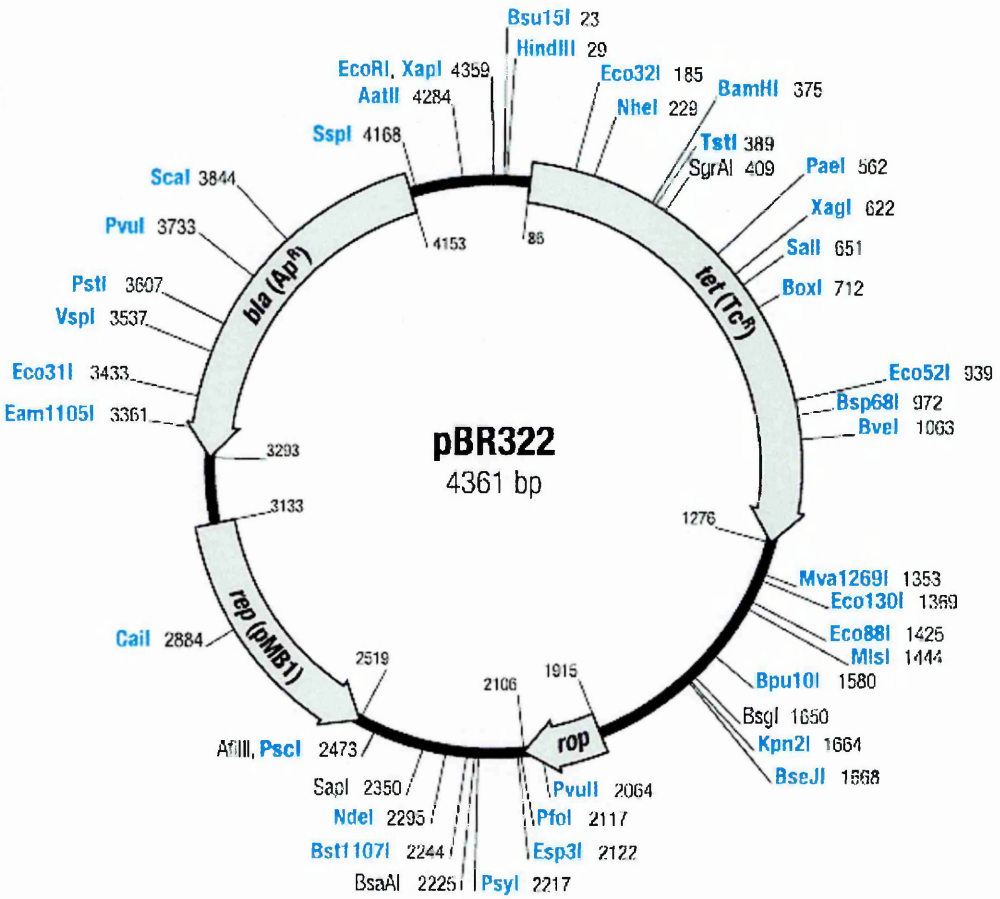

Figure 1-4. Restriction map and gene location in plasmid DNA pBR322. (source: www.fermentas.com).

A TOP10F' strain of *E.coli* that also carries a tetracycline resistance gene, was chosen to host the plasmid (kindly supplied by Dr Kevin M. Prise from Gray Cancer Institute, Northwood).

1.4 Radiation and radiation dose definition

Radiation can be defined as energy transferred in the form of high velocity particles or electromagnetic waves (photons). Radiation can be classified as ionising and non-ionising, depending on the effect it has on matter with which it interacts.

Ionising radiation has enough energy to remove tightly bound electrons from their orbits, causing the atom to become charged (that is ionized). Examples of ionising radiations are gamma rays and neutrons. Non-ionising radiation does not possess sufficient energy to remove electrons from atoms. Examples non-ionising radiation are microwaves and visible light.

In Table 1-1 the electromagnetic spectrum is presented with respect to the wavelengths, frequencies and energies of different types of electromagnetic waves. In this thesis the main radiation used was UV light. Depending on the criteria, UV light can either be divided into three smaller subregions (UVA, UVB and UVC) or simply into UV and VUV subregions (Figure 1-5).

Table 1-1. The electromagnetic spectrum.

	Wavelengths	Frequencies	Energies
Radio waves	100 m – 30 cm	3 – 10^3 MHz	$1.2 \cdot 10^{-2}$-4.1 μeV
Microwaves	30 cm – 0.3 mm	1 – 10^3 GHz	$4.1 \cdot 10^{-3}$-4.1 meV
Infrared	0.3 mm – 600 nm	10 – $5 \cdot 10^2$ THz	$4.1 \cdot 10^{-3}$-2.1 eV
Visible	600 nm – 400 nm	0.5 – 0.75 PHz	2.1-3.1 eV
Near UV	400 nm – 200 nm	0.75 – 1.5 PHz	3.1-6.2 eV
VUV	200 nm – 10 nm	1.5 – 10 PHz	6.2-124 eV
X-ray	10 nm – 10^{-2} nm	10 – 10^4 PHz	$124\text{-}124 \cdot 10^3$ eV
γ-ray	10^{-2} nm – 10^{-6} nm	10 – 10^5 EHz	$124 - 124 \cdot 10^4$ keV

Radiation interactions with matter are primarily quantified in terms of 'dose'. The absorbed dose D in Grays [Gy] delivered to a small mass M in kg is D[Gy]=E/M [J·kg^{-1}], where E is the energy in joules absorbed by the small mass. The energy E is the total energy deposited in the small volume, corrected for energy removed from the volume (e.g. loss of ionisation and radiative energy loss caused by

bremsstrahlung and characteristic radiation) that is not compensated by energy entering the volume from outside (Hendee et al., 2005).

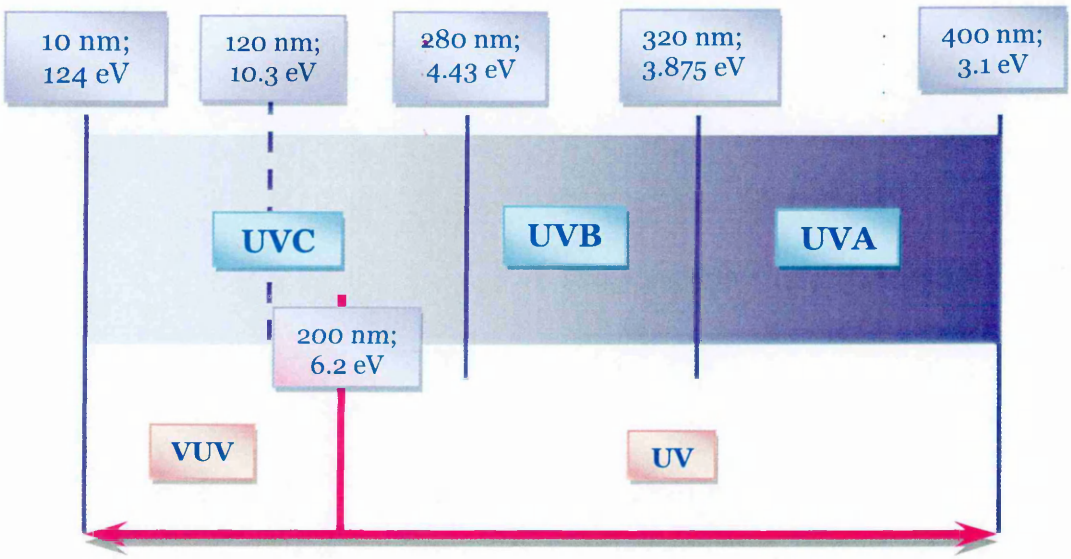

Figure 1-5. Different ways of dividing the UV light range.

1.5 VUV - UV absorption

The absorbance, A, of a medium can be determined by measuring the ratio between the intensity of an incident light, I_o, and the light, I, that has passed through a medium of a thickness d, concentration c and which has an absorption coefficient α (see Figure 1-6). All these parameters are combined together in the Lambert-Beer-Bouguer law

$$A = -\ln(\frac{I}{I_0}),$$

where $A = c \cdot d \cdot \alpha$.

The absorbance is usually described in arbitrary units, a.u. Very often it is also called an optical density (OD).

The absorbance of DNA and RNA (or single stranded DNA) in solution at 260 nm (A_{260}) is used to determine the concentration of the sample. At a wavelength of 260

nm, the absorption coefficient for double stranded DNA is 20 (ml·cm)/mg; for single stranded DNA and ribonucleic acid (RNA) it is 25 (ml·cm)/mg. Therefore, an OD of 1 corresponds to 50 μg/ml for double-stranded DNA, 40 μg/ml for single-stranded DNA and RNA. The ratio between the absorbence at 260 nm and 280 nm allows the purity of DNA sample to be determined, i.e. shows the content of RNA and proteins in the solution. For a pure DNA sample this ratio should be close to 1.8. If the ratio is higher (around 2 and more), it indicates RNA contamination, whereas if it is lower (below 1.7), a protein contamination is to be expected.

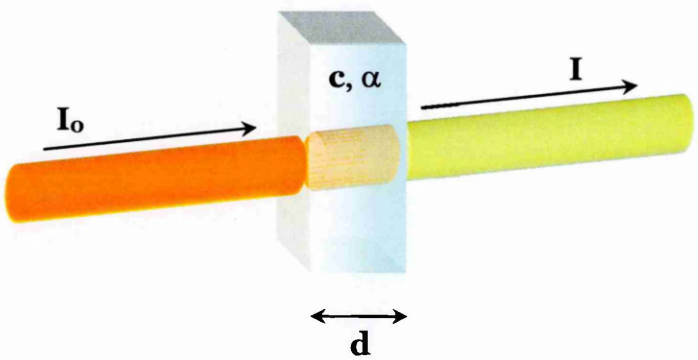

Figure 1-6. Diagram of the absorption of light travelling through a cuvette of thickness d, filled with medium of a concentration c and absorption coefficient α.

Similarly by measuring the absorption of bacteria culture at 600 nm it is possible to determine the cell density in the culture (see The QIAGEN Guide to Good Microbiological Practice; Part III; *QIAGEN News*; 1; 1999; 17-19; available from www.qiagen.com). For the *Escherichia coli* 10^8 bacteria per 1 ml of the culture has $OD_{600} = 0.1$. From OD_{600} measurements of bacteria culture densities it is possible to establish what stage of growth the bacteria culture has reached. Table 1-2 shows various phases, OD_{600} values and culture densities.

In addition, it is also possible using the above principle to measure the absorbance of molecular dry films at various wavelengths to obtain more information of their

properties. In this work absorption was used to study the properties of plasmid DNA and its constituents in the VUV region.

Table 1-2. Phases of the bacteria culture growth.

phase	description	OD_{600}	cells/ml
lag	Bacteria adapt themselves to growth conditions; the period where the individual bacteria are maturing and not yet able to divide.	almost zero	N/A
log (exponential)	The number of new bacteria appearing per unit time is proportional to the present population. This gives rise to the classic exponential growth curve, in which the logarithm of the population density rises linearly with time. The actual rate of growth depends upon the growth conditions, which affect the frequency of cell division events and the probability of both daughter cells surviving. Exponential growth cannot continue indefinitely, because the medium is soon depleted of nutrients and enriched with wastes.	early log <0.4 mid-log 0.4-1.7 late log 1.7-6.6	early log $<10^7$ mid-log $1 - 5 \cdot 10^7$ late log $5 \cdot 10^7 - 2 \cdot 10^8$
stationary	The growth rate slows down as a result of nutrient depletion and accumulation of toxic products. This phase is reached as the bacteria begin to exhaust the resources that are available to them.	>6.6	$>2 \cdot 10^8$
death	Bacteria run out of nutrients and die	decrease with respect to stationary	decrease with respect to stationary

1.6 Types of DNA damage

Among the particles that are able to cause damage to DNA one can distinguish between those with sufficient energy to cause DNA breaks, e.g. X-rays, γ-rays, ions, high energy electrons (above 20 eV), and those that have sufficient energy to excite the molecule and its environment but not high enough to cause strand breaks. Examples of such particles are VUV photons and low energy electrons (below 20 eV) that were of the main interest in this work.

DNA is frequently damaged by both internal and external factors. The external factors, like radiation, are responsible for direct damage, whereas the damage caused by reactive species formed in cells upon such radiation is called an indirect damage. By damage one understands either single-strand breaks (SSBs) or double-

strand breaks (DSBs) or multiple double strand breaks (MDSBs), presented in Figure 1-7. Damage also means modification to single DNA bases. The term 'cluster damage' means all the above types of damage combined and present in the DNA after irradiation.

Several previous studies have sought to explore how VUV radiation and low energy electrons damage DNA molecules. In this subsection the results of earlier investigations will be reviewed.

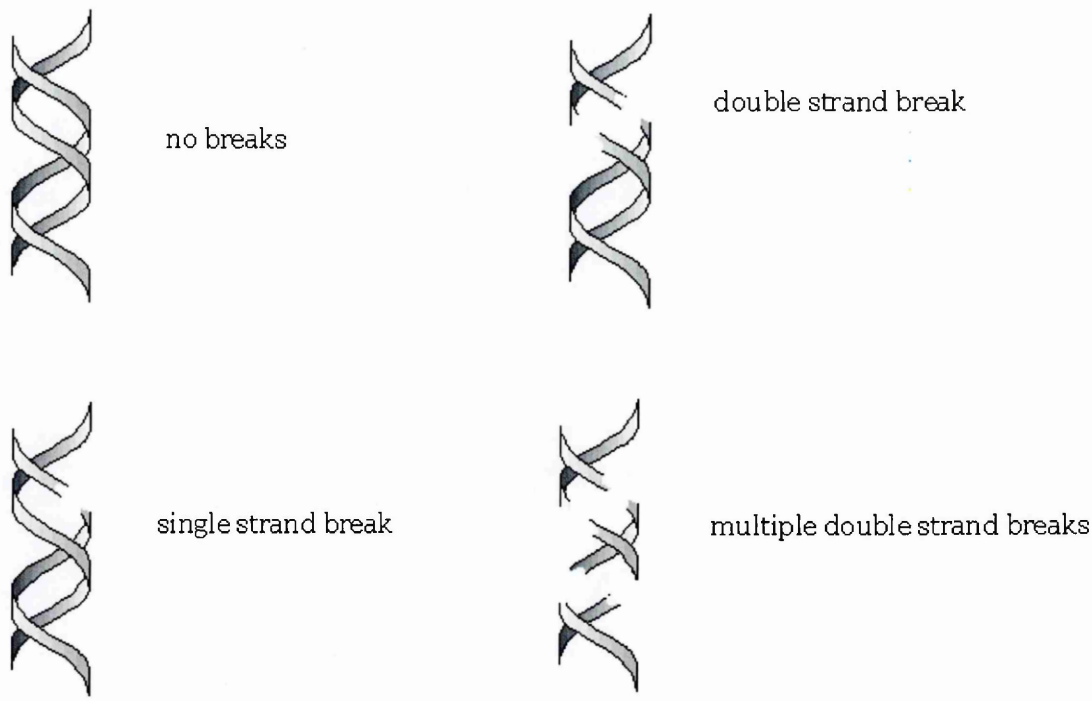

Figure 1-7. Representations of DNA damage. Various possible damage types to sugar-phosphate backbone of a double-stranded DNA. DSB occurs when SSB on opposite strands were separated by not more than 10 bp.

1.6.1 VUV radiation damage to DNA

The significance of DNA – UV interactions has been known for a long time and extensive studies have been undertaken to understand the mechanisms by which the VUV damage to DNA takes place and to predict all of the possible damage pathways.

The first studies of interactions of VUV-UV photons with dry DNA films were undertaken by Sontag and Dertinger (1975). It was shown that the survival of

unbroken DNA after VUV irradiation was very low, whereas irradiation by UV around 260 nm, although highly absorbed, does not cause any damage. The data obtained correlated with their earlier work on VUV-UV absorption of DNA films (Sontag and Weibezahn, 1975). In addition they reported that in the UV region (4.9 eV, 253.5 nm) there were large numbers of pyrimidine dimers being produced.

Later studies on the dinucleotides showed that the damage induced by VUV is bond selective (Ito and Saito, 1988; Ito et al., 1987) and that the most efficient combination of the mononucleotides that can undergo disruption is the adenosine dimer. The authors also showed that all the investigated complexes decomposed to fragments containing 5'-deoxymononucleotides and that the minimum energy required to decompose this complex was 7.3 eV.

DNA damage by VUV radiation is expected due to its ionising capabilities but damage induced by UV light in the range from 254 nm to 365 nm has also been reported (Boullard and Giacomoni, 1988). It was shown to cause both DNA nicking and pyrimidine dimer formation at high irradiation doses.

Thymine dimer formation (the most abundant species) has been explored over the VUV region (Matsunaga et al., 1991). It was found that between 150 – 365 nm region the dimers were formed at all the investigated wavelengths, yet a large increase in the amount of these lesions for wavelengths below 160 nm was reported.

Irradiation studies of dry plasmid pBR322 have been carried out (Ito, 1992) revealing that the cross section for SSB formation increases steadily from 200 nm up to 120 nm. It was suggested that over such a wavelength range the cross section did not behave like the photoabsorption spectrum, i.e. lesion formation was not influenced by photoabsorption in the DNA bases.

Solid films of plasmid DNA have been irradiated at photon energies ranging from 8.3 eV to 20.7 eV (Hieda et al., 1994) and the damage obtained was quantified to

be 5.4 times greater for SSBs and 12 times greater for DSBs at 20.7 eV compared to 8.3 eV. VUV photons were shown to introduce DSBs in DNA molecules, yet the yield obtained was much lower than in the case of X - or γ - rays. A short report was then presented (Hieda, 1994) to summarise the VUV and X-ray irradiation results. It was stated that the difference in the number of photons that are required to induce a SSB in DNA molecule is twice as great at 8.3 eV as at 20.7 eV. It was also mentioned that there is no particular change in this number between the irradiations carried out at 20.7 eV and 2153 eV. In addition, an interesting conclusion was made that the VUV region is an important one for studying the OH and H radical interactions and their effects on DNA molecules.

Dose – response experiments for dry plasmid DNA films were repeated (Michael et al., 1994) with the photons ranging from 8 eV to 25 eV. A slow increase in both SSBs and DSBs yields below 10 eV was reported and a 12 to 20 fold difference between the yield of SSBs and DSBs for energies investigated. Additionally, all the responses obtained showed energy-dependent plateaus at higher doses, which could have been caused by DNA shielding. For the first time it was suggested to irradiate plasmid DNA in the aqueous solution to obtain data that would be more representative of the natural environment of DNA.

Irradiations of vacuum dried plasmid DNA were performed at 160 nm, 190 nm, 220 nm and 254 nm (Wehner and Horneck, 1995) and it was concluded that the cross sections (the probability of interaction between the target and the projectile expressed as a virtual size of the target 'as seen' by the projectile – hence the unit of the cross section is cm^2/m^2) for SSB induction are $(1.5\pm0.1)\times10^{-17}$ cm^2, $(4.4\pm0.6)\times10^{-19}$ cm^2, $(5.0\pm1.3)\times10^{-19}$ cm^2 and $(2.1\pm0.2)\times10^{-19}$ cm^2, respectively. The authors conducted irradiations at 254 nm of DNA in aqueous solution and the air-dried plasmid. The cross sections obtained for the SSB formation were

$(5.0\pm0.4)\times10^{-19}$ cm^2 and $(6.6\pm1.0)\times10^{-19}$ cm^2, respectively. The authors obtained the DSBs formation only for 160 nm with the cross section $(1.4\pm0.1)\times10^{-18}$ cm^2.

The first results obtained (Folkard et al., 1999) for an aqueous solution of plasmid DNA irradiated with photons of energy of 8 eV showed that there is a strong influence of the medium on the damage induced. Their preliminary results showed a high increase in the damage yield compared to the dry plasmid DNA. The authors showed that this was due to OH radical-induced damage by introducing the scavenger (a chemical substance that can remove or deactivate unwanted species in the reaction mixture) into the solution (see Figure 1-8). The damage was halved with the scavenger present compared to the pure water solution. In later studies (Folkard et al., 2002) using 8.5 eV photons and ^{60}Co γ-rays the authors noticed a very little difference between the damage induced to plasmid DNA in aqueous solution by both types of radiation. It was concluded from the experiments that all the wavelengths that can be absorbed by water will induce damage to DNA depending on the yield of OH radicals.

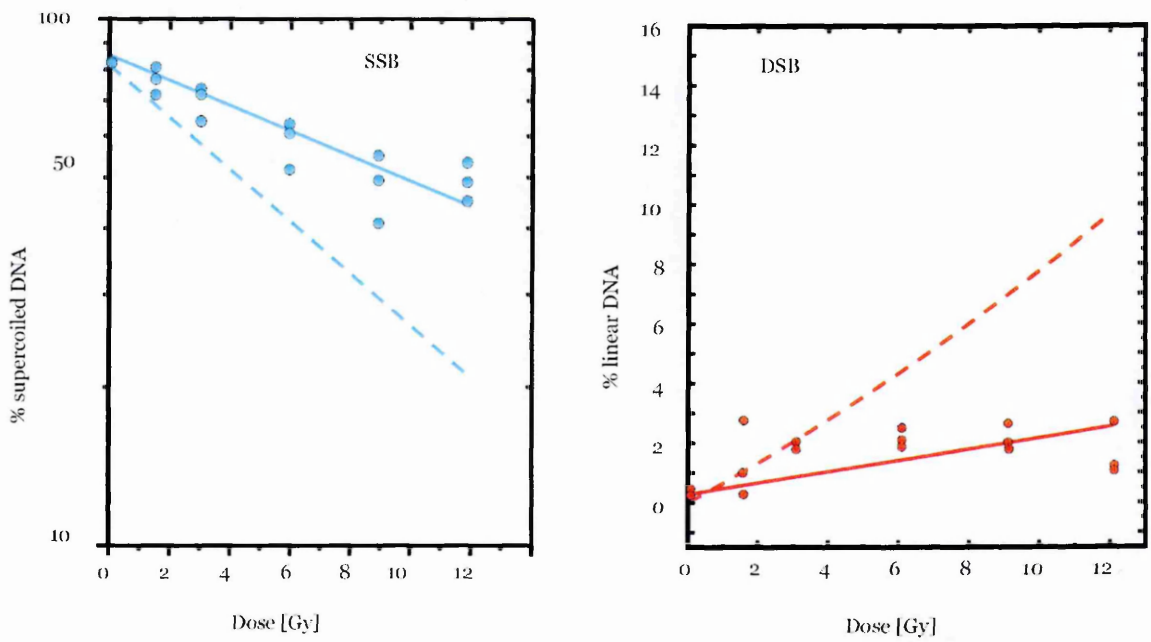

Figure 1-8. Loss of supercoiled DNA and DSBs formation in samples irradiated at 150 nm in aqueous solution (Folkard et al., 2002); dashed line denotes samples irradiated in absence of hydroxyl radical scavenger whereas solid lines denote samples irradiated in presence of 10 mM tris buffer.

Using a specially designed apparatus (Folkard et al., 2000) the authors examined various energies from 7 eV to 150 eV for the rate at which the damage is produced in the dry DNA films (Prise et al., 2000). Their results were found to be in a good agreement with the data published previously (Hieda et al., 1994).

1.6.2 Electron damage to DNA

When ionising radiation is used to irradiate living cells, the most abundant species that are produced in the cell are secondary electrons with energies between 1 and 20 eV. Such species can cause damage in the cell almost as efficiently as the original particles of high energy; therefore, it became important to investigate the interactions and damage mechanism between low energy electrons and DNA.

The primary results of Folkard et al. (1993) showed the dose-response curves for damage of dry DNA film induced by the electrons of energies between 25 and 4000 eV. It was shown that the threshold for the induction of single strand breaks is below 25 eV, whereas for double strand breaks it lies between 25 and 50 eV. These results were later reproduced by Boudaïffa et al. (2000b).

In a later paper Huels et al. (1998) showed that there is a vast production of DNA base ions due to resonant attachment of low energy electrons upon irradiation. Resonant attachment is the process in which the electron attaches itself to a target molecule to form a temporary negative ion. The authors concluded that a resonant mechanism might be responsible for the cellular DNA damage by secondary electrons. This assumption was soon confirmed by Boudaïffa et al. (2000a), who showed that both single and double strand breaks can be induced in dry plasmid DNA by irradiating it with the electrons of energies between 0 and 20 eV (see Figure 1-9). Moreover, it was shown that there is a peak around 10 eV for DSB, SSB formation and loss of the supercoiled form of DNA that the authors ascribed to the dissociative electron attachment (DEA) to the constituents of DNA (e.g. thymine,

water). In their later work (Boudaiffa et al., 2002) the cross sections were determined for SSB and DSB production for electron irradiation at 10, 30 and 50 eV.

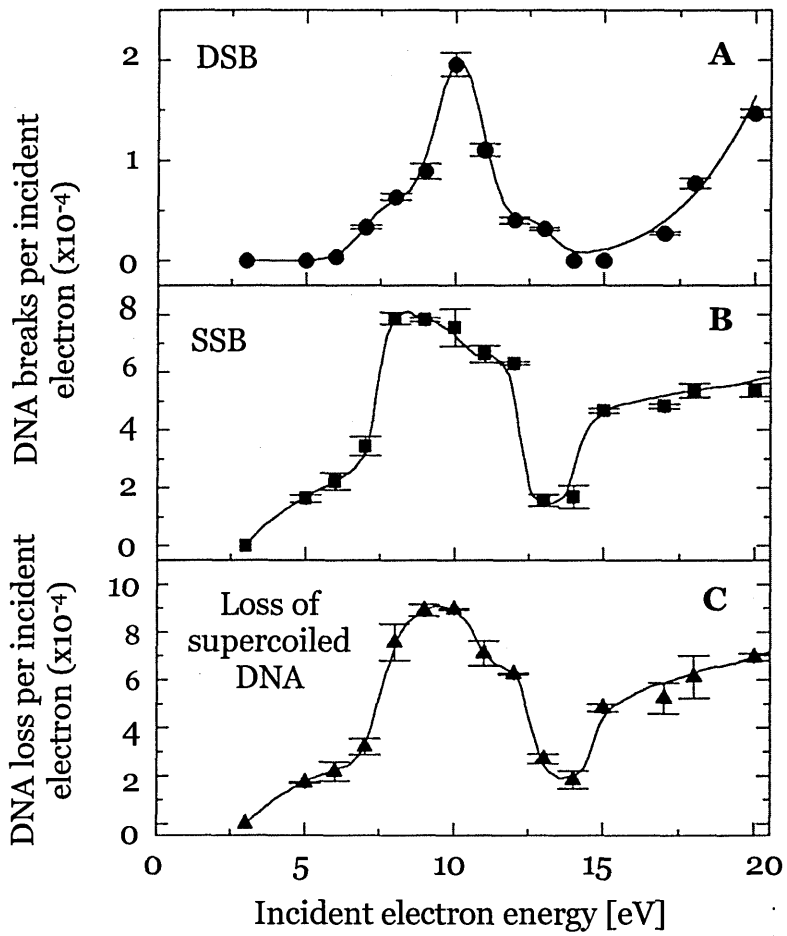

Figure 1-9. Measured quantum yields, per incident electron, for the induction of DSBs (A), SSBs (B), and loss of the supercoiled DNA form (C), in DNA solids by low-energy electron irradiation as a function of incident electron energy (Boudaiffa et al., 2000a).

Resonant structure formation via dissociative electron attachment was later broadly discussed by Abdoul-Carime (Abdoul-Carime and Sanche, 2002), Pan (Pan et al., 2003; Pan and Sanche, 2005; Pan and Sanche, 2006), Huels (Huels et al., 2003) and Martin (Martin et al., 2004), who investigated the formation of resonance structures in irradiated DNA films via desorption of H^-, O^- and OH^- anions from those films as well as the multiple double strand break formation (MDSB) and the relation between the base identity and sequence with respect to damage obtained. These studies have contributed to determining the possible mechanisms by which damage is induced.

Possible pathways for the damage formation were experimentally examined by Pan (Pan and Sanche, 2006) regarding DEA formation on the DNA backbone and bond scission and Zheng (Zheng et al., 2005; Zheng et al., 2006) regarding phosphodiester bond cleavage. These results led to the conclusion that upon irradiation with low energy electrons the base is responsible for the resonant electron capture and its transfer to the sugar-phosphate backbone, where the C-O bond is the most likely one to be cleaved.

Some interesting studies were performed on the low energy (<2 eV) electron capturing by DNA thin monolayers (Ray et al., 2005). It was found that the probability of capturing an electron increases with the amount of the guanine bases in the DNA strand and that this value is much higher for single stranded DNA than for the double stranded DNA. It was also shown that once captured, the electrons are bound more strongly to the double stranded than to the single stranded DNA.

Simultaneously, theoretical investigations were conducted to determine what is the most possible mechanism for the damage at low energies (Barrios et al., 2002) and whether the DEA can play role in strand break formation below 5 eV (Li et al., 2003). From these calculations it was deduced that SSB might form via shape-resonance states that can be produced on the DNA base and then transferred to sugar-phosphate C-O bond where the break over a very small barrier to produce SSB occurs. The cross sections for electron scattering from the DNA bases at higher energies, such as 50-5000 eV (Mozejko and Sanche, 2003) and selected analogues of DNA backbone components (Mozejko and Sanche, 2005) were studied, although there is, as yet, no experimental data available to verify these calculations.

The investigations of the distortion of the base structure and sequence in single stranded DNA and their influence on the elastic scattering cross section (Caron and Sanche, 2006) seem to show that the structural distortion itself increases the elastic scattering cross section and the attachment probability at low energies. However, the sequence disorder did not seem to have any influence on either the elastic scattering cross section or the attachment probability.

Some analysis has been made on other interactions between low energy electrons and helical molecules, like diffraction and resonance structure formation, (Caron and Sanche, 2004; Caron and Sanche, 2005; Caron and Sanche, 2003). It was shown that electron diffraction plays a significant role in electron attachment to the bases and shape and core-excited resonance formation can lead subsequently to strand break formation, as mentioned above. In addition, it was found that the sugar-phosphate backbone plays a major role in screening bases from electron bombardment and also that at low energies (2-5 eV) electron localization at the phosphate unit is highly favoured.

1.6.3 Other types of radiation damage: X-rays, γ-rays and ions

Other types of radiation, such as X-rays, γ-rays and ions that can be considered as ionising have also been extensively investigated. With X-ray irradiation base alteration and strand breaks are the main types of damage. X-rays were also used to investigate clusters of DNA damage formation upon absorption by the phosphorus atoms in the DNA backbone (Hieda, 1994). It was concluded that there is no increase in the damage yield due to this absorption although followed by the Auger process (a process in which upon ejecting one electron from the core level of atom an electron that occupies higher energy level is moving to a resulting gap at lower energy level and releases energy by either emitting a photon or passing it to another electron at the same lower energy level causing its emission).

These studies were extended to the formation of SSBs and DSBs by irradiation of dry plasmid DNA with X-rays of energies of 388 eV, 435 eV and 573 eV, that are close to nitrogen K-edge and oxygen K-edge (K-edge is the energy of the K shell electrons in an atom) (Yokoya et al., 1999). It was concluded that in all cases the absorbed energy required for a SSB formation was around 60 eV and 1 keV for the DSB formation. The main conclusion was that in case of X-ray irradiation of solid DNA films both SSBs and DSBs are formed due to photo- and Auger-electrons and that the process depends only marginally on the type of atom that ejects them.

The use of γ-rays allows DNA damage to be studied in a more natural environment, such as aqueous solutions. These studies showed for the first time that, apart from the direct effect, there is also additional damage which results from the interaction of radiation with solvent molecules. The majority of studies showed that in aqueous solutions it is primarily the OH radicals that enhance the damage (Achey and Duryea, 1974; Bonura and Smith, 1976; Siddiqi and Bothe, 1987).

Damage induced by low energy heavy ions (krypton, lead, gold; of energy depositions 750-5000 keV/μm) was focused on the strand break formation and DNA unwinding (Rydberg, 1984) and it was shown that all the ions investigated were a few orders of magnitude less efficient in creating breaks in the DNA molecules than conventional X-rays. In one of the latest papers using carbon ions of energies below 500 eV it was also shown that upon irradiation apart from the SSBs and DSBs additionally MDSBs are being induced (Hunniford et al., 2007). The authors also concluded that the amount of damage depended on both the kinetic and potential energies of carbon ions.

Chapter 2

DNA damage analysis

In order to quantify the damage induced in DNA by irradiation, such as SSBs and DSBs formation, several methods have been developed. Gel electrophoresis allows for separation of different DNA fragments and provides quantitative analysis of the damage induced. Atomic force microscopy directly visualises the damaged molecules, whereas the ELISA-based assay labels all the breaks induced to the DNA molecules upon irradiation. In this thesis all these analysis methods were used and will now be described in some detail.

2.1 Gel electrophoresis

The most commonly used method used for DNA damage analysis is gel electrophoresis. Electrophoresis through agarose and polyacrylamide gels is used to separate, identify and purify DNA fragments being relatively easy and quick to perform. Moreover, the presence and localisation of DNA fragments in the gel can be determined by direct staining with fluorescent dyes such as ethidium bromide or SYBR green that bind with DNA molecules. This technique allows detecting as few as 20 pg of double-stranded DNA and allows recovery of DNA for further examination (Sambrook and Russell, 2001).

Taking into account all varieties of gels configuration (shapes, sizes, porosities and concentrations) one has at one's disposal a powerful tool for DNA investigations. The choice of gel configuration determines the size of the DNA fragments that can be separated.

For visualisation of the damage induced in the experiments presented in this work an agarose gel electrophoresis (AGE) was used. Agarose is a linear polymer composed of alternating residues of D-α- and L-β- galactose joined by glycosidic

linkages (see Figure 2-1). Helical fibers are formed using chains of agarose. They aggregate into supercoiled structures with diameter of 40-60nm. After gelating, a three-dimensional mesh of channels is obtained with a wide range of diameters, depending on agarose concentration.

The migration rate of linear DNA fragments in such gels is linearly dependent on the gel concentration, given by

$$\log\mu = \log\mu_0 - K_r \cdot \rho$$

where μ is electrophoretic mobility of DNA, μ_0 is the free electrophoretic mobility of DNA, ρ is gel concentration and K_r – retardation coefficient (constant dependent on the gel properties, size and shape of migrating molecules).

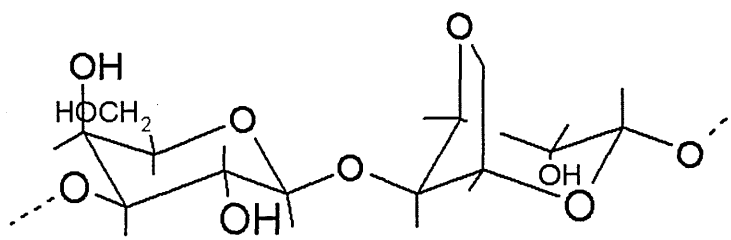

Figure 2-1. Structure of agarose sub-unit.

Different conformations of DNA migrate at different rates (Figure 2-2). Supercoiled DNA is the fastest one; the slowest one is relaxed DNA. The linear form appears on the gel between these two. This phenomenon occurs due to different gyration radius the three forms have.

In the past, two-dimensional gel electrophoresis was used to separate all the three forms of DNA (Oppenheim, 1981). The method was based on difference of mobility of the three forms of DNA in the presence and absence of ethidium bromide.

The migration speed also depends on the applied voltage. At low voltages the migration rate of the linear DNA is proportional to the applied voltage. However, raising the voltage makes the mobility of heavy molecules increase differentially and resolving properties are lost. Thus, for DNA fragments bigger than 2 kbp gels should be run at about 5-8 V/cm.

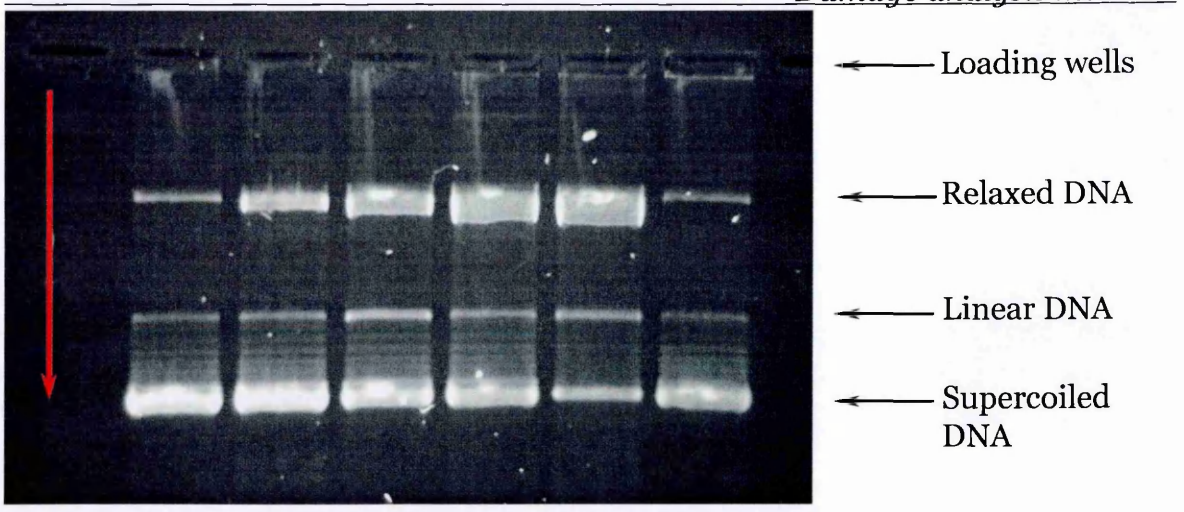

Figure 2-2. 1.2 % agarose gel with pBR322 plasmid DNA developed in the lines created by the comb; red arrow indicates the direction of the DNA motion in the gel.

Electrophoretic mobility of DNA is affected by the type of electrophoresis buffer (its composition and ionic strength). In absence of ions, electrical conductivity is minimal and the DNA migrates very slowly. On the other hand if the buffer has high ionic strength, the electrical conductance is higher and a lot of heat is generated, which in the worst case might cause gel melting and DNA denaturation. The buffer used in the experiments was a tris – borate – edta (TBE) buffer (5 x TBE stock: 54 g trizma base, 27.5 g boric acid and 4.65 g ethylenediamine tetraacetic acid (EDTA) dissolved in 1 L of ultra high purity (UHP) water).

The conditions that were chosen for the agarose electrophoresis in the experiments performed were: 1.2 % agarose gel run for 6 hours at 1.5 V/cm in 1 x TBE buffer. Gels were prepared by dissolving 1.2 g of agarose (from Cambrex) in 100 ml of 1 x TBE buffer and microwaving for 90 seconds. Once the agarose solution had cooled down, it was poured into a vessel with a comb (for creating the loading wells, see Figure 2-2). The mixture was then allowed to set for 1 hour at room temperature. Gels were loaded with the samples (1 µl of glycerol-based loading buffer per 5 µl of DNA solution) and either run immediately or wrapped in foil and stored in the fridge. After the electrophoresis was complete, gels were stained with 1 x SYBR Green I (from New England Biolabs) in 1 x TBE solution for 45 min and gel images were taken using commercially available imagers (e.g. from BioRad).

Polyacrylamide gels are more effective in terms of separating small fragments of DNA (5 – 500 bp). It is therefore possible to resolve fragments in polyacrylamide gels that differ by 1 bp in length or as little as 0.1 % in their mass. Polyacrylamide gels are run vertically in a static electric field. Unfortunately polyacrylamide gels have the disadvantage of being more difficult to handle and prepare than agarose gels.

In terms of mass resolution agarose gels are not as good as polyacrylamide gels but separate DNA of greater sizes. DNA composed of 50 bp up to 20000 bp are best resolved when run in horizontal configuration and in constant electric field. In the agarose gel DNA fragments migrate with a velocity that is proportional to the applied electric field and depends inversely on the size of the fragments (the smaller the fragment the faster it migrates). The greater the pore size (the pore size is inversely proportional to the concentration of the gel) the greater the fragment size that can be resolved. However, when the fragment size exceeds 750 kbp it is no longer possible to resolve DNA using a standard method and pulsed-field gel electrophoresis (PFGE) is used instead. This method uses alternated orthogonal electric applied to the gel. Large molecules will be then trapped every time the electric field changes direction and will not move unless they have reoriented themselves along the new axis of the electric field. The time that is necessary for the molecule to change orientation depends on its size – the bigger the molecule the longer it takes to realign. Therefore, if the molecule needs less time to reorientate than the period of the electric field it will continue moving inside the gel contrary to other molecules whose time of realignment is longer and which will therefore be trapped.

2.2 Atomic force microscopy

In order for nanosience to develop there was a need to design tools that would make it possible to investigate directly the structure of surfaces on the atomic scale. The first solution was proposed in 1986 by Binning (Binnig et al., 1986) who suggested to monitor elastic deflections of a very small probe examining a sample surface and from that calculate the force between the probe and sample which provides a 'map' of the surface structure. This new tool, an atomic force microscope (Figure 2-3), allows scanning of non-conductive samples and can work in two modes: contact and non-contact (or tapping) mode, each having different variants and applications.

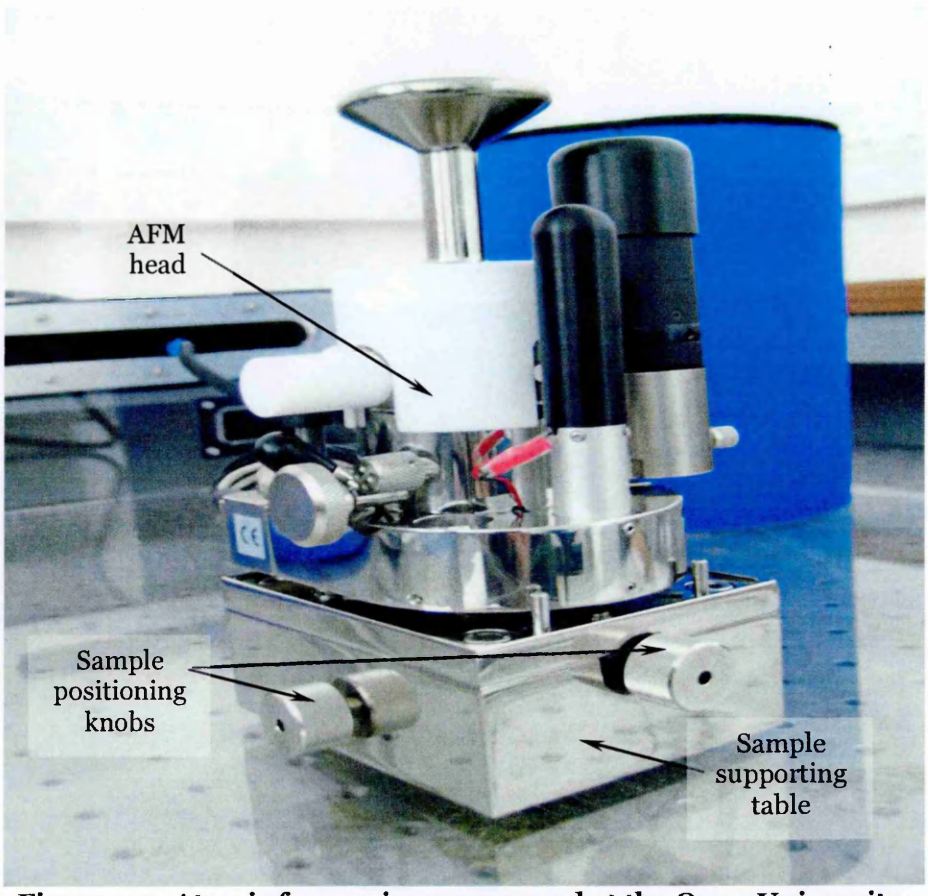

Figure 2-3. Atomic force microscope used at the Open University.

In the contact mode (Figure 2-4) there is direct physical contact between the probe tip (mounted at the end of a cantilever) and the sample surface. The motion of the cantilever is monitored by reflecting a laser beam off its back surface onto split

photodiode. The sharpness of the tip is usually around 10 nm or better. During the scan all the deflections in the cantilever caused by the surface morphology will be detected as a difference in the light intensity on a four-sector photodetector. From these signals it is possible to calculate the cantilever deflection and the force it applies to sample. An AFM works under the conditions where Hook's law applies. According to Hooke's law the relationship between the force F and motion that is generated d is given by

$$F = -k \cdot d$$

It is now possible to produce cantilevers with force constants k of less than 1 Nm^{-1}, so motions of less than 0.1 nm or forces of less than 0.1 nN can be resolved.

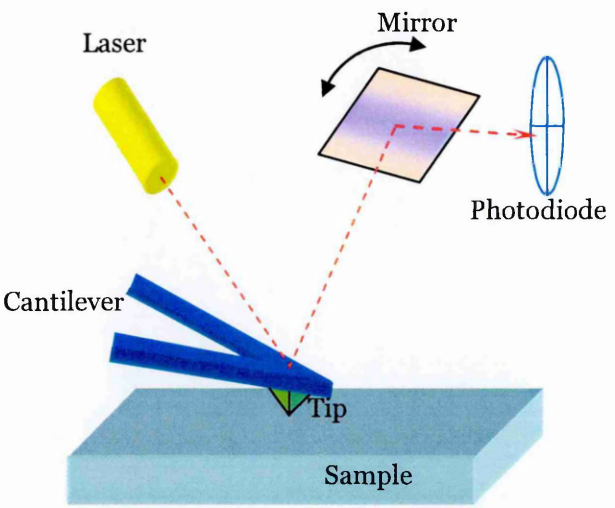

Figure 2-4. Contact AFM.

Contact mode AFM is useful for imaging solid samples but the moving tip may cause damage to soft or fragile samples, hence to probe biological molecules or polymers non-contact AFM is used.

In tapping mode AFM a tip on the end of an oscillating cantilever briefly touches the surface during each oscillation as it scans the sample. The cantilever is driven by an oscillating piezoelectric transducer that provides a driving force of constant amplitude and frequency (Figure 2-5). In this mode the cantilever is driven into resonant oscillation and changes in resonant frequency caused by changes in the force between the tip and the sample (even though they are not in contact) are

measured. When the probe approaches the sample surface, the force gradient changes and both the oscillation amplitude and phase of the vibrating cantilever are changed. It is possible to detect both of these changes and use them to control the track of the probe over the surface. Amplitude detection is usually used when the cantilever oscillates with high amplitude, whereas phase detection control is required when this amplitude is relatively small and, to obtain a stable feedback, higher sensitivity is required.

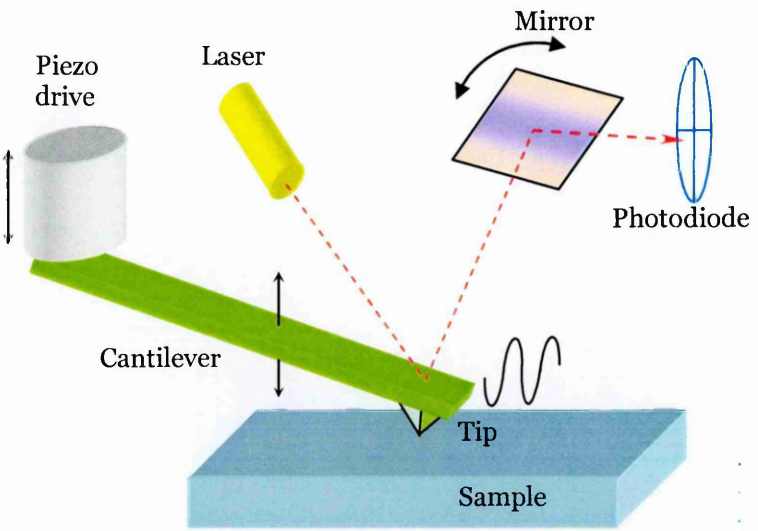

Figure 2-5. Non-contact AFM.

Because of the limited response of the AFM in the z-direction, changes in the topography of very flat samples (e.g. DNA molecules), except for topographic images, can be recorded as phase images. Phase images show the phase difference between the oscillation of the piezoelectric crystal that drives the cantilever and oscillation of the cantilever as it interacts with the sample surface (Argaman et al., 1997). The AFM generates signals representing dynamic motion of the cantilever: its amplitude and phase. The amplitude is the magnitude of the cantilever's response to the driving force and decreases when the cantilever touches the surface. A feedback loop adjusts height of the sample through a piezoelectric transducer to keep the amplitude at its set point. The height changes in the sample

form the height image, representing the topography of the sample. The phase signal measures the time lag between the piezo drive and the actual motion of the cantilever (Figure 2-6). The changes in the phase lag of the cantilever motion form the phase image.

To control the position and vibrations of the probe over very small distances piezoelectric ceramics are used. These materials change their dimensions according to changes in the applied electric field. An electric feedback circuit uses the output of the probe to drive the z-piezo ceramic and control z-positioning mechanism. There are three factors that this system uses: Proportional, Integral and Derivative (known as PID factors); values of all of them depend on the sample properties. The feedback response is based on the combination of terms proportional to the error signal, integral of the error signal and derivative of the error signal to set the z position so a constant sensor signal is obtained.

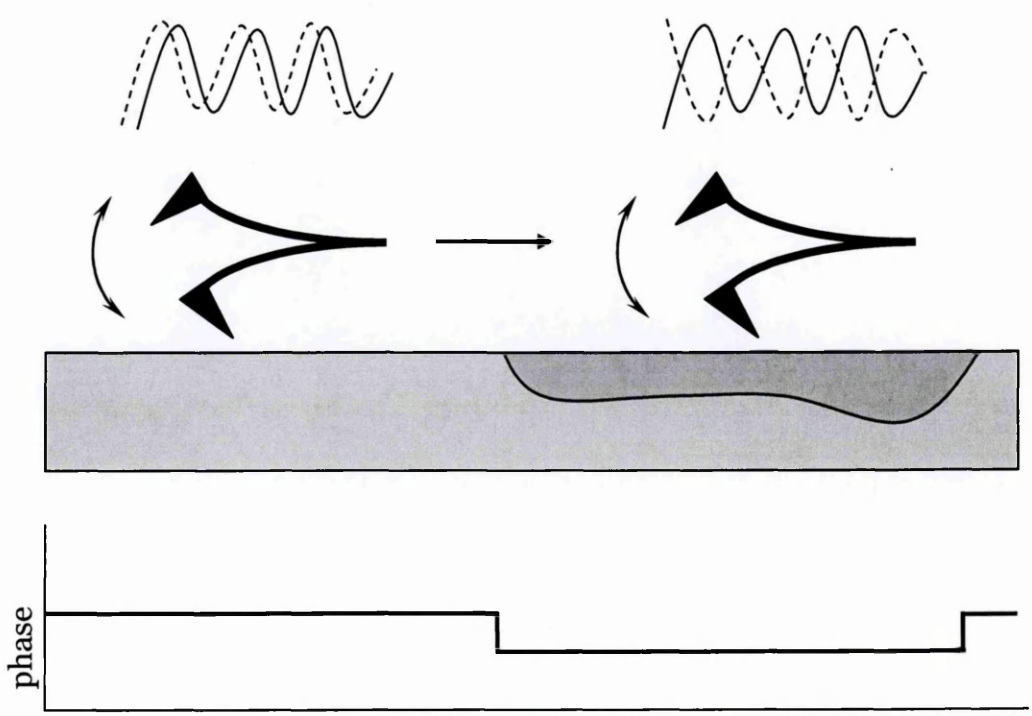

Figure 2-6. Diagram of phase imaging with the tapping mode AFM. Phase imaging measures the phase lag of the cantilever oscillation (solid wave) relative to the piezo drive (dashed wave). Spatial variations in sample properties cause shifts in the phase of the two waves, which are mapped to produce phase images.

Apart from the feedback loop adjustment, the quality of the image depends critically on the sharpness of the tip (Figure 2-7). When the scanned sample is extremely flat the resolution of the image is determined mostly by the diameter of the tip end. Sometimes the tip might be additionally sharpened by a glow discharge or by growing nanotubes at the end of the tip (Akita et al., 1999; Bunch et al., 2004).

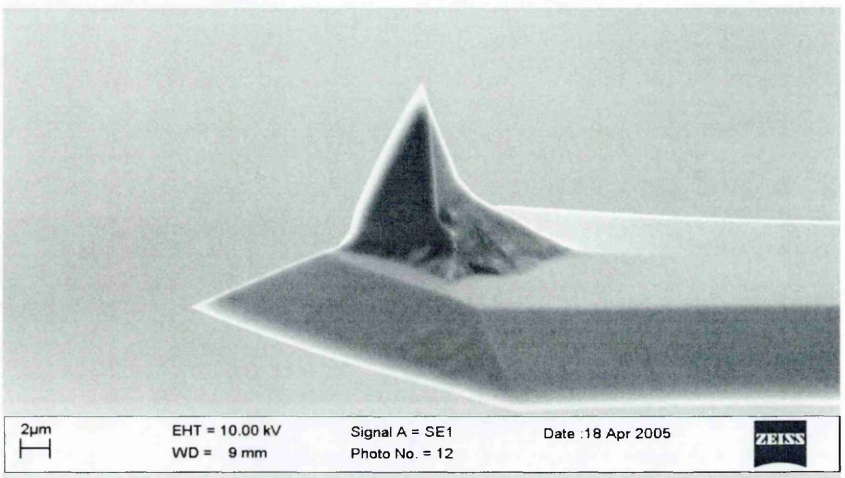

Figure 2-7. Electron Microscope picture of the tapping mode tip.

AFM has been used to study many biosystems and biomolecules (Fotiadis et al., 2002; Santos and Castanho, 2004), for example: human ocular mucins (McMaster et al., 1999), human amylin fibrillar assemblies, human erythrocyte aquaporin, bacterial layers and liposomes (Muller et al., 1997) but the greatest advanced have been made in the study of DNA. Because of high resolution provided by AFM it is now possible to investigate not only single nucleosome structure (Davies et al., 2005) but also complexes between DNA and restriction enzymes (Anselmetti et al., 2000), drugs (Berge et al., 2002; Onoa et al., 1998), and even dynamic protein-DNA interactions (van Noort et al., 1998). Using the attractive force between the tip and a DNA molecule it is possible to manipulate DNA, stretch or even cut it in any desired position and then collect the fragment for further examination with the AFM tip (Lu et al., 2004; Zlatanova and Leuba, 2002)

AFM has also been widely used for imaging and quantification of radiation damage by UV (Lysetska et al., 2002), ionising radiation and high energy electrons (Pang et al., 1996) and γ-rays (Murakami et al., 2000). Some interesting studies have also been made using neutrons (Pang et al., 1998) as bombarding beam. When AFM is used, damage quantification is realised by measuring the length of fragments that appear after irradiation and comparing them with the length or form of DNA from non treated sample. In most cases comparison with gel electrophoresis was performed.

Another way for improving the image of soft (bio) samples is by performing the measurements in their natural environment, liquid. To perform such experiment, a special part needs to be installed to cover the AFM parts from the liquid, allowing only the cantilever to operate in it (Wright and Revenko, 2004). There have been some studies made on the differences in the images obtained for dry samples and ones obtained in the presence of liquid (Lyubchenko et al., 1993), namely in the water conditions DNA supercoils are looser than in case of the dried samples. Also the interactions of DNA with other molecules, such as ethidium bromide, (Utsuno et al., 2001) and complexes with proteins (van Noort et al., 1998) and even the motion of those molecules itself (Rippe et al., 1997). Theoretical dependence on cantilever properties and the quality of phase images has been determined (Garcia et al., 1998; Tamayo and Garcia, 1997) as well as interaction between tip and the sample (Garcia and San Paulo, 1999).

As AFM is a very useful tool for imaging biomolecules, a lot of studies have been made to optimise the substrates for biological specimens (Hansma, 2001; Muller et al., 1997). Many studies have been made of materials such as gold (Csaki et al., 2001; Davies et al., 2005), graphite (Klinov et al., 2003), sapphire (Yoshida et al., 1998) or diamond (Yang et al., 2002; Yang et al., 2004) but no reasonable results had been reported for imaging plasmid DNA on such surfaces.

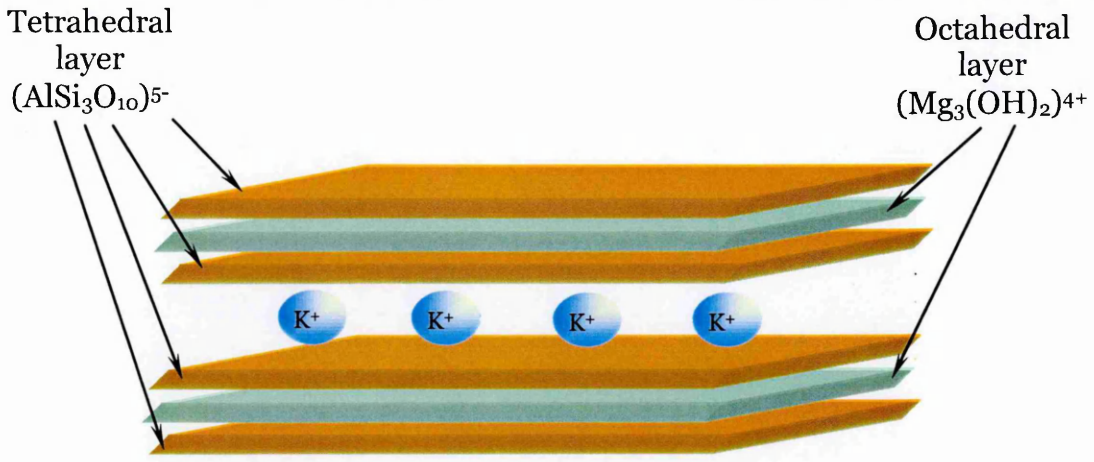

Figure 2-8. A scheme of an example of mica structure.

The most commonly used substrate for depositing DNA and imaging with AFM is mica. Mica itself is a kind of multilayer silicate with alternating sequence of tetrahedral and octahedral layers, presented in Figure 2-8. Depending on the contents of the octahedral layer, different types of mica exist.

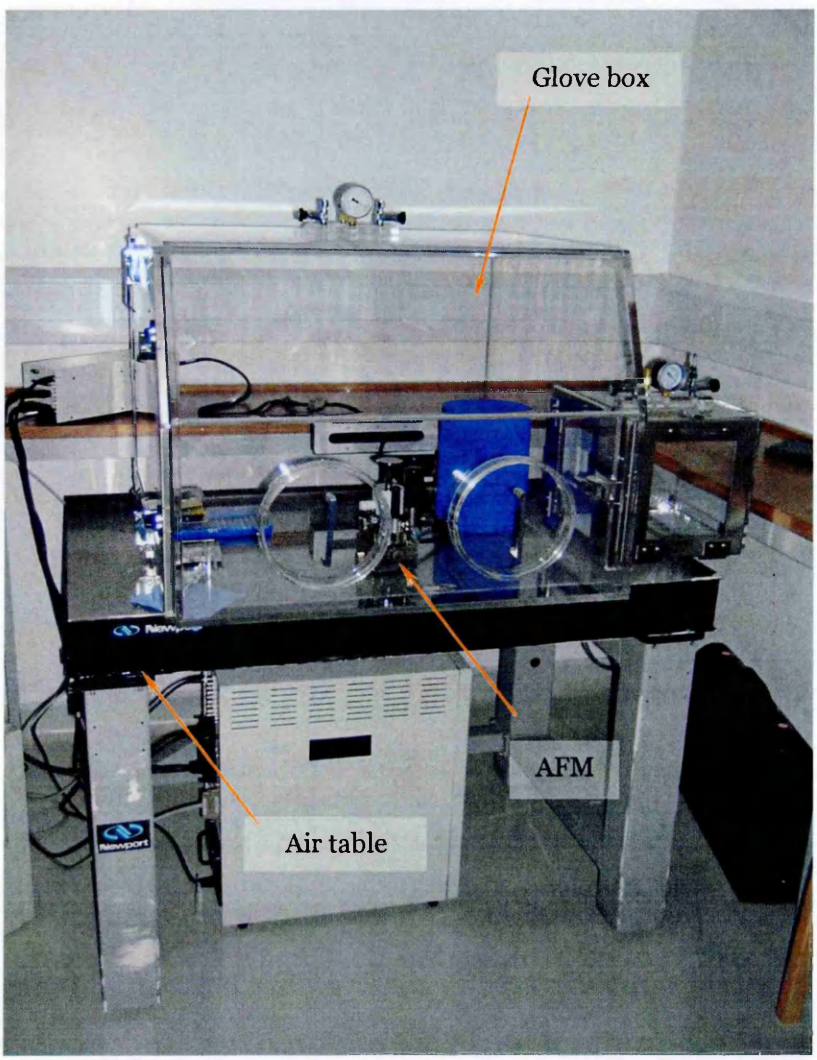

Figure 2-9. AFM system used in measurements at the Open University.

For all the investigations shown in this work a Veeco Explorer atomic force microscope was used (see also Figure 2-3). To reduce the influence of external factors, such as light or vibrations, the whole instrument was placed in a glove-box on the air table. The whole system is shown in Figure 2-9.

2.3 ELISA assay

Typically the amount of SSBs and DSBs in the irradiated samples was determined by AGE. In case of determining the amount of DSBs this method is sufficient, whereas in case of SSBs an implicit assumption is being made, namely that the only molecules that possess a SSB form a relaxed band on the gel and that there is just one SSB per molecule. Such an assumption does not have to be true as both the molecules forming the relaxed and linear bands can contain multiple SSBs. This situation is illustrated in Figure 2-10.

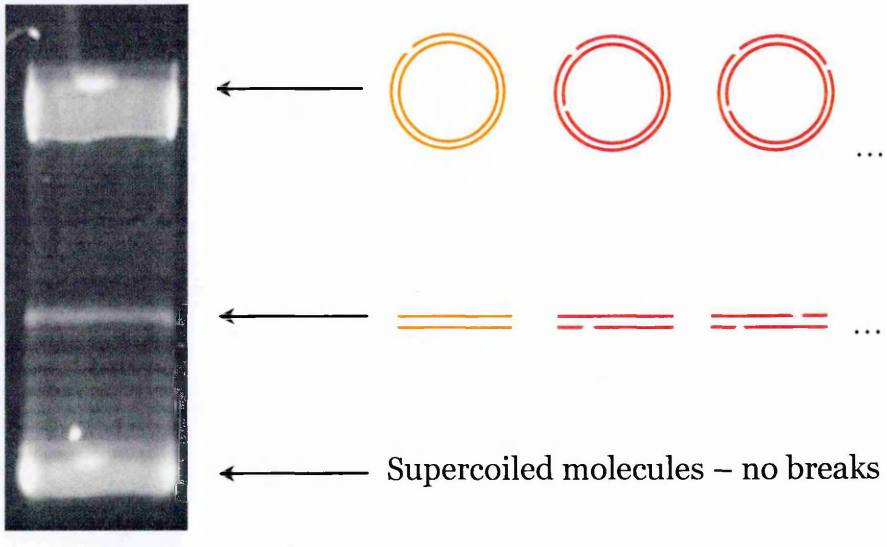

Figure 2-10. Plasmid DNA molecules that can form the relaxed (upper) and linear (middle) band on AGE.

To determine accurately the level of SSBs in the samples that underwent UV irradiation a new assay was tested. A new method should allow for labelling all SSBs and therefore it should be possible to calculate the cross sections for SSB

formation more accurately. The new method was based on the TUNEL (Terminal deoxynucleotide transferase dUTP Nick End Labelling) assay, which is used for labelling of SSBs in cellular DNA to detect apoptotic (dying) cells (Chen et al., 1997). The assay has been translated into ELISA (Enzyme-Linked ImmunoSorbent Assay) conditions (see Harrison et al., 1997, for an example of an ELISA assay on which the current method was based).

The new assay employs labelling of the 3'-hydroxyl ends with brominated deoxyuridine triphosphate (BrdUTP) nucleotides which are the most probable to be generated upon the SSB formation. The reaction is catalysed by the terminal deoxynucleotidyl transferase (TdT) enzyme.

Once added, an anti-BrdU mouse monoclonal antibody (a protein used by immune system to recognise and neutralise foreign objects like bacteria or viruses) can be attached to it. Another step might require addition of anti-mouse antibody that has horseradish peroxidase (HRP) conjugated to it if the primary antibody did not have one. Horseradish peroxidase is an enzyme (a hemoprotein) catalyzing the oxidation of hydrogen peroxide to a reactive species that oxidise a number of substrates, such as 3', 3', 5', 5'-Tetramethylbenzidine (TMB). TMB forms a blue product oxidised in the presence of horseradish peroxidase. An optical density (OD) measurement can be then taken either at 370 or 655 nm, whereas completion of the reaction (addition of a hydrochloric acid) results in a yellow product that can be read at 450 nm.

Chapter 3

Apparatus for irradiation studies and absorption measurements

3.1 Synchrotron radiation and its sources

Synchrotron radiation is electromagnetic radiation that is generated by the acceleration of charged particles moving through magnetic fields with speeds close to the speed of light. Radio waves, infrared light, visible light, ultraviolet light, and X-rays are typical components of synchrotron radiation. Such behaviour can occur naturally, e.g. when fast electrons travel through the magnetic fields in space but it can also be induced artificially in synchrotron storage rings.

A synchrotron is a particular type of cyclic particle accelerator in which the particles are deflected by a magnetic field and accelerated by an electric field. A high degree of synchronisation is required between both fields and the accelerated beam to ensure maximum performance. By varying the electric field the beam can be accelerated, whereas variation of the magnetic field ensures that the electron path will not change. In practise such a performance is realised by having some straight sections in the storage ring that are connected to one another by bending magnets. This means that instead of having a toroidal chamber the beam can be stored in round-cornered polygon ring. With such an arrangement it is then possible to use multiple bending magnets, which can later serve as light emitting points, i.e. beamlines.

Only charged particles can be accelerated in the synchrotron nonetheless such species under acceleration lose their energy by emitting photons. The maximum energy for the stored beam is reached when the energy lost during acceleration

(required to maintain the beam path) equals the energy added in each cycle. This applies to light particles, like electrons or positrons, whereas in the case of ions the energy is limited only by the strength of the magnets used to bend the beam.

Synchrotron radiation is characterized by:

- High brightness [flux/(unit source size, unit solid angle)] and high intensity [energy flux/(time)]; e.g. X-ray intensities that are many orders of magnitude higher than those produced in conventional X-ray tubes can be generated;
- High collimation – the product light beams have a very small angular divergence;
- Low emittance - the product of source cross section and solid angle of emission is small;
- Highly tuneable in energy/wavelength (sub eV up to the MeV range);
- High degree of polarization (linear or elliptical);
- Pulsed light emission - pulse durations at or below one nanosecond.

An electron beam is produced by electrons that are accelerated and accumulated at the synchrotron and then injected into a storage ring. They circulate around the ring losing energy as synchrotron radiation. Synchrotron light is produced by bending magnets and insertion devices (undulators or wigglers) in storage rings, shown in Figure 3-1.

The radiation from the synchrotron beam is projected at a tangent to the electron storage ring (see c) in Figure 3-1) and directed towards 'beamlines'. Such beamlines are usually situated next to the bending magnets, i.e. on the corners of the ring or next to the insertion devices located in the straight sections of the storage ring. Beamlines that operate on the UV light are usually situated by the bending magnets.

The most important parameter in positioning a beamline is to produce a high photon flux in a small area. The way the beamline is designed depends purely on its purpose. All experiments are performed at the end of the beamline.

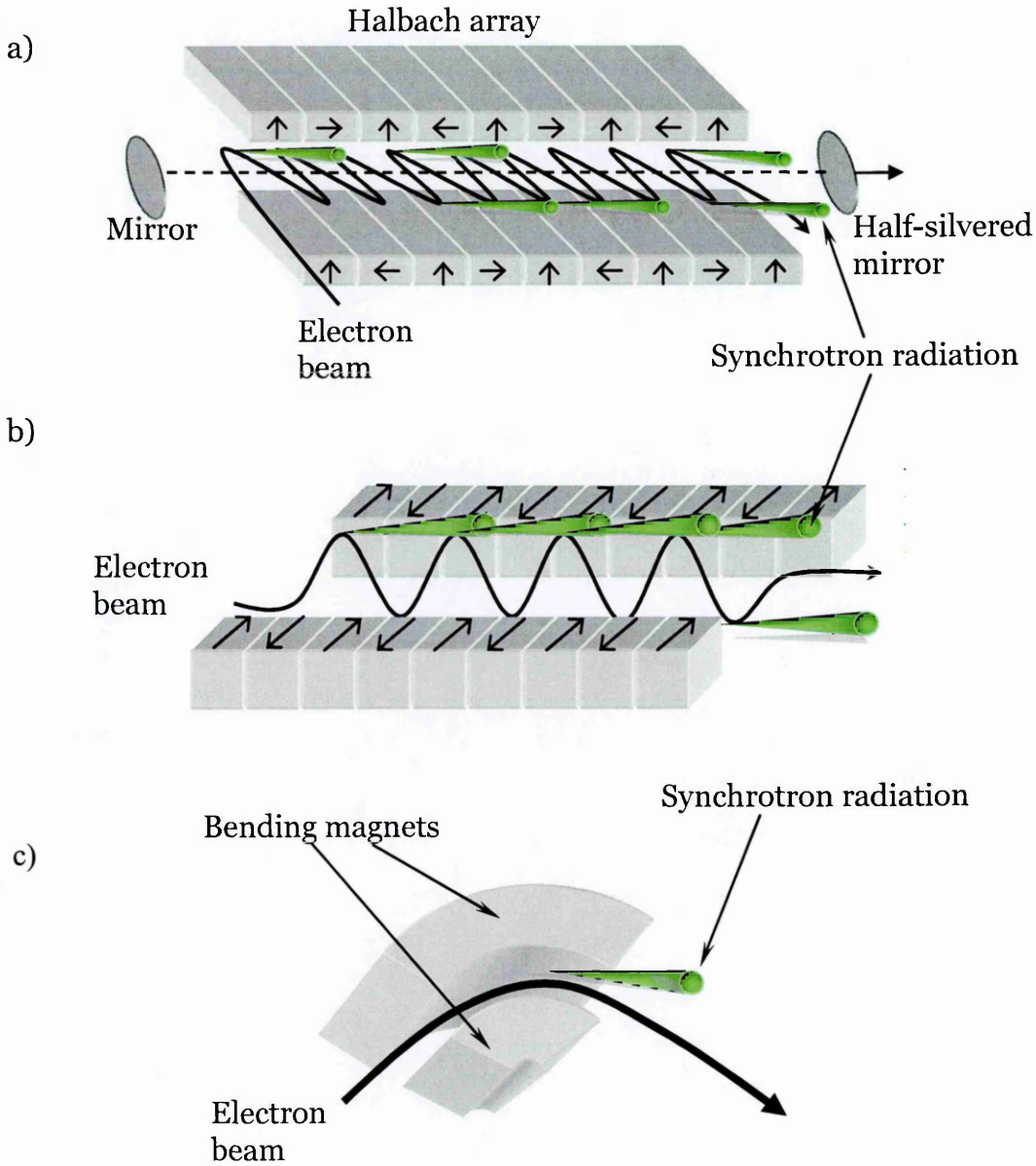

Figure 3-1 a) wiggler, b) undulator, c) bending magnet.

3.1.1 ASTRID - synchrotron radiation source at Aarhus University, Denmark

In this work ASTRID synchrotron facility at Århus, Denmark, was used. ASTRID (Aarhus STorage RIng in Denmark) is a small (40 m circumference) dual purpose

storage ring which has been in operation since 1990 (Figure 3-2). The Synchrotron Radiation (SR) research program is focused on the following areas:

- Atomic and Molecular Physics;
- Surface and Materials Science;
- X-Ray Imaging;
- Spectroscopy of Biological Materials.

Originally both ion and electron storage used to alternate over the ASTRID operational cycle, whereas now ASTRID operates mostly in electron mode. The ring functions in electron mode at a typical energy of 580 MeV, injected from a 100 MeV racetrack microtron (a small electron accelerator).

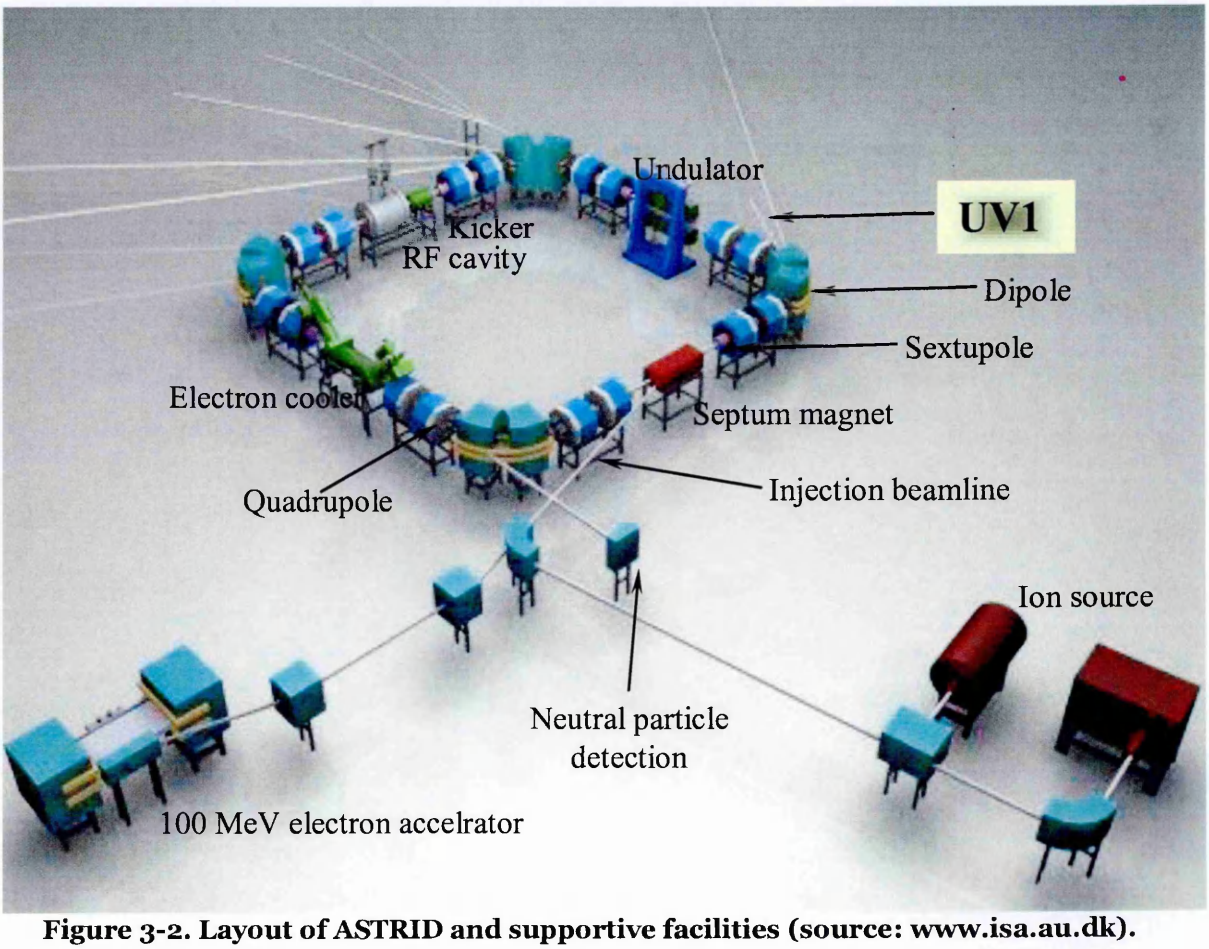

Figure 3-2. Layout of ASTRID and supportive facilities (source: www.isa.au.dk).

Presently ASTRID has 8 operational beamlines, whose energy spans from about 1.5 eV to about 1 keV.

3.1.2 Beamline UV1

The ultra violet beamline, UV1, has been designed to cover the low photon energy region from about 100 to 700 nm using two gratings. The monochromator has been designed to provide a high flux with a moderate resolution and to preserve a high degree of linear polarisation from the synchrotron radiation source. UV1 has been used for two major experimental programmes: UV photoabsorption spectroscopy and Circular Dichroism (CD). Figure 3-3 shows the schematic setup of the beamline.

The beamline consists of only two optical elements: a toroidal pre-mirror which provides independent horizontal and vertical focusing and a toroidal grating to disperse the synchrotron radiation.

The beamline is also equipped with interchangeable exit (100, 200, 500, 1000 μm) and fixed entrance (50, 100, 200, 500 μm) slits that allow control of the intensity of the light that is delivered to the experiment. The control of the light intensity can be also performed with manually operated apertures.

Two gratings are required to cover the whole wavelength range while maintaining satisfactory resolution (below one Å). Therefore UV1 contains a High Energy Grating (HEG) that covers the wavelength range 100-350 nm and a Low Energy Grating (LEG), which covers 200-700 nm range.

The wavelength range of the high energy grating, 100 to 350 nm, covers the most biologically important wavelength region and there is a high degree of linear polarisation of the radiation from UV1, therefore this beamline is suitable for Synchrotron Radiation Circular Dichroism (SRCD) spectroscopy of optically active macromolecules as well as irradiation studies of DNA described in this thesis.

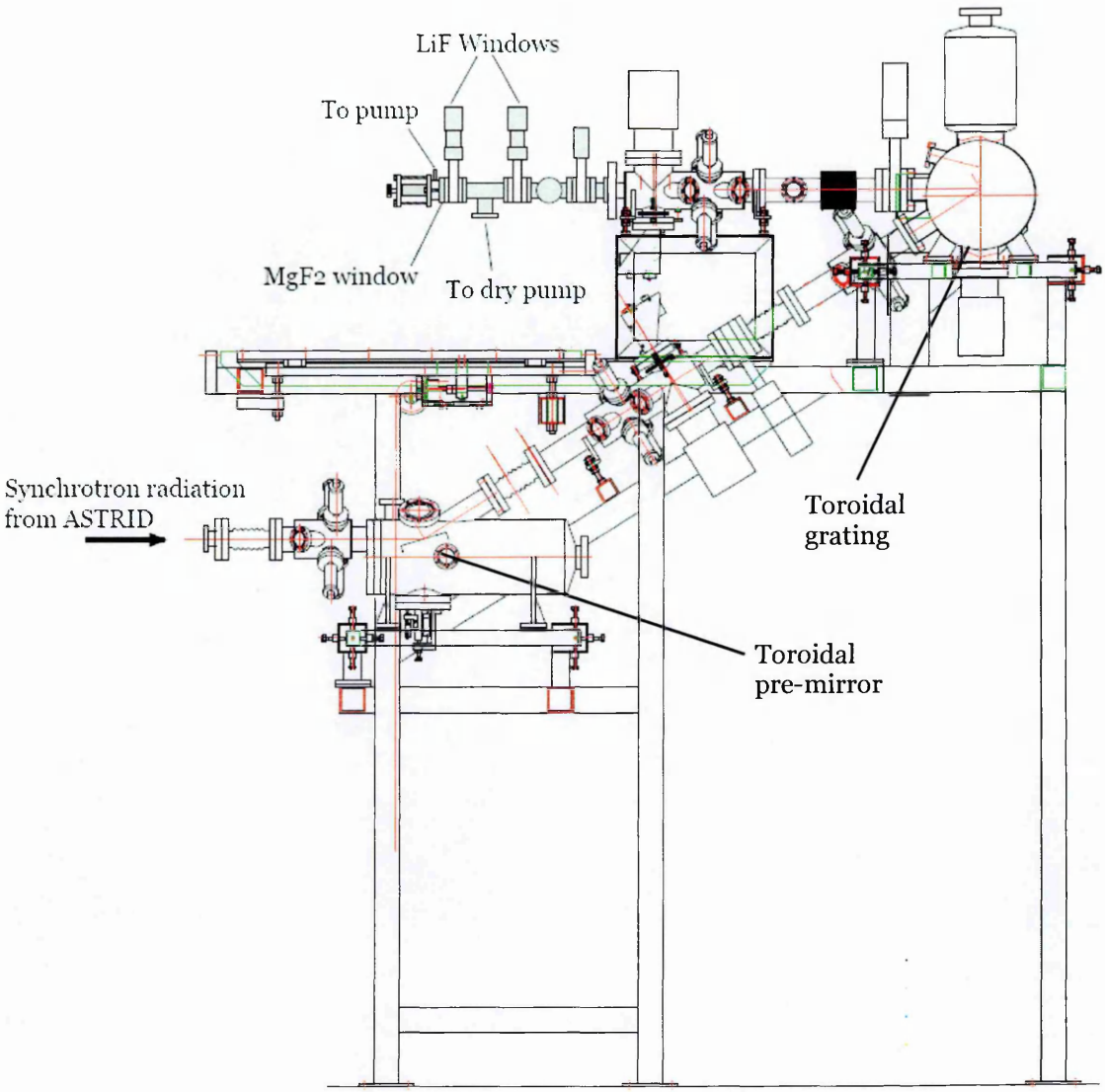

Figure 3-3. Schematic diagram of UV1 beamline with the DNA irradiation setup attached (figure made by Dr S. V. Hoffmann).

3.2 Apparatus used for VUV irradiation of DNA

The experiments were performed using a VUV apparatus assembled as a part of this project at the Open University, presented in Figure 3-4. As a source of VUV light either Xe or D_2 lamps (both purchased from Resonance, Canada) or synchrotron radiation were used. Both lamps have a sharp emission peak, Xe lamp at around 150 nm and D_2 lamp at 163 nm, and a broad, although low intensity emission band in the UV region. The emission spectra of both lamps are shown in Figure 3-5.

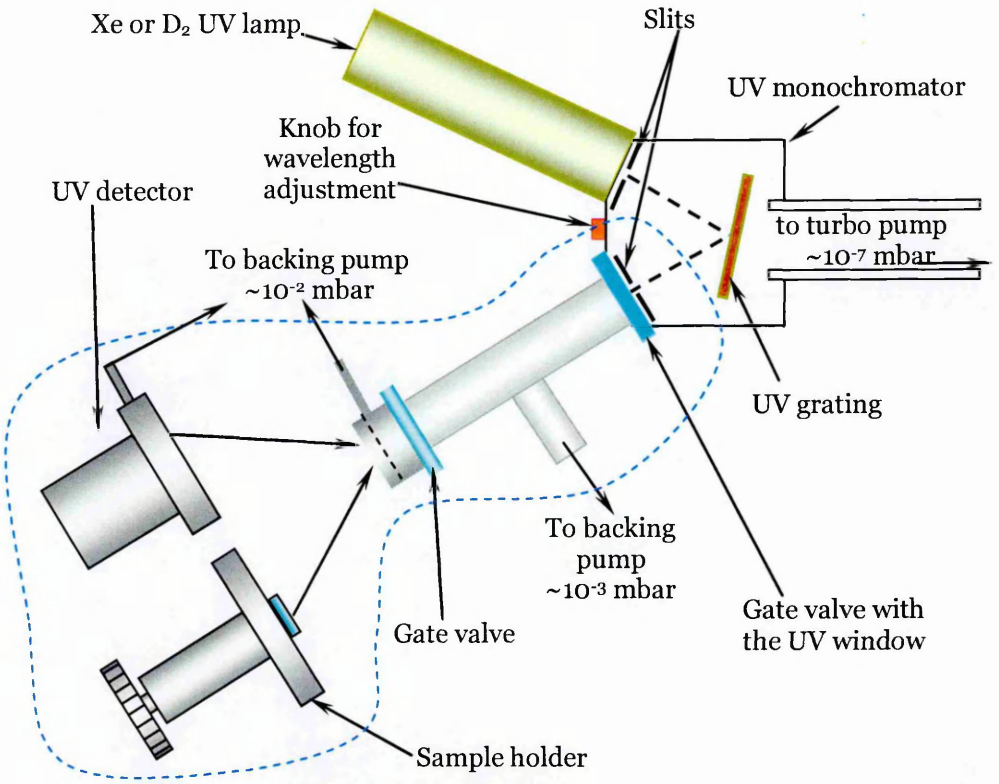

Figure 3-4. Schematic diagram of the irradiation apparatus used with UV lamps; the blue dashed line indicates those parts of equipment that can be detached and assembled onto a synchrotron beamline.

Second-order peaks (around 290 nm for the Xe lamp and 330 nm for the D_2 lamp) are also present in the spectrum. Therefore one needs to introduce air into the system, if irradiation at wavelengths longer than 200 nm is required, to remove the VUV wavelengths that contribute to the peak.

The resolution of the system can be estimated from the full width at half-maximum of the main peak of the Xe lamp at 150 nm in the figure 1-2 and is found to be ± 10 nm. To increase the resolution, two slits have been mounted on the exit and entrance of the monochromator (purchased from Resonance, Canada), each are 10 mm in length and 1 mm in width. The wavelength of interest is selected by careful adjustment of the position of the holographic UV grating and the broad spectrum that comes from the lamp cut down to the desired wavelength.

After passing through the exit slit of the monochromator, the light illuminates the surface of a VUV detector. The VUV detector used for the photon flux measurements was a GaP VUV diode with an active surface of 10.9 mm^2,

purchased from Roithner Laser Technik and calibrated over the VUV region (100 nm to 200 nm) at Phsikalisch-Technischen Bundesanstalt (PTB), Germany.

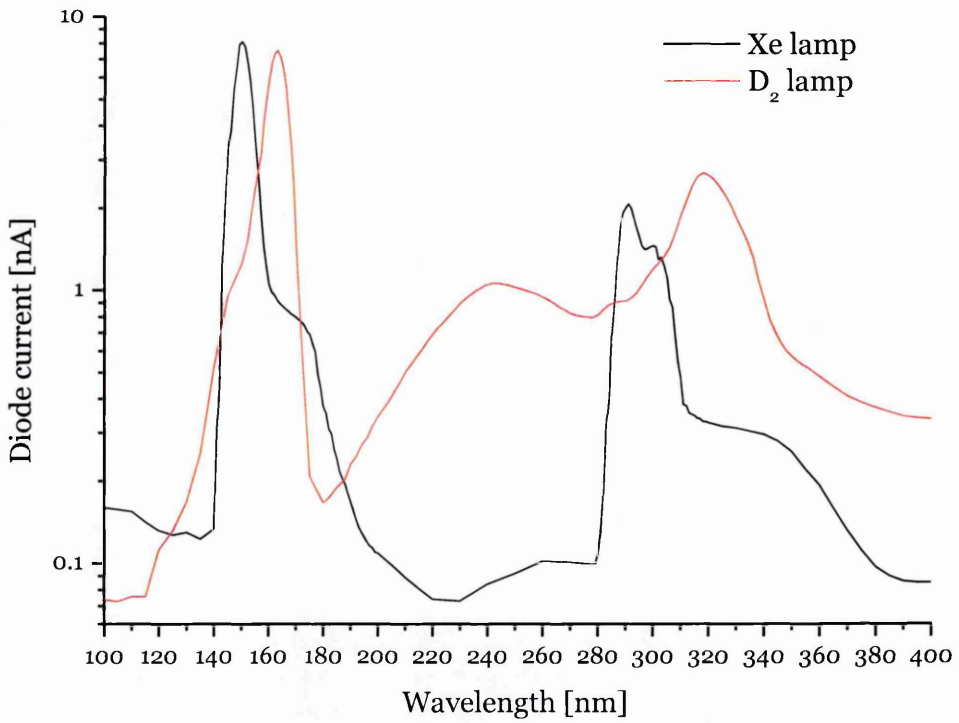

Figure 3-5. Emission spectra of the VUV lamps used in the experiments; measurements taken with 1 mm width exit and entrance slits.

Once the current was measured the irradiation time necessary for a desired dose was obtained and a sample was placed in the former position of the UV detector. Figure 3-6 presents the schematic arrangement for the sample placement.

Rotation of the sample during irradiation allows for the uniform mixing of the material, so all the molecules can reach the area of the VUV light penetration (typically a fraction of μm in water). Rotation also prevents local overheating of the sample and thus reduces the amount of damage caused by direct heating of the DNA sample.

The part of equipment that is marked with dashed blue line in Figure 3-4 can be detached from the monochromator and assembled on the synchrotron beamline, described in 3.1.2.

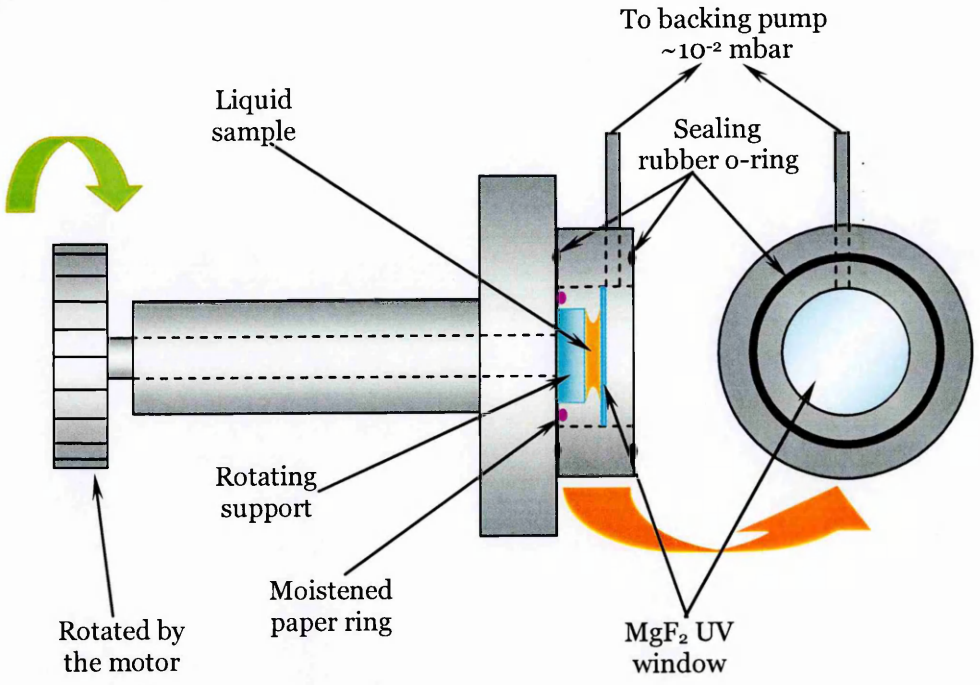

Figure 3-6. Schematic diagram of the sample holder with the sample in place.

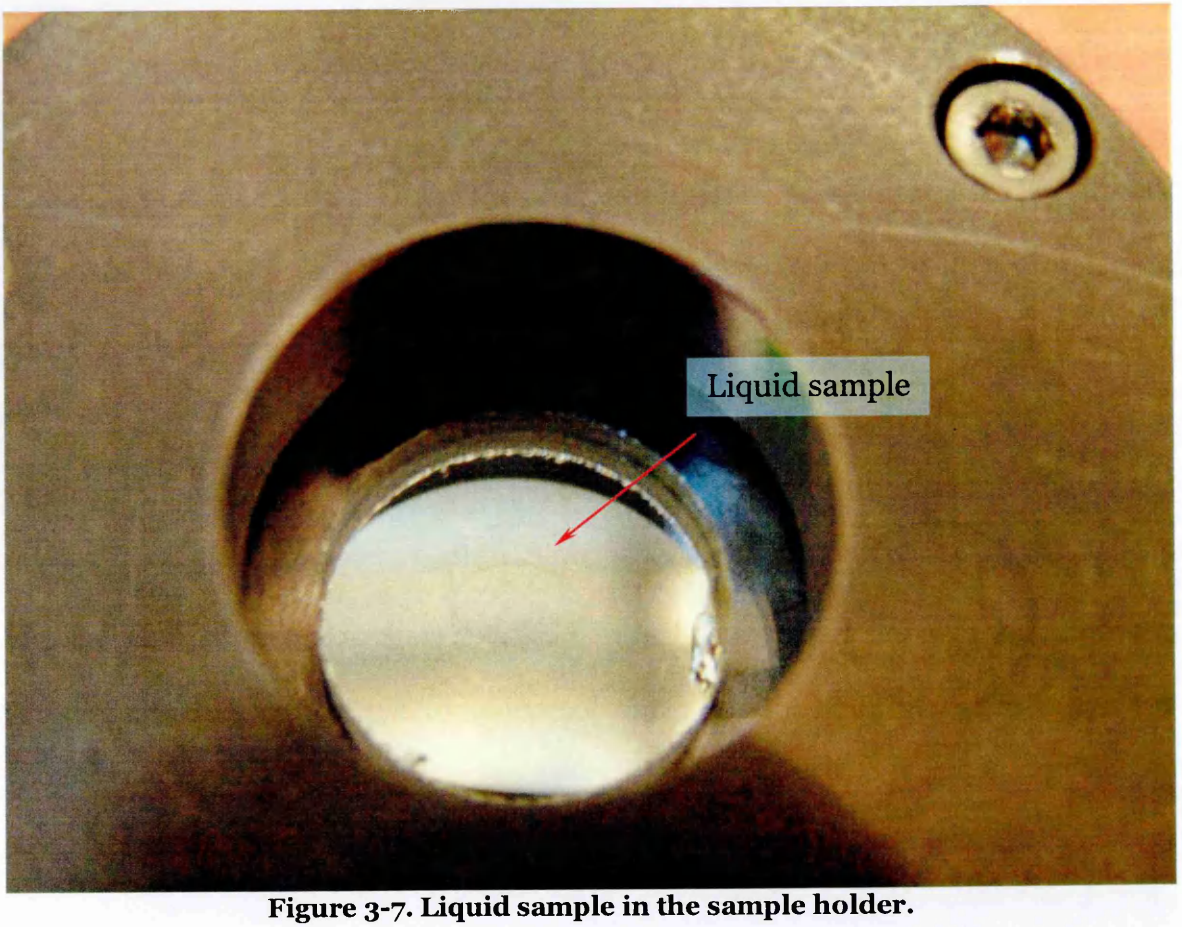

Figure 3-7. Liquid sample in the sample holder.

3.3 Apparatus for VUV absorption studies

An absorption cell was designed to study absorption of DNA films and DNA in liquid solution (Figure 3-8).

Absorption experiments were performed over two wavelengths ranges, vacuum UV and UV. It was necessary to perform the absorption scans over the VUV range (110 – 220 nm) with helium gas flowing continuously through the UV diode and the cell since molecular oxygen absorbes UV light quite strongly in that range. In the UV range, 200 – 350 nm, air was introduced to the system. The reason for introducing air into the system (oxygen especially) while scanning over the UV range was to cut off the second-order VUV spectrum. Second order VUV light might interfere with the true absorption of the sample over the UV range by adding features that are characteristic to the VUV region.

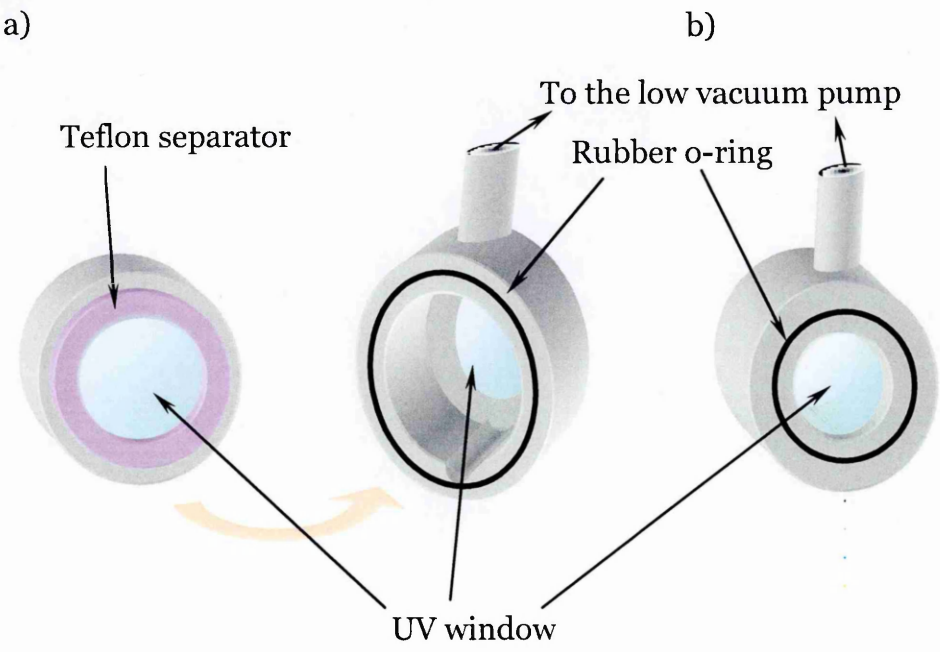

Figure 3-8. UV cell for DNA absorption measurements; a) back view; b) front view.

3.4 Apparatus used for electron irradiations of DNA samples

The apparatus used to study electron irradiation of DNA samples is shown in Figure 3-9 and was specifically designed for the irradiation of solid material.

The instrument is equipped with two independent electron sources. One of them produces highly monochromatic (of a resolution of around 1 meV) electron beams by argon photoionisation by the UV light of fixed energy of 15.795 eV from the synchrotron. The second source, which consists of a trochoidal electron monochromator (TEM), can deliver low energy (0-10 eV) electron beams with resolutions of around 300 meV and can be used in absence of the synchrotron radiation. The performed experiments employed the second type of electron source. TEM beam spot size was estimated to be of the size of the exit slit in the last electrode, which is 2 mm in diameter.

DNA samples were deposited on a tantalum substrate via a loadlock (see Figure 3-9) and, after gentle pumping down to 10^{-3} mbar, were moved up into the first UHV chamber (UHV1). At this stage it is also possible to cool the sample with liquid nitrogen down to 77 K. In the first chamber the pressure is reduced to ~10^{-9} mbar and once that is achieved, the sample is placed in the second UHV chamber (UHV2) where it is placed approximately 2 cm from the electron source.

The transmission of the incident electron current through the DNA films was measured on the sample support (tantalum disc) by connecting it to a femtoammeter. The energy resolution of the electrons generated by TEM was around 300 meV. It was determined from the rise on the onset of the electrons that can be seen in Figure 9-3.

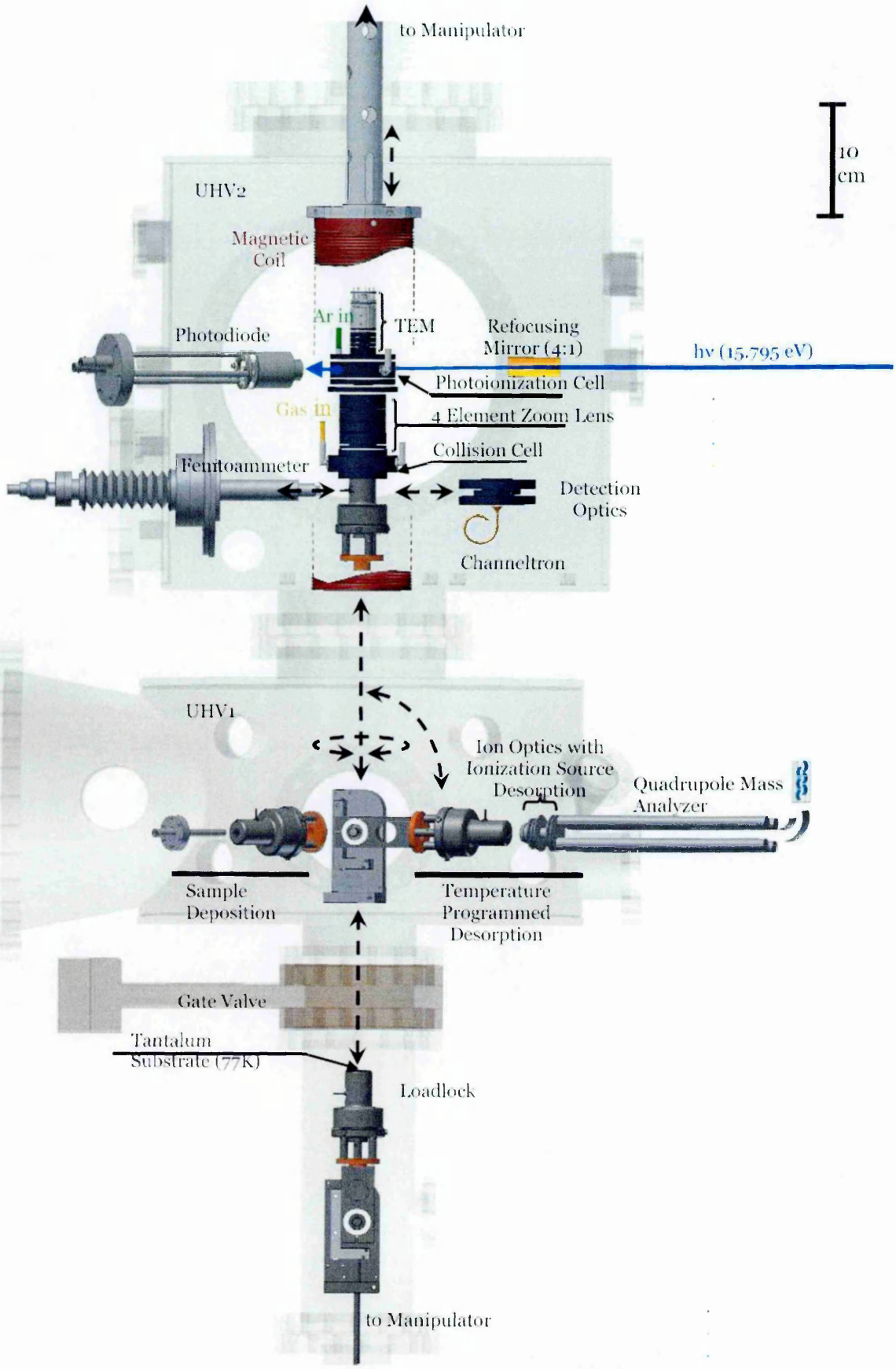

Figure 3-9. Experimental setup for dry DNA films irradiation with low energy electrons (figure made by Dr Nykola Jones).

Chapter 4

Plasmid DNA preparation and purification

Plasmid DNA pBR322 was prepared by purification from the *Escherichia coli* (*E. coli*) bacteria cultures grown on the Luria-Bertani medium. For purification commercially available kits were used (from QIAGEN). The quantification was done by absorption at 260 nm measurements and quality (amount of supercoiled DNA compared to the content of relaxed and linear forms of plasmid present in the sample after purification) was estimated from agarose gels.

4.1 Protocol for bacteria growth and plasmid DNA purification

Bacteria colonies were grown in presence of ampicillin (Sigma, working concentration 50 μg/ml) as a selective antibiotic. Agar plates were prepared by dissolving 20 g of Luria-Bertani (LB) medium (Sigma) and 7.5 g of agar (Sigma) in 1 L of UHP water. The solution was then autoclaved and once cooled down to about 35 °C, ampicillin (Sigma) solution (in water, sterilised through 35 micron Waterman filter with a syringe) was added to obtain a working concentration of 50 μg/ml. This mixture was then poured into Petri dishes (25 ml per each plate) and cooled down to set at room temperature.

Once set, bacteria from the glycerol stock were transferred onto plates and incubated at 37 °C overnight. On the following day the plates were removed from the incubator and single colonies were collected from the plates and inoculated in 10 ml of LB medium each of 50 μg/ml of working concentration of ampicillin for approx. 12 h in shaker-incubator at 37 °C, until bacteria reached their mid-log phase (OD_{600} 1.3). Aliquots (0.25 ml) of that culture were transferred into the flask

containing 50 ml of ampicillin-LB and incubated for 4 h, until the beginning of the mid-log phase was reached (OD_{600} 0.6).

After primary incubation, 10 ml of the colony was transferred into 1 l flask containing 200 ml of LB-ampicillin medium each, and incubated for further 3 h, until the beginning of the mid-log phase was reached (OD_{600} 0.6). 5 ml of the colony was removed for plasmid prep analysis (stage 1). Colony was incubated for further 4 h and OD_{600} was determined to be 1.6. In addition, 5 ml of culture was removed for the plasmid prep analysis (stage 2).

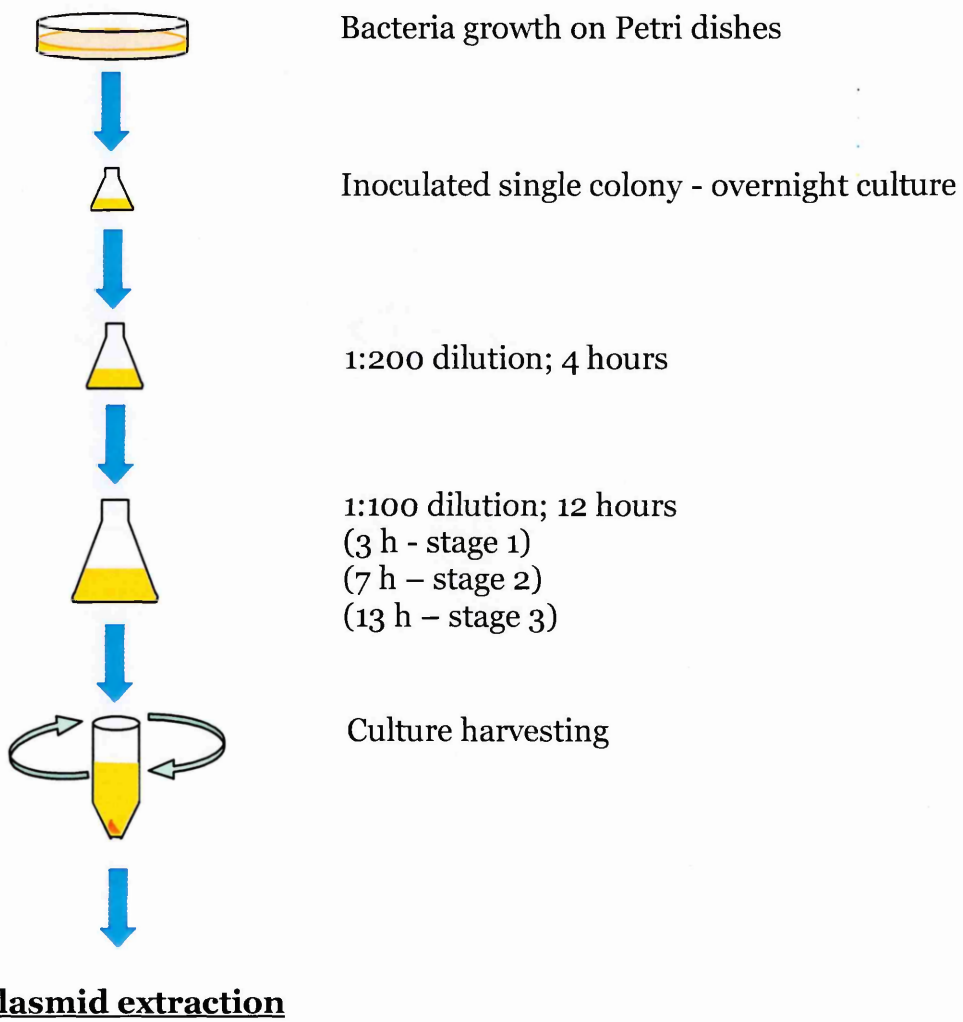

Figure 4-1. Flow chart of bacteria culture growth.

Bacteria culture was incubated for further 6 h at 37 °C in a shaker incubator and 5 ml of the culture was removed for the plasmid prep analysis (stage 3) and the

OD_{600} was found to be 1.6. All collected fractions of bacteria cultures from different stages were spun at 8000 revolutions per minute and masses of the dried pellets were measured (see Table 4-1).

Plasmid was extracted from the bacteria using a QIAGEN spin mini prep kit, according to the enclosed protocol (see Appendix A). Plasmid was eluted into 60 µl of UHP water (pH 8.0 adjusted with 1 M NaOH) and analysed using UV spectrophotometer to determine plasmid concentration and the protein content (Table 4-1). The ratio between supercoiled form of DNA and linear and relaxed forms fractions in the purified samples was determined via AGE.

Table 4-1. Results obtained for the experiments on the bacteria growth.

Stage	Bacteria mass per 1 ml of the culture [mg/ml]	Plasmid yield [µg]	$A_{260/280}$	Plasmid yield per 1 mg of bacteria culture [ng/mg]	$\frac{\text{supercoiled}}{\text{linear + relaxed}}$
1	2	0.7	1.971	68.0	8.5
2	7	2.7	2.017	77.5	7.0
3	6.6	3.0	1.978	90.4	6.6

Another 5 ml of bacteria culture was harvested and plasmid was extracted as described in Appendix A with the difference that volumes of resuspension, lysis and inactivation/binding buffers were doubled. Increasing amounts of those buffers was beneficial as the culture density was quite high (OD_{600} 1.6) so the purity of the plasmid should be greater. Table 4-2 presents the results obtained in this experiment.

Table 4-2. Plasmid purification from even amounts of cultured bacteria.

Bacteria mass per 1 ml of the culture [mg/ml]	Plasmid yield [µg]	$A_{260/280}$	Plasmid yield per 1 mg of bacteria culture [ng/mg]
2	2.8	1.902	281.5

It can be seen from Table 4-2 that the purity of the plasmid extracted improved when compared to the samples shown in Table 4-1. Plasmid purity improved as the $A_{260/280}$ ratio decreased and the relative amount of plasmid obtained per 1 mg of bacteria culture significantly increased.

4.2 Chloramphenicol amplification of plasmid yields.

Early work of Clewell and Helinski (1969) indicated that as in case of other known factors, such as SDS, sarkosyl or heat treatment, growth of *E. coli* culture with the additional incubation with chloremphenicol (CAM) resulted in the appearance of the relaxed form of plasmid-protein complex to a greater extent than in the case of the culture grown without it. In their later work (Clewell and Helinski, 1970) reported a linear increase of the plasmid ColE1 yield upon incubation with chloremphenicol, although the authors claimed the amount of relaxed DNA form was unchanged when compared with the levels found prior addition of chloremphenicol. It was also reported (Amati, 1970) that addition of chloramphenicol during phage development in *E. coli* decreases both the synthesis of the bacterial as well as the phage DNA. This suggests that chloramphenicol is inactivating proteins used for the replication *E. coli* DNA as well as those used for the amplification of phage DNA.

All these observations supported an earlier conclusion (Wisseman et al., 1954) that chloramphenicol strongly inhibits protein synthesis by suppressing assimilation of ammonia associated with the synthesis.

It was later shown (Clewell, 1972) that during incubation in the presence of chloramphenicol, plasmid DNA replicates long after chromosomal DNA replication has terminated. After addition of chloramphenicol the rate of DNA synthesis also increases. After 4 hours of incubation the level of chromosomal DNA did not change anymore and could be used to normalise the level of plasmid that underwent replication. It was shown that after exposure to chloramphenicol, plasmid replicates at a linear rate for several more hours before reaching a plateau. Clewell determined that the change of replication rate of the plasmid increases from 0.48 copies/min to 4.1 copies/min upon chloramphenicol treatment. From measurements earlier in the colonies growth they concluded that before the rate

becomes linear, it exhibits a logarithmic nature. It was not clear to the author why such a phenomenon occurs – one possible explanation was that as the synthesis of the genomic DNA was blocked, the excess amount of replicating enzymes is causing every single plasmid molecule to be a template for the next one until saturation resulting from the amount of replicating enzymes is achieved. It has also been suggested that it is the nitro group of chloramphenicol that is responsible for its action (Smith and Worrel, 1953).

In later work (Clewell and Helinski, 1972) it was reported that in the presence of chloramphenicol there is a relaxation induced in plasmid DNA–replication protein complex. Accumulated this way amount of plasmid is 3 times greater than in case of the colonies not treated with chloramphenicol and additional molecules appear as non-complexed, covalently closed molecules, which, during replication upon chloramphenicol treatment, freely associate themselves with or dissociate from the protein components of the relaxation complex.

The overall influence of chloramphenicol on the DNA replication in *E. coli* bacteria was studied by Lark (1973). Results indicate that the cycle of replication requires two types of proteins to be synthesised: one that is sensitive to low concentrations of chloramphenicol (< 50 $\mu g \cdot ml^{-1}$) and another that is rather resistant to low doses but is susceptible to higher concentrations of the drug (≥ 150 $\mu g \cdot ml^{-1}$). These results were confirmed by Jackson *et al.* (Jackson et al., 1977), who studied the influence of both optical isomers of CAM, D(-)CAM and L(+)CAM, on strand break formation in *E. coli* and *S. typhimurium*. From their negative results for two chloramphenicol analogues lacking the nitro group (L(+)-p-methylsulphonyl and L(+)-p-methylthio chloramphenicol) they concluded that the nitro group is necessary for DNA damage.

It was shown (Donoghue and Sharp, 1978) that there is no correlation between chromosomal and plasmid ColE1 DNA as it amplifies for several hours after CAM-

treated *E. coli* cells were infected with phage DNA. It was concluded that there were no plasmid-encoded proteins present in the host cell that were required for the amplification – just the host-specified ones that recognise certain sites in the plasmid sequence.

A three-fold increase in the amount of pBR322 (ColE1-type one) plasmid recovered was observed from the preparation method that incorporated medium enriched with nucleotides as well as CAM treatment (Norgard et al., 1979). The appearance of linear and nicked circle forms was reported as a result of the purification method used. The majority of the recovered form was reported to be supercoiled. Changes in the pBR322 concentration as well in its replication inhibitor, RNAI, and preprimer, RNAII, were observed in the *E. coli* strain K12, grown on the Luria Bertani (LB) medium containing 10ug/ml ampicillin (Linchao and Bremer, 1986b). It was noted that although the copy number decreased, the amount of plasmid molecules per cells increased, yet the plasmid concentrations per unit of the cell mass decreased as well. It was reported that even though the concentration of both RNAI and RNAII decreased, the ratio RNAI/RNAII, increased. As a consequence the plasmid replication was inhibited. In another experiment (Linchao and Bremer, 1986a) they proved that upon incubation with CAM, the synthesis of RNAII discontinues thus the amplification rate of the plasmid decreases.

Increased amplification at low (10-20 μg/ml) concentrations of CAM was reported for K12 strains of *E. coli* hosting pBR322 plasmid DNA (Frenkel and Bremer, 1986), that possesses a *rel*A$^+$ gene and thus exhibits a stringent response. It was reported that at high concentrations of CAM in both cases reduced final concentration of plasmid DNA in cells.

The decomposition of chloramphenicol by bacteria was investigated (Smith and Worrel, 1950) with the attention being placed upon the formation of possible

decomposition products. It was shown that bacteria are able to hydrolyse the amide linkage, reducing the nitro group, oxidizing the secondary hydroxyl group, and bringing about the cleavage of the molecule between the first and second carbons of the propanediol (IPA) part of the molecule.

Simultaneously to the culture grown as described in 4.1 a second culture was grown from the same colony from agar plate but with the difference that during bacteria cultures incubation chloramphenicol (Fluka, working concentration 170 μg/ml in ethanol) was added to increase the yield of plasmid (see Figure 4-2 for diagram of the incubation).

The same protocol was adopted as described in 4.1 was used with the difference at stage 1 where after 3 hours of incubation the second antibiotic was added. Colonies were then incubated for further 4 hours and OD_{600} was measured to be 0.5. At all the same stages 5 ml of cultures were removed for the plasmid prep analysis and OD_{600} values were measured. Table 4-3 shows the comparison between the results obtained in this experiment and the one described in 4.1.

Table 4-3. Comparison of results obtained for bacteria grown in presence and absence of chloramphenicol.

		Bacteria mass per 1 ml of the culture [mg/ml]	Plasmid yield [μg]	$A_{260/280}$	Plasmid yield per 1 mg of bacteria culture [ng/mg]	$\frac{\text{supercoiled}}{\text{linear + relaxed}}$
Stage 1	No CAM	2	0.7	1.971	68.0	8.5
	No CAM	2.2	0.7	1.985	60.9	9.0
Stage 2	No CAM	7	2.7	2.017	77.5	7.0
	CAM	1.8	1.3	1.953	148.6	6.5
Stage 3	No CAM	6.6	3.0	1.978	90.4	6.6
	CAM	2.6	1.7	1.95	128.3	6.0

Samples of obtained plasmid DNA were also analysed with agarose gel electrophoresis for the possible influence of chloramphenicol incubation on the plasmid relaxation (again, see Table 4-3). There was no distinguishable effect of

CAM incubation on the loss of supercoiled DNA form due to nicking during bacteria incubation. From the results presented in Table 4-3 it can be see that there is a rapid growth in the yield of plasmid molecules per bacteria cell once chloramphenicol was added to the culture.

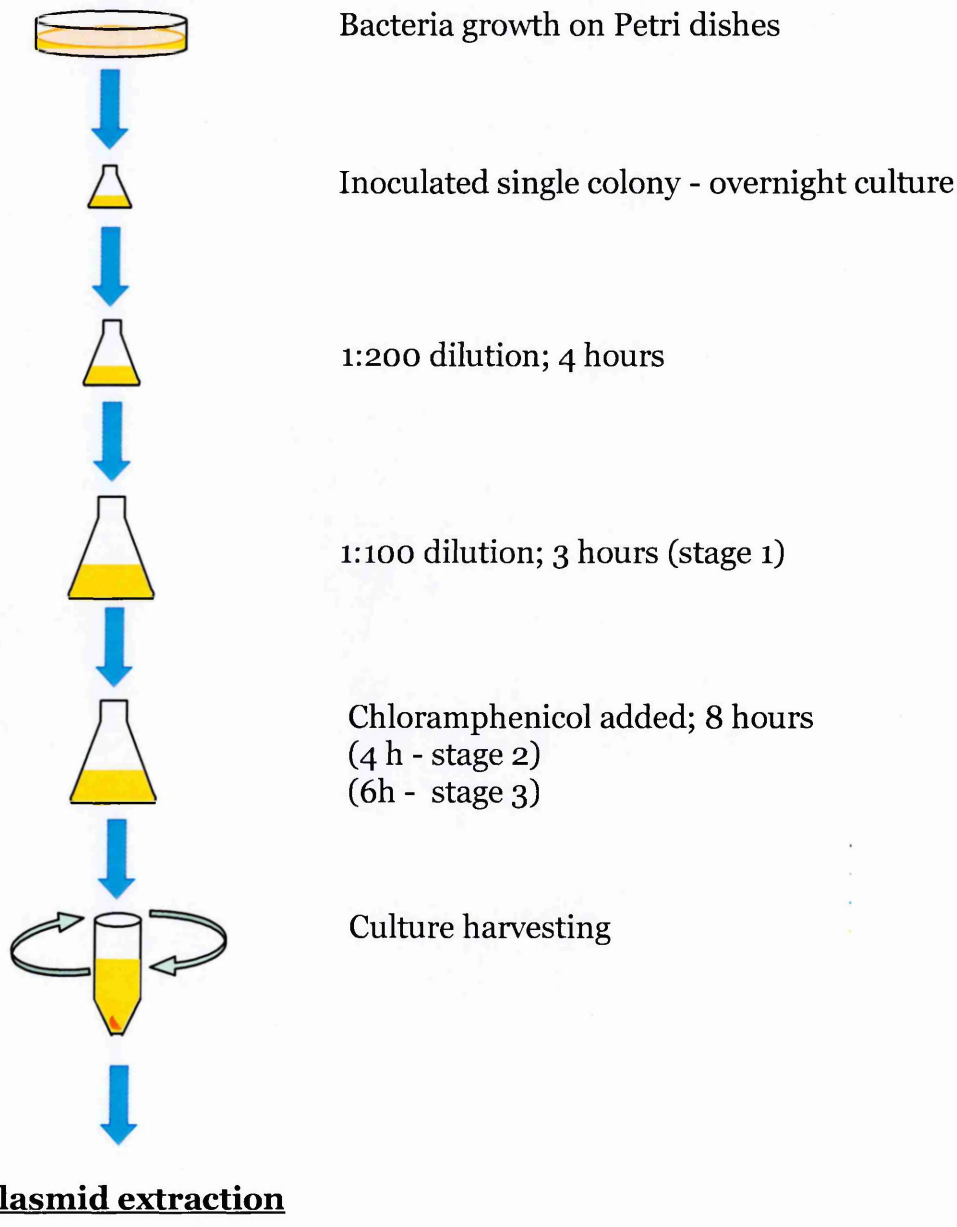

Figure 4-2. Flow chart of bacteria culture growth in presence of chloramphenicol.

The remaining bacteria cultures were harvested in the volume ratio of 1:3 of AMP : AMP+CAM to give the same amount of bacteria (10 mg), i.e. 5 ml : 15 ml.

Plasmid was extracted as described in Appendix A with the difference that volumes of resuspension, lysis and inactivation/binding buffers were doubled. Table 4-4 presents the results obtained in this experiment. It can be seen that the amount of plasmid that can be obtained from the same amount of bacteria can be almost doubled by adding chloramphenicol.

Table 4-4. Comparison of results obtained for bacteria grown in presence and absence of chloramphenicol; plasmid purification was made from even amounts of cultured bacteria.

	Bacteria mass per 1 ml of the culture [mg/ml]	Plasmid yield [µg]	$A_{260/280}$	Plasmid yield per 1 mg of bacteria culture [ng/mg]
No CAM	2	2.8	1.902	281.5
CAM	0.7	4.8	1.932	480.0

4.3 Bacteria growth in the presence of various concentrations of chloramphenicol

Bacterial colonies were tested for their response to various concentrations of chloramphenicol with respect to the yield of plasmid DNA that was obtained and its purity ($A_{260/280}$ ratio).

Each treatment was performed on three independent colonies; therefore, it was possible to determine the standard deviation for each measurement taken.

The protocol from 4.2 was used and after 3h incubation (stage 1) chloramphenicol solutions in EtOH (equal volumes of alcohol) were added to all colonies to obtain working concentrations of: 0, 10, 25, 100, 170 and 250 µg/ml. Cultures were then incubated overnight in the shaker at 37 °C. Next day cultures were harvested by centrifugation at 4 °C, 8500 rpm and bacteria pellets were air-dried. Once dried, the pellets were weighted and their mass was established (see Table 4-5). The decrease in the yield of bacteria in colony with increase of chloramphenicol can be clearly seen.

Table 4-5. Bacteria mass after chloramphenicol treatment.

Working concentration [μg/ml]	0		10		25		100		170		250	
	value	St. dev.	value	St. dev.	value	St. dev.	value	St. dev.	value	St. dev.	value	St. dev.
Bacteria mass per 1 ml of culture [mg/ml]	4.35	0.39	1.69	0.41	1.43	0.40	1.29	0.36	1.46	0.19	1.57	0.30

Plasmid DNA was purified from bacteria as described previously in 4.2. Plasmid DNA was eluted from the binding column with 70 μl of 10 mM Tris-Cl (pH 8.3) buffer. Samples were examined both with agarose gel electrophoresis as well as UV spectrophotometry to determine both their purity and concentration. UV spectrophotometer readings allowed determination of the exact amount of plasmid DNA obtained and whether it is free from protein or RNA impurities (see Table 4-6). It can be seen that the purity of plasmid improves with the increase of the antibiotic concentration.

Table 4-6. Plasmid quantification using UV-spectrophotometry.

Working concentration [μg/ml]	0		10		25		100		170		250	
	value	St. dev.	value	St. dev.	value	St. dev.	value	St. dev.	value	St. dev.	value	St. dev.
Plasmid mass [μg]	4.9	0.1	2.3	0.2	1.8	0.2	1.5	0.1	1.8	0.5	1.5	0.2
$A_{260/280}$	1.92	0.02	1.95	0.02	1.97	0.06	1.95	0.04	1.94	0.06	1.98	0.02

Samples were also examined by electrophoresis through 1.2 % agarose gel and run at 31 V for 6 h. The gel was stained with 1 x TBE/SYBRGreenI solution for 40 min and de-stained in 1 x TBE for another 30 min (see Figure 4-3).

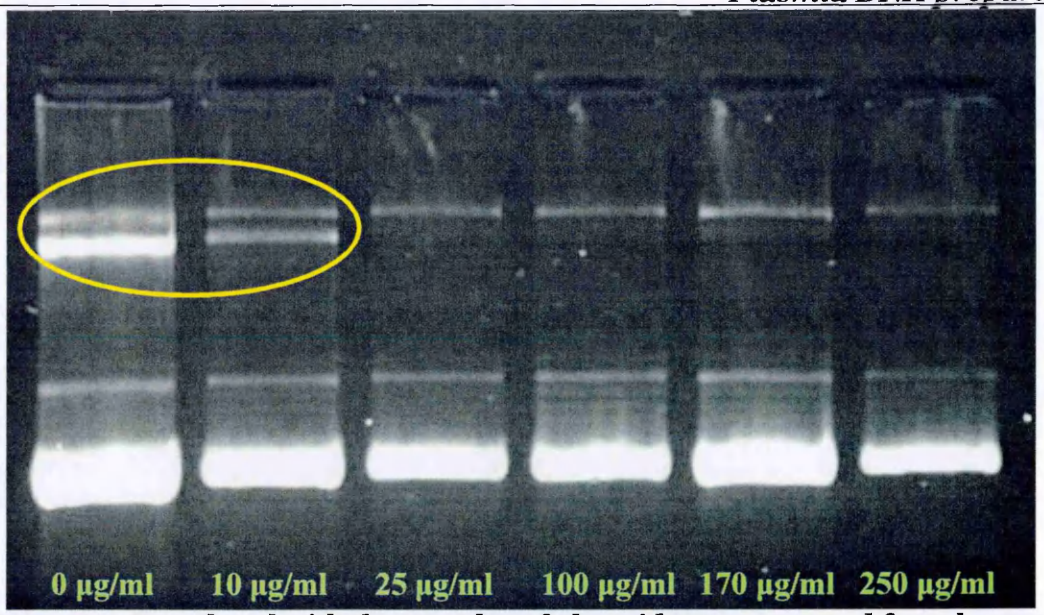

Figure 4-3. Sample gel with the samples of plasmid DNA extracted from bacteria grown on various concentrations of chloramphenicol. The yellow ellipse marks topoisomer formation in the sample not treated with chloramphenicol and treated with the smallest working concentration.

It can be clearly seen that the increased amounts of chloramphenicol reduced the appearance of the topoisomer form (see Figure 4-3, bands marked with yellow loop, lower band). Analysis of the gel allowed the ratio between supercoiled and relaxed forms to be determined (see Table 4-7). The ratio between the amounts of plasmid obtained per mg of bacteria colony was also calculated. It can be seen that both the quantity and quality of the plasmid improved. As the optimal value of working concentration 170 µg/ml was chosen for further plasmid preparations.

Table 4-7. Plasmid yields per cell mass unit and ratio of supercoiled to relaxed form.

Working concentration [µg/ml]	0		10		25		100		170		250	
	value	St. dev.	value	St. dev.	value	St. dev.	value	St. dev.	value	St. dev.	value	St. dev.
ng plasmid/ mg bacteria	113.2	9.3	133.2	36.7	130.1	43.1	125.4	47.8	123.4	43.4	99.6	32.1
supercoild / relaxed+ linear	5.9	1.7	9.9	3.8	13.1	6.6	13.1	4.8	12.3	4.1	18.5	13.9

4.4 Bacteria growth with ampicillin and tetracycline as selective antibiotics

Another set of experiments was performed to determine whether both ampicillin and tetracycline need to be used for bacteria growth and if both of them have the same influence on the yields of the purified plasmid. At the same time response to

a stringent growth conditions was checked by using lower concentrations of both the selective antibiotics and CAM as recommended by Sambrook *et al.* (Sambrook and Russell, 2001) for the stringent type plasmids (see Table 4-8).

Bacteria were plated on either ampicillin-, tetracycline- or ampicillin- and tetracycline-containing plates and incubated overnight at 37 °C.

Table 4-8. Concentrations of antibiotics used in the experiment.

Antibiotic	Working concentration [μg/ml]
Ampicillin	20
Tetracycline	10
Chloramphenicol	25

Due to the photosensitivity of tetracycline, both plates and culture flasks were wrapped in aluminium foil throughout the whole incubation period. Next day single colonies were picked up from plates and inoculated in 10 ml of LB medium containing the appropriate antibiotic or antibiotics. Cultures were then incubated for 8 h at 37 °C in a shaker-incubator. At that point OD_{600} measurements were performed to determine the growth stage of all cultures (see Table 4-9).

Table 4-9. OD_{600} measurements of bacteria cultures.

Culture growth conditions	OD_{600}
Ampicillin	0.92
Tetracycline	0.67
Ampicillin+Tetracycline	0.75

Colonies were then diluted 1:500 times and incubated overnight at 37 °C in shaker incubator. After 3 hours another OD_{600} measurement was performed (0.52 for AMP, 0.39 for TET and 0.35 for AMP+TET) and CAM was added to half of the colonies. Cultures were left to incubate overnight at 37 °C in the shaker incubator. Next day OD_{600} measurements were taken for all the colonies (see Table 4-10)

Table 4-10. OD_{600} measurements for the overnight cultures.

OD_{600} / Antibiotic	No CAM	CAM
AMP	1.58	0.50
TET	1.45	0.36
AMP+TET	1.38	0.37

All the colonies were harvested at 8000 rpm at 4 °C and their mass was determined (data presented in Table 4-11). Plasmid DNA was purified from all colonies using QIAGEN spin mini prep kit. Plasmid was eluted with 60 µl of UHP water (pH 8.0 adjusted with 1 M NaOH). Samples were then examined by UV spectrophotometry for plasmid yields and its purity (Table 4-11). It can be seen that ampicillin itself was a better choice in terms of the quantity and quality of plasmid obtained if the photosensitivity of tetracycline was taken into account.

Table 4-11. Results for the bacteria growth on various selective antibiotics in the presence and absence of chloramphenicol.

	Bacteria mass per 1 ml of the culture [mg/ml]		Plasmid yield [µg]		$A_{260/280}$		Plasmid yield per 1 mg of bacteria culture [ng/mg]	
	No CAM	CAM	No CAM	CAM	No CAM	CAM	No CAM	CAM
AMP	11.2	2.7	2.6	1.1	1.904	2.047	51.5	114.9
TET	9.0	3.3	2.0	0.9	1.968	2.000	55.4	41.7
AMP+TET	7.8	1.0	1.6	0.9	1.978	1.989	44.5	175

4.5 The effect of chloramphenicol decomposition products on plasmid DNA grown in *E. coli*

Preliminary experiments revealed that after adding old CAM aliquots to bacterial cultures there was a significant increase in the amount of relaxed DNA form with respect to the colonies that were grown in the presence of AMP only. An increase was observed already in the clear lysate (see Appendix A) of the cells (see Figure 4-4) which eliminated any influence from the preparation technique. It was concluded that the chloramphenicol must had an influence on the quality of the

plasmid while still in cells. The obtained result was repeatable. When a new batch of the antibiotic was purchased these problems were no longer apparent.

Therefore, chloramphenicol derivatives were tested for influence on plasmid amplification and possible damage induction (plasmid relaxation) upon CAM decomposition. The experiments were performed to establish which functional group or optical isomer of the antibiotic is responsible for such mode of action on bacteria during their amplification and any possible damage upon decomposition.

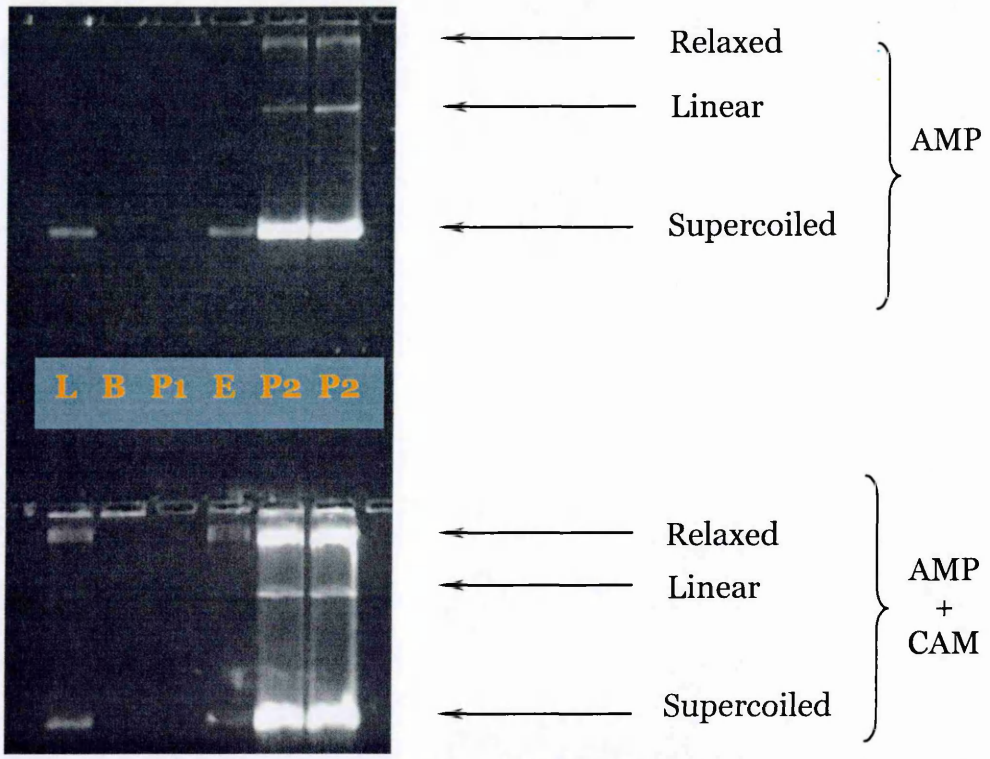

Figure 4-4. Chloramphenicol - induced damage to plasmid DNA during bacteria incubation; L – clear lysate; B – binding to the column; P1 – purification on the column; E – elution; P2 – IPA/EtOH purification; 1.4 % agarose gel run for 16 h at 1 V/cm.

Figure 4-5 shows compounds that were chosen for the experiment. The most probable pathway for D-(-)-chloramphenicol degradation is presented in Figure 4-6. With time the carbon – nitrogen bond is most likely to be disrupted. Due to the break down, (1R,2R)-(-)-2-amino-1-(4-nitrophenyl)-1,3-propanediol will be formed, a compound containing both the aromatic ring and amine group. 2,2-dichloroacetic acid is likely to undergo further hydrolysis to glycolic acid by losing chlorine atoms.

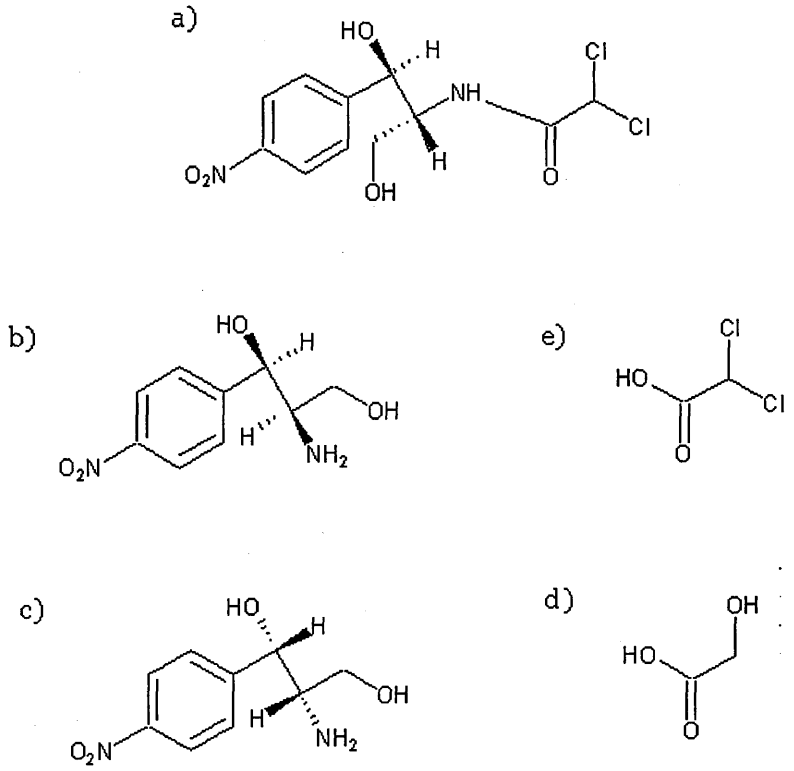

Figure 4-5. Structures of chloramphenicol and its possible decomposition products; a) D-(-)-chloramphenicol; b) (1R,2R)-(-)-2-amino-1-(4-nitrophenyl)-1,3-propanediol; c) (1S,2S)-(+)-2-amino-1-(4-nitrophenyl)-1,3-propanediol; d) 2,2-dichloroacetic acid; e) glycolic acid.

A standard protocol for bacteria culture growth was used (as described in 4.2) but 10 ml final cultures were prepared. In the stage 1, where CAM is usually added (5 μmole in 10 ml to obtain working concentration of 170 μg/ml), 5 μmoles of each compound from Figure 4-5 were added and the rest of the incubation and plasmid purification were performed as mentioned above. Plasmid DNA was eluted from the binding column with 70μl of 10 mM Tris-Cl (pH 8.3) buffer.

Samples were analysed both by UV spectrophotometry and agarose gel electrophoresis such that plasmid yield, purity and quality were determined. Also the mass of pelleted bacteria was determined after harvesting cultures at 8500 rpm for 15 min and air-drying for another 15 min. Table 4-12 presents the results obtained.

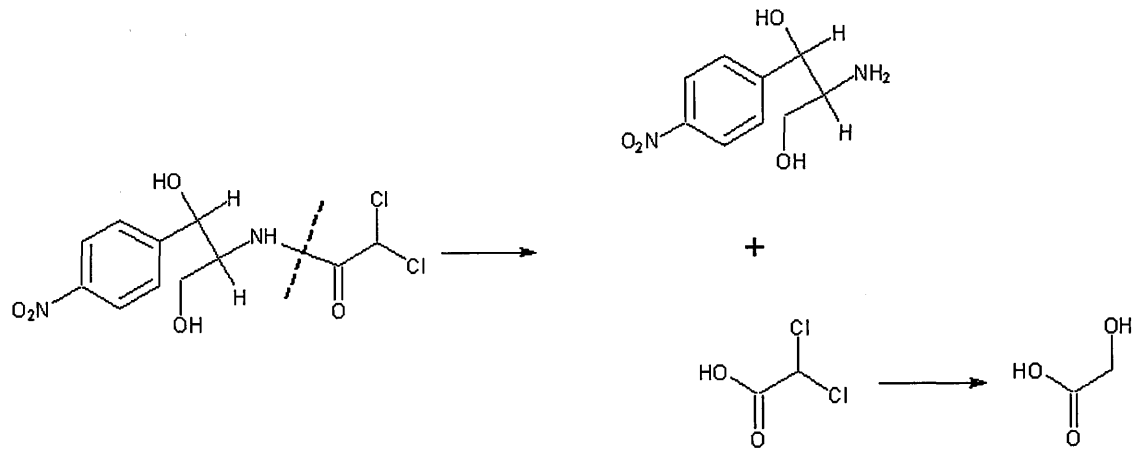

Figure 4-6. Possible pathway for CAM decomposition and products formation.

It can be seen that CAM derivatives that contain the aromatic ring and amino group possess the property of plasmid amplification. Also, the purity seemed to be greater in this case, which would support the assumption of reduction of the protein content in bacteria cells upon chloramphenicol treatment.

Table 4-12. Results obtained for the chloramphenicol derivatives.

Compound	(1R,2R)-(-)-2-amino-1-(4-nitrophenyl)-1,3-propanediol		(1S,2S)-(+)-2-amino-1-(4-nitrophenyl)-1,3-propanediol		2,2-dichloroacetic acid		Glycolic acid	
Parameter	value	St. dev.	value	St. dev.	value	St. dev.	value	St. dev.
Bacteria mass per 1 ml of the culture [mg/ml]	4.9	0.7	4.6	0.3	5.8	0.4	5.2	0.2
Plasmid mass [μg]	5.5	1.0	5.6	1.4	6.3	1.2	5.8	1.7
$A_{260/280}$	1.888	0.084	1.854	0.058	1.702	0.227	1.782	0.116
ng plasmid/ mg bacteria	115.6	33.1	122.2	35.6	110.3	28.1	112.7	35.5
$\frac{\text{supercoild}}{\text{relaxed+ linear}}$	2.7	0.8	3.0	1.2	3.0	1.1	2.5	0.5

Figure 4-7 shows a sample gel with plasmid obtained from bacteria grown in presence of the chosen derivatives (gel picture intensity was saturated to show all the features).

Comparing samples grown on AMP both in the presence and absence of CAM, a dimer was formed in all the cases (Figure 4-7, yellow ellipse). Moreover, a characteristic laddering occurred in all cases between the relaxed and linear bands that was not present in the original samples (for comparison see Figure 4-3).

In all cases the ratio between the supercoiled form and the remaining ones was lower than in case of plasmid prepared from the cultures grown in presence or absence of CAM (for comparison see Table 4-7).

From the results above one can conclude that upon hydrolysis CAM can decompose into the products that will influence plasmid DNA conformation.

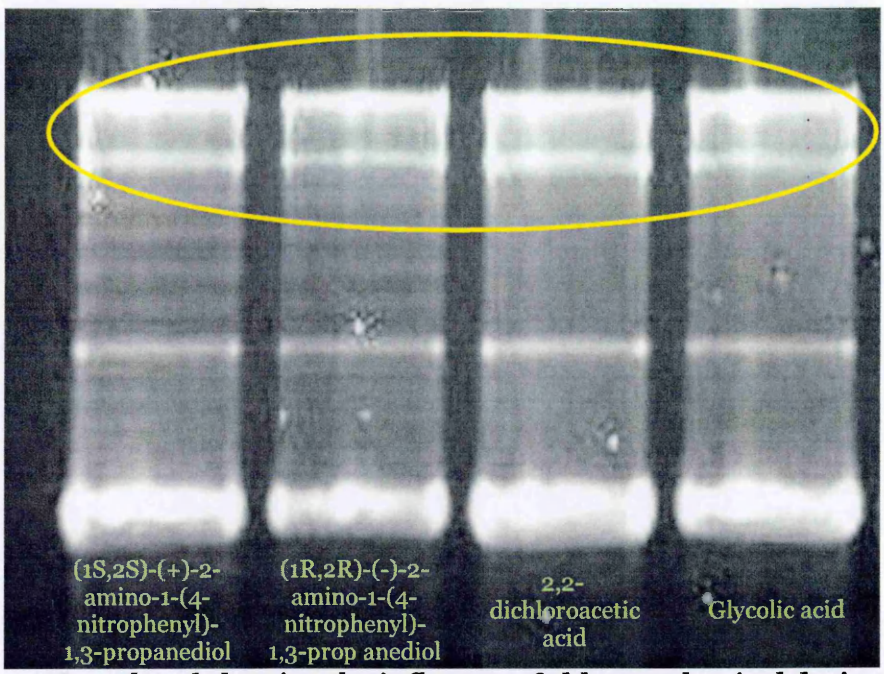

Figure 4-7. Sample gel showing the influence of chloramphenicol derivatives on plasmid amplification. Yellow ellipse marks the dimer formation that occurred in all cases.

4.6 Conclusions

From the experiment in which bacteria colonies were grown in presence of ampicillin it can be clearly seen that an increase in the buffer volumes improved the purity of plasmid.

A second experiment showed that plasmid amplification upon CAM treatment greatly increases. By varying concentration of CAM it was concluded that different concentrations of this antibiotic influence both the quantity and the quality of the purified plasmid DNA. The obtained data showed in Table 4-5, Table 4-6 and Table 4-7 can also be presented in a graph to compare of the effect of CAM treatment (see Figure 4-8).

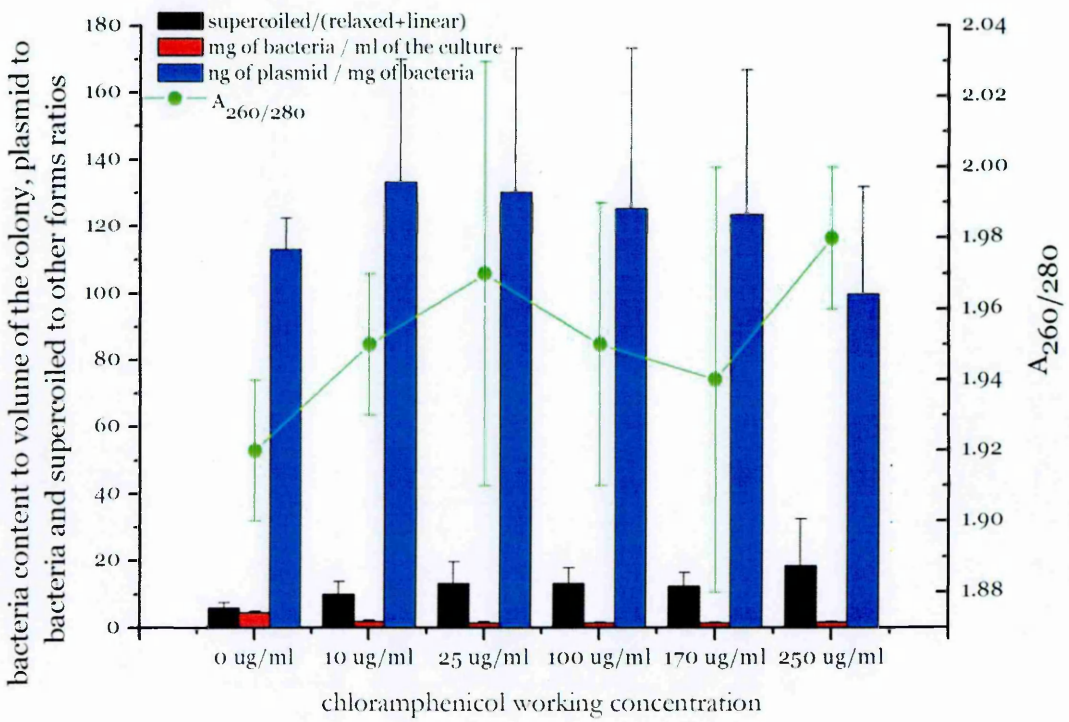

Figure 4-8. Comparisons of different effects of chloramphenicol treatments of various concentrations of the antibiotic.

As a result of this experiment, a working concentration of 170 µg/ml was chosen for all further plasmid preparations as it seemed to give the best results regarding both the quantity and the quality of the plasmid.

The experiment concerning the choice of selective antibiotics showed that the best choice for the bacteria growth and plasmid preparation was ampicillin. TET cultures, grown in the presence of CAM, revealed lower amplification yields upon CAM treatments compared with samples treated with ampicillin. A combination of all the antibiotics seemed to bring the greatest amplification rate and highest

purity. As growth on TET is more difficult due to its photosensitivity, a method that employs AMP and CAM was chosen for plasmid preparation in the irradiation experiments.

The last set of the experiments proved that the products formed upon chloramphenicol decomposition can influence plasmid DNA conformation by causing dimmers formation if host cells are cultured in their presence.

Chapter 5

VUV irradiation studies of plasmid DNA in aqueous solution

To investigate VUV damage to plasmid DNA molecules in aqueous solutions several experiments were conducted. Various wavelengths were tested for the damage yield that can be obtained upon irradiation. Numerous measurements were performed to optimise the experimental setup and maximise the damage obtained.

5.1 Sample preparation and analysis

For all the irradiation experiments described in this chapter plasmid pBR322 DNA samples were prepared as shown in 4.2. Samples were eluted into (1) pure water, (2) 10 mM tris buffer or (3) 5 μM EDTA buffer. The plasmid concentration varied from ~150 ng/μl to ~200 ng/μl. Samples were then placed in the sample holder as described in 3.2. VUV radiation was then applied using either lamps or synchrotron (described in 3.1 and 3.2).

After irradiation small samples of irradiated product (2 μl) were collected from the sample holder, diluted up to the volume of 5 μl with tris buffer and either stored in the freezer awaiting further analysis or mixed with 2 μl of loading buffer and run immediately on a 1.2 % agarose gel for 6 hours at 1.6 V/cm. Gels were then stained with 1 x SYBRGreenI solution in 1 x TBE buffer for 30 to 45 minutes.

Fluorescent images of the gel were then recorded using commercial gel imagers and damage analysis was performed using ImageJ software (available from http://rsb.info.nih.gov/ij/). ImageJ is densitometry software, which allows integration of bands corresponding to different conformations of plasmid DNA.

In most cases sample recovery from the sample holder measured by AGE was close to 100 %, therefore the assumption was made that no multistrand breaks are induced upon the irradiations over VUV-UV range. The loss of the material occurred only in cases where sample was irradiated for a very long time (i.e. above 4 hours) and was associated with the interaction between the glass support and DNA molecules.

5.2 Dose and cross section calculations

A set of DNA irradiations was performed to obtain dose response curves at certain photon energies. The absorbed dose, $D_{absorbed}$, is given by (see Appendix B)

$$D_{absorbed} = \frac{D}{[\text{sec}]} = \frac{h \cdot c \cdot I_{el} \cdot \Delta S}{\lambda \cdot M \cdot q_e \cdot Q_E \cdot s_{\text{det}}}, \tag{5-1}$$

where:

h – Planck's constant = $6.662 \cdot 10^{-34}$ J·s,

c – speed of light = 299792458 m·s^{-1},

λ – wavelength [m],

I_{el} – electron current on the UV detector [A],

M – sample mass [kg],

ΔS – surface area of the sample [mm^2],

s_{det} – surface area of the UV detector [mm^2],

q_e - electron charge = $1.602 \cdot 10^{-19}$ C,

Q_E – quantum efficiency of the UV detector.

The time (number of seconds) needed for irradiation to reach the required dose can then be derived as

$$[\text{sec}] = \frac{D \cdot \lambda \cdot M \cdot q_e \cdot Q_E \cdot s_{\text{det}}}{h \cdot c \cdot I_{el} \cdot \Delta S}. \tag{5-2}$$

Once the data was obtained and the dose response curves plotted, cross sections for loss of supercoiled DNA and both SSBs and DSBs formation were calculated using the following expression (see Appendix C)

$$\sigma_X(\lambda) = \frac{N_X}{N_{oX}} \cdot \frac{s_{\det} \cdot Q_E \cdot q_e}{I_{el} \cdot T_{irr}}, \qquad (5\text{-}3)$$

where

X = S for loss of the supercoiled DNA, SSB for SSBs formation, DSB for DSBs formation, $\sigma_X(\lambda)$ is the cross section for wavelength λ for process X, N_X is the remaining form of DNA after irradiation, N_{oX} is amount of the X DNA form in the non-irradiated sample, T_{irr} is total time of irradiation [sec].

The expression can also be written as

$$\sigma_X(\lambda) = \frac{N_X}{D} \cdot \frac{h \cdot c \cdot \Delta S}{N_{oX} \cdot \lambda \cdot M}. \qquad (5\text{-}4)$$

Such rearrangement will allow for further data modelling described in section 5.3.7.

A total cross section, $\sigma_{TS}(\lambda)$, for the loss of the supercoiled DNA over the whole dose delivered is a parameter that can be used to describe the probability of further supercoiled DNA loss over the increasing dose that was delivered to the sample. It was derived as an integral of the cross section for the supercoiled DNA loss, $\sigma_S(\lambda)$, (see Appendix D)

$$\sigma_{TS}(\lambda) = P_1 \cdot \int_{D_o}^{D_f} \frac{N_S(D)}{D} \mathrm{d}D, \qquad (5\text{-}5)$$

where

$$P_1 = \frac{h \cdot c \cdot \Delta S}{\lambda \cdot M \cdot N_{oS}}$$

and

D_o is the starting dose [Gy], D_f is the final dose [Gy] and $N_S(D)$ is a function describing loss of supercoiled DNA with the dose, D, obtained from the data modelling.

5.3 Results and discussion

All the graphs presented below are based on an agarose gel electrophoresis analysis (2.1). All points in the curves represent an average of three independent irradiations and the error bars represent the standard deviation of these experiments. The experiments were performed at the ASTRID synchrotron source, Denmark, unless stated otherwise.

5.3.1 Control for the mechanical damage

The first experiment that was performed was to ensure that there is no damage induced to the samples by the experimental methodology itself. Therefore samples were placed in the sample holder and left there for the times corresponding to the times used to irradiate DNA at 150 nm equivalent to doses of 10, 20, 30, 40 and 50 Gy. In all cases the light source was cut off, so all observed damage would be attributed only to the experimental methodology, i.e. rotation, evaporation, etc. Figure 5-1 shows that there is no change between the yields of supercoiled, relaxed and linear forms with respect to samples that were not placed in the holder.

It was therefore assumed that all the damage that will be observed in irradiation experiments, will be induced purely from the irradiation delivered to the samples and no correction needed to be made for the influence of the experimental setup itself.

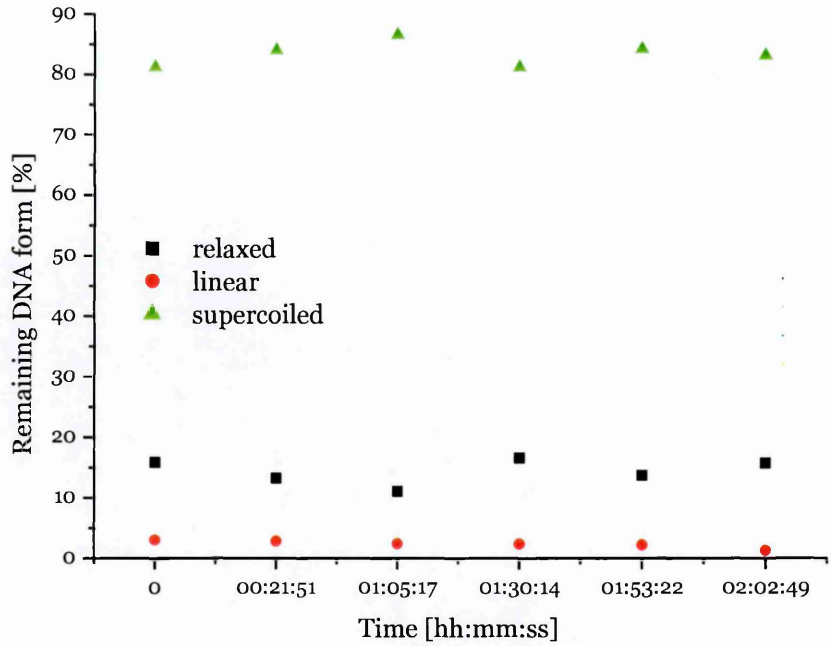

Figure 5-1. Damage induced by rotating samples over the time needed for irradiation in the sample holder (no light coming through).

5.3.2 Investigation of the influence of mixing rate on damage yields

An additional experiment was performed to investigate the influence of the rotation speed of the step motor on the sample mixing and DNA damage yield. Samples were irradiated at 150 nm up to a dose of 20 Gy. The photon flux was kept at $2.54 \cdot 10^9$ photons per second during all the irradiations.

Figure 5-2 shows the results obtained. It can be clearly seen that there is an effect on the damage due to the rotation speed. Loss of supercoiled DNA and breaks formation increase with increasing rotation speed. The maximum damage can be seen for samples irradiated at rotation speed of 0.5 revolutions per second. With further increase of the rotation speed, the yield of damage decreases. The observed phenomenon is related both to the penetration depth of the UV light into the water solution and the behaviour of the plasmid molecules in the water in the investigated system.

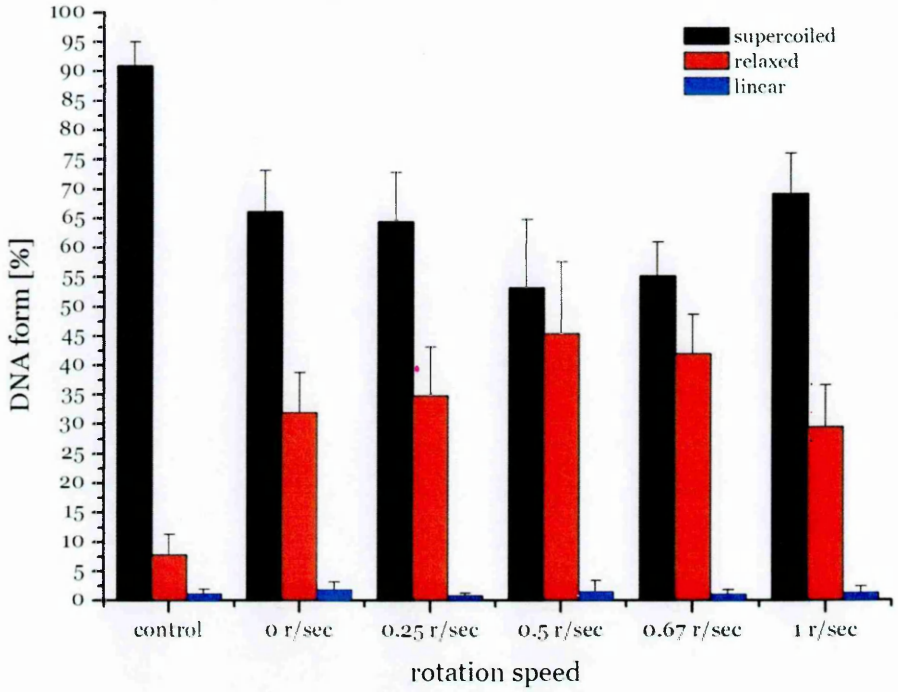

Figure 5-2. The influence of the rotation speed of the sample holder on the observed DNA damage; the control is a sample that did not undergo irradiation.

At low rotation speeds not all the molecules are brought up to the UV window surface and thus the amount of damage is reduced. With increasing rotation speed the maximum damage is achieved at around 0.5 revolutions per second. Interestingly, on increasing the rotation speed further, the damage yield starts to decrease again. It is believed that at higher speeds the molecules in liquid, instead of being mixed, are starting to be "centrifuged" to the edges of the sample and thus are not evenly exposed to the irradiation.

5.3.3 Light intensity – the importance of the dose delivery rate.

Figure 5-3 and Figure 5-4 show preliminary data obtained in dose response experiments (loss of the supercoiled DNA and appearance of DSBs). Plasmid samples were irradiated at 150 nm with a photon flux of $5 \cdot 10^9$ photons per second. Plasmid DNA was irradiated both in the presence (tris, EDTA) and absence (UHP water) of OH radical scavengers.

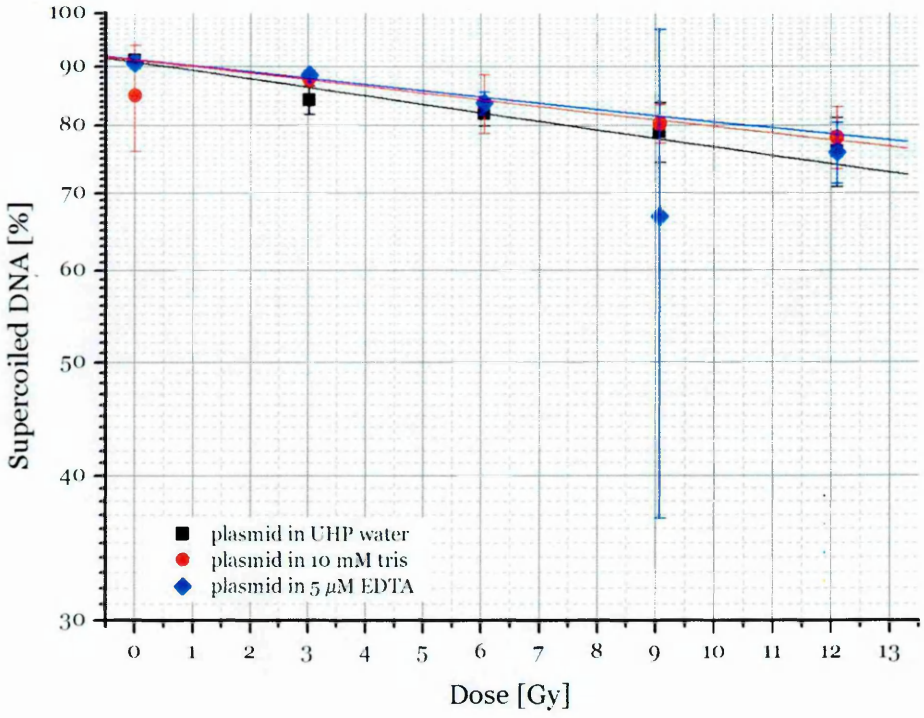

Figure 5-3. Loss of supercoiled DNA in a plasmid irradiated in pure water (■), and in solutions containing tris (●) and EDTA (♦).

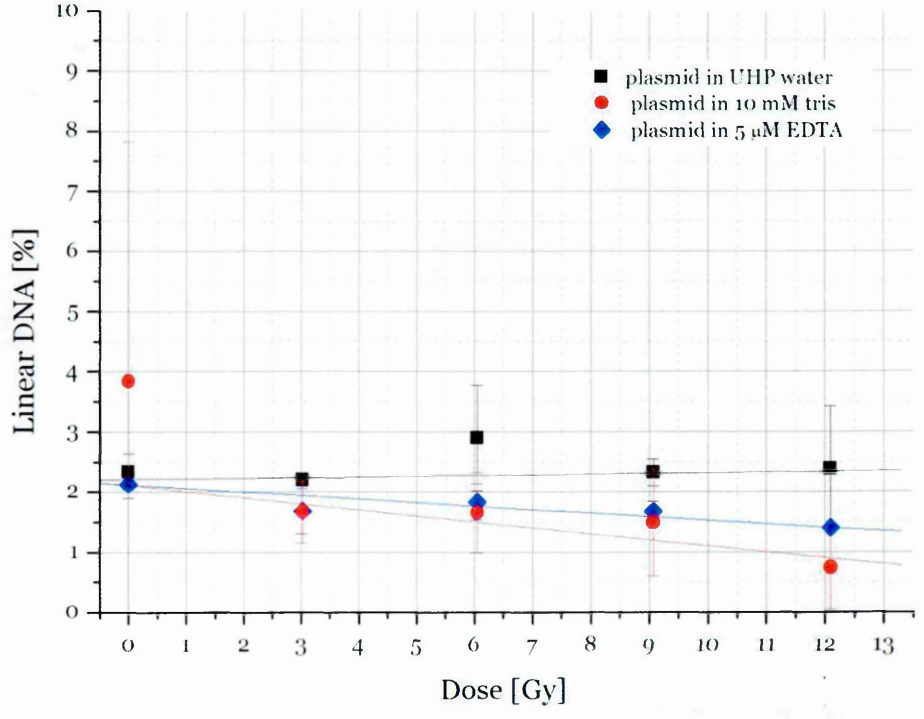

Figure 5-4. Appearance of the linear DNA in a plasmid irradiated in pure water (■), and in solutions containing tris (●) and EDTA (♦).

When compared with the previous data (see Figure 1-8) of Folkard (2002), obtained using the same apparatus, the amount of DNA damage was low (20 % of supercoiled DNA loss at 12 Gy was seen in this experiment compared with 80 % loss seen by Folkard). Hence some additional measurements were performed to investigate the influence of the photon flux intensity on the yield of DNA damage. To see how the photon flux can affect the damage yield, samples were irradiated at 150 nm up to a dose of 6 Gy (Figure 5-5) and 20 Gy (Figure 5-6) for different photon fluxes.

It can be clearly seen from Figure 5-5 and Figure 5-6 that the amount of DNA damage increases with the decreasing photon flux. Therefore one can conclude that the slower the rate of dose delivery the greater the probability of damage.

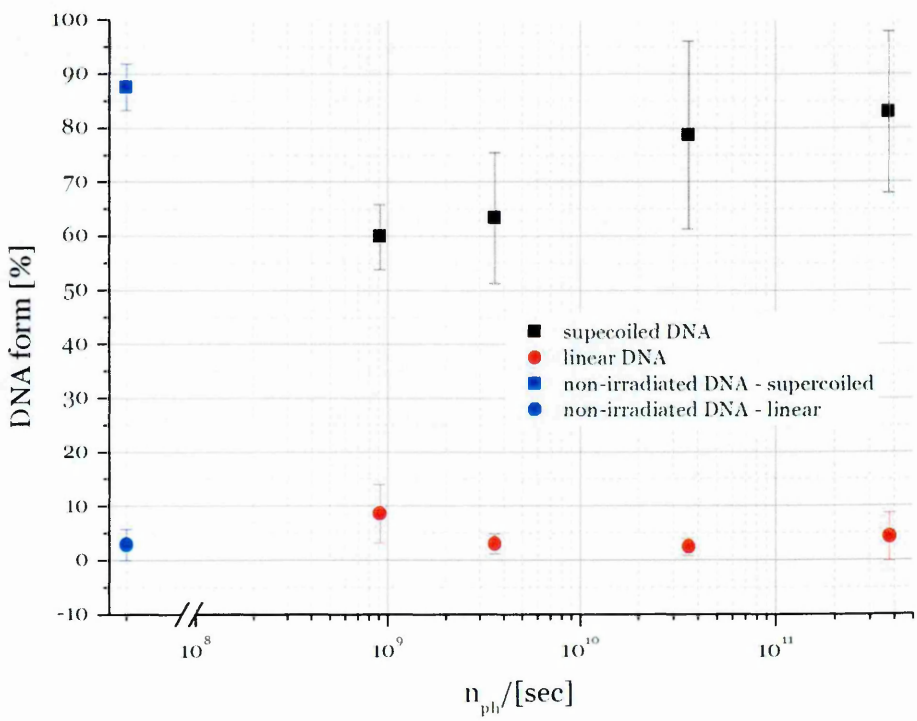

Figure 5-5. DNA damage obtained at various photon fluxes for the irradiation dose of 6 Gy.

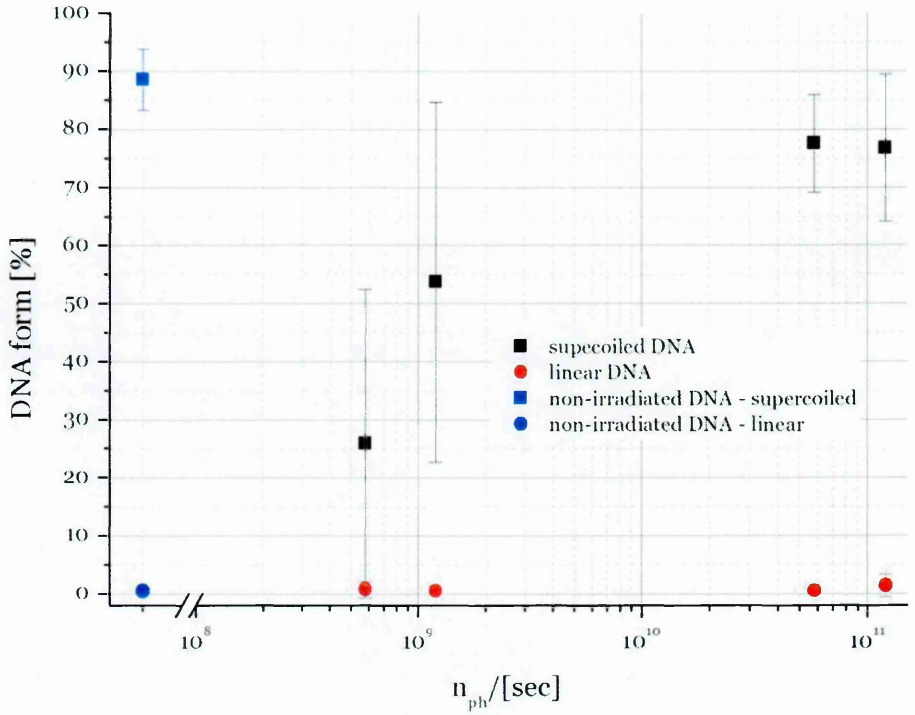

Figure 5-6. DNA damage obtained at various photon fluxes for the irradiation dose of 20 Gy.

Dose response curves were plotted for samples irradiated at two different photon fluxes at 150 nm and 170 nm. The data obtained at 150 nm is presented in Figure 5-7 and Figure 5-8 (lines indicate a linear fit to the data points). It can be seen that there is a somewhat greater loss of the supercoiled DNA for low photon flux irradiations (Figure 5-7), whereas no perceptible difference was obtained in case of the DSB formation (Figure 5-8). For the samples irradiated at 170 nm similar results were obtained (Figure 5-9 and Figure 5-10). In all the cases hardly any formation of DSB was seen, moreover, due to high statistical distribution it was not possible to determine the actual level of this type of damage. Interestingly, it seems that a greater amount of damage was induced at 170 nm than at 150 nm for both fluxes. This is in contrast to the basic assumption that the amount of DNA damage should decrease with the decreasing photon energy, i.e. increasing wavelength. Therefore dose-response curves were measured for two more wavelengths (130 nm and 190 nm) to monitor damage as a function of wavelength.

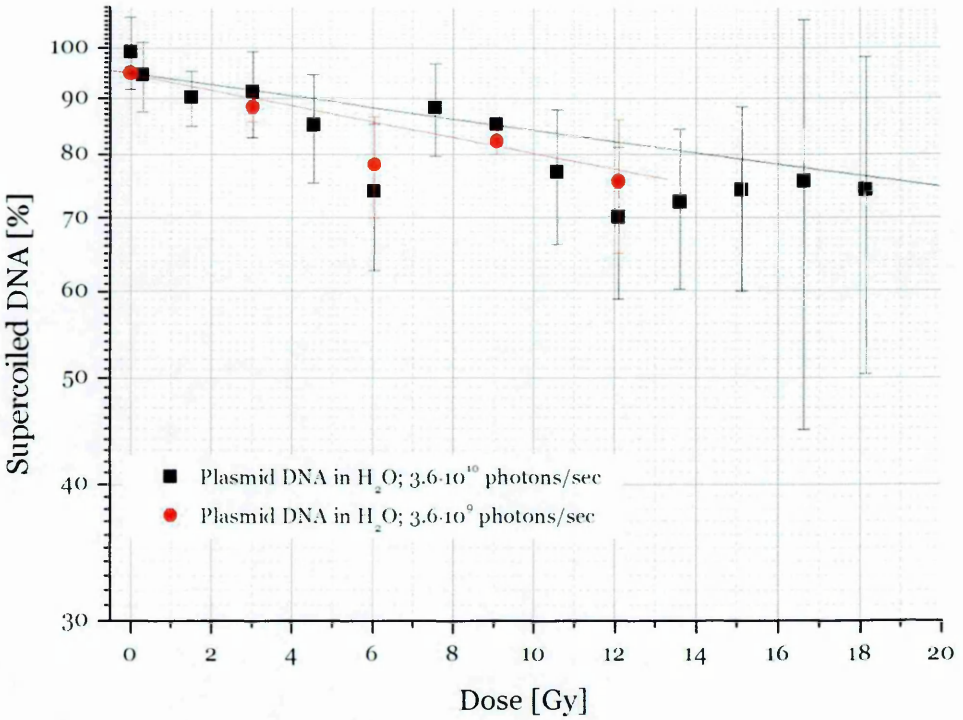

Figure 5-7. Loss of supercoiled DNA versus dose delivered at two different photon fluxes; samples irradiated at 150 nm; lines show a linear fit to the data.

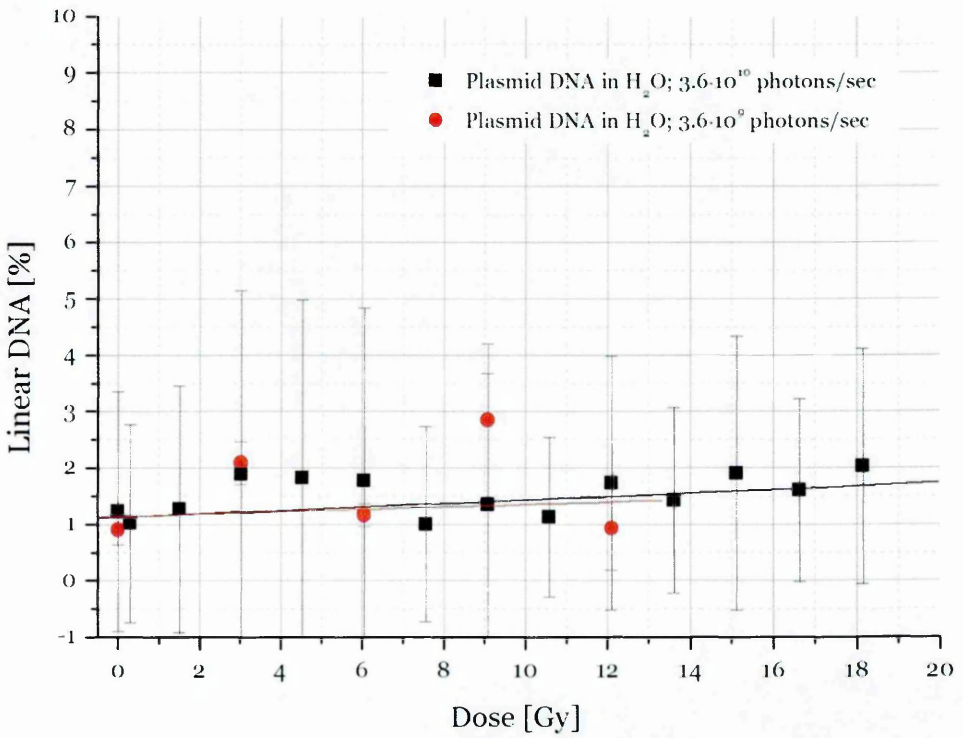

Figure 5-8. DSBs formation versus dose delivered at two different photon fluxes; samples irradiated at 150 nm; lines show a linear fit to the data.

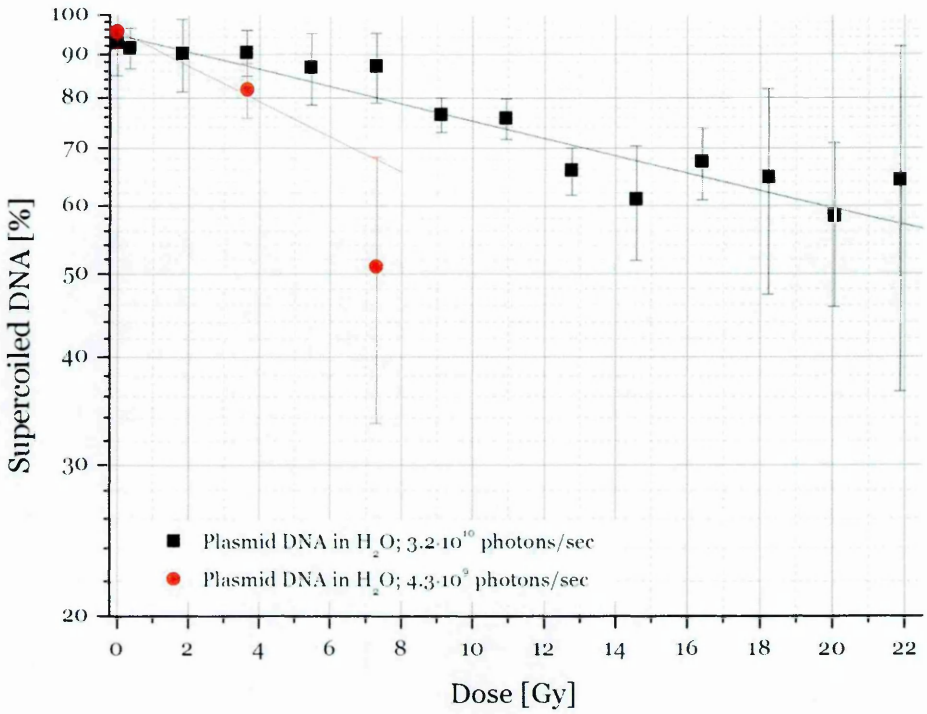

Figure 5-9. Loss of supercoiled DNA versus dose delivered at two different photon fluxes; samples irradiated at 170 nm; lines show a linear fit to the data.

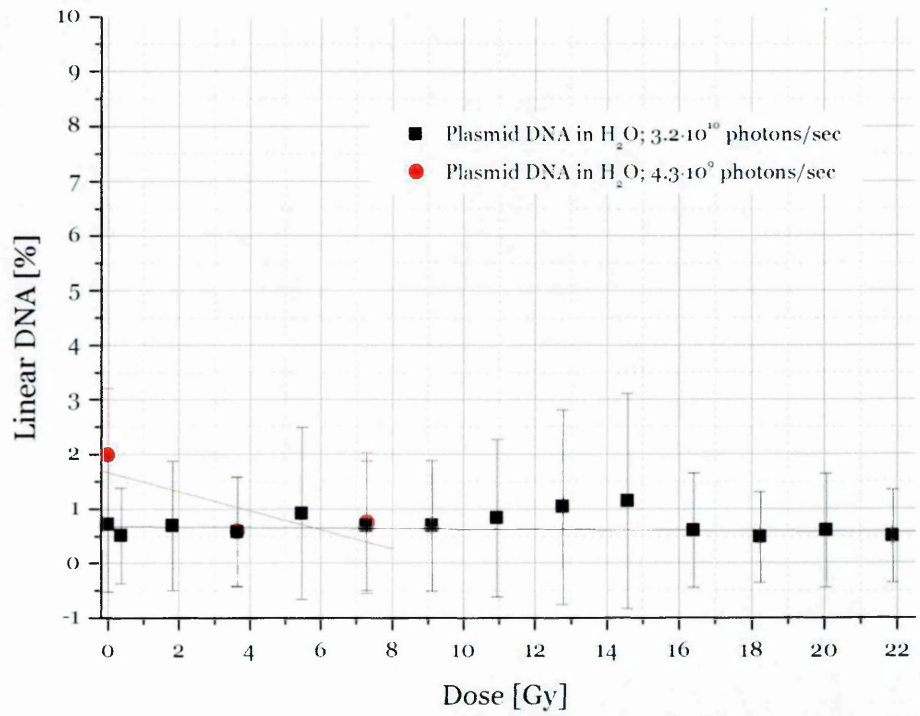

Figure 5-10. DSBs formation versus dose delivered at two different photon fluxes; samples irradiated at 170 nm; lines show a linear fit to the data.

5.3.4 VUV irradiation of plasmid DNA in a water solution at various wavelengths.

Plasmid DNA was irradiated at 130 nm, 150 nm, 170 nm and 190 nm and the dose-response curves were measured. The photon fluxes used in these irradiations are listed in the Table 5-1

Table 5-1. Photon fluxes used for the irradiation experiments at various wavelengths.

Wavelength [nm]	130	150	170	190
$\frac{n_{ph}}{[\text{sec}]}$	$2.3 \cdot 10^9$	$5.8 \cdot 10^9$	$6.8 \cdot 10^9$	$7.7 \cdot 10^9$

The rotation speed of the sample holder used in these experiments was set to be 1 revolution per second.

Figure 5-11 and Figure 5-12 present data obtained for the loss of the supercoiled DNA with increasing dose, whereas Figure 5-13 and Figure 5-14 show DSBs formation under the same conditions conditions. The lines in Figure 5-11, Figure 5-12, Figure 5-13 and Figure 5-14 are linear fits to the data points.

The smallest amount of damage and hence smallest loss of the supercoiled DNA was found using 190 nm radiation. Surprisingly, the damage at 130 nm was almost the same as that obtained for 150 nm, whereas the amount of DNA damage was greatest at 170 nm. It was possible to observe DSB formation, although due to the large statistical variation it was hard to make any significant analysis of the data.

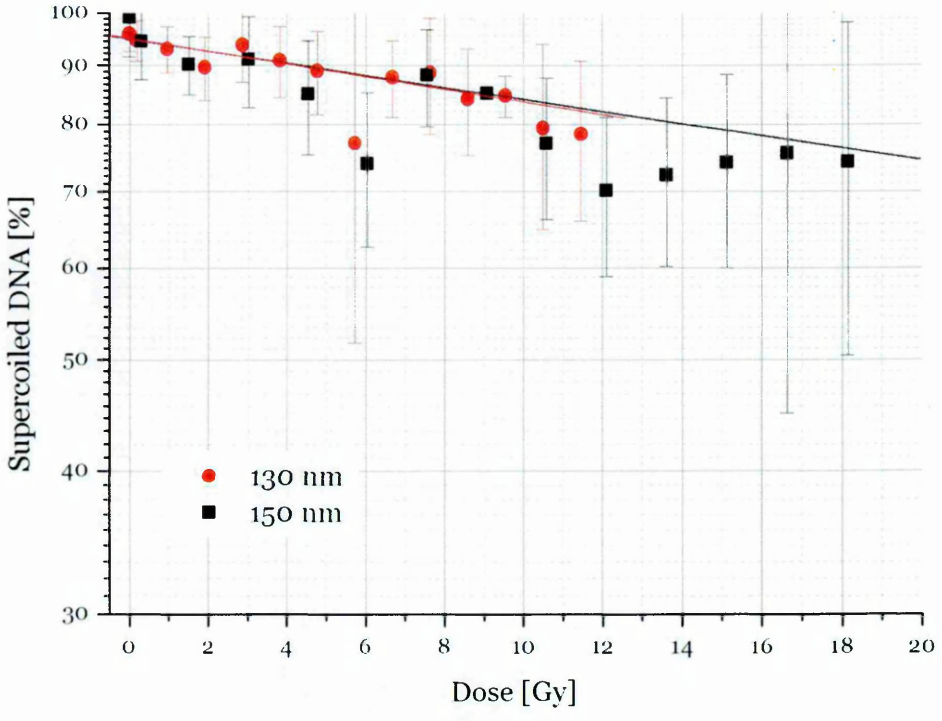

Figure 5-11. Dose-response curves for the loss of supercoiled DNA for plasmid samples irradiated at 130 nm and 150 nm; the lines represent a linear fit to the data.

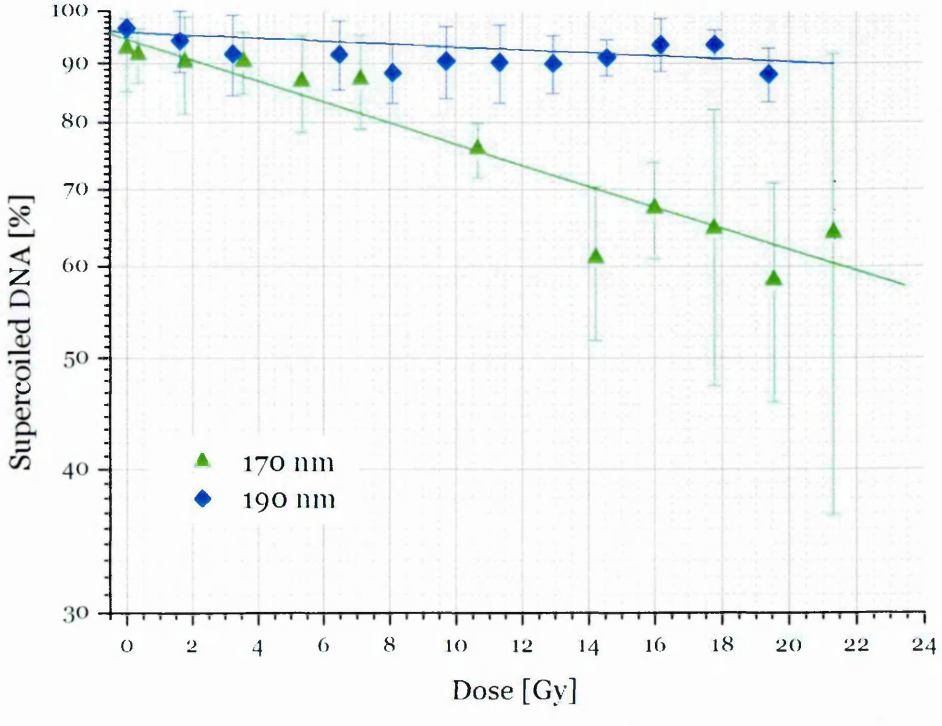

Figure 5-12. Dose-response curves for the loss of supercoiled DNA for plasmid samples irradiated at 170 nm and 190 nm; the lines represent a linear fit to the data.

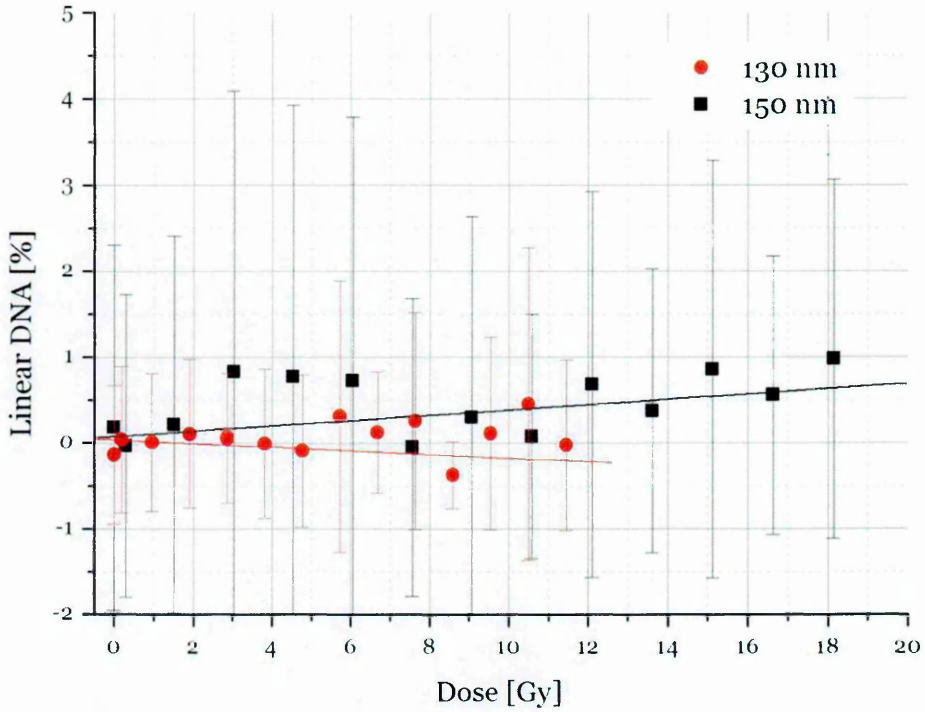

Figure 5-13. Dose-response curves for the DSB formation for plasmid samples irradiated at 130 nm and 150 nm; the lines represent a linear fit to the data.

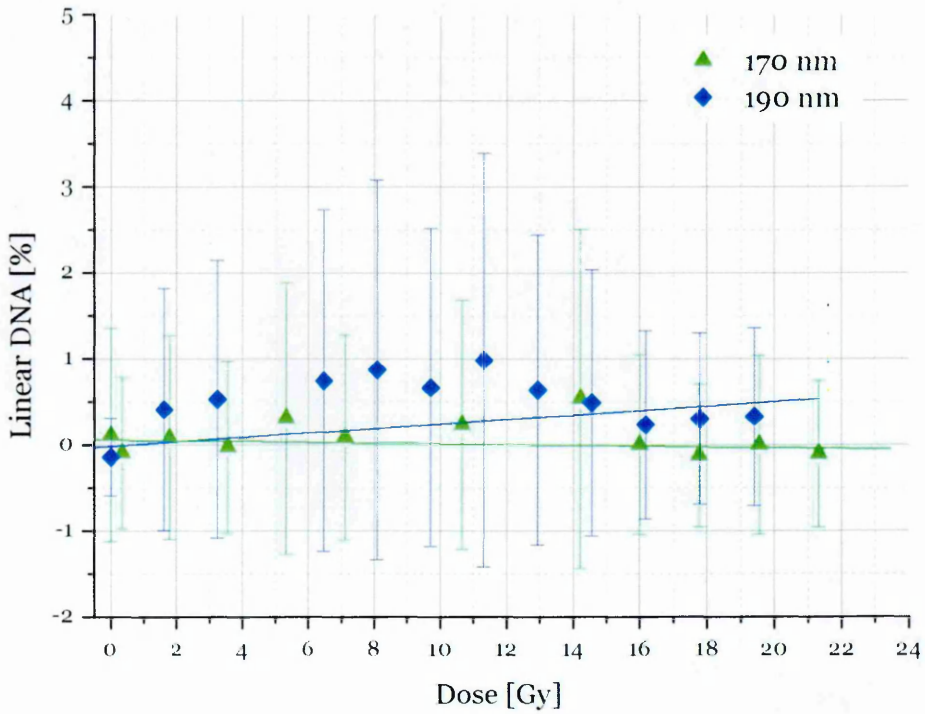

Figure 5-14. Dose-response curves for the DSB formation for plasmid samples irradiated at 170 nm and 190 nm; the lines represent the linear fit to the data.

5.3.5 VUV irradiation of plasmid DNA in the presence of scavengers

In order to probe the effect of hydroxyl radicals in such VUV radiation plasmid samples were irradiated using UV light from both the Xe and D_2 lamps (apparatus described in 3.2). The error bars on the dose were caused by the loss of lamp intensity during the irradiation period. Due to the lower stability of the lamp photon flux comparing to the synchrotron, the photon flux varied over the irradiation period from ~$7 \cdot 10^7$ to ~$3 \cdot 10^8$ photons per second. Samples were irradiated at 150 nm in (1) UHP water and (2) 10 mM tris solution.

Figure 5-15 and Figure 5-16 show the loss of the supercoiled DNA and appearance of DSBs formation, respectively. Lines in figures represent a linear fit to the data.

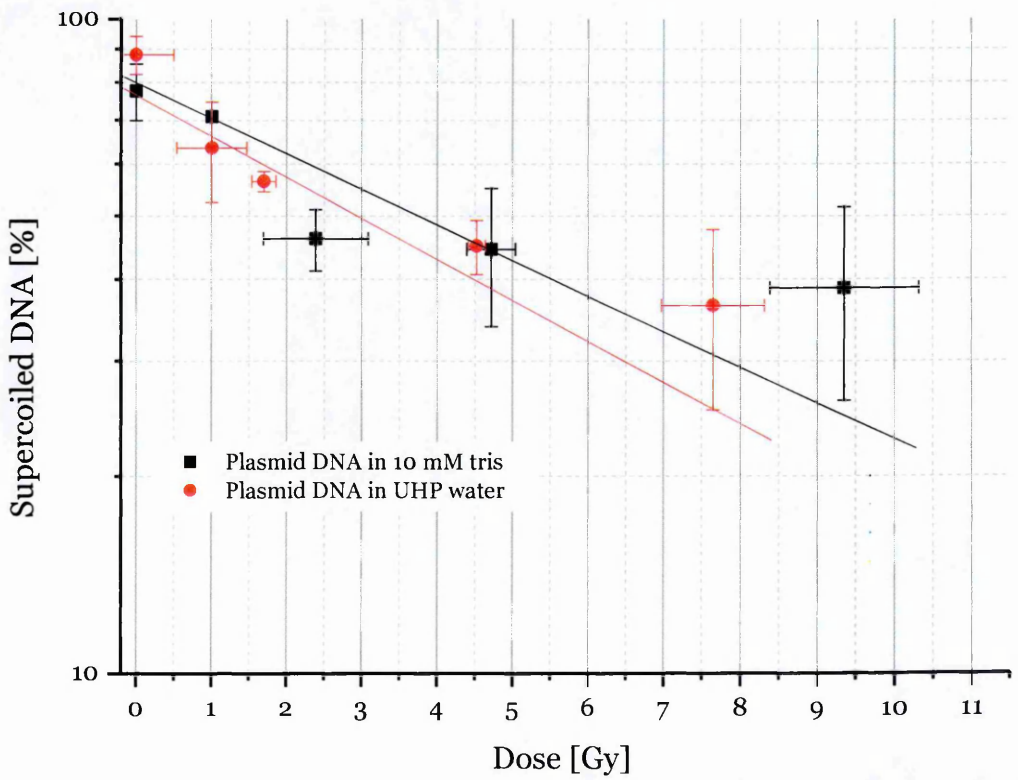

Figure 5-15. Loss of the supercoiled DNA form in the samples irradiated at 150 nm in the presence and absence of OH radical scavengers.

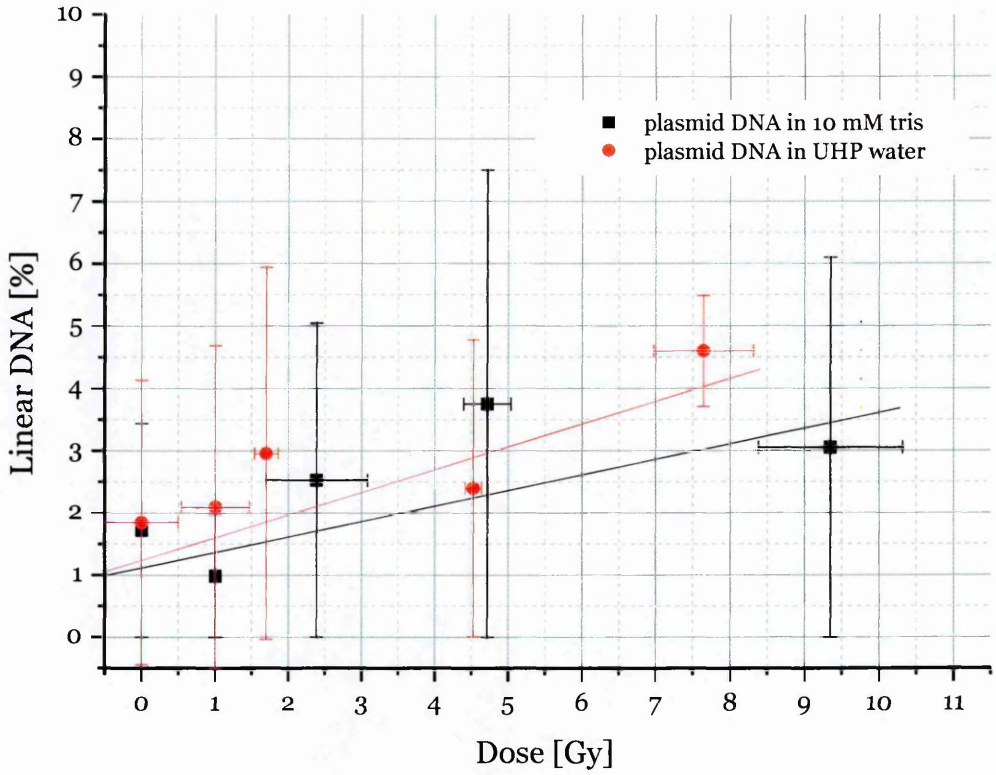

Figure 5-16. DSBs formation in the samples irradiated at 150 nm in the presence and absence of OH radical scavengers.

It can be seen in both figures that there is an OH radical influence on the damage of DNA as there is a visible difference in the rate of damage formation between the samples that were in water and those that contained tris buffer. In addition there was a noticeable difference in the level of DSBs in the two solutions.

5.3.6 Estimation of the cross sections for DNA damage induced by VUV radiation

Cross sections for loss of supercoiled DNA and for formation of both SSBs and DSBs formation were derived using the measured data. Using equation (5-3), dose-dependent graphs were obtained. Figure 5-17, Figure 5-18 and Figure 5-19 present the cross sections for loss of the supercoiled DNA, SSBs and DSBs formation, respectively, at 130 nm, 150 nm, 170 nm and 190 nm. The estimated error was based on the standard deviation obtained for each point from AGE ± 20 % for the

loss of the supercoiled DNA and ± 150 % for SSB formation and ± 300 % for DSB formation. Such high error values for the SSBs and DSBs formation cross sections were caused by the nature of the process, namely it is not certain whereas the loss of the supercoiled DNA form will result in SSB or in DSB formation. From the statistical distribution of these points (i.e. the values of standard deviation) one can say that their appearence is random.

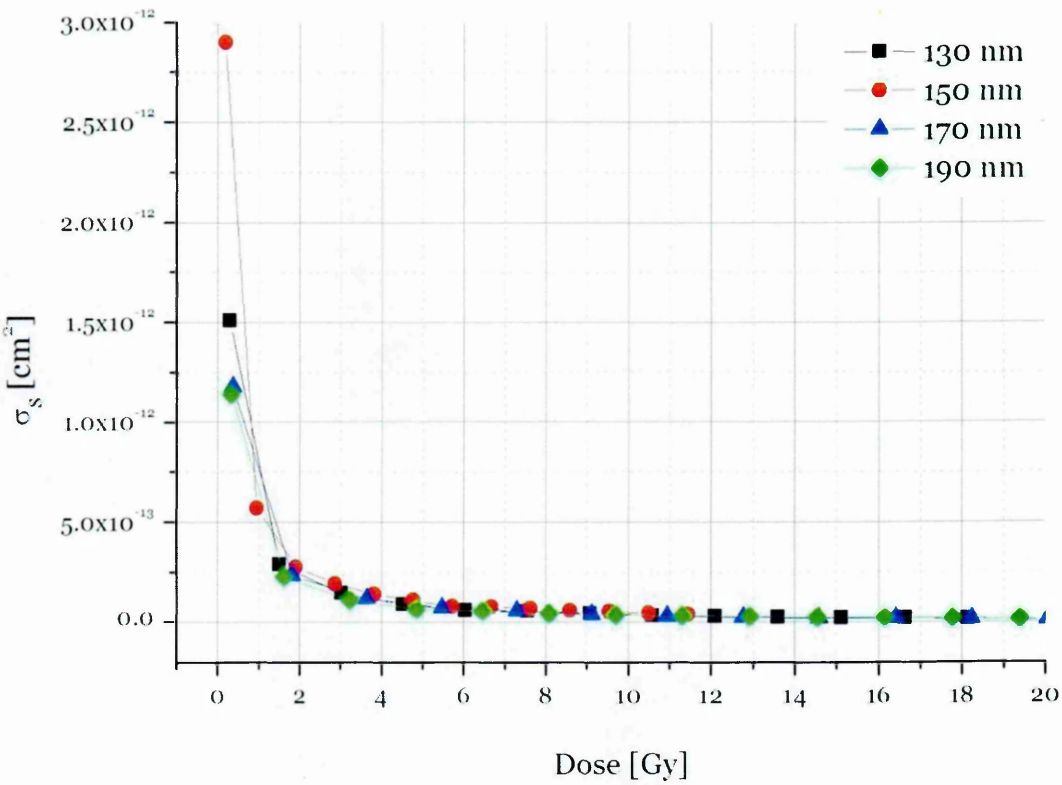

Figure 5-17. Cross section for loss of supercoiled DNA as a function of dose at 130 nm, 150 nm, 170 nm and 190 nm.

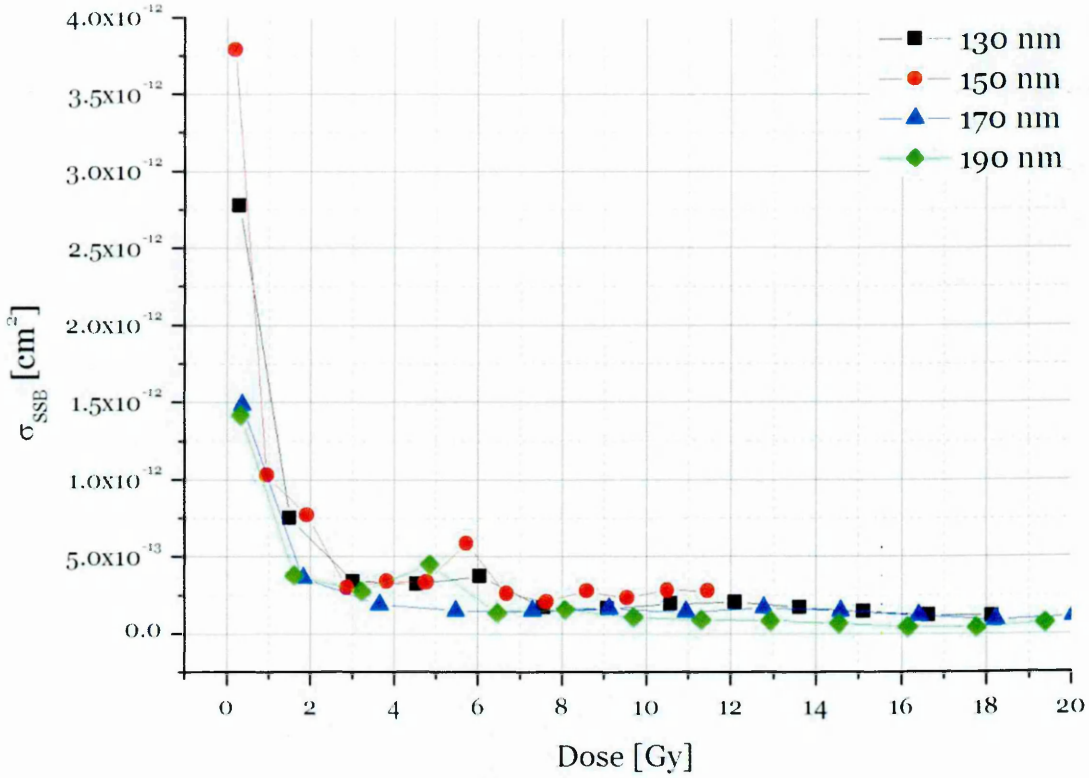

Figure 5-18. Cross section for SSBs formation as a function of dose at 130 nm, 150 nm, 170 nm and 190 nm.

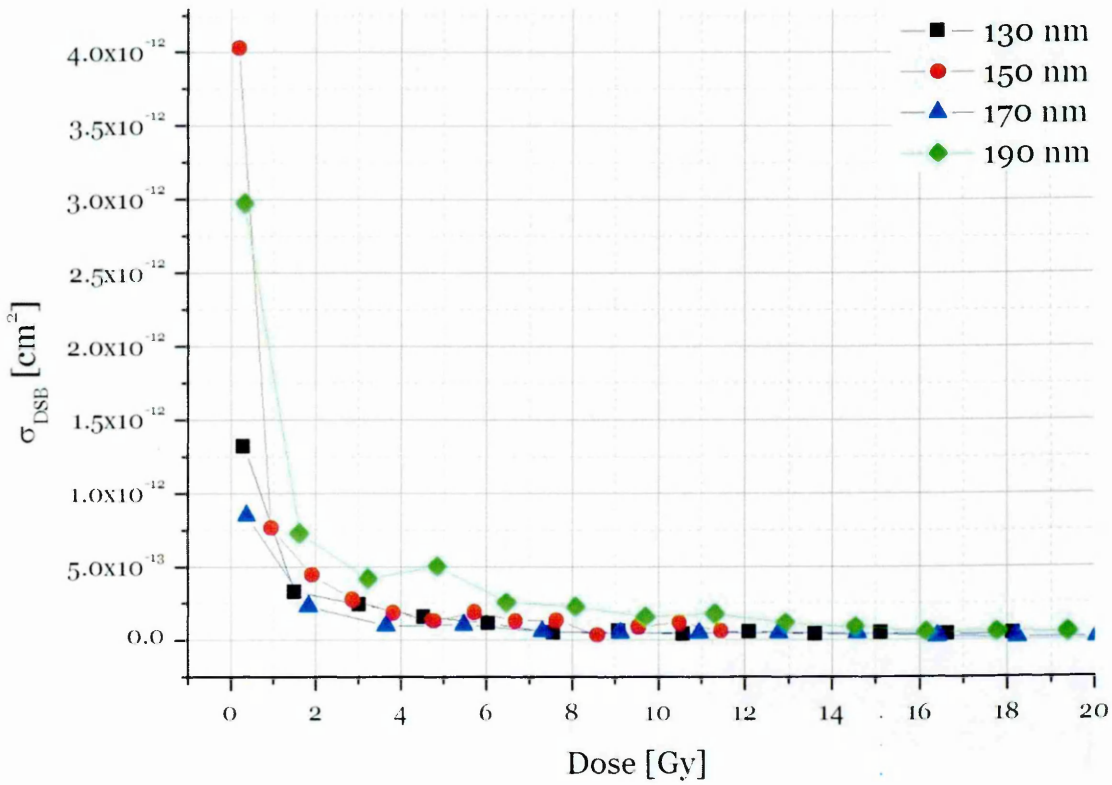

Figure 5-19. Cross section for DSBs formation as a function of dose at 130 nm, 150 nm, 170 nm and 190 nm.

To interpret the data in Figure 5-17, Figure 5-18 and Figure 5-19 one needs to understand what the cross section for the DNA damage means. In general the cross section describes the probability of an interaction between a projectile and a target in terms of the virtual size of the target. Therefore if the projectiles are small and subject to a low flux and yet the event occurred, the virtual size of the target must be big to ensure the interaction. This is nicely illustrated by the data presented in Figure 5-17, Figure 5-18 and Figure 5-19. At low doses, below 2 Gy, where the amount of photons targeting the sample is small, the virtual size of the DNA molecule (i.e. the cross section) is large to ensure that that the event (i.e. damage) will occur. As the amount of photons targeting the sample increases (i.e. the dose increases), the cross section value decreases, as the probability of the interaction of photons with DNA molecules in such conditions is much greater. The slow decrease in the cross section as a function of dose reflects the nature of damage formation, namely the amount supercoiled DNA in the sample decays exponentially with radiation dose. In addition, lower values of cross sections for the supercoiled DNA loss in comparison with larger ones for SSBs and DSB formation express the greater probability of supercoiled DNA loss than the probability of breaks formation. Due to the large uncertainty in the cross sections for inducing strand breaks the notion that SSBs formation is more probable than DSBs formation cannot be conclusive. Looking at doses above 8 Gy one can see that the cross section values for DSB formation are smaller than those for SSB formation, which might indicate that using irradiation at large doses DSBs are more likely to be formed than SSBs.

Cross sections for damage induced using low photon fluxes were also calculated (although, due to the small number of data points, cross sections were not fitted to any curve). Figure 5-20 presents the cross sections for damage obtained for DNA

irradiated in the water solution, whereas Figure 5-21 shows the results obtained for the samples irradiated in the presence of tris buffer.

The cross section for the loss of the supercoiled form at 1 Gy is half that obtained for the samples irradiated at the synchrotron at higher photon fluxes. In terms of cross section it means that at low photon fluxes the probability of the damage formation for the same radiation dose is greater in case of the irradiation carried at low photon fluxes than in case of irradiations carried out using higher fluxes. In case of cross sections for SSBs and DSBs formation, the values obtained in the low flux case were ten times smaller than the ones obtained for the high fluxes. That allowed making an assumption that in case of VUV irradiations of DNA samples in aqueous solution, not only the dose, but more importantly the rate of dose delivery over the irradiation time might be a key parameter to the damage formation.

The calculated values carried an average error of about 30 % for the cross sections for the loss of supercoiled DNA and ~60 % and ~70 % for SSB and DSB formation, respectively.

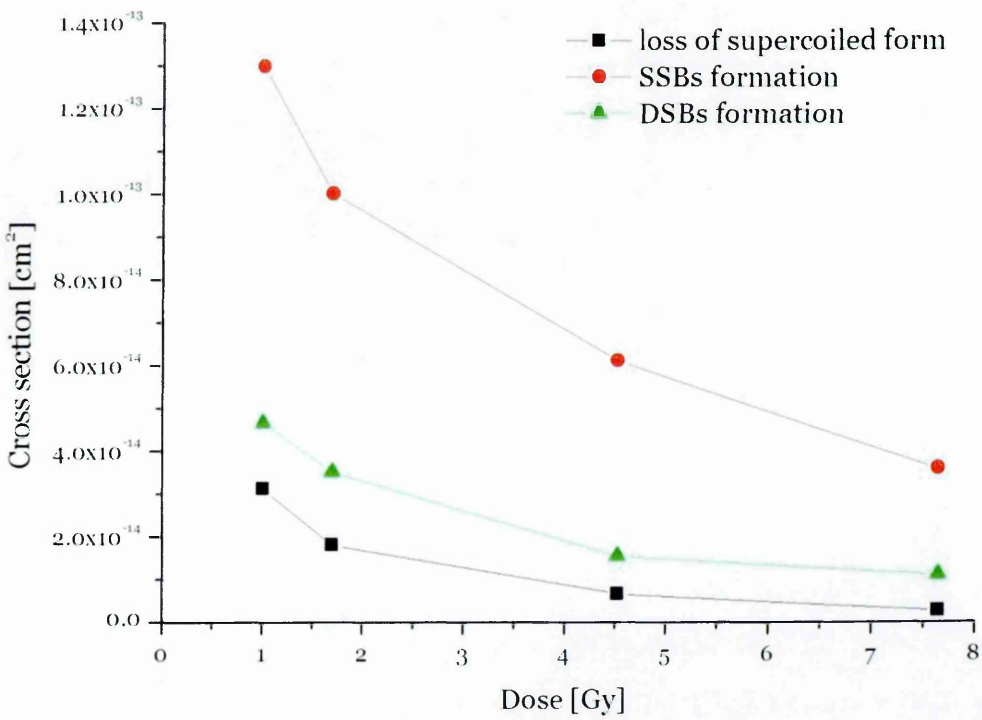

Figure 5-20. Damage cross sections obtained for samples irradiated in pure water.

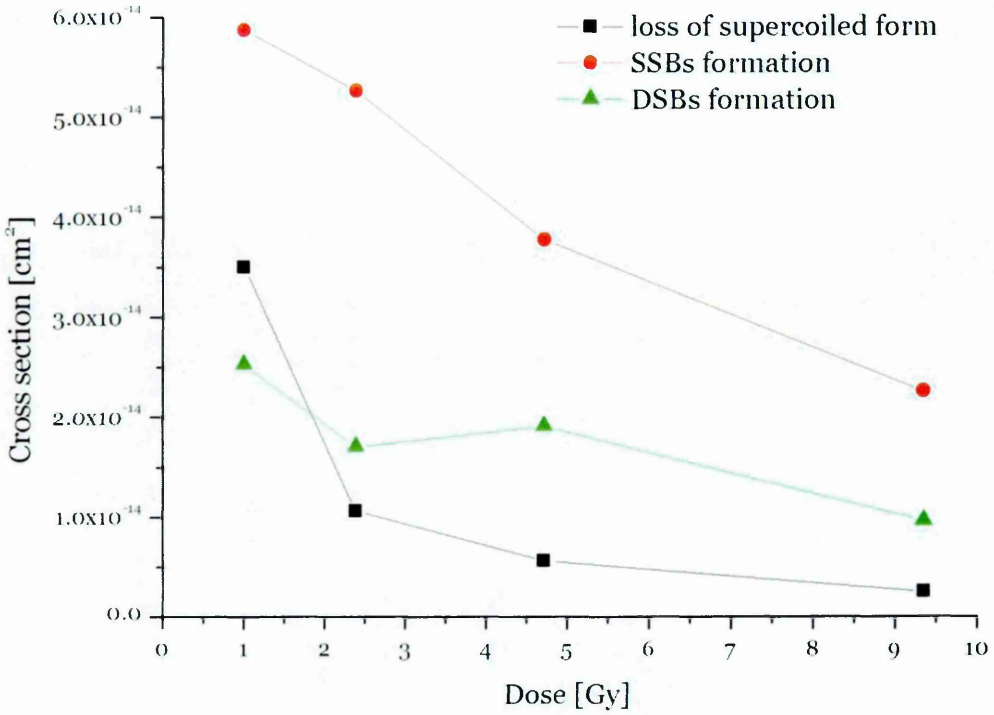

Figure 5-21. Damage cross sections obtained for samples irradiated in tris buffer.

These cross sections clearly illustrate the influence of the action of OH radical scavengers in the irradiated solution. In the case of irradiations carried in the presence of tris buffer, the cross section values are smaller to start with and tend to decrease more slowly than in the case of samples irradiated in water.

5.3.7 Data fitting

The derived cross sections were fitted using Microcal Origin to a function of the form given by (5-4). Two types of fitting were performed: one, where the function was fitted only on the cross section values without taking into account the uncertainties and the second one, where the fitted function was fitted on the same values but weighted over the uncertainty that was obtained for each value. In both cases a chi-square test, $\frac{\chi^2}{DoF}$, and the coefficient of determination, R^2, were calculated to estimate the accuracy of the fit. A chi-squared test gives the proximity

of the fitted data points to the actual ones on which the fit was performed. In the present case it was also weighted over the degrees of freedom of the system (*DoF*), which is given as difference between the number of points used for the fitting procedure (number of cross section values calculated from the experimental data) and the number of floating parameters (number of the changeable parameters in the fitting formula). In order to test whether the fitting procedure was accurate, $\frac{\chi^2}{DoF}$ should have a value close to 1.0 (in the ideal case should be equal to zero). The coefficient of determination describes the degree of correlation between the data points and the fitted line. The higher the correlation the closer to one the value of the coefficient.

The cross section for the loss of supercoiled DNA was fitted with both exponential, σ_S^E, and linear, σ_S^L, functions of the form:

$$\sigma_S^E(\lambda) = P_1 \frac{P_2 \cdot e^{-P_3 \cdot D} + P_4}{D} \qquad \sigma_S^L(\lambda) = P_1 \frac{P'_2 \cdot D + P'_3}{D}$$

where:

$$P_1 = \frac{h \cdot c \cdot \Delta S}{\lambda \cdot M \cdot N_{oS}}$$

and P_2, P'_2, P_3, P'_3 and P_4 were determined by the fitting procedure. Table 5-2 shows the values of the coefficients obtained in these fits.

Figure 5-22, Figure 5-24, Figure 5-26 and Figure 5-28 show derived fits to the experimental data without any uncertainties being taken into account for 130 nm, 150 nm, 170 nm and 190 nm, respectively. Figure 5-23, Figure 5-25, Figure 5-27 and Figure 5-29 show derived fits to the experimental data with the uncertainty being taken into account for 130 nm, 150 nm, 170 nm and 190 nm, respectively. The red dotted line shows an exponential fit, whereas the blue dotted line shows a linear fit.

Table 5-2. Values of the parameters obtained from the fitting procedure for the cross section for the loss of the supercoiled DNA with and without weighting of the points.

Wavelength [nm] / Parameter	130		150		170		190	
	not weighted	weighted	not weighted	weighted	not weighted	weighted	not weighted	weighted
P_1	$5.90 \cdot 10^{-15}$		$5.06 \cdot 10^{-15}$		$4.58 \cdot 10^{-15}$		$3.95 \cdot 10^{-15}$	
P_2	0.195	-6.138	32.100	-91.138	-20.101	114.111	8.061	0.183
P_3	0.101	-0.102	0.088	-0.015	-0.049	0.019	0.253	-0.131
P_4	0.755	98.976	56.137	180.379	112.032	-16.411	87.498	87.856
$\frac{\chi^2}{DoF}$	$2.39 \cdot 10^{-29}$	0.046	$1.40 \cdot 10^{-29}$	0.118	$4.48 \cdot 10^{-30}$	0.101	$1.03 \cdot 10^{-29}$	0.480
R^2	0.99997	0.99902	0.99994	0.99119	0.99996	0.99393	0.99991	0.99123
P'_2	-1.456	-1.108	-1.872	-1.498	-1.396	-1.852	-0.700	0.078
P'_3	94.852	98.542	87.911	89.677	92.109	96.498	95.086	88.029
$\frac{\chi^2}{DoF}$	$2.17 \cdot 10^{-29}$	0.045	$1.58 \cdot 10^{-29}$	0.108	$5.41 \cdot 10^{-30}$	0.095	$1.23 \cdot 10^{-29}$	0.443
R^2	0.99997	0.99895	0.99991	0.99115	0.99995	0.99471	0.99988	0.99110

There are significant differences between both types of fits. It can be seen that the curves fitted using only the data points are much better than those fitted with a correction for the measurement uncertainty. Statistical tests, both the chi-squared and the coefficient of determination, show better values for the fits performed on the data points only.

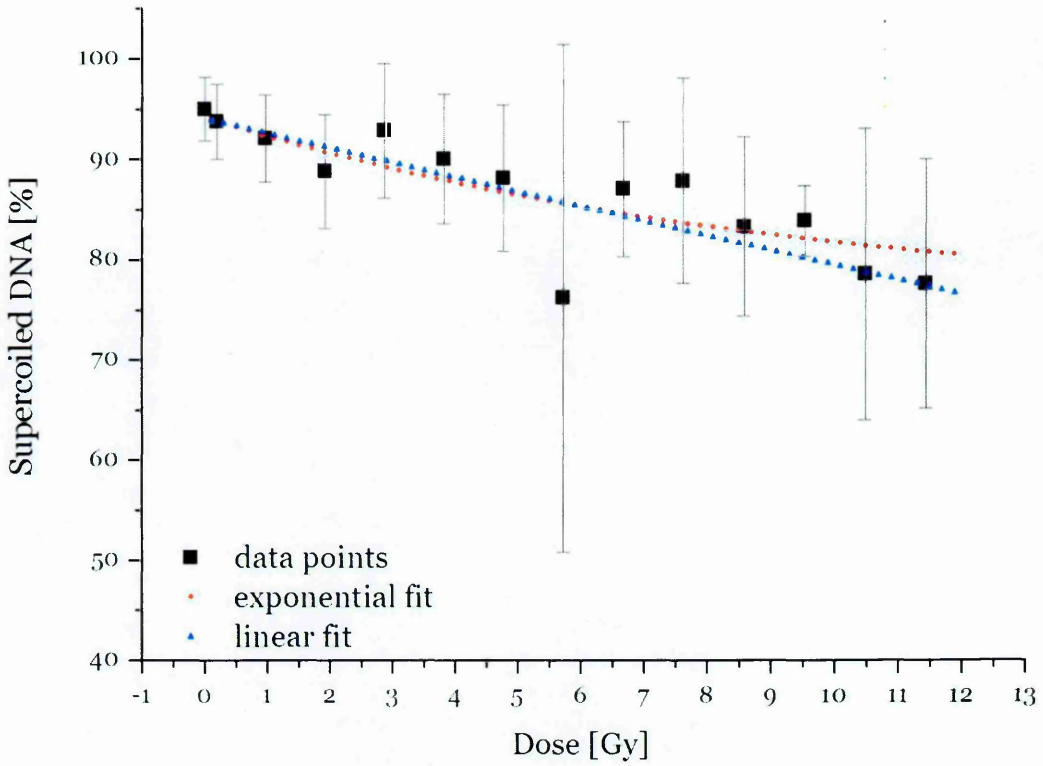

Figure 5-22. Exponential and linear fits for the loss of the supercoiled DNA at 130 nm.

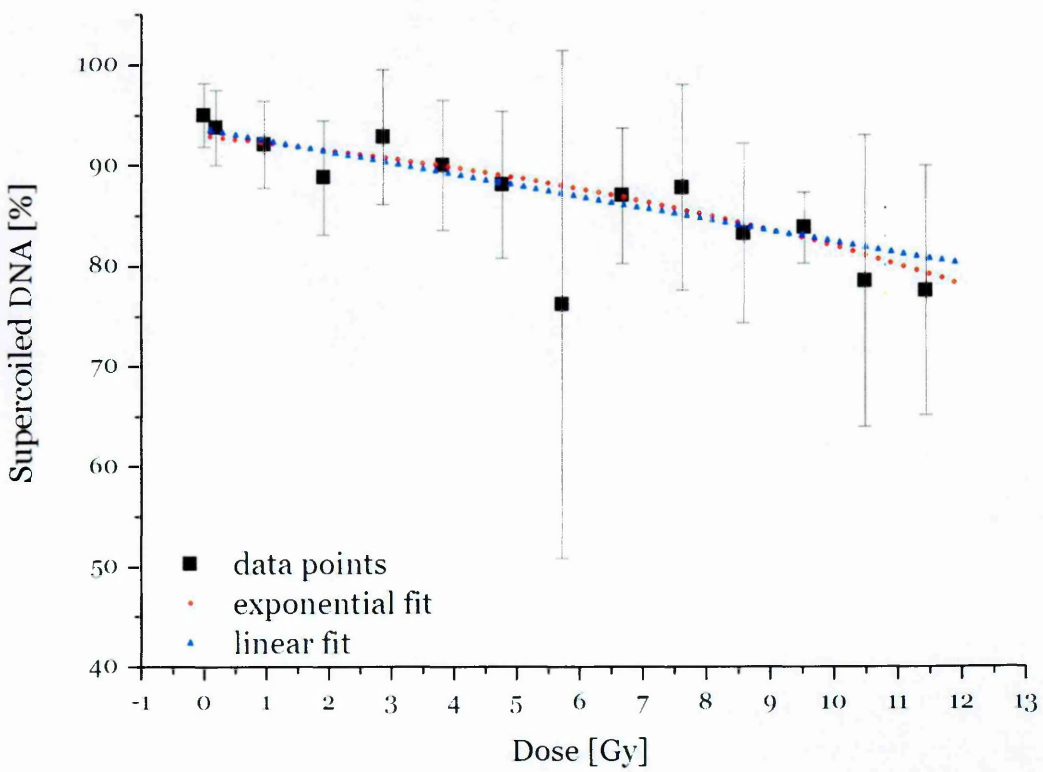

Figure 5-23. Exponential and linear fits for the loss of the supercoiled DNA at 130 nm; fits performed on the weighted data points.

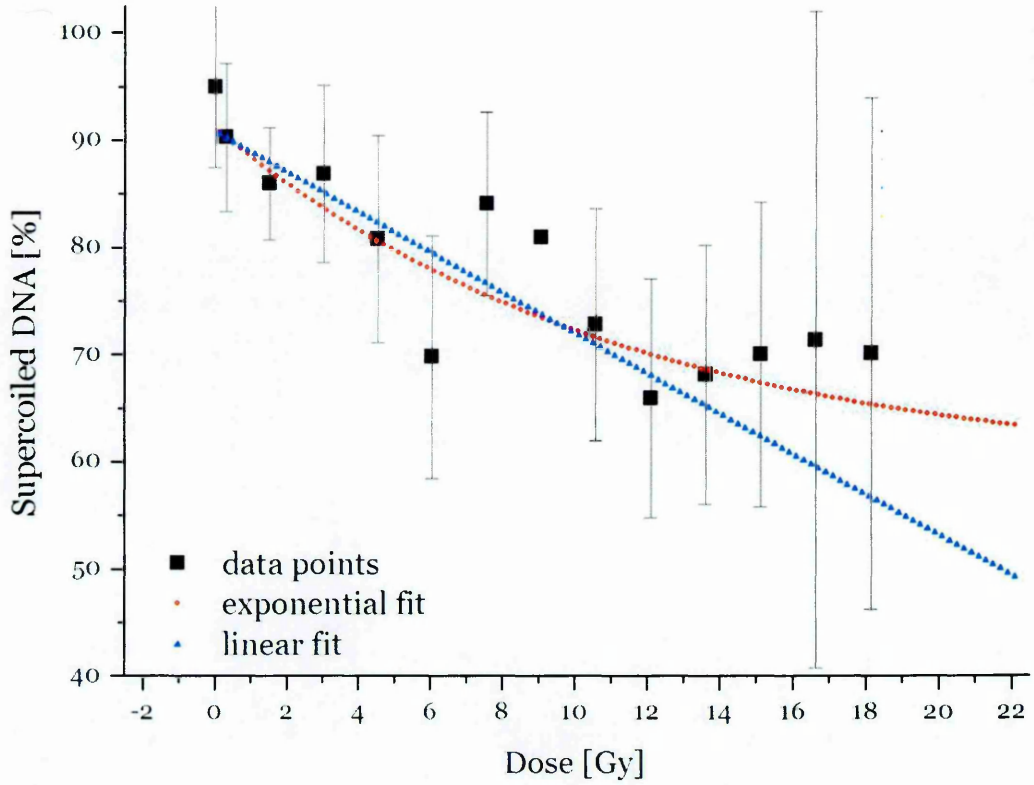

Figure 5-24. Exponential and linear fits for the loss of the supercoiled DNA at 150 nm.

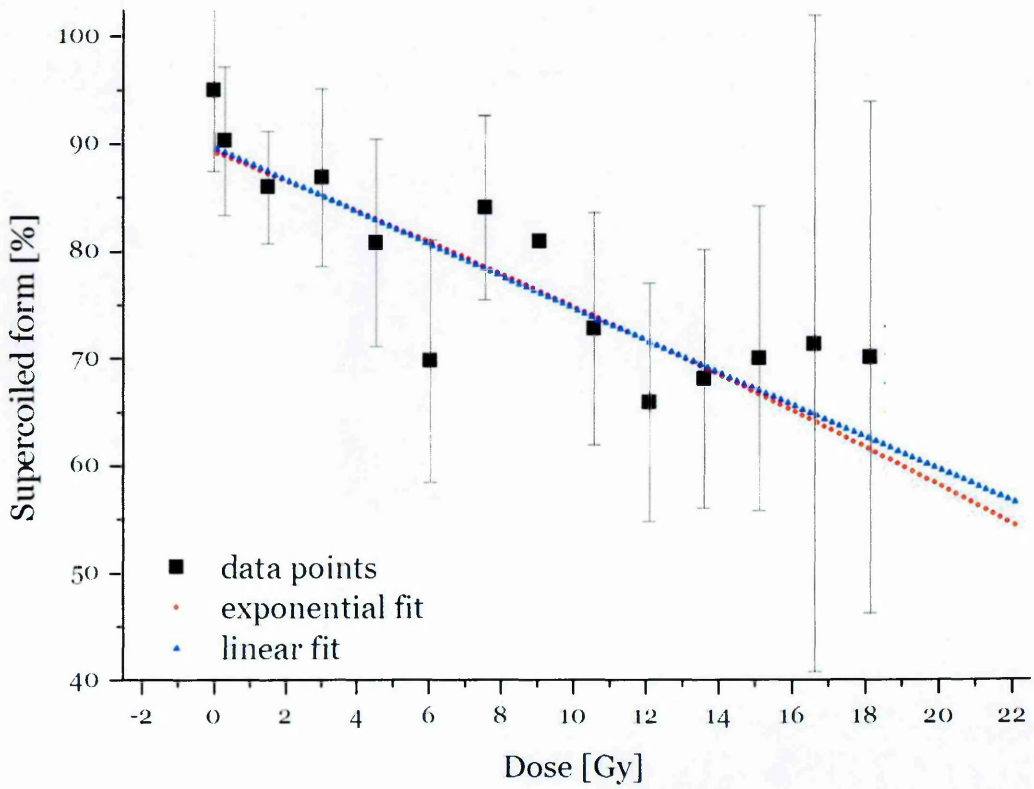

Figure 5-25. Exponential and linear fits for the loss of the supercoiled DNA at 150 nm; fits performed on the weighted data points

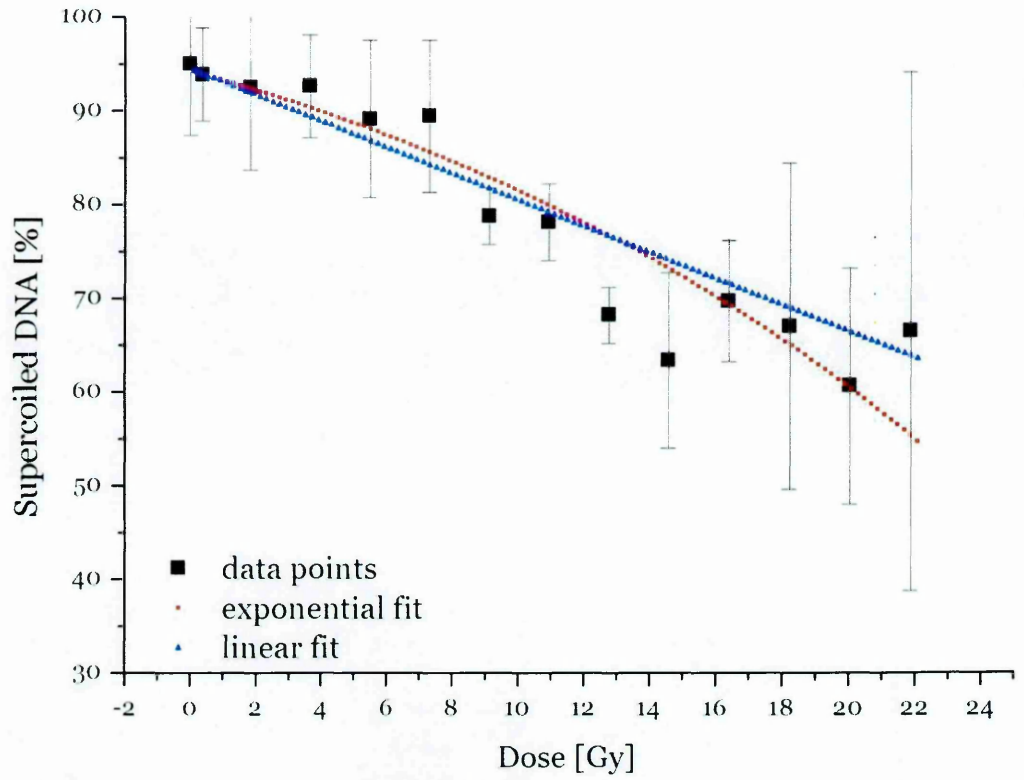

Figure 5-26. Exponential and linear fits for the loss of the supercoiled DNA at 170 nm.

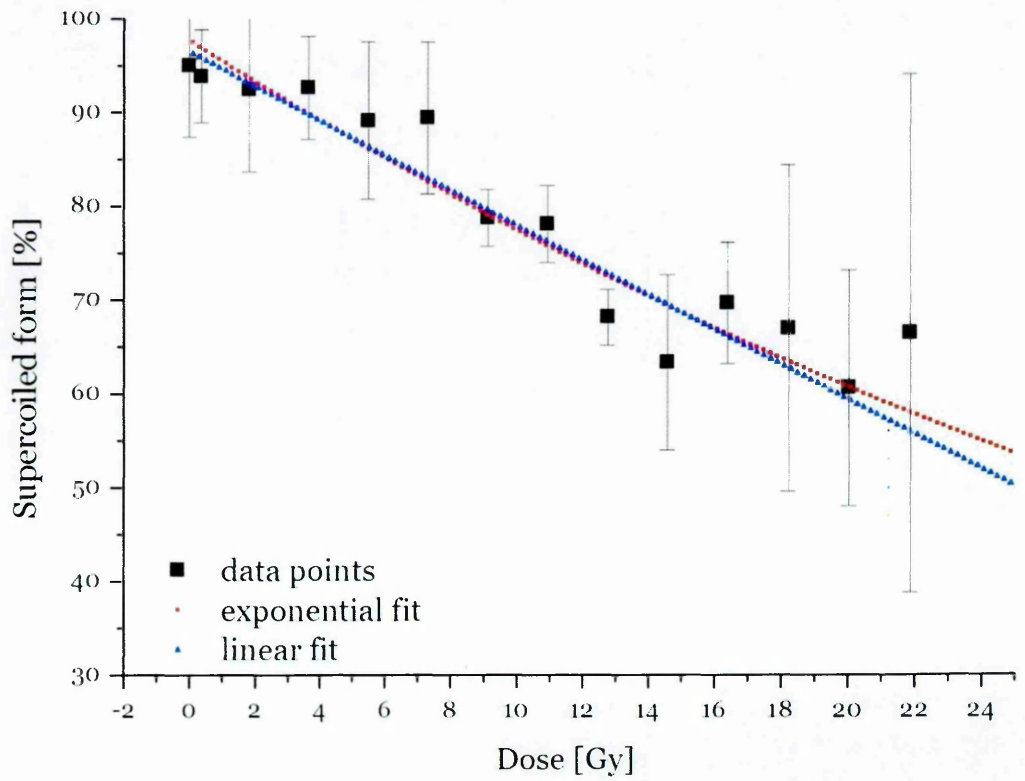

Figure 5-27. Exponential and linear fits for the loss of the supercoiled DNA at 170 nm; fits performed on the weighted data points

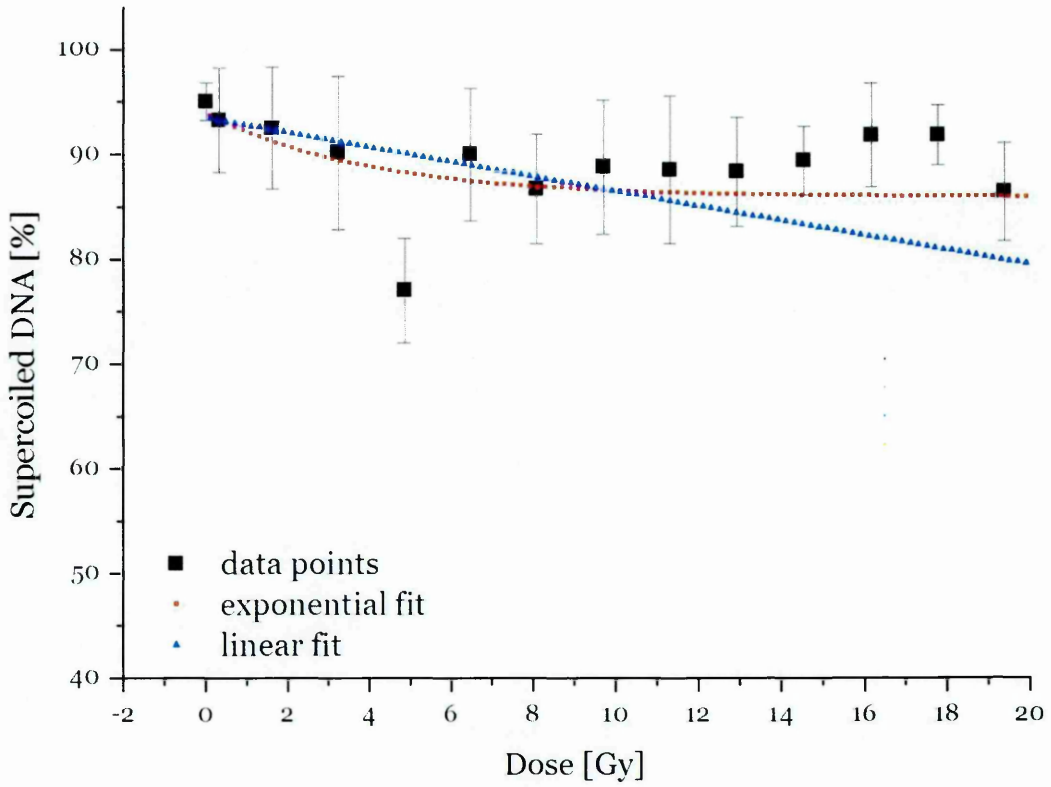

Figure 5-28. Exponential and linear fits for the loss of the supercoiled DNA at 190 nm.

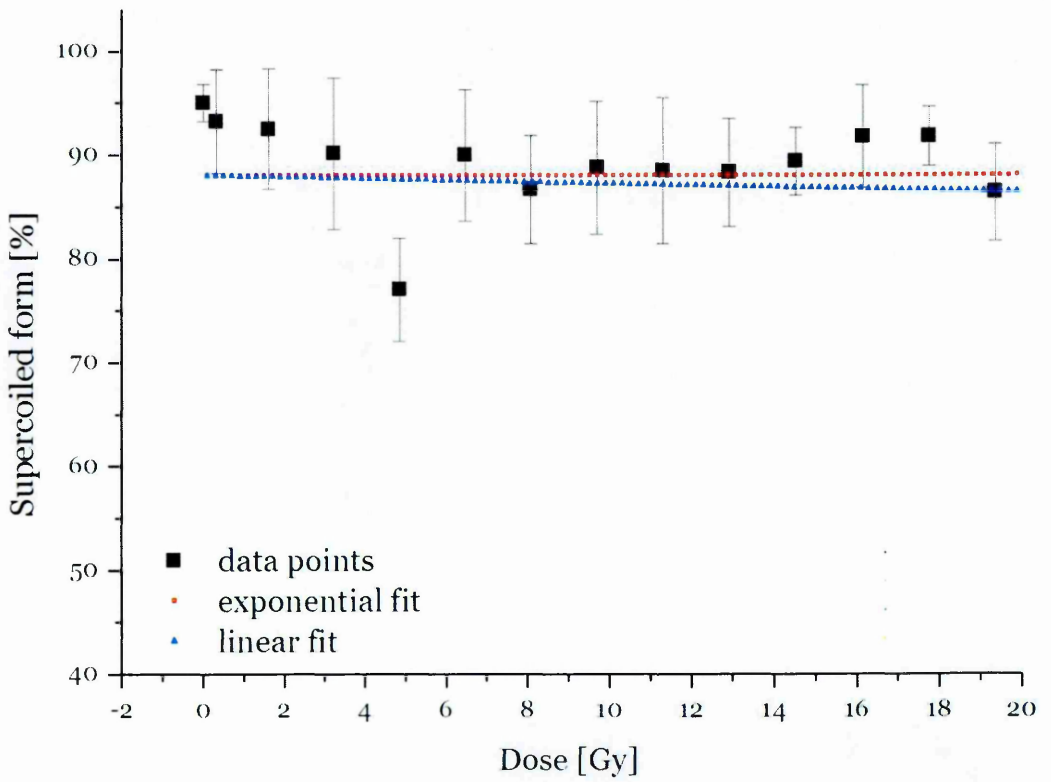

Figure 5-29. Exponential and linear fits for the loss of the supercoiled DNA at 190 nm; fits performed on the weighted data points.

In all cases it can be clearly seen that an exponential function is a better fit to the experimental data than a linear fit. In all cases apart from that irradiated at 170 nm the curves follow the same trend, which is a steadily falling damage as a function of dose. Although also exponential, the trend line for the data points recorded using 170 nm follows another direction (also the parameters P_2 and P_3 are the only ones negative in the case of data fitting just on the points and positive for the second type of fit). Figure 5-30 and Figure 5-31 illustrate the difference between the used fitting methods for the exponential function. The curves fitted only on the data points for 130 nm, 150 nm and 190 nm irradiations show similar trends. In case of the weighted values of the cross sections the curve for 170 nm irradiations shows a different trend to the other ones. In addition, fits on the weighted data present a much closer approximation to the damage observed in the irradiation experiments. This suggests that there was not enough mixing during the irradiations carried at 130 nm as the trend line follows a different tendency to the 150 nm and 190 nm ones.

In Figure 5-32 and Figure 5-33 the fitted cross sections, based on the exponential function, are shown in detail. In both cases the cross section for loss of supercoiled DNA at 170 nm has a smaller value than the one for the damage at 150 nm (see the inserts in Figure 5-32 and Figure 5-33) through the whole dose range, but it shifts of the original trend to higher values. None of the other fitted lines changes their positions with respect to the other ones.

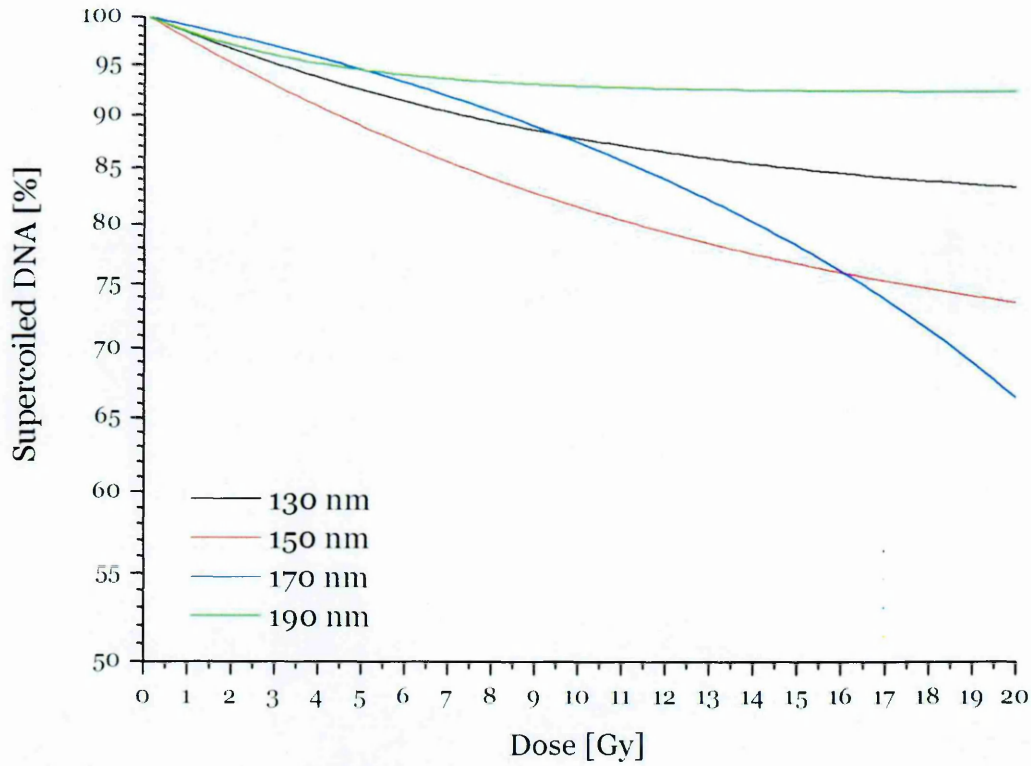

Figure 5-30. Comparison of the exponentially fitted trend lines for the loss of supercoiled DNA.

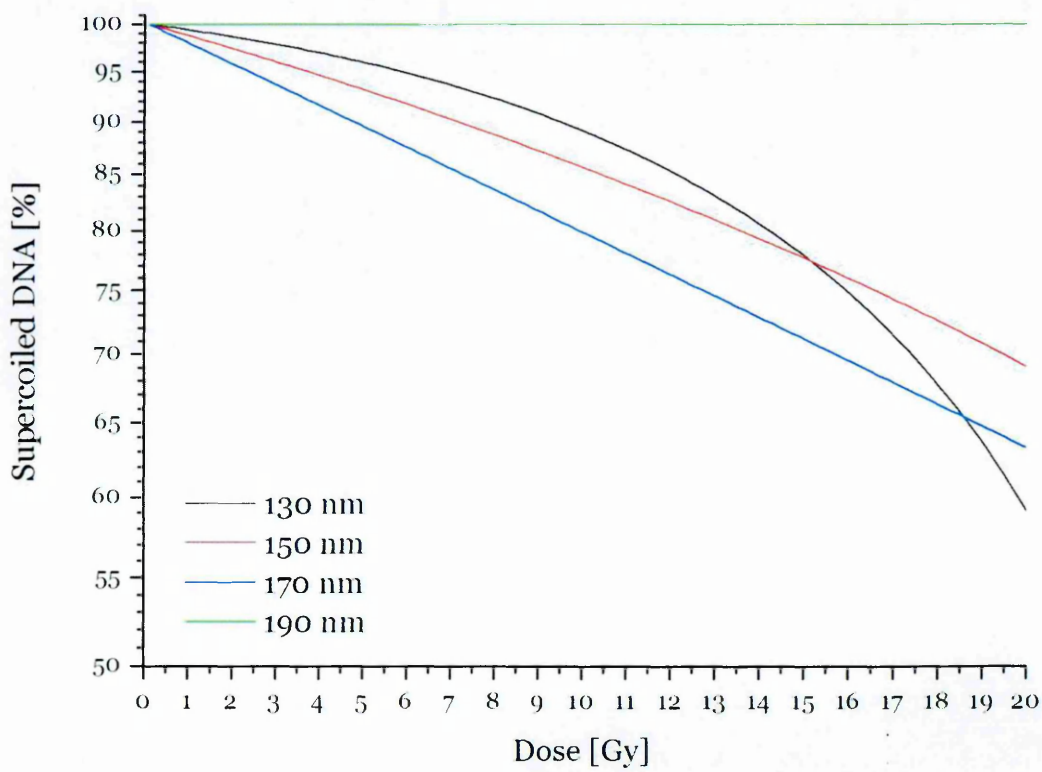

Figure 5-31. Comparison of the exponentially fitted trend lines for the loss of supercoiled DNA; fits performed on the weighted data points.

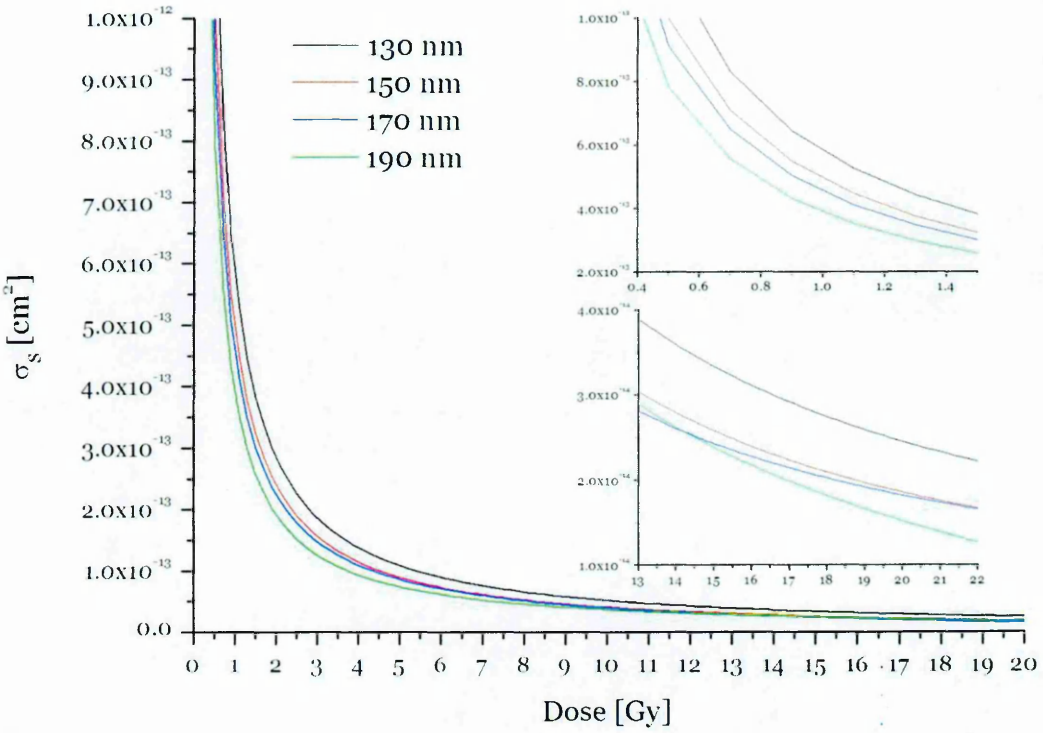

Figure 5-32. Fitted cross sections for supercoiled DNA loss.

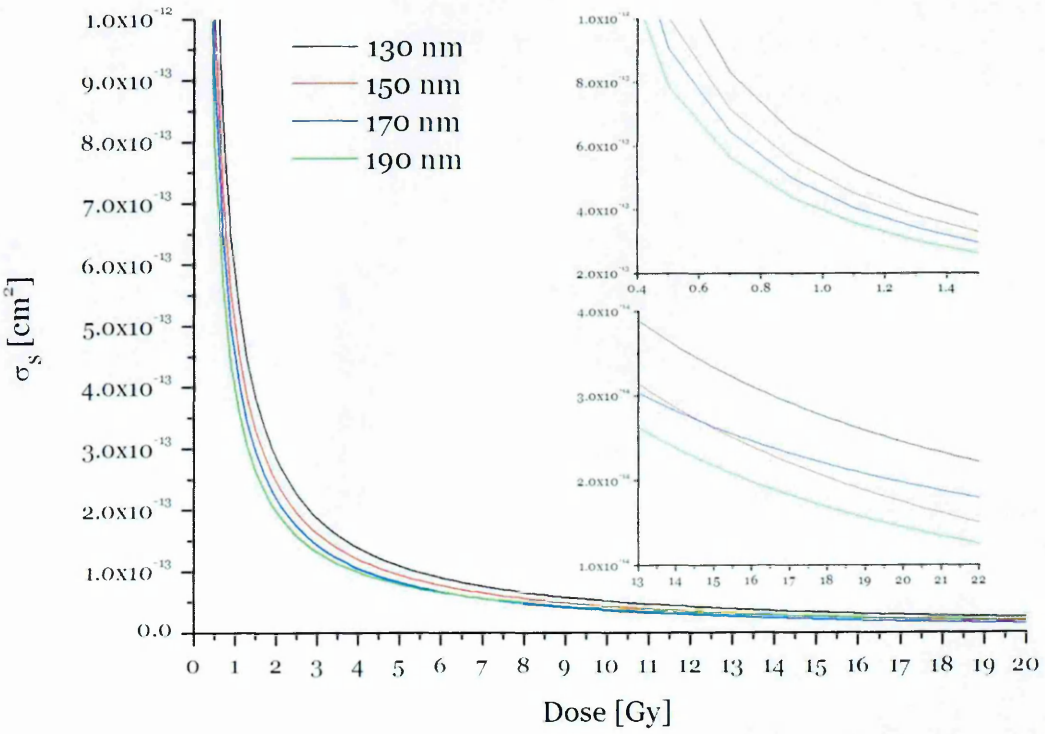

Figure 5-33. Fitted cross sections for supercoiled DNA loss; fits performed on the weighted data points.

If double strand breaks are caused by a single photon event rather than two independent events a linear curve is to be expected, whereas if the damage is due to two independent events a square function would be expected to fit the data. The cross sections for formation of double strand breaks were therefore fitted with both linear, σ^{L}_{DSB}, and square, σ^{S}_{DSB}, functions of the form

$$\sigma^{L}_{DSB}(\lambda) = P_1 \frac{P_2 \cdot D + P_3}{D} \qquad \sigma^{S}_{DSB}(\lambda) = P_1 \frac{P'_2 \cdot D^2 + P'_3}{D}$$

where:

$$P_1 = \frac{h \cdot c \cdot \Delta S}{\lambda \cdot M \cdot N_{oDSB}}$$

and P_2, P'_2, P_3 and P'_3 were determined by the fitting procedure.

Table 5-3 shows the values of the coefficients obtained.

Table 5-3. Values of the parameters obtained from the fitting procedure for the cross section for the double strand breaks formation with and without the weight.

Wavelength [nm] / Parameter	130		150		170		190	
	not weighted	weighted	not weighted	weighted	not weighted	weighted	not weighted	weighted
P_1	$1.20 \cdot 10^{-12}$		$3.92 \cdot 10^{-13}$		$6.11 \cdot 10^{-13}$		$1.44 \cdot 10^{-12}$	
P_2	0.005	-0.029	0.083	0.25	0.134	-0.004	0.058	-0.006
P_3	0.638	0.682	1.003	1.135	0.836	0.666	0.652	0.914
$\frac{\chi^2}{DoF}$	$1.34 \cdot 10^{-27}$	0.017	$1.22 \cdot 10^{-27}$	0.005	$3.63 \cdot 10^{-28}$	0.006	$7.52 \cdot 10^{-27}$	0.007
R^2	0.999	0.698	0.991	0.811	0.993	0.852	0.989	0.828
P'_2	0.001	-0.002	0.004	0.112	0.001	-0.0003	0.002	-0.0006
P'_3	0.639	0.612	1.036	1.187	0.516	0.678	0.677	0.942
$\frac{\chi^2}{DoF}$	$1.33 \cdot 10^{-27}$	0.018	$1.89 \cdot 10^{-27}$	0.005	$5.72 \cdot 10^{-28}$	0.005	$1.23 \cdot 10^{-26}$	0.007
R^2	0.999	0.685	0.986	0.823	0.990	0.863	0.982	0.843

Figure 5-34, Figure 5-36, Figure 5-38 and Figure 5-40 present the fits obtained to the experimental data without the uncertainty being taken into account for 130 nm, 150 nm, 170 nm and 190 nm, respectively. Figure 5-35, Figure 5-37, Figure 5-39 and Figure 5-41 present the fits obtained to the experimental data with the uncertainty being taken into account for 130 nm, 150 nm, 170 nm and 190 nm, respectively. The red dotted line shows the linear fit, whereas the blue dotted line shows the square fit.

The curves obtained for the weighted data did not seem to differ very much for either of functions used. Statistical tests both the chi-squared and the coefficient of determination, shown better values for the fits performed only with data points. In all the cases the fitted curves lay within the experimental errors, so one can conclude that both phenomena described above are equally probable.

Due to the large statistical uncertainties it was therefore not possible to tell which fit is more appropriate to describe the phenomenon of double strand breaks formation. Therefore an attempt was taken to fit the data that correspond to single strand break formation. The motivation was that the statistical spread of the data was smaller than for the DSB formation so any function that describes changes should be better defined.

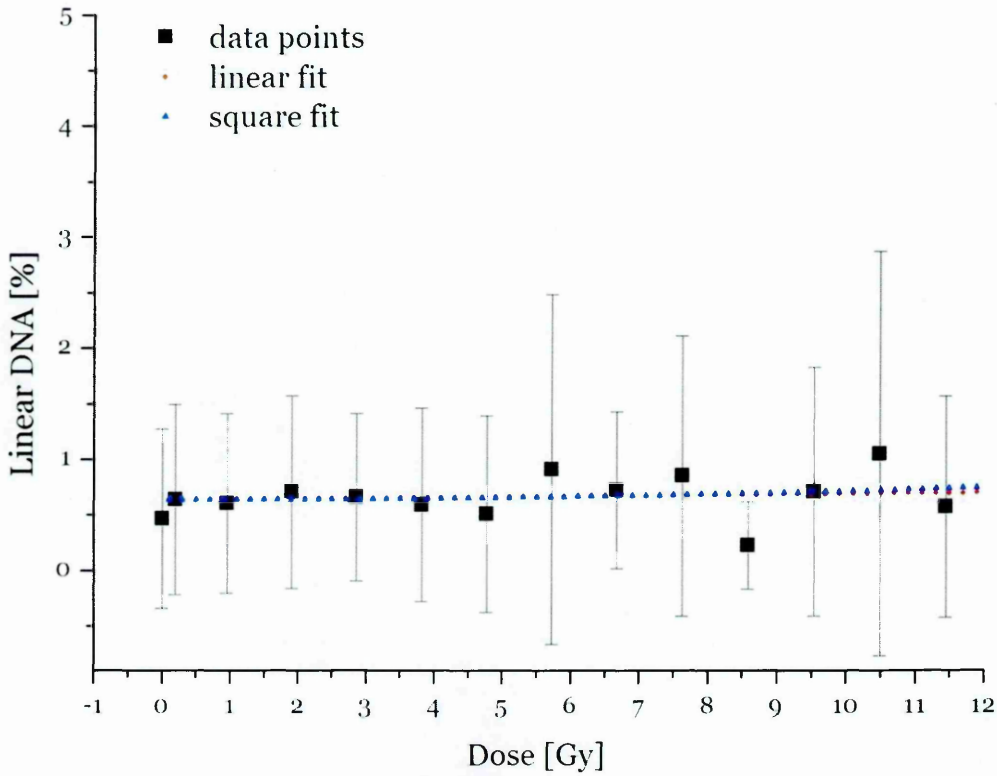

Figure 5-34. Linear and square functions fitted to double strand break formation as function of dose at 130 nm.

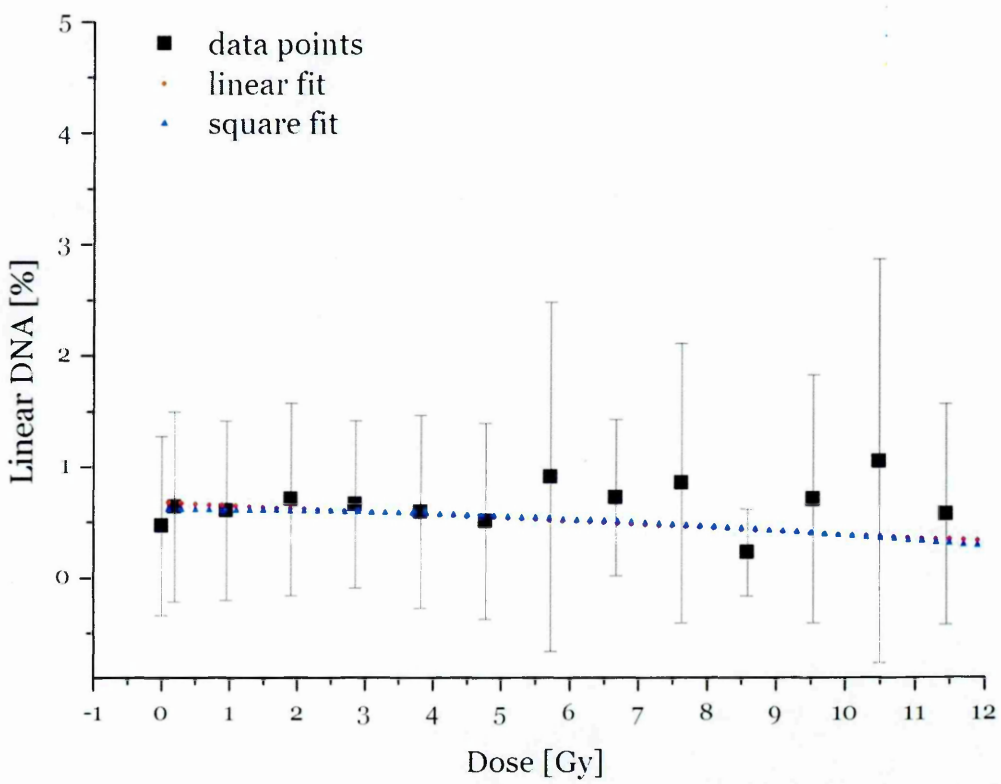

Figure 5-35. Linear and square functions fitted to double strand break formation as function of dose at 130 nm; fits performed on the weighted data points.

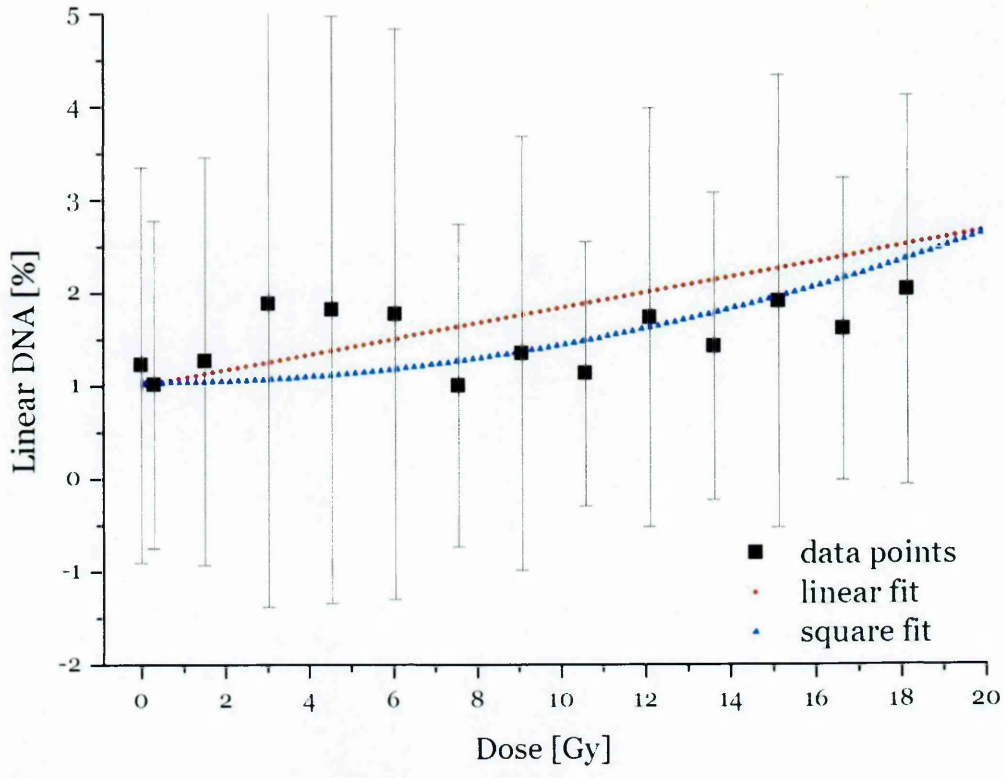

Figure 5-36. Linear and square functions fitted to double strand break formation as function of dose at 150 nm.

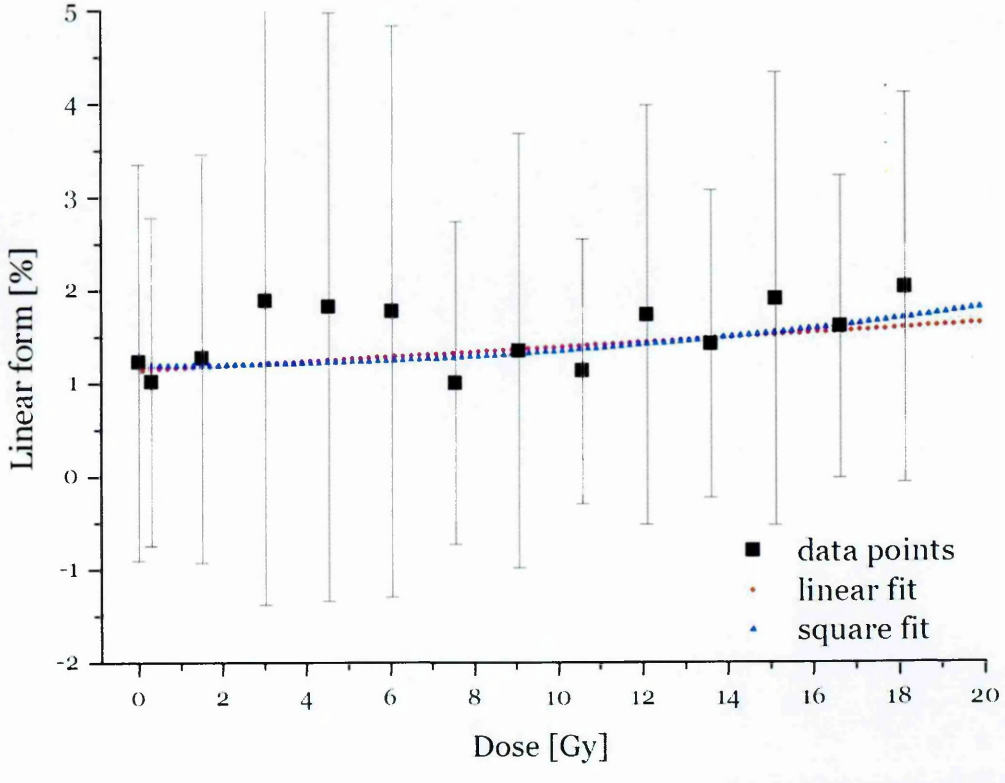

Figure 5-37. Linear and square functions fitted to double strand break formation as function of dose at 150 nm; fits performed on the weighted data points.

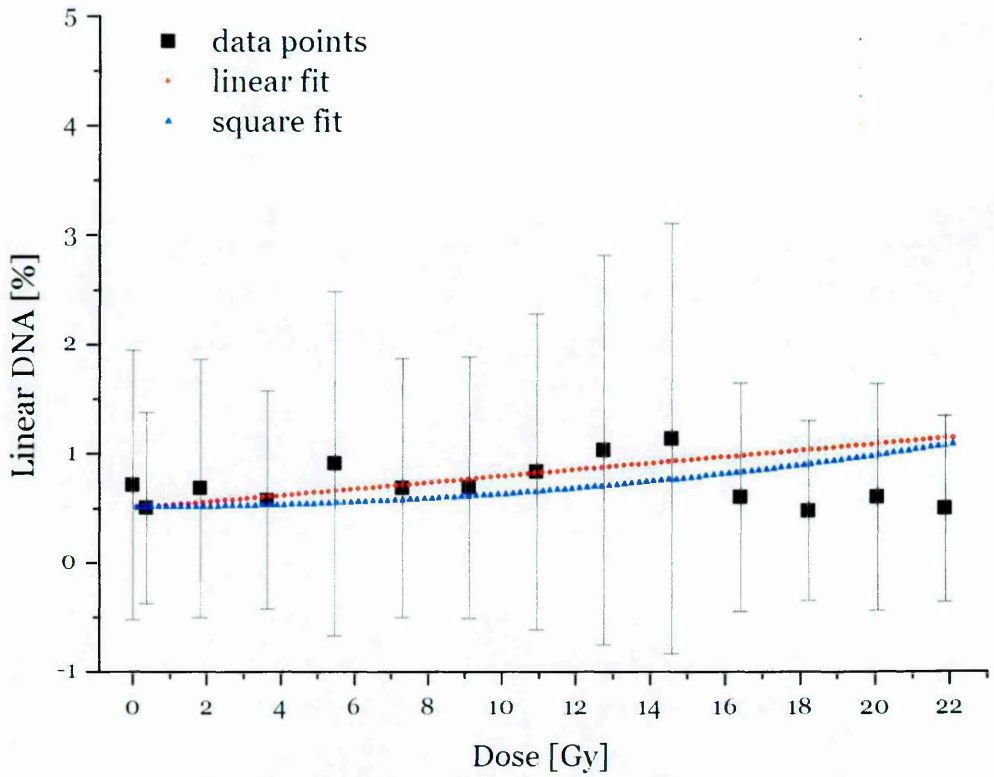

Figure 5-38. Linear and square functions fitted to double strand break formation as function of dose at 170 nm.

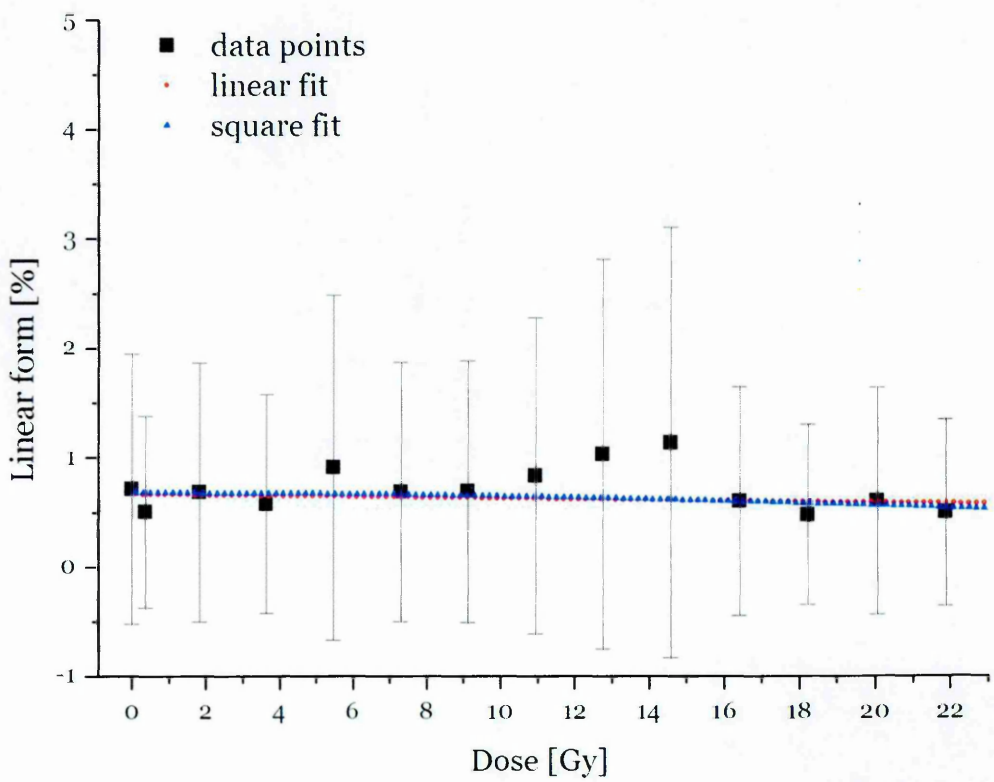

Figure 5-39. Linear and square functions fitted to double strand break formation as function of dose at 170 nm; fits performed on the weighted data points.

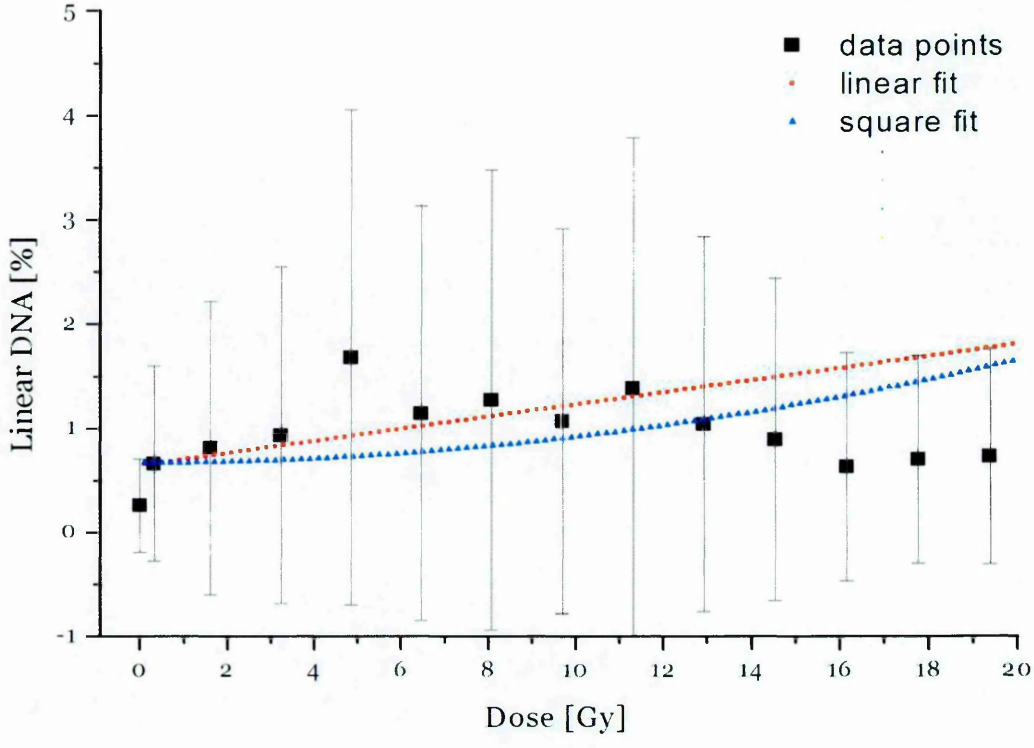

Figure 5-40. Linear and square functions fitted to double strand break formation as function of dose at 190 nm.

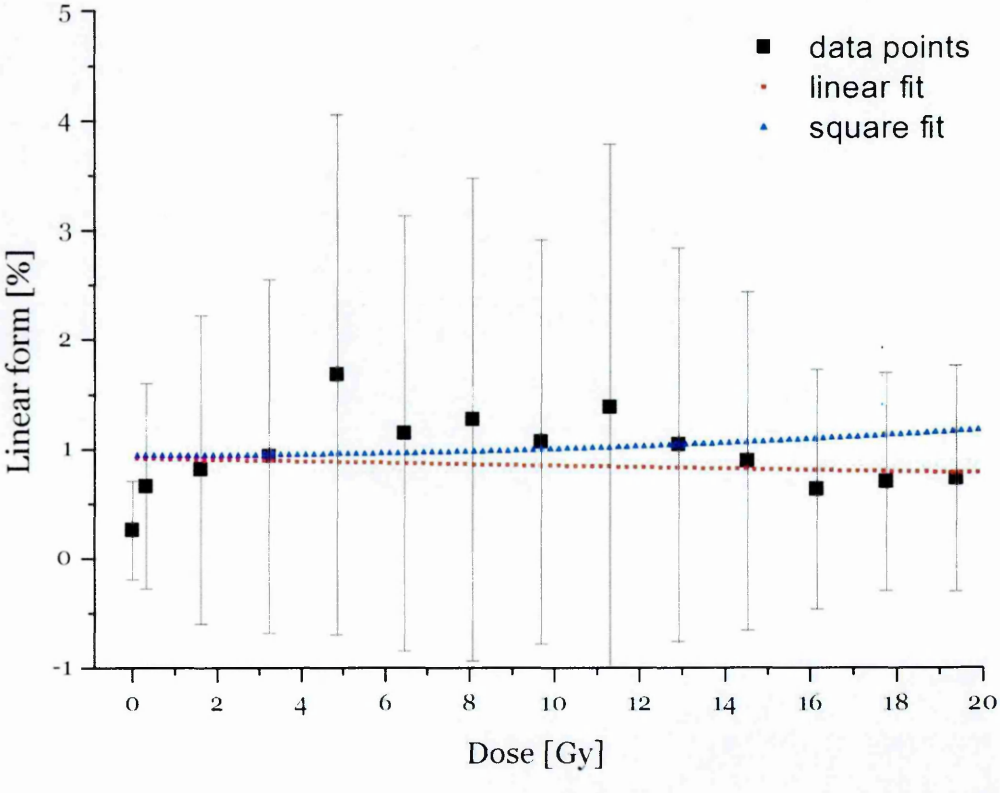

Figure 5-41. Linear and square functions fitted to double strand break formation as function of dose at 190 nm; fits performed on the weighted data points.

Knowing that the amount of supercoiled DNA decays exponentially with dose, two fits were performed for a SSB formation curves. One that combined an exponential decay of the supercoiled DNA with a linear increase in DSBs, σ_{SSB}^{L}, and a second fit that combined an exponential decay of the supercoiled DNA with a squared increase in DSBs, σ_{SSB}^{S}. These two fitting functions can be written as:

$$\sigma_{SSB}^{L}(\lambda) = P_1 \frac{P_2 \cdot e^{-P_3 \cdot D} + P_4 \cdot D + P_5}{D} \qquad \sigma_{SSB}^{S}(\lambda) = P_1 \frac{P'_2 \cdot e^{-P'_3 \cdot D} + P'_4 \cdot D^2 + P'_5}{D}$$

where:

$$P_1 = \frac{h \cdot c \cdot \Delta S}{\lambda \cdot M \cdot N_{oSSB}}$$

and P_2, P'_2, P_3, P'_3, P_4, P'_4, P_5 and P'_5 were determined by the fitting procedure. Table 5-4 shows the values of the coefficients obtained.

Figure 5-42, Figure 5-44, Figure 5-46 and Figure 5-48 present the fits obtained to the experimental data without the uncertainty being taken into account for 130 nm, 150 nm, 170 nm and 190 nm, respectively. Figure 5-43, Figure 5-45, Figure 5-47 and Figure 5-49 present the fits obtained to the experimental data with the uncertainty being taken into account for 130 nm, 150 nm, 170 nm and 190 nm, respectively. The red dotted line shows the fit based on combination of exponential decay of supercoiled DNA with linear increase of DSBs, whereas the blue dotted line shows the fit based on combination of exponential decay of supercoiled DNA with square increase of DSBs.

It can be clearly seen that in the case of irradiations carried at 130 nm and 150 nm and 170 nm better fits were obtained for the combination of exponential and square functions. Also, the fit to the weighted data follows the data points more closely than the fits based only on the points. In case of the irradiations carried at 190 nm the differences between both fits are small enough such that both are

equally valid to describe the data obtained. Statistical tests showed that both the chi-squared and the coefficient of determination, show better values for the fits performed only on the data points.

Table 5-4. Values of the parameters obtained from the fitting procedure for the cross section for the single strand breaks formation with and without weighting.

Wavelength [nm]	130		150		170		190	
Parameter	not weighted	weighted	not weighted	weighted	not weighted	weighted	not weighted	weighted
P_1	$1.52 \cdot 10^{-13}$		$7.30 \cdot 10^{-14}$		$6.88 \cdot 10^{-14}$		$1.21 \cdot 10^{-13}$	
P_2	1.984	0.0004	4.950	1.957	1.228	0.796	-43.515	-9.577
P_3	0.002	-0.830	-0.001	$-6.381 \cdot 10^{-8}$	0.531	1.507	0.086	0.323
P_4	1.454	0.961	1.575	1.160	1.308	1.228	-1.721	-0.302
P_5	2.526	4.986	6.215	10.466	6.388	6.977	46.631	12.329
$\frac{\chi^2}{DoF}$	$1.72 \cdot 10^{-26}$	0.024	$4.17 \cdot 10^{-27}$	0.030	$8.74 \cdot 10^{-28}$	0.030	$6.38 \cdot 10^{-27}$	0.082
R^2	0.986	0.822	0.994	0.854	0.995	0.715	0.965	0.814
P'_2	16.127	-3.408	-18.239	-102.343	-9.022	-941.713	-16.117	-7.276
P'_3	-0.142	2.304	0.156	0.015	4.126	0.002	0.123	0.394
P'_4	-0.377	0.097	0.010	-0.015	0.064	-0.035	-0.035	-0.010
P'_5	-11.794	6.938	28.977	114.076	9.870	947.448	19.243	10.025
$\frac{\chi^2}{DoF}$	$1.56 \cdot 10^{-26}$	0.023	$3.17 \cdot 10^{-27}$	0.029	$9.15 \cdot 10^{-28}$	0.025	$6.41 \cdot 10^{-27}$	0.084
R^2	0.987	0.828	0.995	0.858	0.955	0.760	0.965	0.810

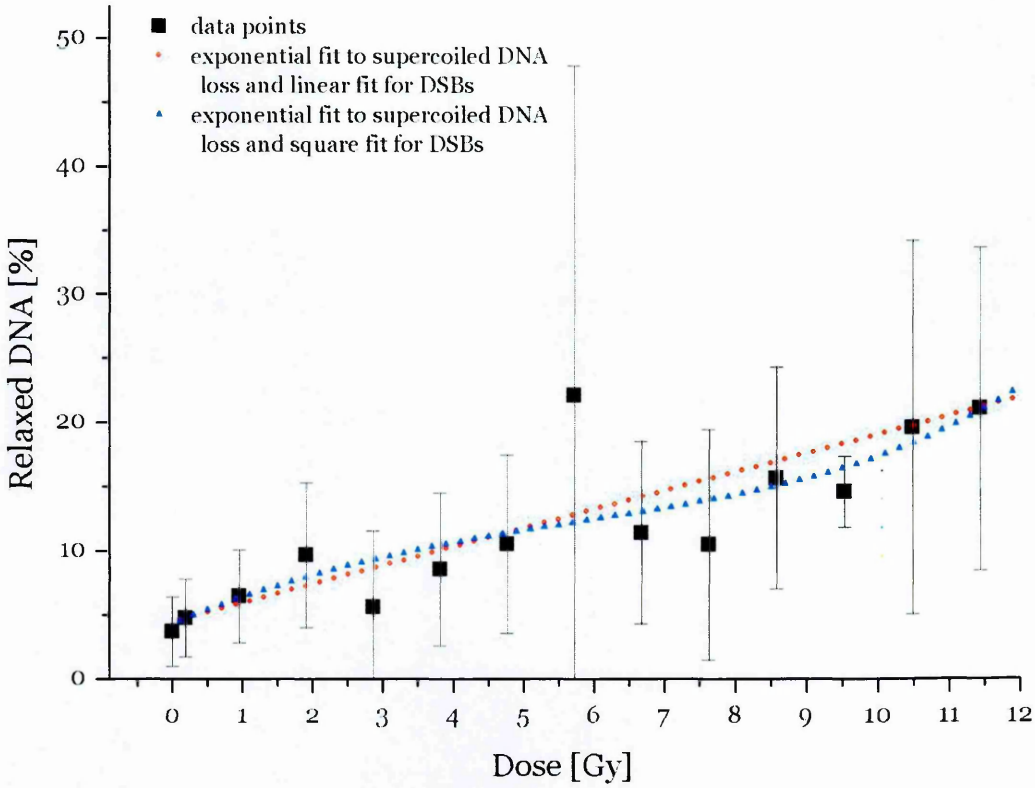

Figure 5-42. Fit of the SSBs formation after irradiation at 130 nm.

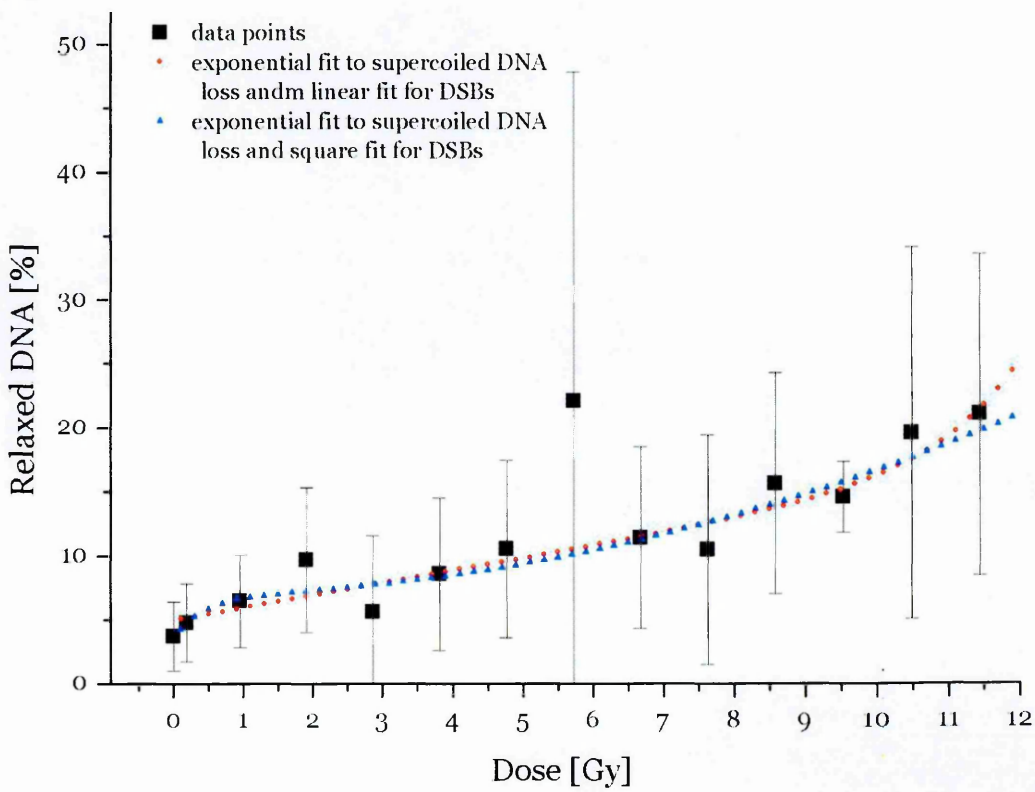

Figure 5-43. Fit of the SSBs formation after irradiation at 130 nm; fits performed on the weighted data points.

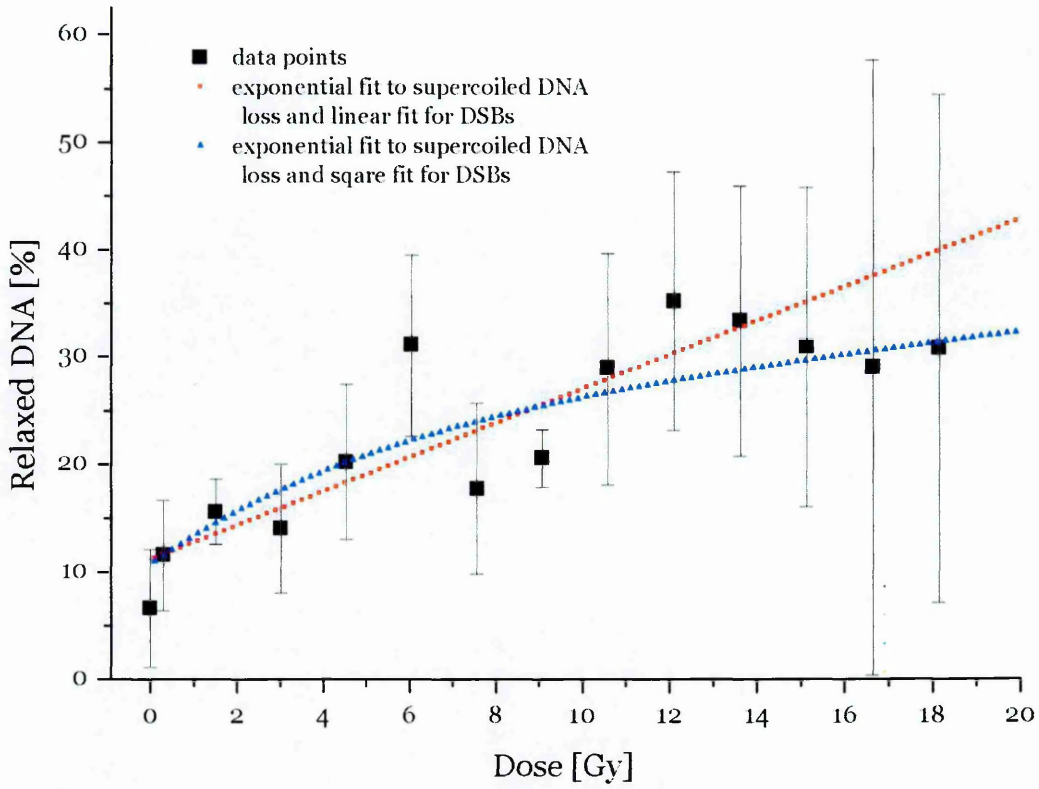

Figure 5-44. Fit of the SSBs formation after irradiation at 150 nm.

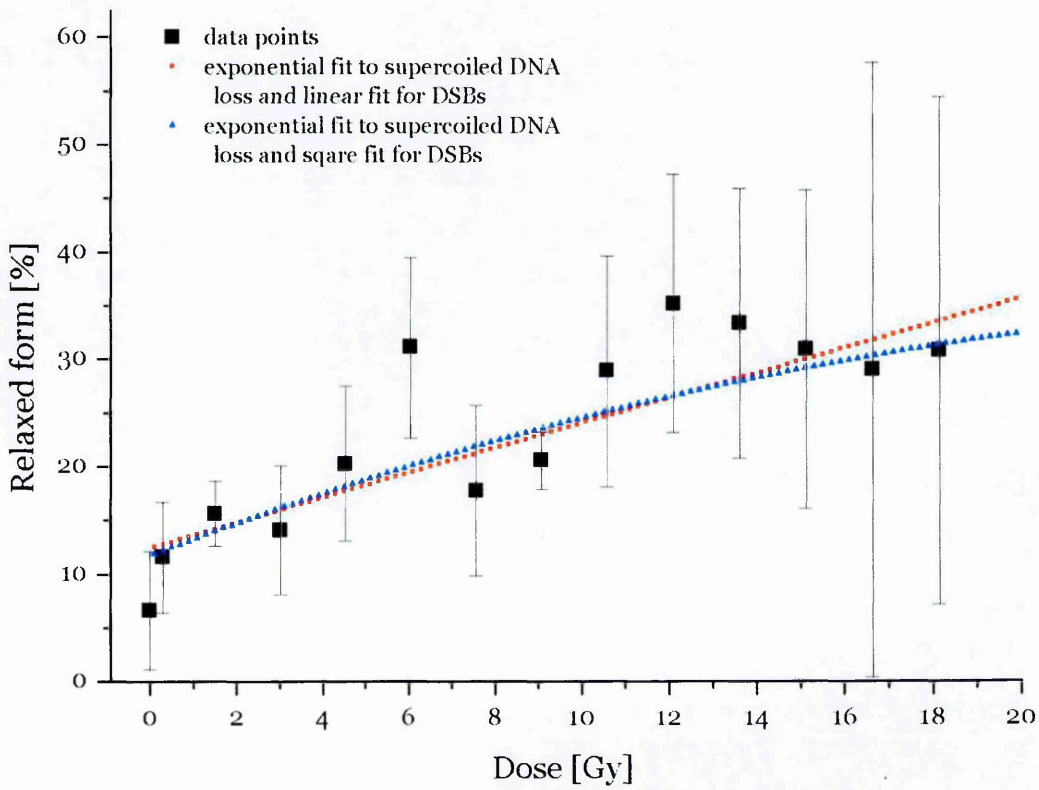

Figure 5-45. Fit of the SSBs formation after irradiation at 150 nm; fits performed on the weighted data points.

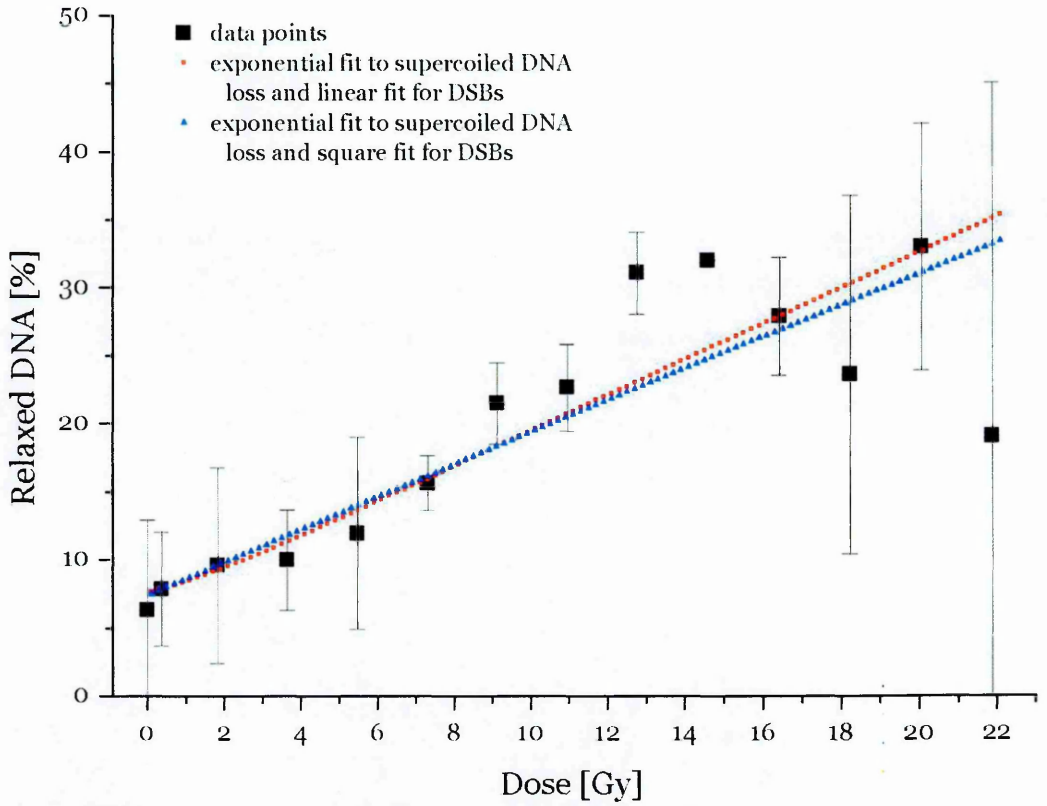

Figure 5-46. Fit of the SSBs formation after irradiation at 170 nm.

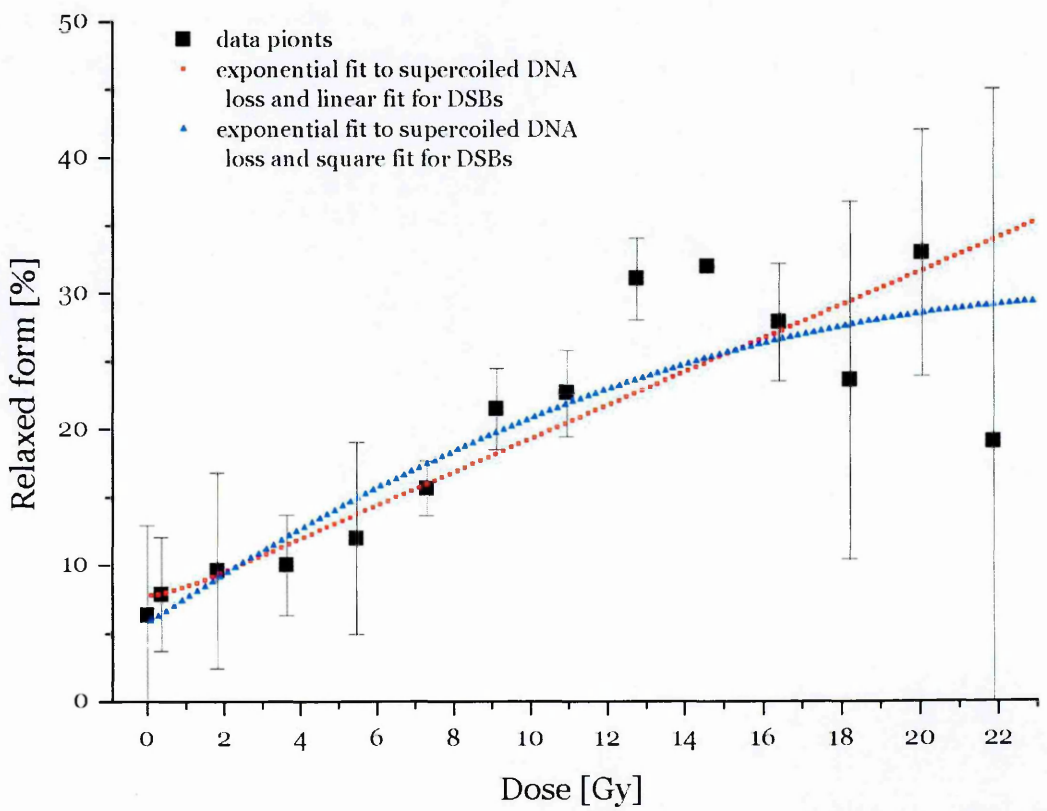

Figure 5-47. Fit of the SSBs formation after irradiation at 170 nm; fits performed on the weighted data points.

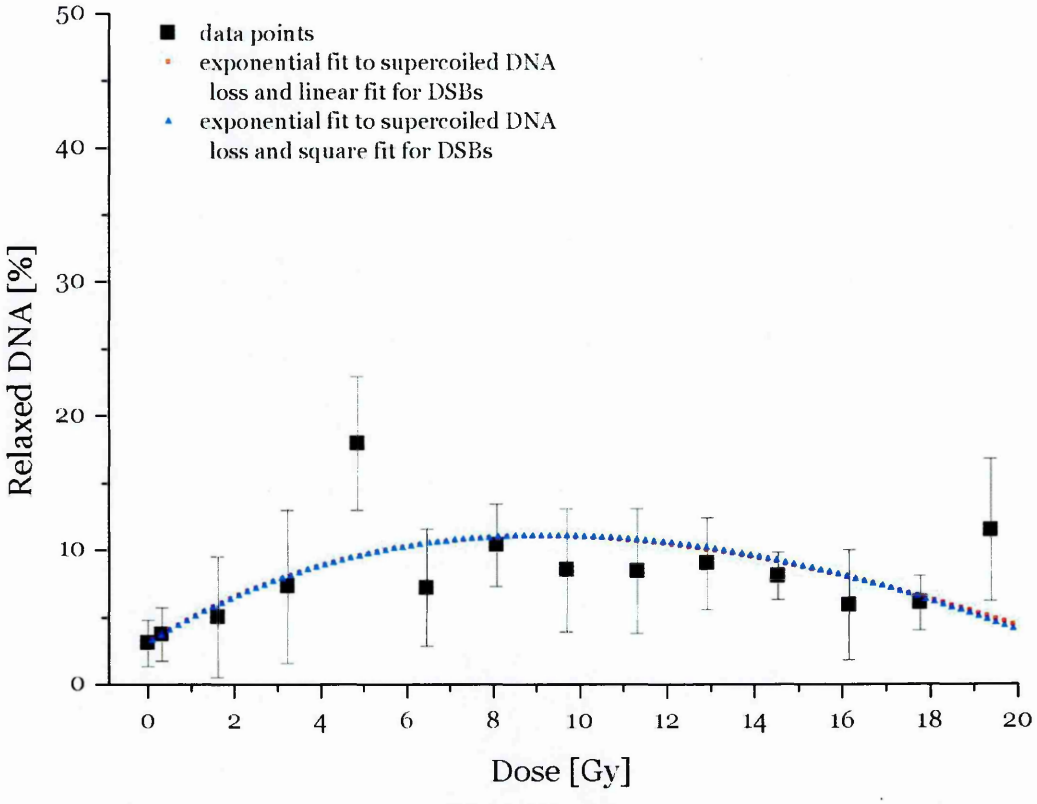

Figure 5-48. Fit of the SSBs formation after irradiation at 190 nm.

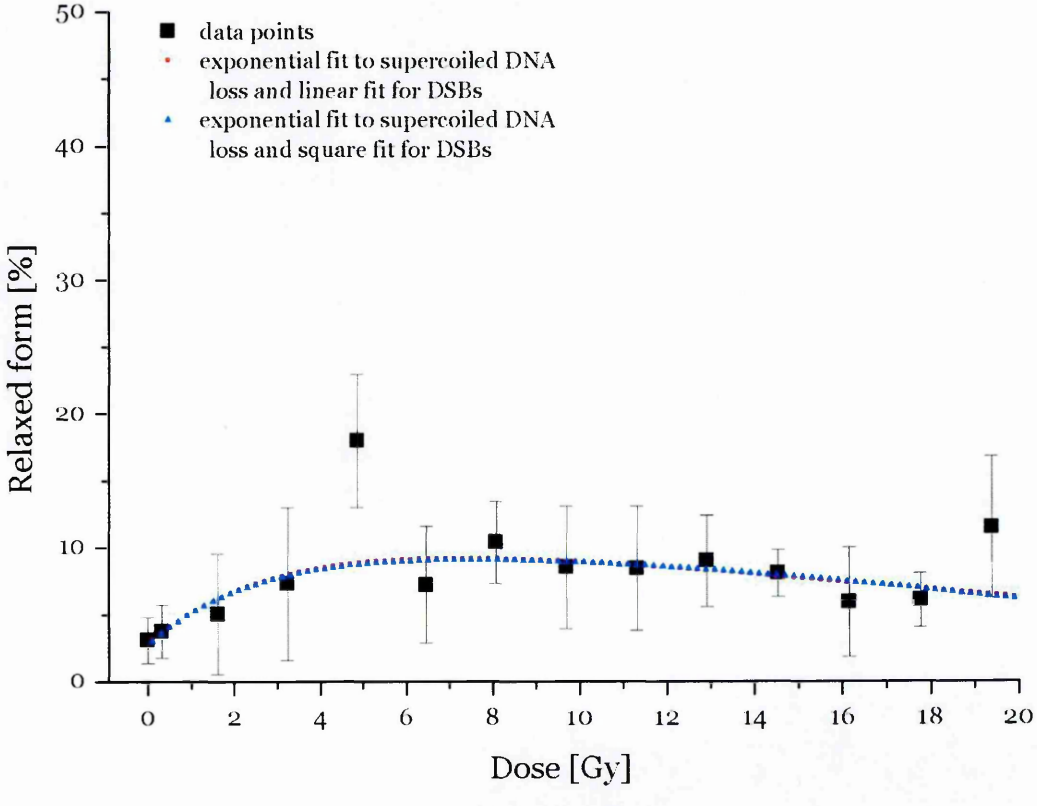

Figure 5-49. Fit of the SSBs formation after irradiation at 190 nm; fits performed on the weighted data points.

5.3.8 Integral cross section – probability of supercoiled DNA loss with dose applied.

Knowing the form of the function that describes loss of the supercoiled DNA, it was possible to integrate over the function to obtain the total cross section $\sigma_{TS}(\lambda)$ for the loss of supercoiled DNA form, which describes the probability of the further loss of supercoiled DNA over the dose that was put into the sample during irradiation. The total cross section will be given as (see Appendix D)

$$\sigma_{TS}(\lambda) = \int_{D_0}^{D_f} \sigma_S^E(\lambda, D)\mathrm{d}D \cong$$

$$\cong P_1\left\{P_2\left[\ln\left(\frac{D_f}{D_0}\right) - P_3(D_f - D_0) + \frac{P_3^2}{4}(D_f^2 - D_0^2) - \frac{P_3^3}{18}(D_f^3 - D_0^3)\right] + P_4 \ln\left(\frac{D_f}{D_0}\right)\right\}$$

where:

σ_S^E is the cross section for the loss of supercoiled DNA with the decay function expressed in exponential form, D_o and D_f denote the range over which the integration took place and P_1, P_2, P_3 and P_4 are constants obtained from data fitting procedure for the loss of the supercoiled DNA, described in 5.3.7.

A choice was made to analyse only the cross section obtained for fittings made on the data points without the uncertainties being taken into account. The argument behind that was that due to large uncertainties fits based only on data points correspond better to the actual damage than the fits based on the weighted points. Figure 5-50 present the results obtained from integrations of cross sections fitted on the data points for all wavelengths over ranges of the applied dose. It can be seen that in case of the data calculated for the cross sections evaluated from the average data points (Figure 5-50) the probability for DNA damage, showed similar trend for 130 nm, 150 nm and 190 nm increasing to a maximum value before decreasing. Such behaviour can be explained in terms of the total amount of

supercoiled DNA that remained in the sample after irradiation and the probability of damaging it as additional photons are delivered to the sample.

The total cross section increases with the dose applied as the number of supercoiled molecules in the sample decreases and thus the possibility of damaging the next molecule is smaller. At some point the curves show a turnover, which means that the number of photons delivered to the sample is so high that although the number of supercoiled molecules that are still in the sample is small, the probability of damaging them is high.

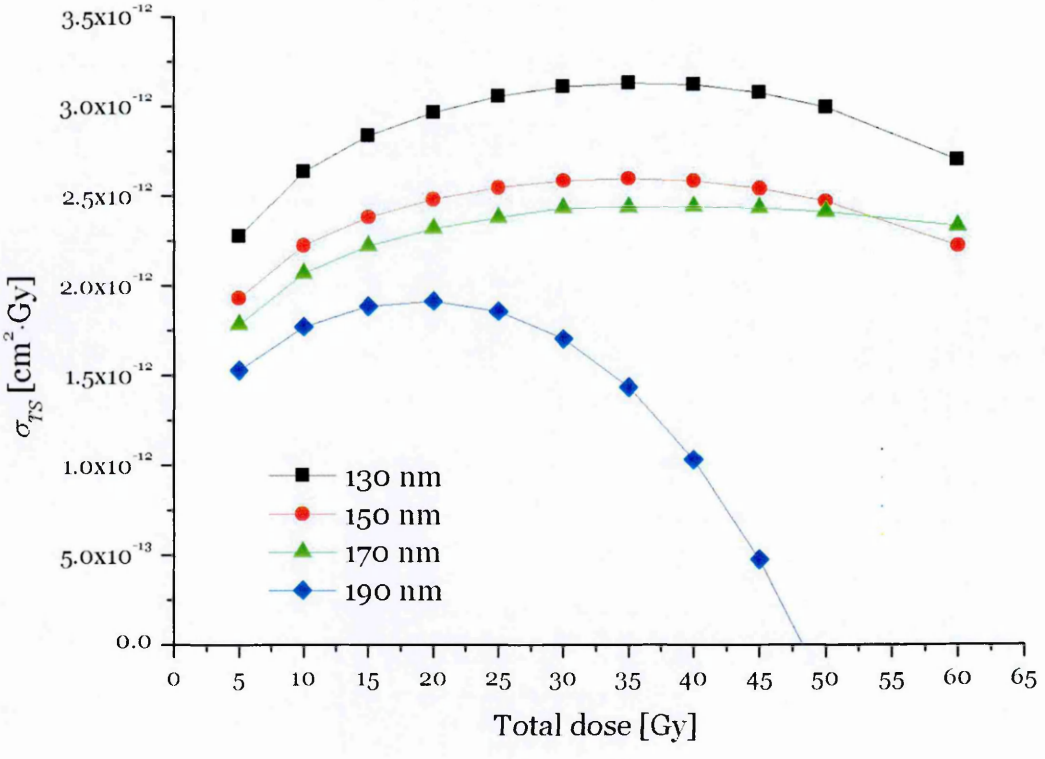

Figure 5-50. Total cross sections for loss of supercoiled DNA at different wavelengths; fits performed on data points only.

The probability of damage decreases most rapidly for the irradiations carried at 190 nm (Figure 5-50), which can be explained by the low energy of the radiation, below excitation region for both DNA and surrounding medium. As the penetration depth of 190 nm wavelength in the water is high (due to the oxygen molecules that are present in water, the water starts absorbing the VUV light

strongly from 185 nm thus the light can penetrate through liquid sample at 190 nm quite well), one can assume that all the molecules were exposed to it, so there is just a very little damage being obtained. The minimum probability of DNA damage at 190 nm is calculated to be after delivering 20 Gy to the sample (Figure 5-50). Similar tendencies can be observed for the samples irradiated at 130 nm and 150 nm with the minimum probabilities of any further damage to be 40 Gy and 35 Gy, respectively (Figure 5-50). The total cross section for damage at those wavelengths also show a minimal probability of the DNA damage, yet both have much higher σ_{TS} values than the one at 190 nm and occur for the higher dose delivered. In both cases it was possible that the penetration of the UV photons and sample mixing was not sufficient and therefore lower yields of damage were observed (see the data from Figure 5-11 and Figure 5-13 obtained for irradiations at 150 nm at high photon fluxes and the data obtained for the low flux irradiations performed at 150 nm with the UV lamp, Figure 5-15 and Figure 5-16). Also lower damage for 130 nm could be caused by the high absorption of water at this wavelength (Mota et al., 2005).

Different behaviour of the total cross section for the samples irradiated at 170 nm was seen. Instead of the minimum for the damage probability that, looking at the other wavelengths, should occurred for around 30 Gy, the probability decreases up to 40 Gy and starts increasing again. If compared with Figure 5-30, one can see that the trend line that fits the supercoiled DNA loss at 170 nm also show a different behaviour to the other lines.

5.4 Conclusions

The data presented in this chapter are consistent with the results published for the damage of DNA in aqueous solution (Folkard et al., 2002). The damage appears to

be strongly influenced by OH radical formation in the irradiated water that surrounds the plasmid.

Due to the initial inability to reproduce the results published by Folkard et al. (2002), when the yield of damage seen after irradiation was four times smaller than in case of the published data, several investigations of the properties of the experimental setup were performed. These show that there is a strong correlation between the choice of variable parameters, such as the light intensity and sample rotation, and the amount of damage induced.

From an analysis of the data one can conclude that there is a decrease in the DNA damage yield with the increasing wavelength of radiation. In contrast to expectations the maximum damage was found to occur at 170 nm. The amount of DNA damage obtained for irradiations at 130 nm was the smallest of all investigated wavelengths. The decrease in the damage yield at 130 nm can be ascribed both to the low penetration of photons of that energy and insufficient sample mixing over the irradiation periods as well as to the absorption of that energy by surrounding water. In case of the irradiations carried at 170 nm, a strong increase in the damage yield and abnormal tendency in the trend line occurred. This led to the conclusion that apart from the direct photon-induced damage there might be another process taking place at this particular wavelength and therefore absorption experiments were conducted to investigate further this phenomenon.

Chapter 6

VUV absorption studies of DNA and its constituents

Due to the unexpectedly high damage observed using 170 nm radiation, reported in Chapter 5, the absorbance of DNA over the vacuum ultraviolet (VUV) region was investigated. The rationale behind this experiment was to explore whether any additional photon absorption occurs at 170 nm compared to 150 nm, which could then explain this unexpected increase in damage at lower photon energy. All experiments were performed on the ASTRID synchrotron radiation source.

6.1 Initial calibration and sample preparation

Before absorption of the DNA samples was measured, a scan was taken through an empty UV cell containing dried solvent (appropriate for the DNA sample to be examined) to determine I_0. The same measurement was also performed after the experiment to ensure uniformity of the results as the UV light beam intensity may have decreased with time.

All solvent films were prepared by evaporating solvent in a desiccator containing silica gel, attached to a small water pump. Between 1.5 to 2 hours were required to dry all the films.

6.2 Absorption spectra of plasmid DNA

Thin films of plasmid DNA were prepared by drying stock solutions of known concentration in the UV cell in the desiccator under low vacuum. Once prepared, the cell was transferred and mounted onto the UV beamline. In the case of the studies concerning increasing thickness of DNA films, plasmid solutions were

evaporated layer by layer in the desiccator and individual scans of films of different thickness were recorded.

6.2.1 Plasmid DNA in water

A pBR322 solution of 8.4 μg in water (50 μl) of pH 8 (adjusted with 1 M NaOH), was evaporated onto a 25 mm diameter UV window (made of MgF_2) of the UV cell. The plasmid film density was estimated to be 1.7 μg/cm².

Spectra over both UV and VUV ranges were recorded separately and then combined together to form a spectrum covering the whole range.

The data was compared (Figure 6-1) with a spectrum found in the literature (Inagaki et al., 1974) for Calf Thymus DNA. This spectrum showed two maxima, one at 190 nm and one at 260 nm, whereas plasmid DNA investigated in this work showed an additional feature at 165 nm.

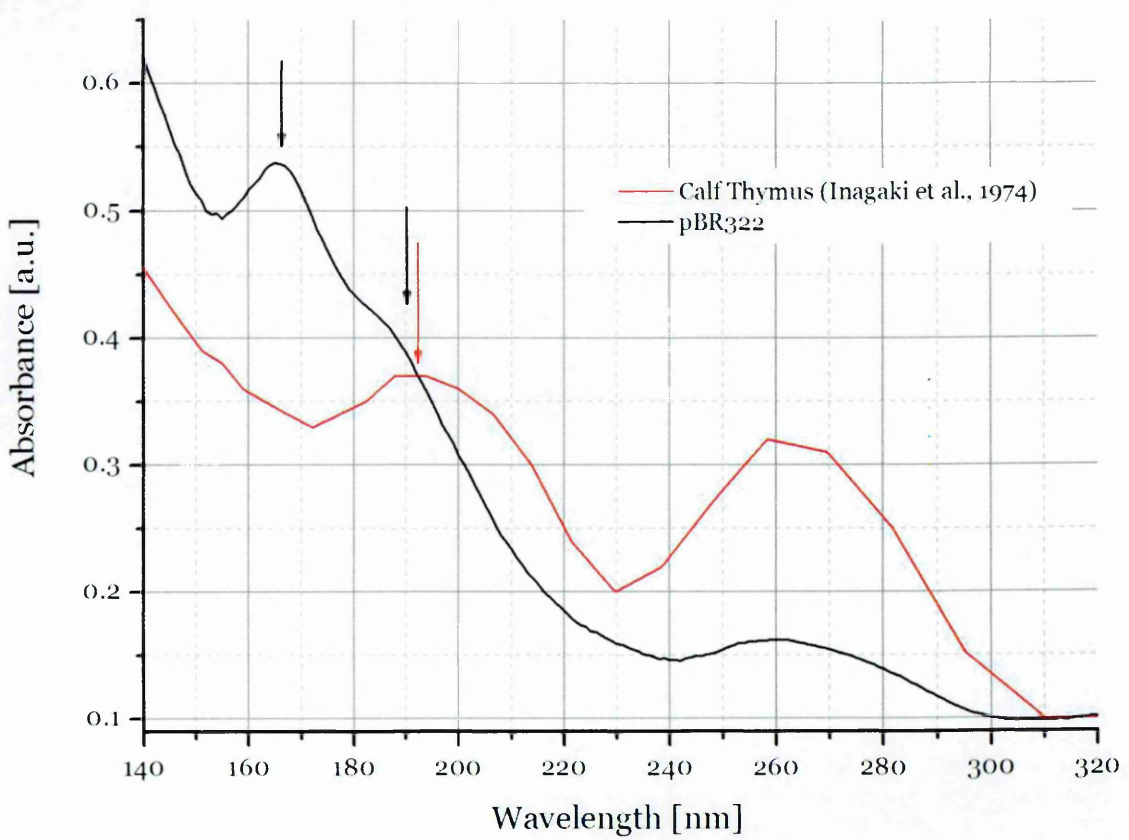

Figure 6-1. Absorption spectrum of pBR322 plasmid DNA dried from water solution compared with a spectrum of Calf thymus DNA.

An attempt was made to see whether the peak observed at 165 nm can be better defined by increasing the amount of plasmid in the sample. Therefore spectra were recorded for films with different thicknesses (Figure 6-2).

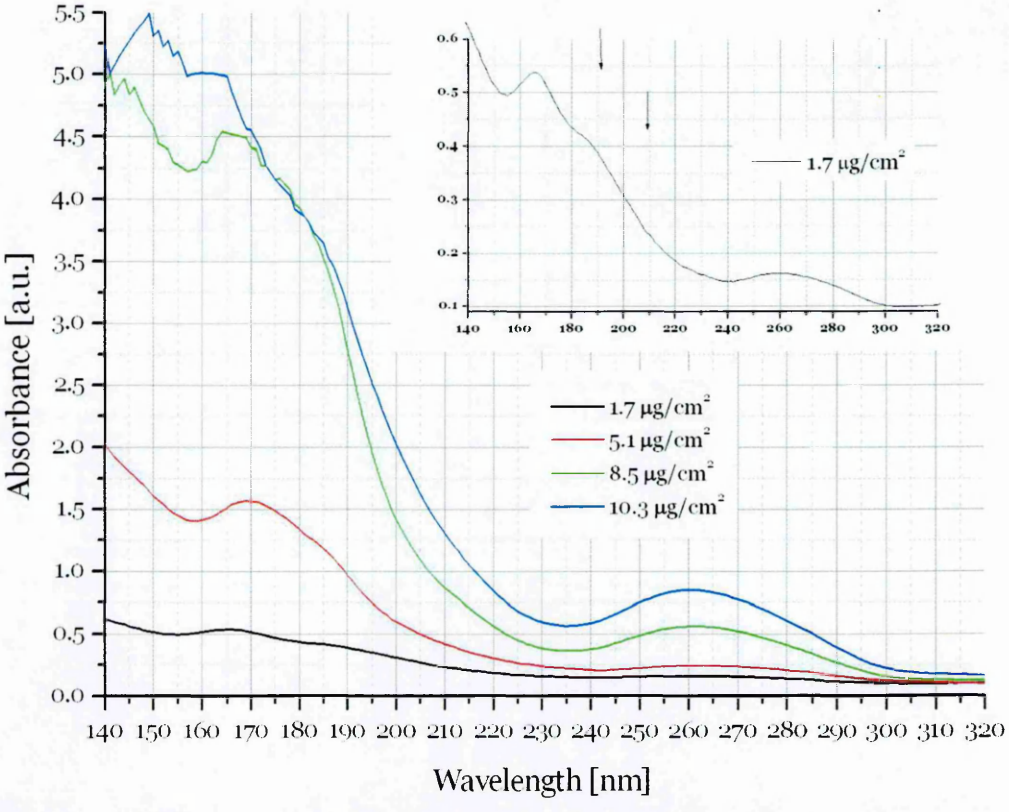

Figure 6-2. Comparison of absorption spectra of various amounts of plasmid DNA (the insert shows the enlarged spectrum of the lowest concentration of DNA).

Unfortunately no clarification of the problem was obtained this way. The peak shifted towards higher wavelengths and with very high concentrations of DNA (close to 10 µg/cm²), disappeared into the background. At highest thickness of DNA film, 10.3 µg/cm², the peak at 262 nm was also observed to shift.

6.2.2 Plasmid DNA in PBS buffer

The spectrum of plasmid dissolved in a phosphate buffered saline (PBS) buffer was also investigated. The purpose of this experiment was to determine if salt contaminants might influence the absorption spectrum of the plasmid DNA and if there is any difference between the absorption spectrum of the DNA dried out from the salt-containing solution and one that was dried out from pure water.

Figure 6-3 shows the comparison of the results obtained for PBS- and UHP water-dissolved samples. It can be clearly seen that the peak at 165 nm in the water-dissolved samples had shifted to 170 nm and the peak at 190 nm had disappeared. Moreover, the background in the VUV region increased more rapidly and had greater values for the PBS-containing sample then in the case of pure water.

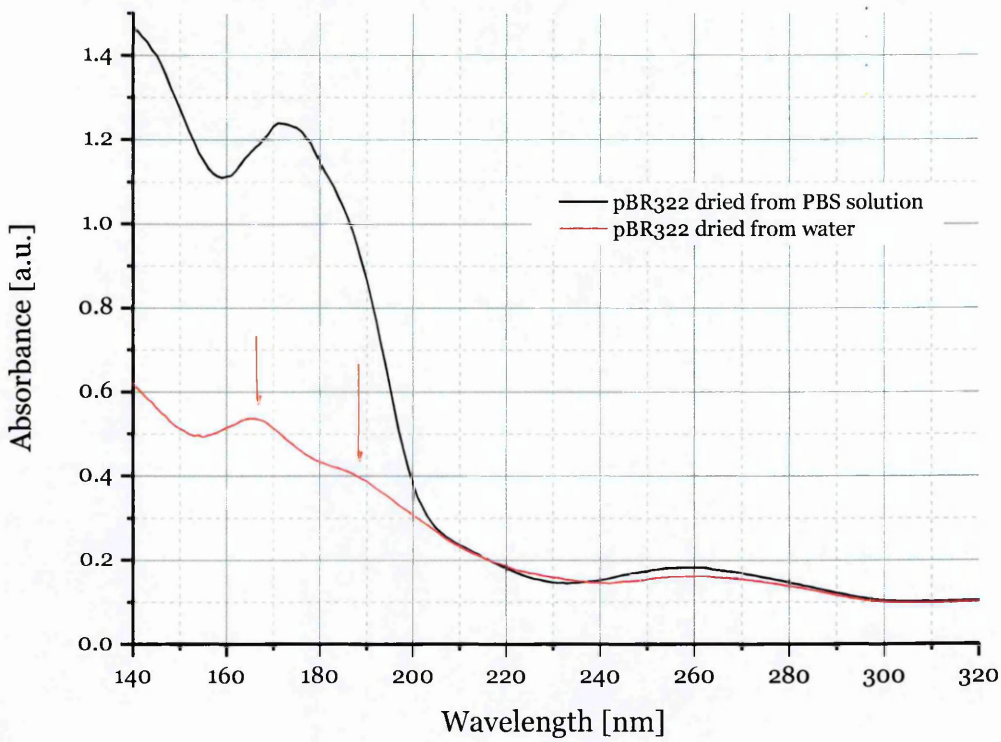

Figure 6-3. Comparison of VUV absorption spectra of DNA dried out from water and PBS solutions; both films containing approximately 2 µg/cm² of DNA (see the absorbance at 260 nm).

A possible explanation for these differences lies in the absorption spectra of dry PBS and water (Figure 6-4). It can be seen that the spectrum of dry PBS contained two peaks at similar positions to these seen in the DNA spectrum – one at 162 nm and the second one at 192 nm, whereas a water spectrum has a single a peak at 165 nm. To check the content of water in the PBS film, the ratio between the spectrum of PBS and water was plotted. As none of the peaks changed their position, it can be concluded that all the water was evaporated from the PBS film.

The damage for samples irradiated in the salt solution was smaller than the damage obtained for the samples irradiated in presence of UHP water (Chapter 5).

As OH radicals are thought to be responsible for the damage, perhaps the damage reduction is due to the salts residues restriction of radicals formation at the investigated wavelengths.

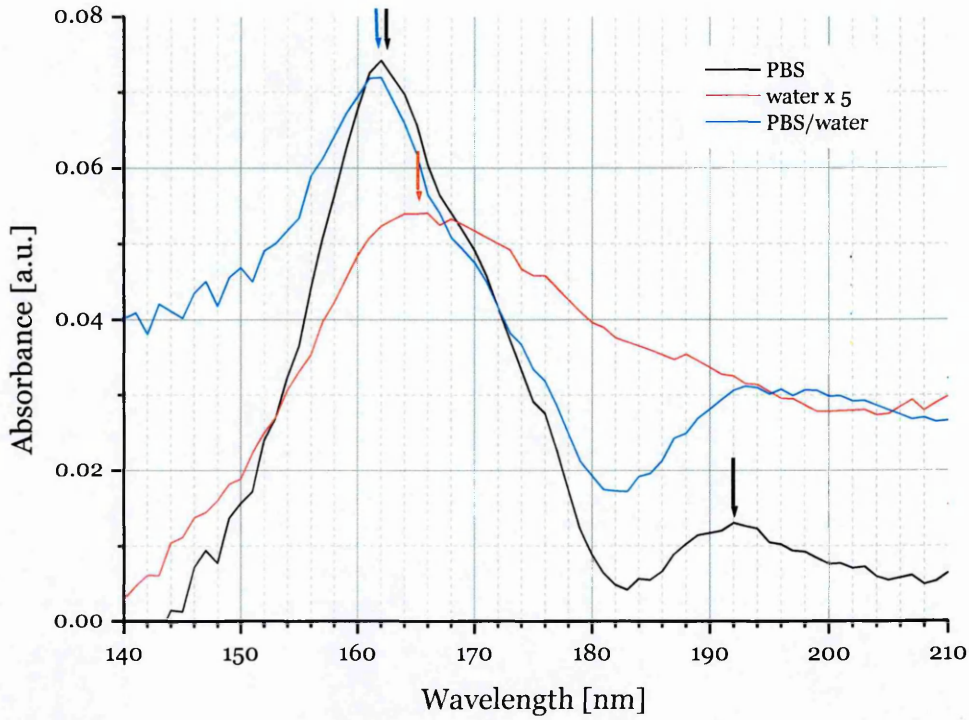

Figure 6-4. VUV absorption spectra of dry films of phosphate buffer, water and their ratio (absorption spectra were normalised against water absorbance).

6.3 Absorption spectra of Calf Thymus DNA

A comparison of the data obtained for the plasmid DNA with absorption spectra taken for Calf Thymus DNA was also made and may be compared with results in the literature. Samples of lyophilised DNA were donated by Dr Sylwia Ptasinska from the Open University. DNA was later dissolved in the UHP water and various amounts were dried out in the UV cell, as described in 6.2, to obtain thin films of 1 cm in diameter.

6.3.1 Spectra of unpurified Calf Thymus DNA

DNA from calf thymus was dissolved in UHP water to obtain 0.5 μg/μl. 20 and 40 μl solutions which were then evaporated into the UV cell to obtain films of the density of 3.2 and 6.4 μg/cm², respectively. Figure 6-5 shows the spectra obtained, plotted against a spectrum reported in the literature (Inagaki et al., 1974).

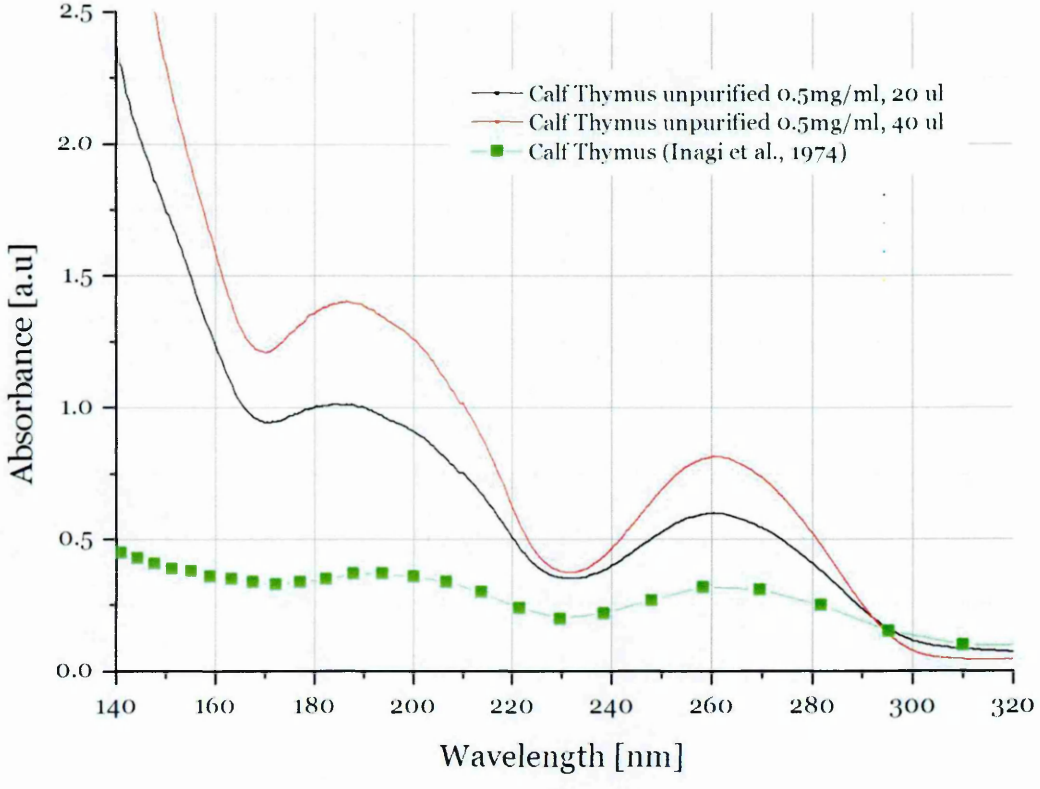

Figure 6-5. VUV-UV absorption spectra of unpurified Calf Thymus DNA.

It can be clearly seen that the results obtained in this experiment closely resemble those in the literature. The literature spectrum contained two peaks, one at 190 nm and another at 260 nm. The investigated DNA spectrum also had 2 absorption peaks, one at 260 nm and another at 186.5 nm. The shift in the VUV peak position can be explained by having much higher resolution (1 nm steps) than the authors of the cited paper (see data points in Figure 6-5).

The peak that was present at 165 nm in the plasmid DNA spectrum was not visible in the one from calf thymus. As the rate at which the background was rising in the

VUV region resembled the situation with the plasmid DNA dried out from the salt solution, an attempt was taken to purify Calf Thymus DNA and look for the possible differences in the obtained spectra.

6.3.2 Spectra of purified Calf Thymus DNA

Calf Thymus DNA was purified by an ethanol precipitation method prior to absorption measurements as follows: 100 µl of 7.5 M ammonia acetate, 300 µl of 70% EtOH and 100 µl of DNA solution were mixed and kept overnight in a freezer at -20°C. Next day the mixture was spun down in the bench-top centrifuge at 13000 rpm for 15 min. The supernatant was decanted and the DNA pellet was dried in a vacuum-oven for 30 min at 37 °C. Purified DNA was then re-dissolved in the UHP water to obtain a final concentration of 0.2 µg/µl.

DNA films were prepared in the same way as in the previous case; films of 4 and 8 µg/cm^2 were obtained. Figure 6-6 shows the spectra obtained.

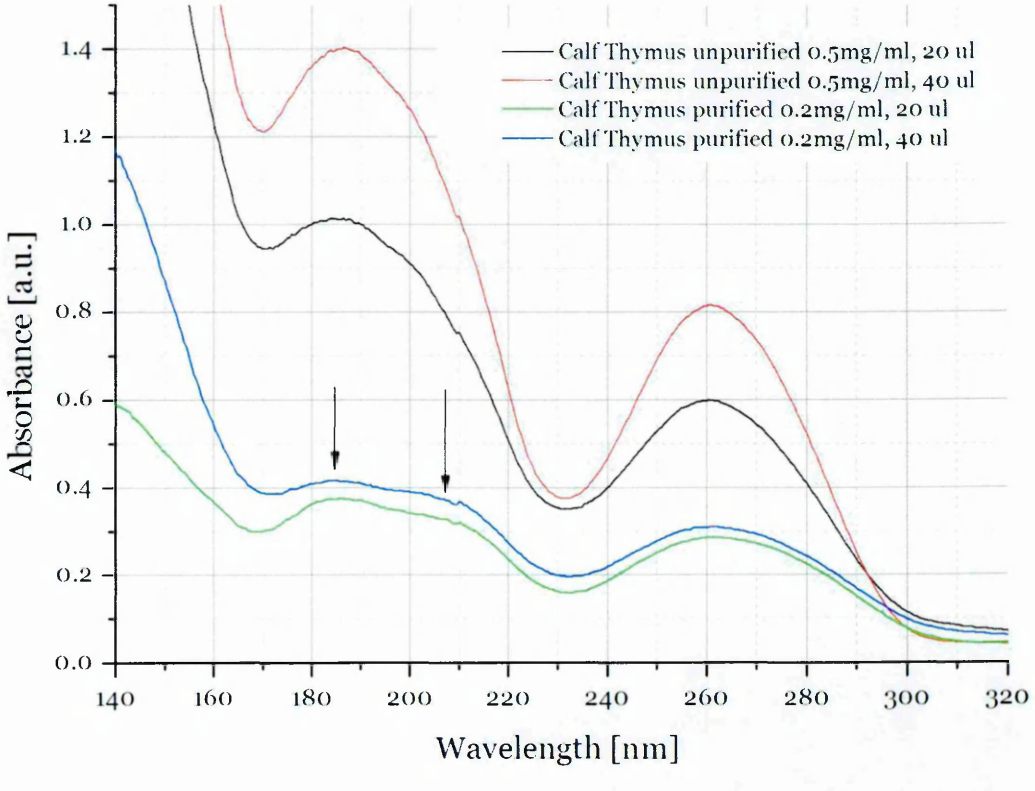

Figure 6-6. VUV-UV absorption spectra of purified and unpurified Calf Thymus DNA.

Once again no peak was seen at 165 nm in the purified Calf Thymus DNA. Comparing the spectra obtained for the samples containing some salt residues (Figure 6-6), the purified DNA showed that, in the VUV range, where in the previous case just one peak at 186.5 nm was seen, two peaks could be seen. One peak can be seen at 185 nm and another one at 205 nm. This data agrees with an earlier one reported in the literature (Falk, 1964). To investigate such behaviour absorption spectra of DNA nucleotides 5'-monophosphates were examined.

6.4 Absorption spectra of DNA nucleotides

2'-deoxy-adenosine, 2'-deoxy-cytidine, 2'-deoxy-guanosine and thymidine 5'-monophosphates (purchased from Sigma-Aldrich) were dissolved in UHP water to obtain 50 mM solutions. 50 µl of the stock solution was evaporated in the UV cell as described before to obtain films of 2 cm in diameter. Figure 6-7 shows the acquired spectra.

Adenosine possesses a broad double peak at 190 nm and 210 nm, cytidine at 195 nm, guanosine at 185 nm and thymidine at 175 nm and 208 nm. These values agree with ones reported in the literature (Zalar et al., 2007).

The recorded spectra were added and plotted against the spectrum of the DNA from calf thymus (Figure 6-8). The obtained spectrum agrees within 2 nm with the one that was found in the literature (Sontag and Weibezahn, 1975). It can be clearly seen that the double peak seen at 185 nm and 205 nm comes from the combined absorbances of the DNA mononucleotides. It also proves that, due to high salt contamination, the spectra published previously were resolved with low resolution, since it is not possible to distinguish between the two maxima.

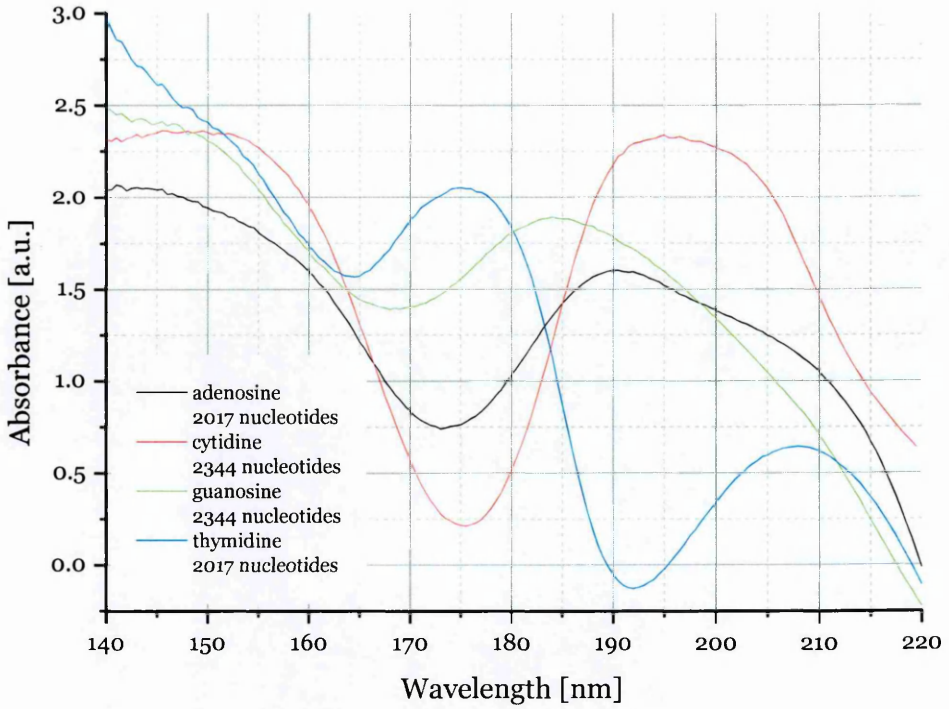

Figure 6-7. VUV absorption spectra of DNA nucleotides; numbers indicate the amount of such in the plasmid pBR322.

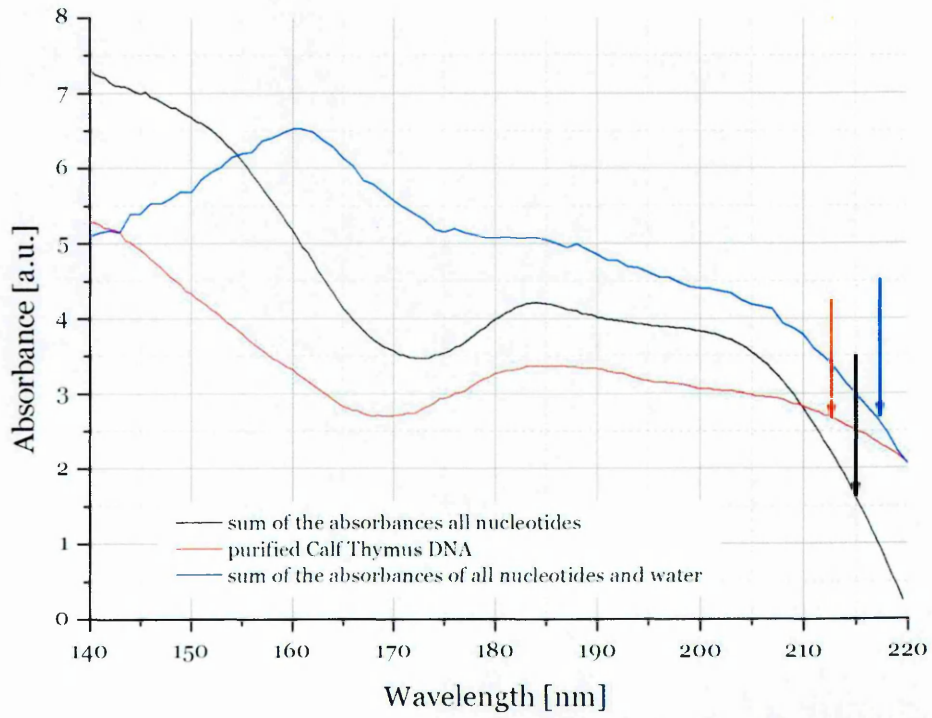

Figure 6-8. VUV absorption spectrum of Calf Thymus DNA plotted against a sum of absorbances of DNA nucleotides and nucleotides and water (spectra were normalised against the sum of nucleotides absorbances).

The influence of water residue can be seen around 210 nm (Figure 6-8), where for the sum of the absorbances of the nucleotides the shoulder of the peak goes down quite quickly, whereas for the purified Calf Thymus DNA the drop is much slower. To prove that this behaviour is due to water, a sum of nucleotides absorbances and water spectrum was plotted as well (Figure 6-8). The shoulder from 210 nm was dropping down slower as in case of Calf Thymus DNA, which allows concluding that water is responsible for its shape.

6.5 Conclusions

From the obtained results one can conclude that there is a strong influence of the structural water on the absorption spectrum of the investigated plasmid DNA.

Figure 6-9 shows the comparison between the results that were obtained for plasmid DNA, water and the nucleotides films.

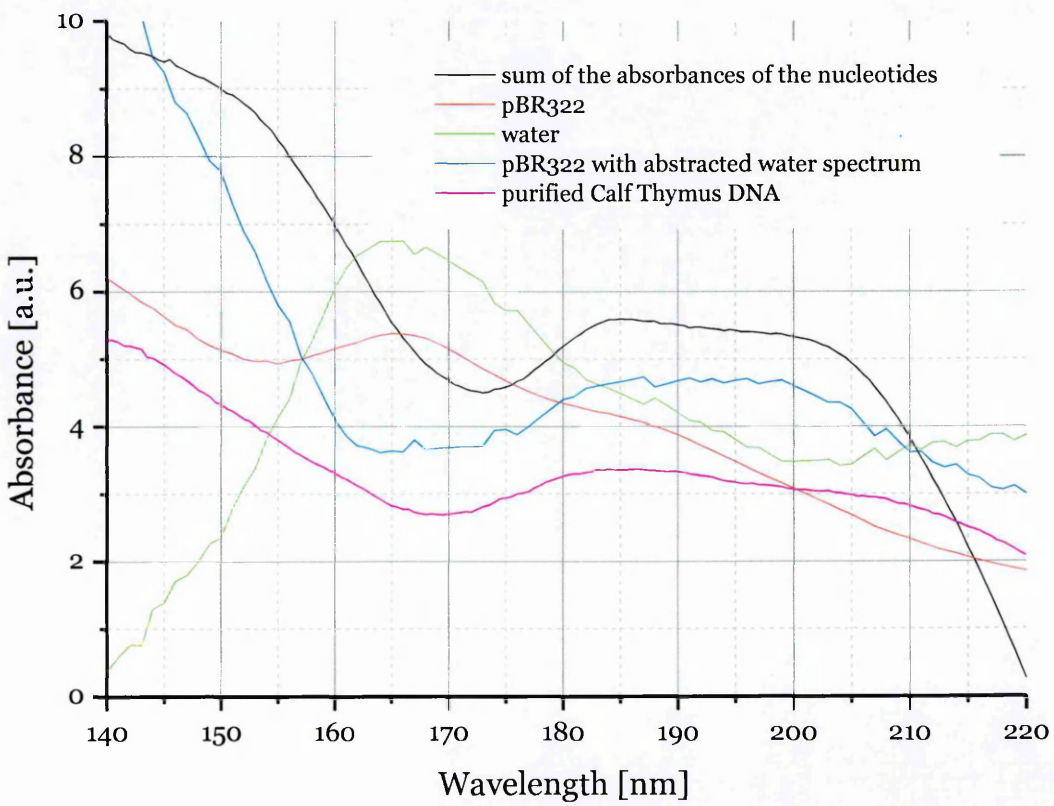

Figure 6-9. Comparison of the results obtained for plasmid DNA, Calf Thymus DNA and DNA nucleotides (spectra were normalised against the sum of the absorbances of the nucleotides).

It can be seen that the peak observed at 165 nm in the pBR322 spectra is due to water. To prove this in Figure 6-9 pBR322 spectrum with the abstracted water is shown. Comparing it to the spectrum of sum of the nucleotides (Figure 6-9) or purified Calf Thymus DNA it can be clearly seen that the shape of the absorbance in this case is the same.

The water peak seen in the plasmid spectra at 260 nm can possibly result from either structural water or from the solvent and could not be removed by evaporation. The peak did not appear either in the DNA from calf thymus or in the nucleotides spectra. The feature was not visible in the spectrum of plasmid DNA that was dried from the salt solution. A possible explanation for this is that the salt contaminant, which caused the background to rise, might also be responsible for the water peak disappearance.

On the other hand the way in which water molecules are bound to the DNA helix might play a role. In case of supercoiled plasmid the structural water that is bound via hydrogen bonds within the double DNA helix and additional supercoiling of the molecule will remain trapped, preventing complete evaporation during film preparation. In the case of Calf Thymus DNA and single nucleotides the interactions are looser (DNA from calf thymus is also double stranded but linear), so water can be easier evaporated from the film and therefore was not visible in the spectrum. The behaviour of the 200 nm peak shoulder around 210 nm seems to support this hypothesis. The peak intensity decreased more rapidly towards higher wavelengths for the combined absorbances of nucleotides, then for Calf Thymus DNA, whereas in case of plasmid DNA the decrease was slow.

It was shown (Mota et al., 2005) that in the VUV region 140 – 190 nm the absorption spectrum exhibits a continuum in the water molecule excitation. It possesses a peak at 166.5 nm and corresponds to the first absorption band of water

$$4a_1 : \tilde{A}^1B_1 \leftarrow 1b_1 : \tilde{X}^1A_1,$$

which was shown to be dissociative one producing $OH(\tilde{X}^2\Pi) + H(^2S)$. At 166.1 nm $2\upsilon_2$ (ΔE = 0.201 eV) bending mode and $1\upsilon_1$ (ΔE = 0.395 eV) stretching mode were seen, whereas at 170.7 nm only the bending mode $1\upsilon_2$ (ΔE = 0.194 eV) was seen. For 150.1 nm again both bending $6\upsilon_2$ (ΔE = 0.193 eV) and stretching $3\upsilon_1$ (ΔE = 0.388 eV) were reported, but structures at this wavelength are diffused.

These results may also explain the results obtained for plasmid DNA in aqueous solutions presented in Chapter 5. The data in this chapter shows that supercoiled plasmid DNA is capable of trapping water molecules efficiently. Since water absorption (and excitation) is much higher at 170 nm than at 150 nm, the water molecules will decompose more readily and OH radical yield will be greater. Because of that the damage due to VUV irradiation of plasmid in aqueous solution at 170 nm will be greater than at 150 nm.

Chapter 7

Development of the ELISA assay for quantifying SSBs in plasmid DNA

To properly quantify the number of SSBs that appeared in plasmid molecules upon VUV irradiation a new assay, described in 2.3, was used. This new method was expected to improve the resolution of damage obtained. It was also hoped to decrease the uncertainty and thus obtain much more accurate values of cross sections for SSBs formation.

7.1 Calibration line preparation

For each set of irradiated plasmid pBR322 samples a calibration has to be made. In the case of SSB labelling, nicking enzymes (enzymes that cut just one strand in double helix, creating a SSB) were employed. The sequence of pBR322 was cross examined against the restriction sites of commercially available enzymes and three of them were chosen to create the calibration samples: Nb.BsmI (1 site), Nb.BsrDI (2 sites) and Nt.BstNBI (3 sites). A combination of these enzymes allowed a standard line to be created based on 0 (no enzyme), 1, 2, 3, 4, 5 and 6 nicks.

Incubation of a known amount of plasmid with Nb.BsmI and Nb.BsrDI was performed at 65 °C for 2 hours and enzyme inactivation at 80 °C for another 30 minutes. In the case of Nt.BstNBI the digestion was performed at 55 °C.

After nicking samples were purified from the enzymes using the QIAGEN MinElute Reaction Cleanup Kit according to the protocol enclosed with it (see Appendix F). Once any remaining enzymes were removed, the concentration of the standard was quantified via UV spectrophotometry.

7.2 ELISA protocol

The assay was performed on 96 well polystyrene microtiter plates (Dynatech). Optimal conditions for ELISA were determined by varying the amount of DNA in plates wells. 10 ng was found to give the most reliable response to the further antibody treatment, not exceeding a value of 1 for OD_{450} final measurement. Figure 7-1 shows the general scheme of the reaction. All samples were placed on the plate in series of three to allow the statistical error to be obtained.

Plates were filled with plasmid pBR322 DNA (50 µl) solution and dried overnight at 37 °C. Plates were protected from light and dust with the aluminium foil. The following day plates were washed six times with PBS/0.005 % Tween 20 solution to remove any excess molecules that do not bind to the plate and dried by tapping onto absorbent paper. Afterwards plates were blocked (the empty places on the plates that were free from DNA molecules) with 0.1 % Marvel solution (100 µl, contains bovine albumins) and washed as previously. A mixture of BrdUTP (2 µg), TdT (2 units / 3 µl), working buffer (20 µl of 5 x stock) and UHP water (75 µl) were added into each well to a total volume of 100 µl and incubated at 37 °C for 2.5 hours. Afterwards the solution was poured out and plates were washed with PBS/Tween as before. Subsequently the antibody with HRP conjugated in PBS/Tween solution (Abcam; 1:100000 dilution) was added to each well (100 µl) and the plates were incubated in the room temperature for another two hours.

Afterwards the remaining antibody solution was decanted and the plates were washed again. Aqueous citrate buffer, pH = 5.3 (100 µl) from a solution (15 ml) containing 3', 3', 5', 5'-tetramethylbenzidine (prepared by addition of 1.5 mg in 150 µl dimethyl sulfoxide) and 2 µl of 30 % solution of H_2O_2, was added to each well and incubated at room temperature for 15 min. Once a blue colour developed, 100 µl of 1 M HCl was added into each well resulting in discoloration of the solution

from blue to yellow. The optical density at 450 nm of each well was then measured using an automatic plate reader.

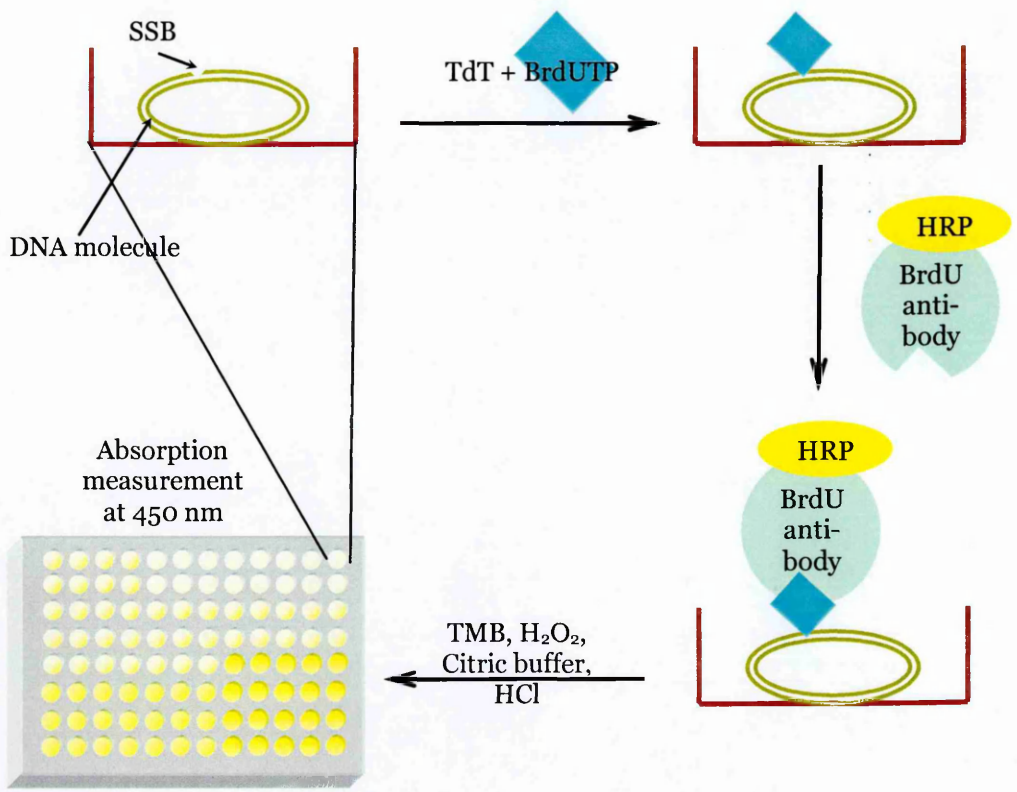

Figure 7-1. General scheme for the ELISA assay.

7.3 Irradiation experiment and samples analysis

The irradiation of plasmid pBR322 samples was performed using the Aarhus synchrotron source. Samples of 2 μl were irradiated at 150, 170 and 190 nm with the doses of 5, 10, 15 (apart from 190 nm series), 20, 25, 30, 35 Gy. Each irradiation was performed three times with identical photon fluxes at each wavelength. After irradiation, samples were frozen and packed for the transport back to the Open University for analysis.

Upon arrival at the Open University, samples (1 μl) were run on a 1.2 % agarose gel for 6 h. Gels were stained with TBE/SYBRGreenI solution and gel images were recorded for damage quantification (see Figure 7-2).

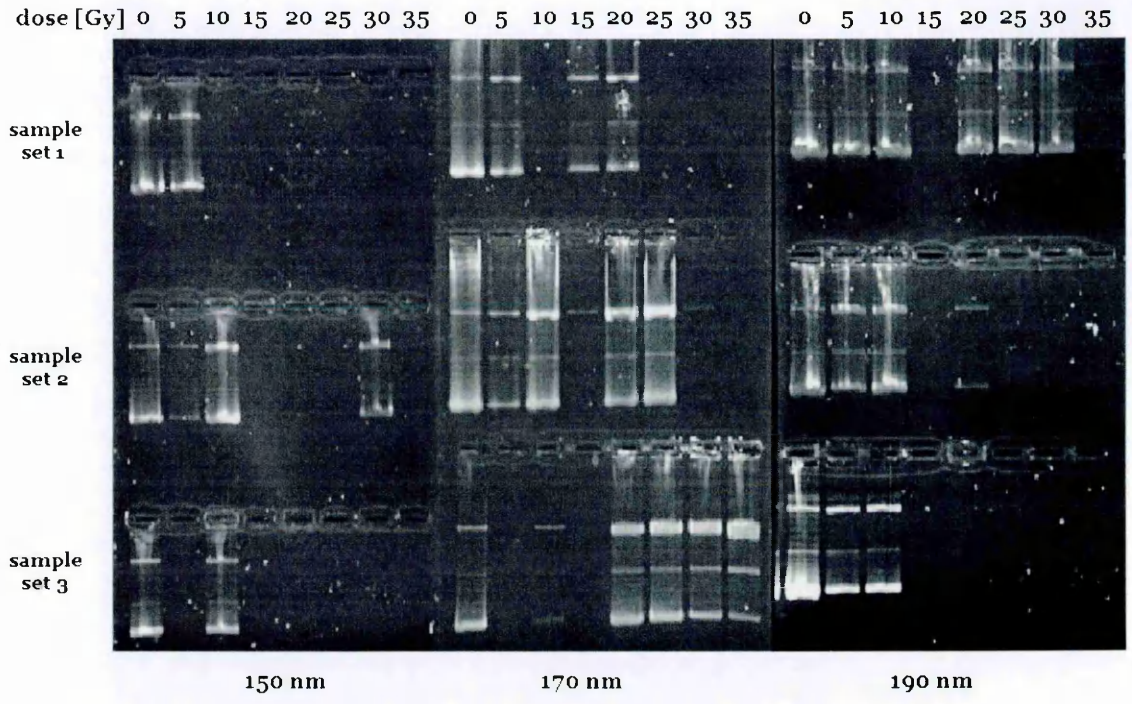

Figure 7-2. Gels used for damage quantification in the ELISA assay.

Samples that developed on the gel properly (i.e. all the forms were visible and clearly separated), were chosen for ELISA assay (see Table 7-1 for details of band analysis, samples marked green were chosen to be analysed with the assay).

Once the damage had been quantified, i.e. the percentage of relaxed and linear molecules with respect to the remaining supercoiled form was assessed from the agarose gels, the remaining samples that were chosen for the assay were diluted up to the total volume of 50 μl and their concentration was quantified using UV spectrophotometry.

To be able to compare the number of breaks in the investigated samples with the calibration line, one must ensure that the amount of the DNA used is exactly the same in both the sample and the calibration line.

It was assumed that the additional breaks will be present both in the relaxed and linear DNA molecules. Their percentages in the total amount of DNA were obtained from the AGE analysis. From concentration measurements the volumes of the all irradiated DNA samples were calculated so each of them contained 10 ng of relaxed and linear DNA forms combined together.

Table 7-1. Results from AGE; S - supercoiled, R - relaxed, L – linear, X – sample did not develop on the gel; green colour indicates samples chosen for the assay; values represent a percentage of the total amount of DNA in the sample.

Wavelength [nm] \ Dose [Gy]			0	5	10	15	20	25	30	35
150	sample set 1	S	78.24	73.77	X	X	X	X	X	X
		R	20.75	24.44	X	X	X	X	X	X
		L	1.01	1.8	X	X	X	X	X	X
	sample set 2	S	83.27	60.27	64.56	X	X	X	48.81	X
		R	14.33	32.99	33.57	X	X	X	47.32	X
		L	2.4	6.74	1.87	X	X	X	3.87	X
	sample set 3	S	77.32	X	67.38	X	X	X	X	X
		R	20.48	X	29.21	X	X	X	X	X
		L	2.19	X	3.4	X	X	X	X	X
170	sample set 1	S	88.53	64.57	X	49.23	39.38	X	X	X
		R	9.45	31.52	X	47.72	55.15	X	X	X
		L	2.03	3.91	X	3.05	5.47	X	X	X
	sample set 2	S	86.32	50.33	48.84	X	33.69	43.74	X	X
		R	11.48	42.94	47.42	X	61.01	52.37	X	X
		L	2.21	6.73	3.73	X	5.29	3.89	X	X
	sample set 3	S	80.02	X	34.05	X	43.74	38.61	26.51	14.28
		R	16.52	X	57.01	X	51.21	56.68	65.33	73.59
		L	3.47	X	8.94	X	5.05	4.71	8.15	12.13
190	sample set 1	S	91.17	77.86	69.81	X	65.94	70.90	62.18	X
		R	5.54	19.63	27.62	X	29.19	25.17	33.25	X
		L	3.29	2.5	2.57	X	4.86	3.92	4.57	X
	sample set 2	S	89.04	49.53	68.41	X	X	X	X	X
		R	7.28	43.95	27.64	X	X	X	X	X
		L	3.68	6.52	3.95	X	X	X	X	X
	sample set 3	S	80.62.	53.30	52.37	X	X	X	X	X
		R	15.03	42.03	42.88	X	X	X	X	X
		L	4.35	4.68	4.75	X	X	X	X	X

7.4 Results and discussion

Two plates were made, each containing a calibration line and a control set, that did not contain DNA samples, but underwent the same overall treatment as the samples and served as the assay background control. On the first plate samples irradiated at 150 nm and at 170 nm were analysed and on the second plate samples irradiated at 170 nm and 190 nm were analysed.

From the first set a background signal with $OD_{450} = 0.14 \pm 0.02$ was measured and subsequently subtracted from all the samples that were analysed. In the second plate the OD_{450} was a little higher, 0.21 ± 0.04, and this was subtracted from all the samples analysed on that plate.

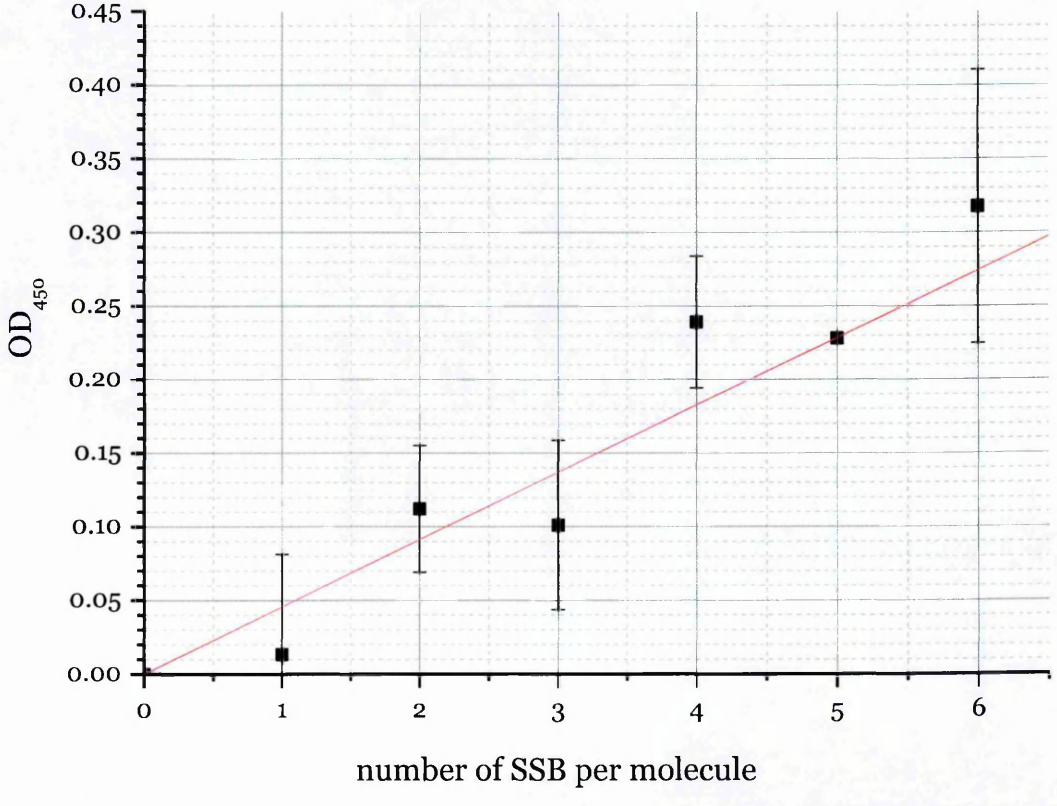

Figure 7-3. Calibration line for the first set of data from the ELISA assay; red line indicates a linear fit to the data points.

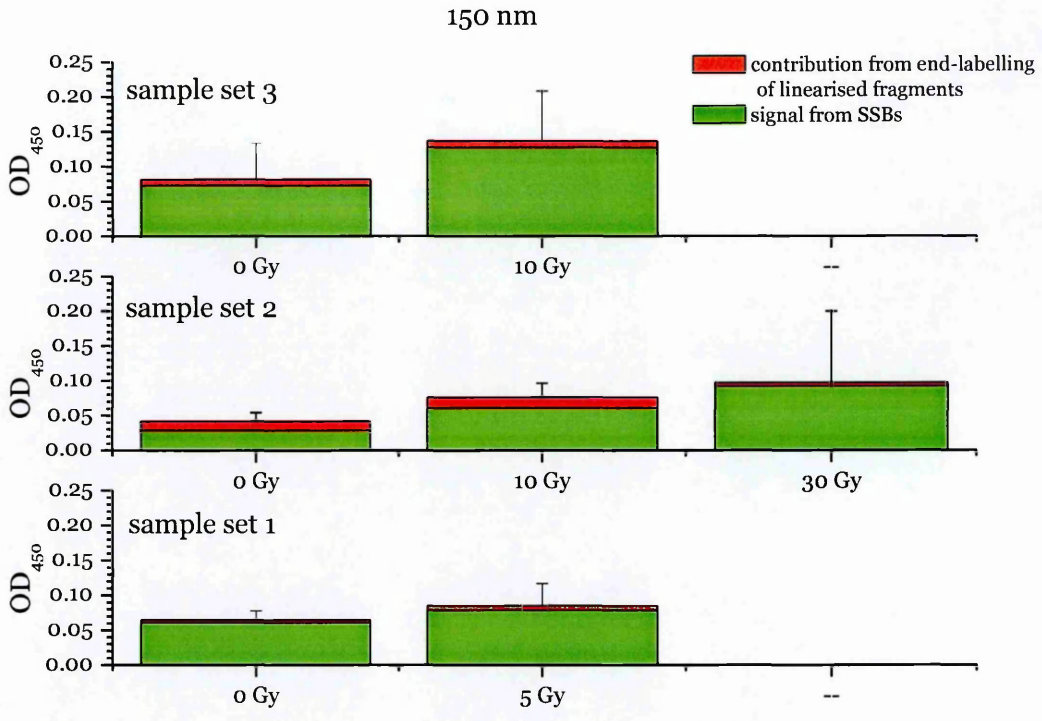

Figure 7-4. Results obtained for irradiation at 150 nm; sample sets numbers correspond to ones on the gels, Figure 7-2, and data in the Table 7-1.

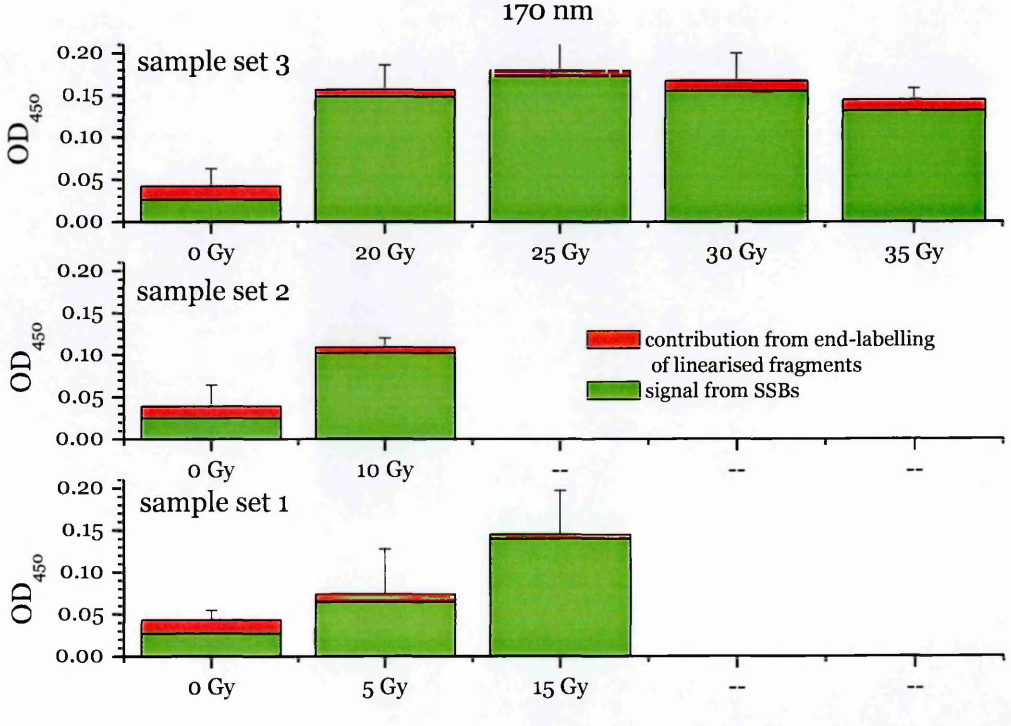

Figure 7-5. Results obtained for irradiation at 170 nm; sample sets numbers correspond to ones on the gels, Figure 7-2, and data in the Table 7-1.

One thing that needs to be taken into account is the correction for the level of the signal that will come from the probe that was attached to the 3'-hydroxyl ends of the linear DNA molecules. If such a correction was not made, the values obtained from the assay would correspond to the total amount of damage, with a doubled signal from a DSB, compared to SSB, which can be interpreted as two SSBs. To correct for such behaviour a signal that comes from 2 SSBs (estimated from calibration lines; Figure 7-3 for the first set of samples and Figure 7-6 for the second set) was multiplied by the amount of DNA that creates the linear band on the gel and subtracted from the total signal obtained. The differences between the total signal (red) and signal with the linear molecules subtracted (green) are presented in the Figure 7-4, Figure 7-5, Figure 7-7 and Figure 7-8.

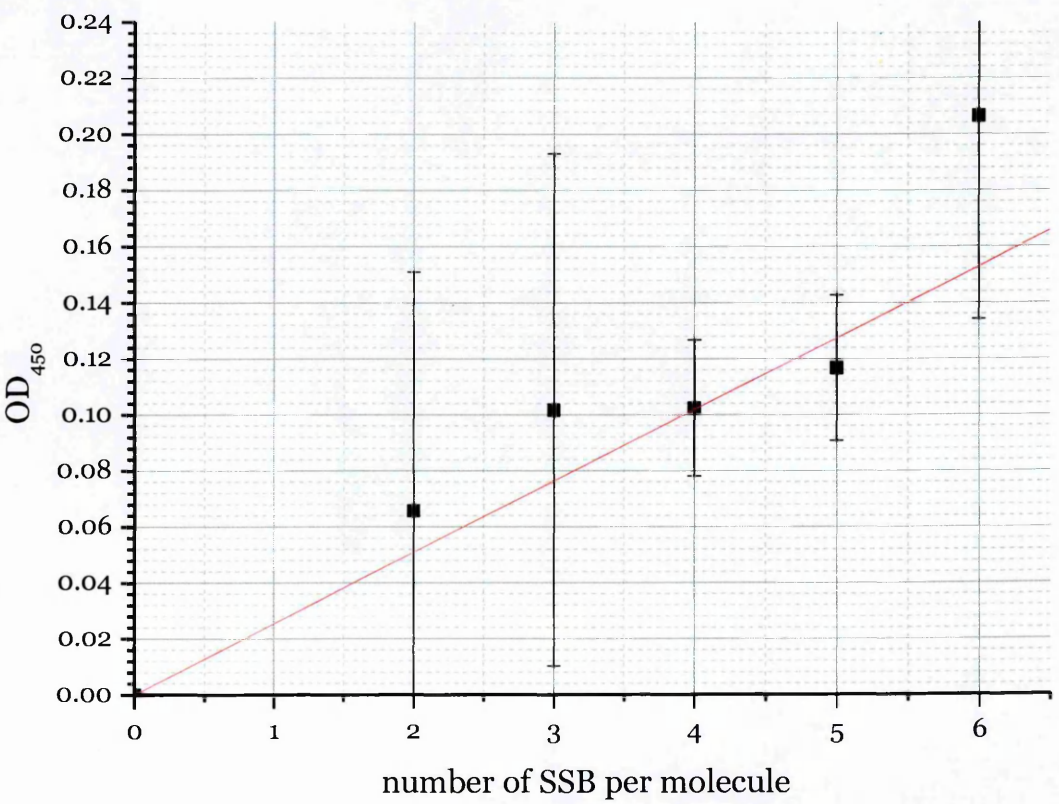

Figure 7-6. Calibration line for the second set of data from the ELISA assay; red line indicates linear fit of the data points.

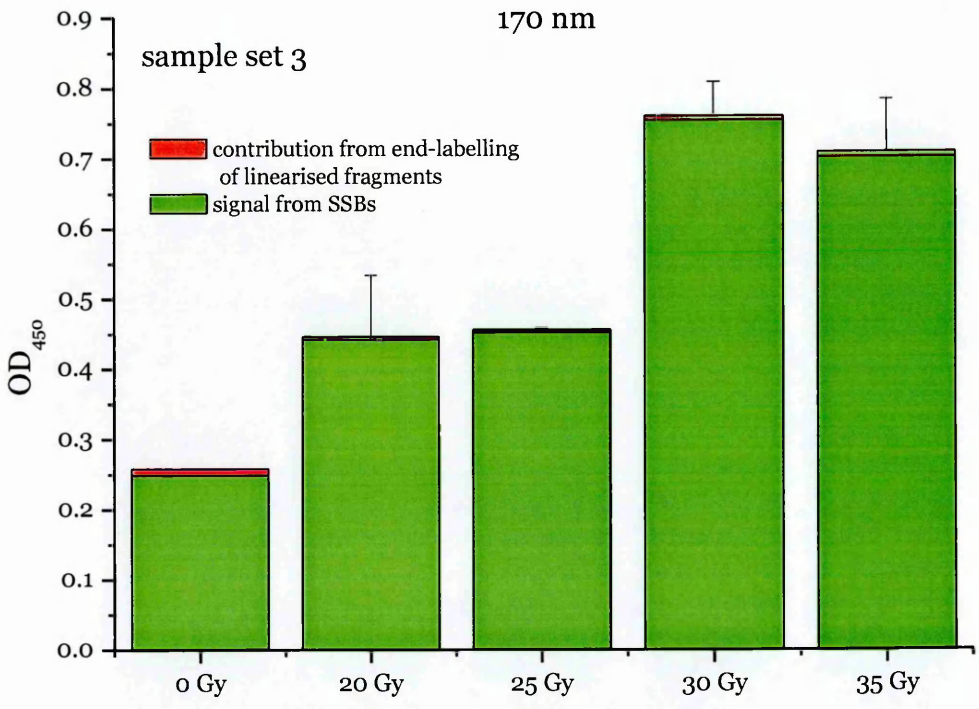

Figure 7-7. Results obtained for irradiations at 170 nm; sample sets numbers correspond to ones on the gels, Figure 7-2, and the data in Table 7-1.

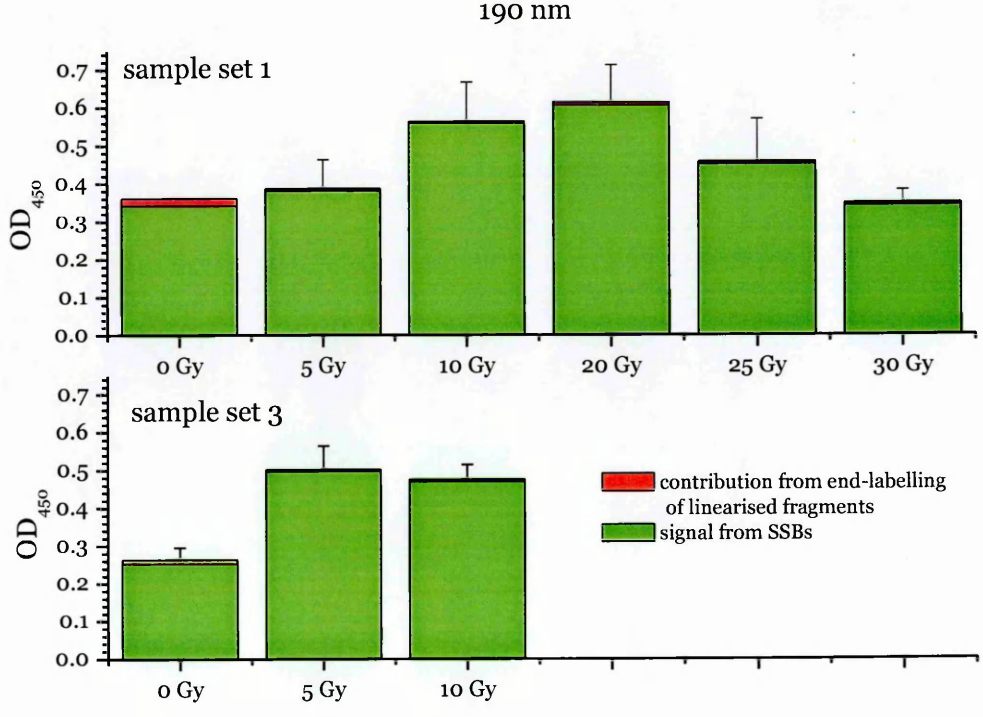

Figure 7-8. Results obtained for irradiations at 190 nm; sample sets numbers correspond to the ones on the gels, Figure 7-2, and data in the Table 7-1.

In Figure 7-3 a calibration line, created from the samples of known amounts of breaks per DNA molecule, for the first set of samples is presented. By comparing the OD_{450} values obtained for the investigated samples with the values that can be read from the line it was possible to estimate the number of breaks in the control samples that did not undergo irradiation as well as in those that were irradiated. The results obtained for the samples that were irradiated at 150 nm and 170 nm are shown in Figure 7-4 and Figure 7-5, respectively.

In Figure 7-6 the calibration line for the second ELISA plate was shown. That line was used as a standard in analysing data shown in Figure 7-7 and Figure 7-8.

To compare the results obtained from the AGE and ELISA, cross sections for SSB, σ_{SSB}, at a wavelength λ were calculated using the following formula (for details of calculations see Appendix E)

$$\sigma_{SSB}(\lambda) = \frac{N_{SSB}}{N_{oSSB}} \cdot \frac{s_{det} \cdot Q_E \cdot q_e}{I_{read} \cdot T_{irr}},$$

where:

ΔN_{SSB} – number of SSB after irradiation;

N_{oSSB} – number of SSB before irradiation;

Q_E – quantum efficiency of the UV diode;

q_e – unit electron charge;

I_{read} – current on the UV diode = 50 pA;

s_{det} – active surface of the UV diode = 10.9 mm^2;

T_{irr} – time of irradiation.

Table 7-2 shows the results obtained.

Table 7-2. Summary of the results obtained from ELISA assay.

Wavelength [nm]			Q_E	T_{irr} [sec]	Dose [Gy]	σ_{SSB} [cm^2]	st. dev. [%]
plate 1	150 nm	sample set 1	0.246	1545	5	$1.57 \cdot 10^{-14}$	46
		sample set 2		3090	10	$6.05 \cdot 10^{-15}$	40
				9270	30	$3.06 \cdot 10^{-15}$	114
		sample set 3		3090	10	$9.36 \cdot 10^{-15}$	61
	170 nm	sample set 1	0.200	1410	5	$2.54 \cdot 10^{-14}$	93
				4230	15	$1.84 \cdot 10^{-14}$	57
		sample set 2		2820	10	$2.24 \cdot 10^{-14}$	102
		sample set 3		5640	20	$1.51 \cdot 10^{-14}$	82
				7050	25	$1.41 \cdot 10^{-14}$	87
				8460	30	$1.05 \cdot 10^{-14}$	82
				9870	35	$7.67 \cdot 10^{-15}$	80
plate 2	170 nm	sample set 3	0.200	5640	20	$4.76 \cdot 10^{-15}$	20
				7050	25	$3.90 \cdot 10^{-15}$	1
				8460	30	$5.42 \cdot 10^{-15}$	6
				9870	35	$4.32 \cdot 10^{-15}$	11
	190 nm	sample set 1	0.202	1586	5	$1.08 \cdot 10^{-14}$	20
				3171	10	$7.90 \cdot 10^{-15}$	19
				6343	20	$4.28 \cdot 10^{-15}$	16
				7928	25	$2.55 \cdot 10^{-15}$	25
				9514	30	$1.61 \cdot 10^{-15}$	10
		sample set 3		1586	5	$1.90 \cdot 10^{-14}$	18
				3171	10	$8.99 \cdot 10^{-15}$	15

If compared with the results obtained from AGE in Chapter 5, it can be clearly seen that the values for the cross sections obtained from the different methods differ quite substantially (see Table 7-3 for comparison of the values obtained from those two methods) , namely the probability of SSB induction upon VUV irradiation appears to be much higher when using the new assay than in the case of results obtained under identical conditions from AGE, presented in Chapter 5. Such differences may be due to the ability of the assay to accurate label all the lesions that occurred upon irradiation contrary to AGE. Also the statistical distribution of the results obtained from the ELISA assay is much smaller than in the case of AGE (see Table 7-3).

Table 7-3. Comparison between the results obtained from AGE (Chapter 5) and ELISA; for the ELISA values carrying smallest error were chosen to be presented in the table.

Wavelength [nm]	Dose [Gy]	ELISA		AGE	
		σ_{SSB} [cm^2]	st. dev. [%]	σ_{SSB} [cm^2]	st. dev. [%]
150	5	$1.57 \cdot 10^{-14}$	46	$3.23 \cdot 10^{-13}$	120
	10	$6.05 \cdot 10^{-15}$	40	$1.93 \cdot 10^{-13}$	120
170	5	$2.54 \cdot 10^{-14}$	93	$1.50 \cdot 10^{-13}$	160
	10	$2.24 \cdot 10^{-14}$	102	$1.52 \cdot 10^{-13}$	120
	15	$1.84 \cdot 10^{-14}$	57	$1.51 \cdot 10^{-13}$	105
	20	$4.76 \cdot 10^{-15}$	20	$1.13 \cdot 10^{-13}$	132
190	5	$1.90 \cdot 10^{-14}$	18	$4.5 \cdot 10^{-13}$	83
	10	$8.99 \cdot 10^{-15}$	15	$1.07 \cdot 10^{-13}$	110
	20	$7.90 \cdot 10^{-15}$	19	$0.72 \cdot 10^{-13}$	101

7.5 Conclusions

If the assumption is made that only the molecules that create the relaxed band possess a SSB and only one such lesion per molecule, the response from all samples used in the new assay should be at the same level or slightly smaller (due to the mass of the molecules that create the linear band) than the response from 10 ng of DNA that has only one SSB in all molecules (used to create the calibration

line). This assumption needs to be made if the quantification of breaks is made purely from the AGE results.

It can be clearly seen that in all cases the damage yield obtained from ELISA was greater than that acquired from the gel electrophoresis. Also damage of the samples that did not undergo irradiation was properly quantified and indicated in many cases a higher degree of damage than assumed from electrophoresis. Furthermore, the uncertainties of the values measured with the ELISA method are smaller than in case of AGE (see Chapter 5).

Contrary to the assumption (Honda et al., 2004) that TdT can only label DSB in non-denaturated DNA due to its catalysing characteristics, the obtained data proves that with the proposed assay it is possible to detect SSBs.

Since only low amounts of DNA are required for the assay (around 10 less than the minimum amount of DNA that can be resolved on the agarose gel), the new ELISA-based method can be used to quantify the damage even in very small samples.

Chapter 8

Atomic force microscopy

In the studies shown in this thesis an attempt was taken to try to image the DNA molecules and the damage obtained using atomic force microscopy. Several experiments were also conducted to improve the quality of this imaging technique. This chapter presents the outcome of those studies.

8.1 The preliminary results

In initial studies AFM images of DNA were obtained when the sample (Sigma, 75 ng of DNA) was placed directly onto a freshly cleaved mica surface without any modification made either to mica or the sample itself. Figure 8-1 presents a phase image of double strands of DNA in its relaxed form.

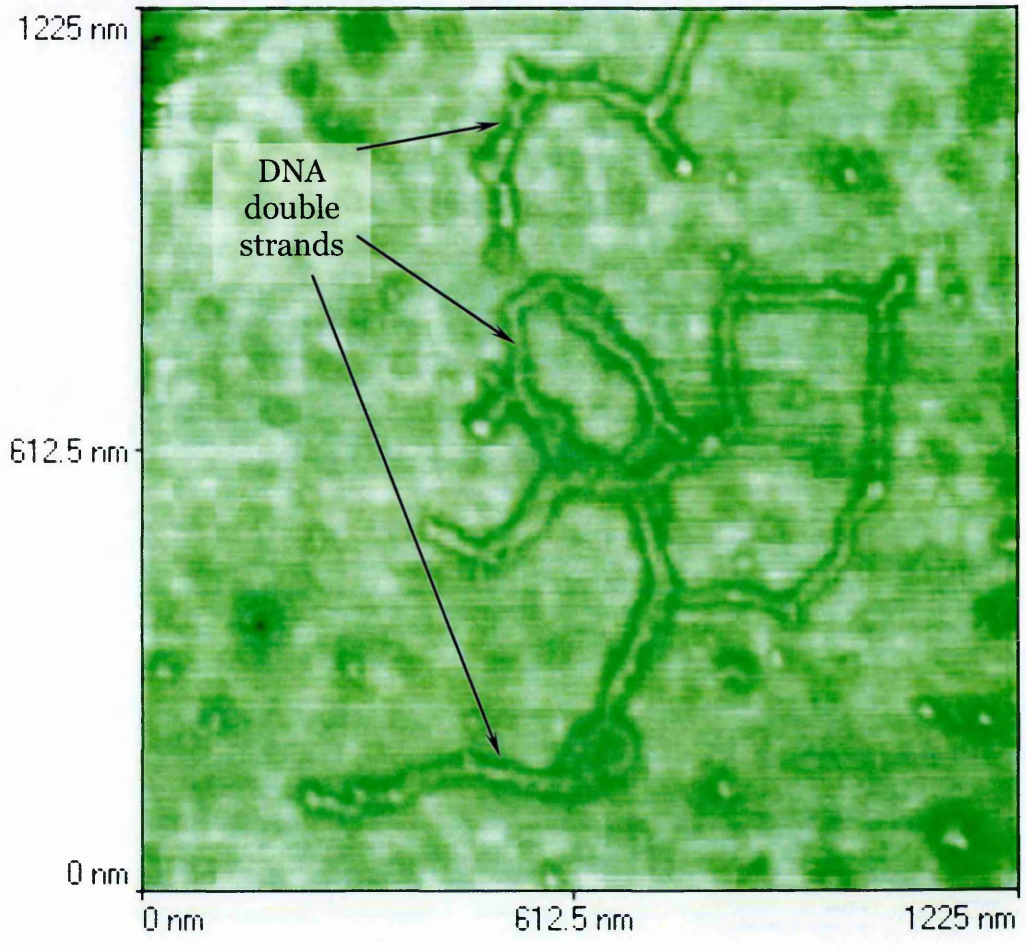

Figure 8-1. Phase image of DNA on non-modified mica.

Figure 8-2 shows the phase image of single and double strands of DNA. This picture shows that using AFM it is possible to image small molecules with very high resolution.

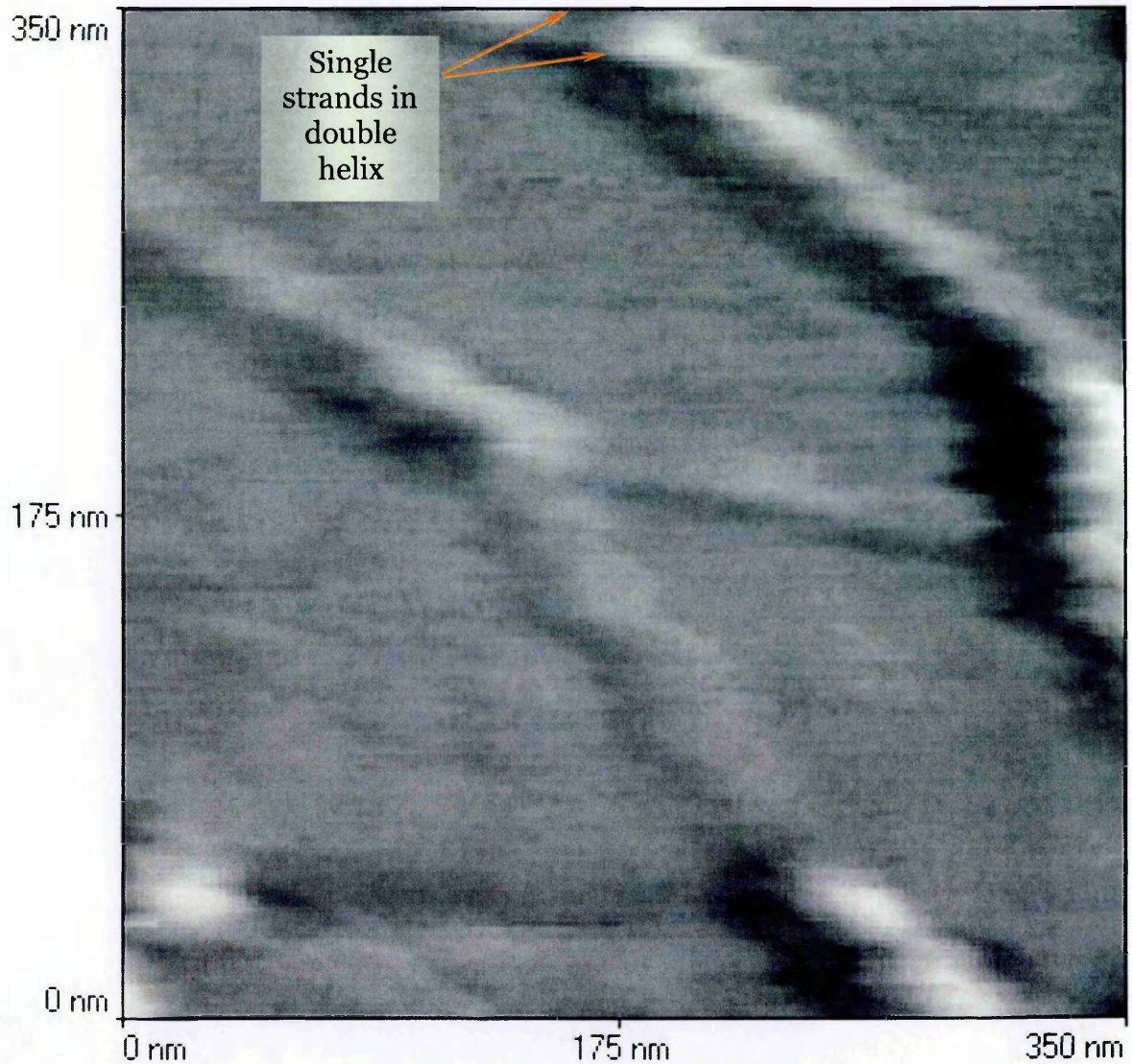

Figure 8-2. Phase image of what appears to be the double helix structure of DNA.

Figure 8-3 shows tight knots of supercoiled DNA molecules. There is no relaxed form present and additionally the plasmid molecules have a uniform distribution over the mica surface. Both surface and phase images of the same area are presented to show the high resolution of the phase images of small and soft molecules compared to low resolution of images obtained through examining of the cantilever deflection (sample topography).

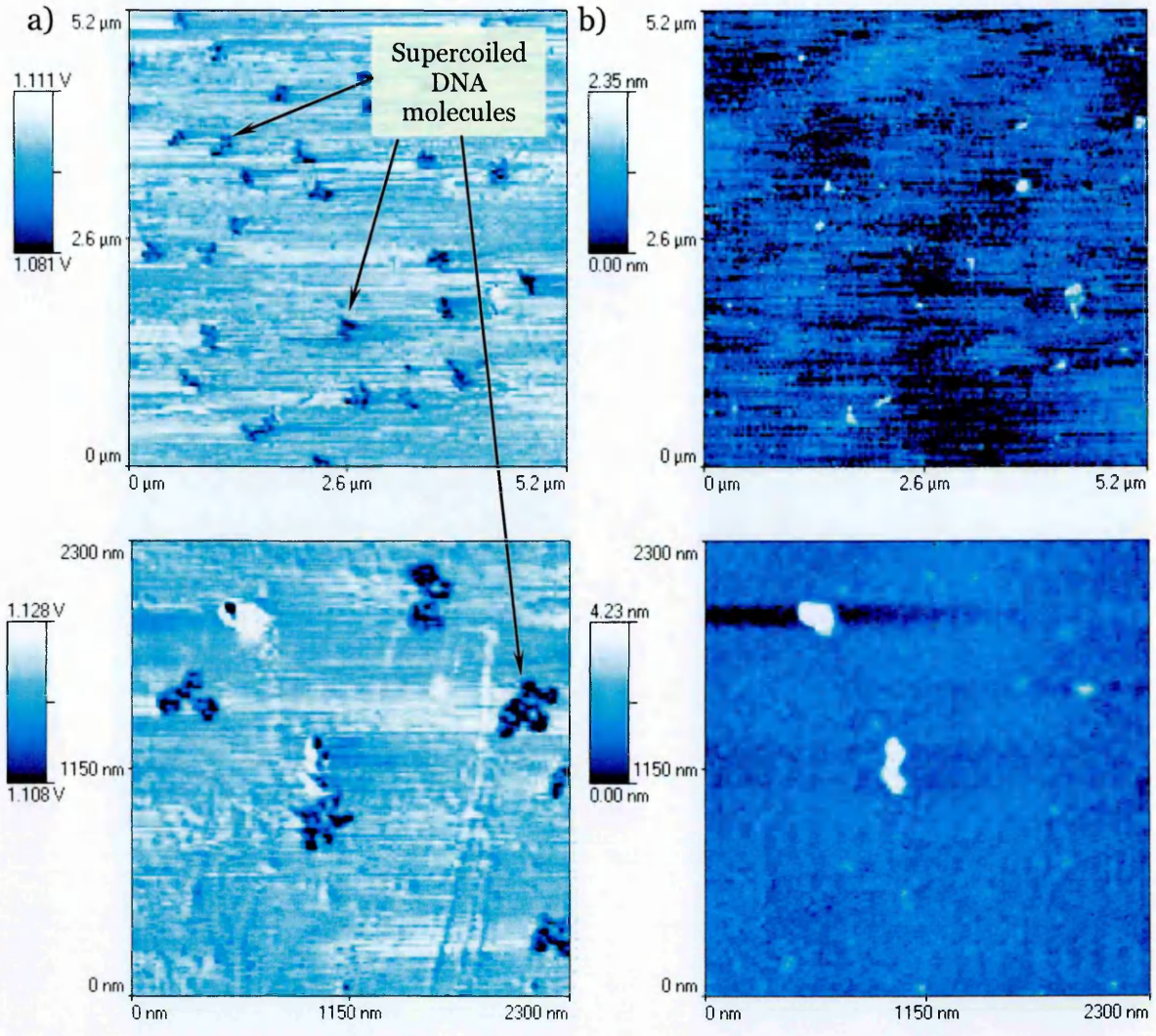

Figure 8-3. Supercoiled DNA molecules; a) phase images; b) topography images.

8.2 Surface and sample modification

The DNA images on mica presented in the previous section were obtained with a high salt content in the DNA solution (arising from the conditions under which DNA was lyophilised by the manufacturer). A major problem with using mica for imaging DNA by AFM is that both mica and DNA acquire negative charge in a water solution, hence DNA might be repelled by the mica surface (Muller et al., 1997). Some modification is therefore needed to 'attach' DNA to a mica surface when in water solution. The most common way to do this is to dissolve DNA with the addition of a divalent cation salt (e.g. $MgCl_2$). However, this may lead to DNA cluster formation and make it impossible to image single DNA molecules. Another method is surface modification, whereby a cationic layer is applied directly onto

mica and DNA solution is introduced after drying. Several attempts have been made to modify the mica surface by depositing cations from various salt solutions: $NiCl_2$ (Argaman et al., 1997; Feng et al., 2000) $MgCl_2$ (Feng et al., 2000; Pope et al., 2000). Silanizing agents also have been used to place amines groups on mica (so-called AP-mica) (Anselmetti et al., 2000; Feng et al., 2000; Lyubchenko and Shlyakhtenko, 1997; Pope et al., 2000) and further modification with glutaraldehyde to obtain GD-mica (Wang et al., 2002). Magnesium acetate treatment has also been explored (Hansma et al., 1992). Also various coatings, like poly-L-ornithine-coated mica (Podesta et al., 2004) were tested. Of course some of those modifications have an influence on DNA conformation on the mica surface and some of them were carried out only for linear plasmids or oligomers. The surface temperature may also have an influence on the DNA conformation (Feng et al., 2000).

In this work an attempt was made to modify the mica surface by treating it with 1 mM $NiCl_2$ for 5 min and drying with nitrogen. In contrast to expectations no supercoiled DNA was observed on the mica (Figure 8-4), only the Ni^{2+} ion layer was seen. Modification of the mica surface with Mg^{2+} ions was also explored (data not shown). Results were very similar to those obtained with Ni^{2+} ions and did not improve the sample quality, moreover, the presence of cations caused DNA sticking and cluster formation.

Another attempt to improve the quality of the samples was made by dissolving DNA in 0.03 M $MgCl_2$ prior placing it on mica. Figure 8-5 shows that the DNA 'net' is visible. This might have been caused by strong interactions between mica and modified DNA molecules, which relaxed the DNA molecules.

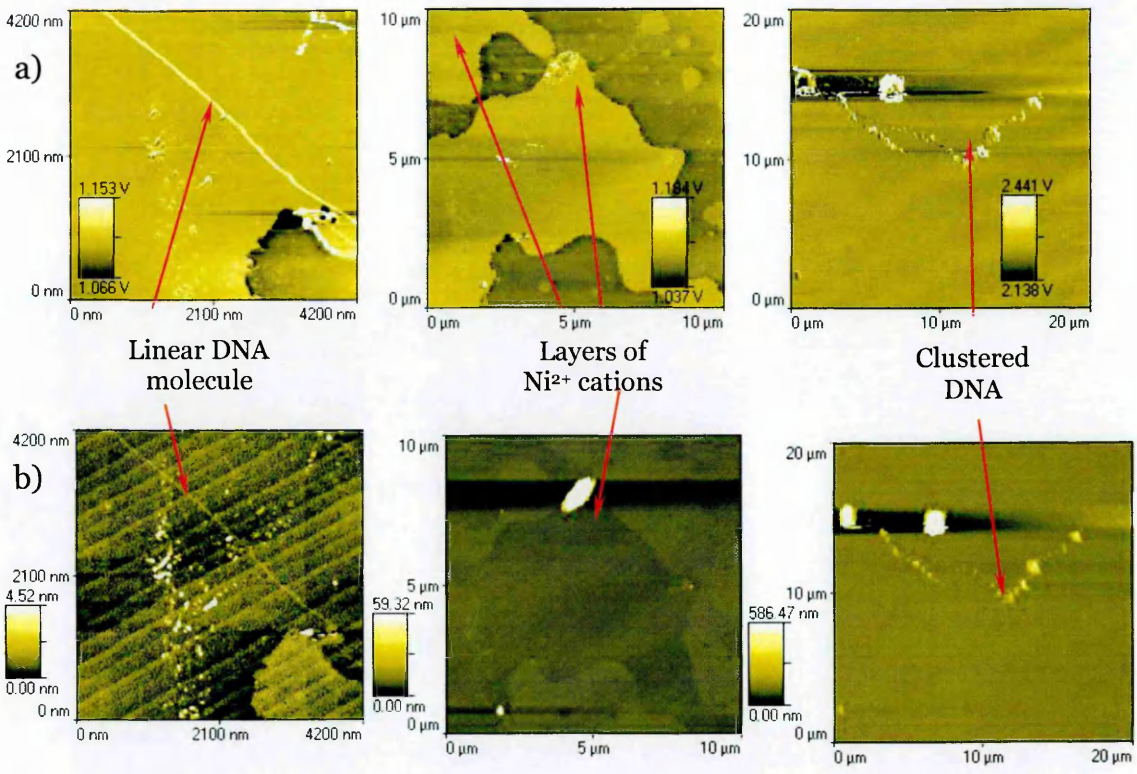

Figure 8-4. a) Phase and b) topography images of Ni^{2+}-modified mica.

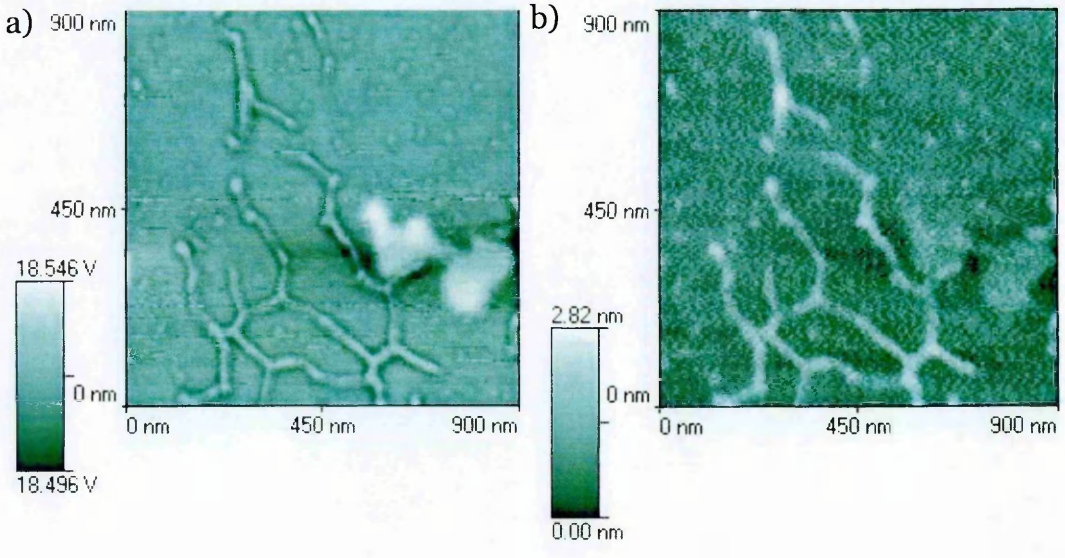

Figure 8-5. a) Phase and b) topography image of DNA placed on mica in 0.03M $MgCl_2$ solution.

8.3 Sample heating

To remove the DNA clusters that appeared on the mica, samples were heated at 75°C for 5 min before placing them on mica. The optimal temperature was estimated from results presented in Figure 8-6. 100 ng/sample, samples were heated for 5 min at: room temperature, 60, 65, 70, 75, 80, 85, 90, 95, 100 °C on a heating block, placed on 1 % agarose gel and run for 1 h at 4 V/cm in the presence of ethidium bromide. At 75 °C it can be clearly seen that a denaturated single strand DNA band appears, being formed from the relaxed DNA form. The temperature of 75 °C was chosen for the experiments. The results obtained are presented in Figure 8-7 and Figure 8-8.

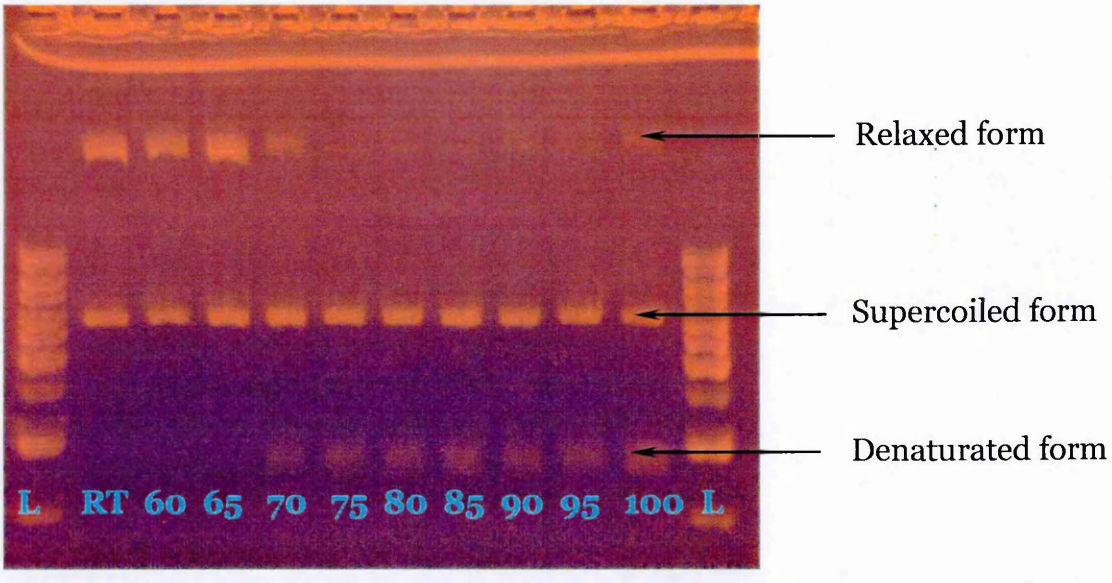

Figure 8-6. Melting point of DNA was determined to be at 70 °C via agarose gel electrophoresis; L – DNA ladder; RT – sample incubated at room temperature.

Heating was found not to be a satisfactory pre-treatment to avoid clustering. Observation of supercoiled form of DNA was still not possible and many impurities were visible in the sample background (see Figure 8-8).

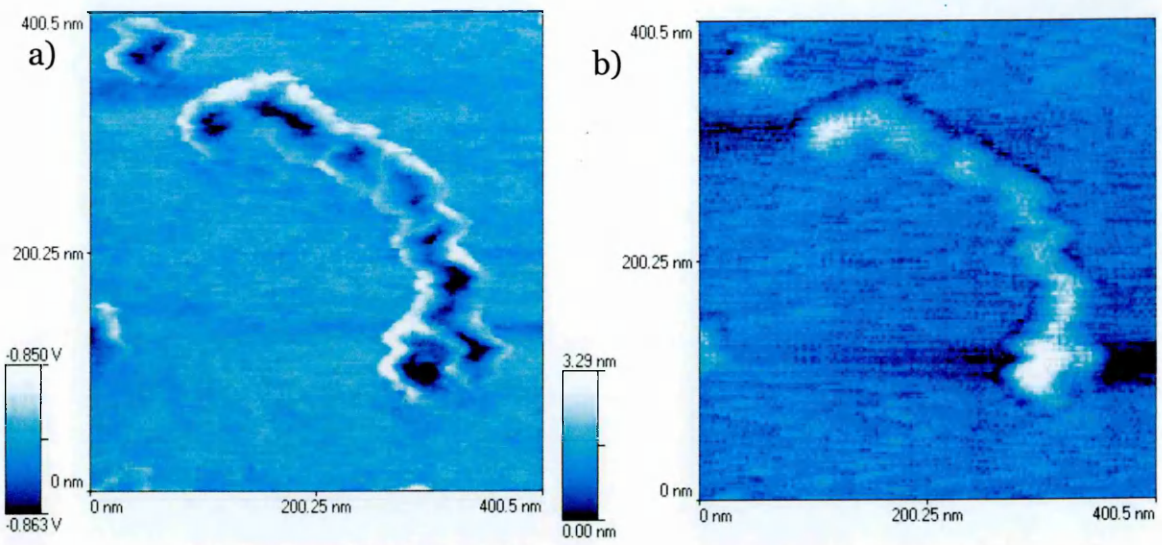

Figure 8-7. a) Phase and b) topography image of DNA molecule following heating.

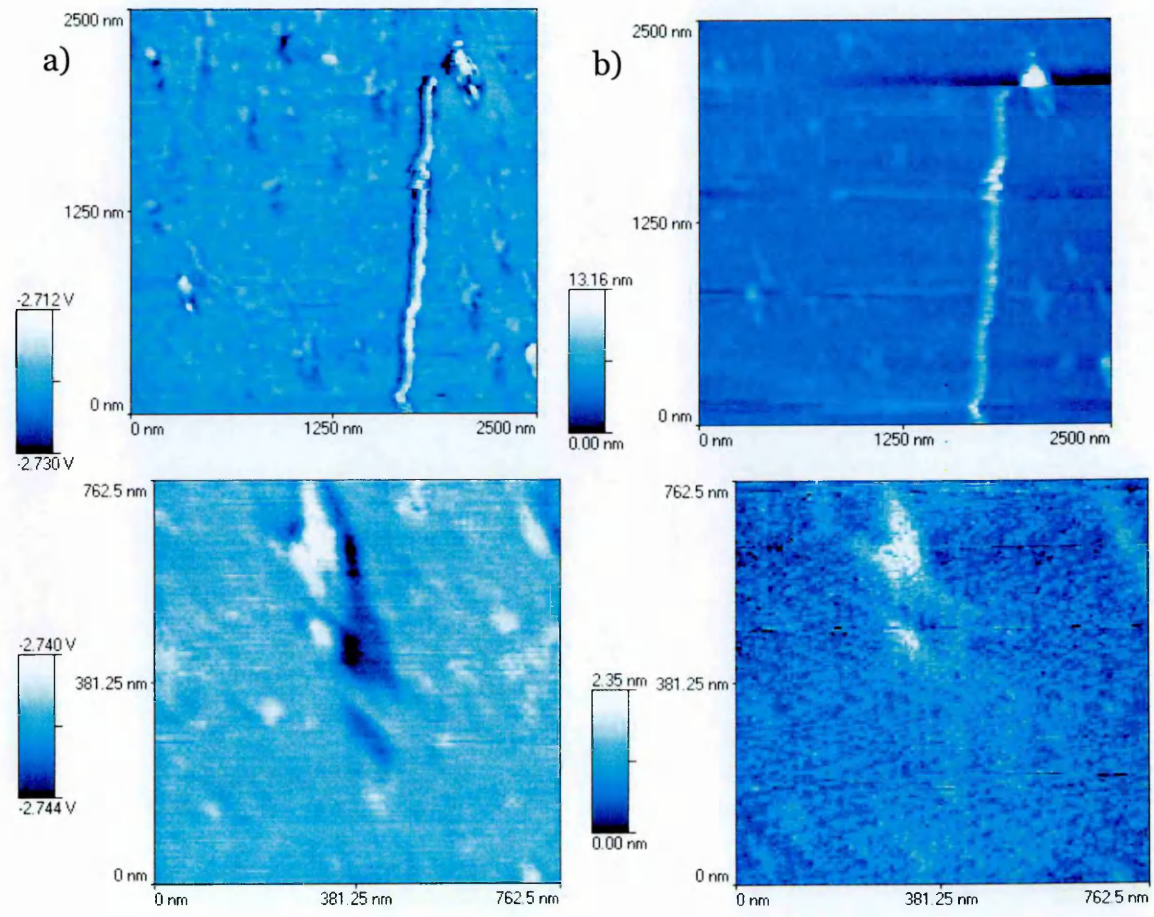

Figure 8-8. a) Phase and b) topography images of DNA molecules deposited on mica after heating.

8.4 Sample irradiation

A single experiment was performed with a DNA sample in a pure water solution placed on a mica surface (Figure 8-9) irradiated with UV light. The UV light source was the D_2 lamp described in 3.2 (with typical flux of > 10^{15} photons per second per steradian in the UV range from 190 nm to 350 nm). The lamp was placed f 10 mm from the sample, which was irradiated for 30 min. The result of irradiation is shown in Figure 8-10. It is clear that this dose of irradiation was much higher than needed to cause complete fragmentation of the DNA with the largest fragments that are visible being about 20 nm long.

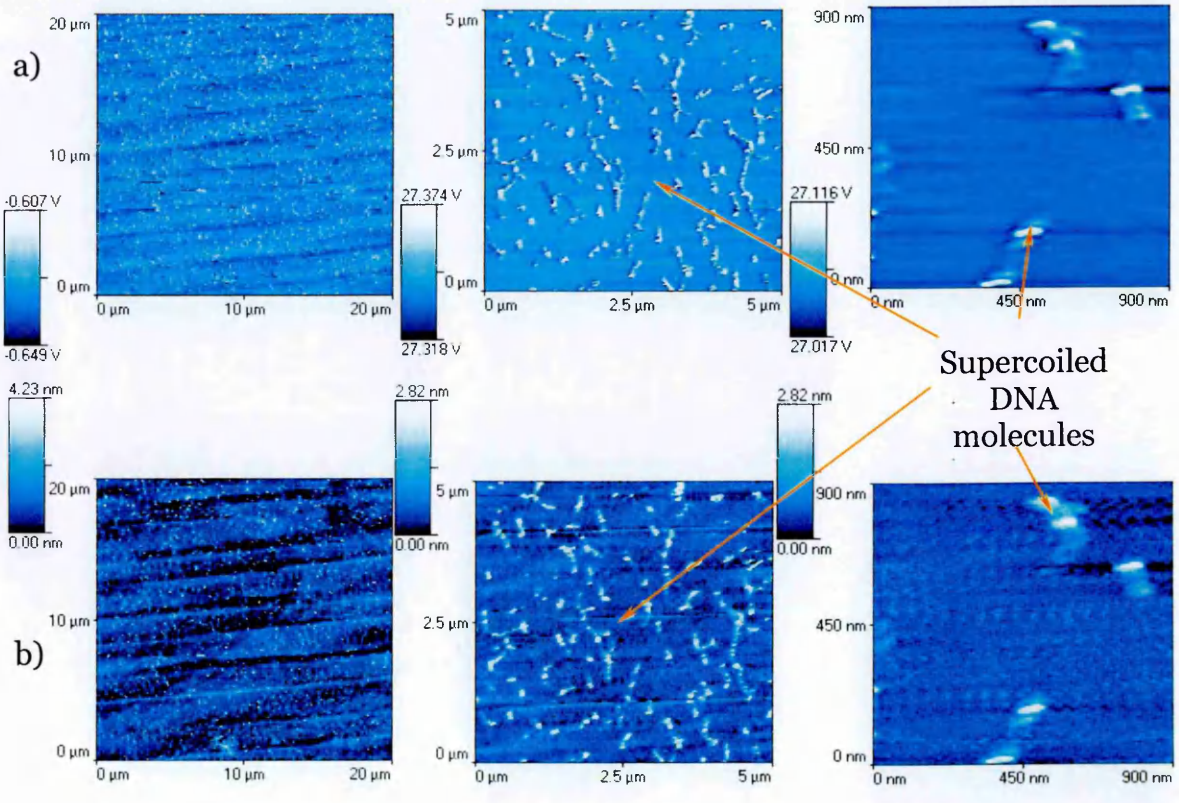

Figure 8-9. a) Phase and b) topography images of supercoiled DNA on mica surface before irradiation.

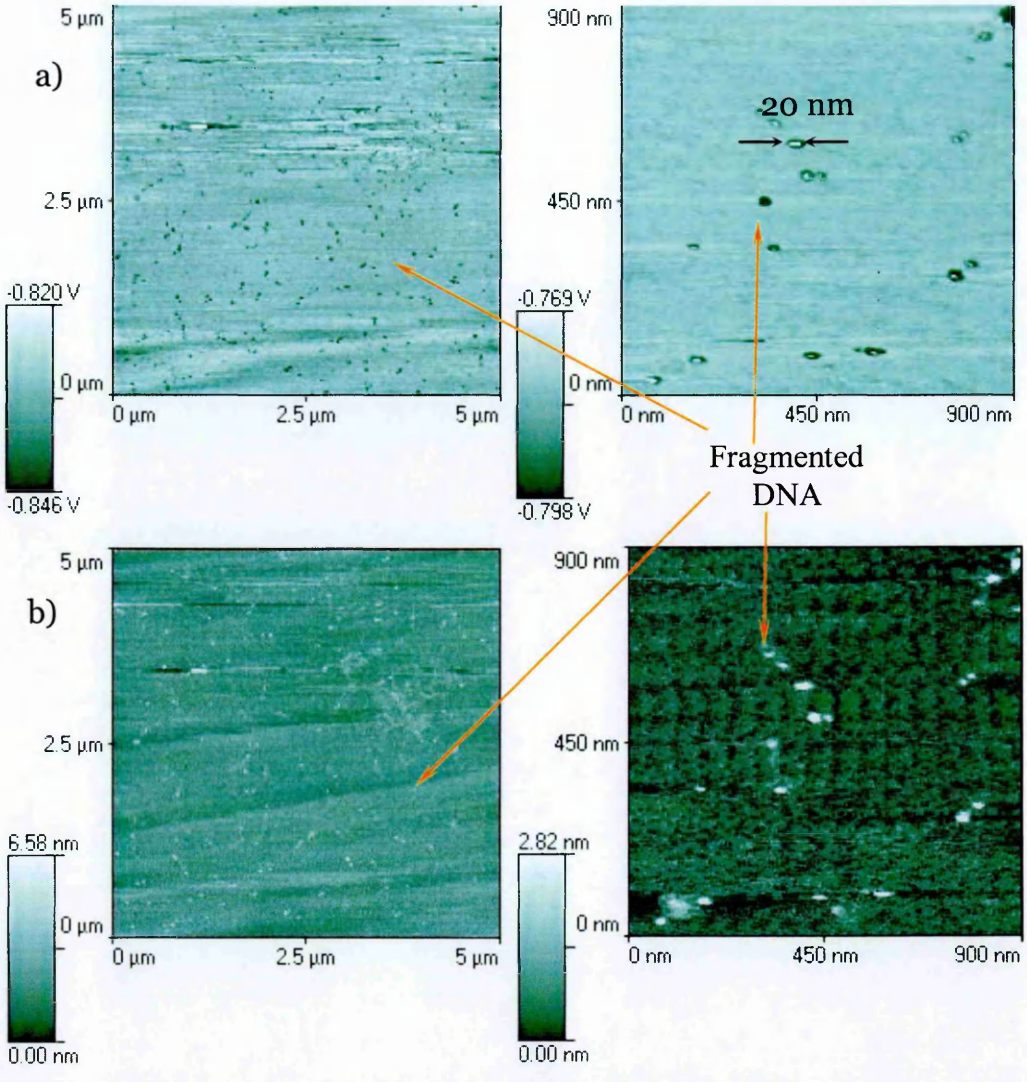

Figure 8-10. a) Phase and b) topography images of the same surface with supercoiled DNA irradiated for 30 min with UV light.

8.5 Conclusions

The main problem with using AFM to image supercoiled DNA was the irreproducibility of the results obtained. Several problems were caused by the AFM itself (e.g. Figure 8-11 shows a distortion in the DNA profile and it is impossible to tell if the image shows double stranded DNA with visible contours of single strands or if it is just deformed). However, the major problem was the sample preparation procedure, which did not yield reproducible results. Figure 8-12 shows images of sample prepared exactly the same way as the one presented in the Figure 8-1. Instead of single molecules (even relaxed ones) the whole surface was covered in a

DNA network. Apart from damaging DNA while placing it onto the mica substrate, one needs to take into account that mica might have different surface charge (Figure 2-8) depending on where the cleavage was done which might affect DNA conformation.

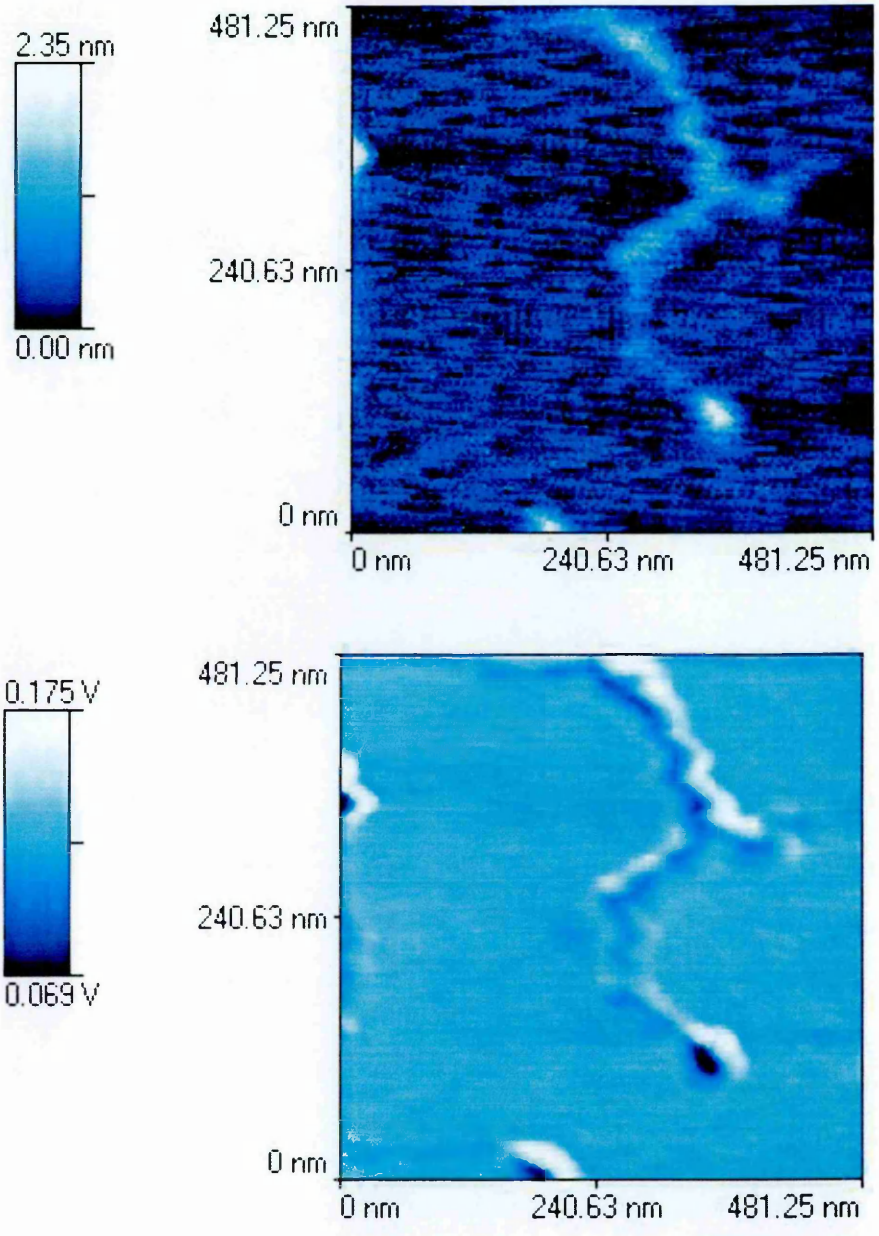

Figure 8-11. Distorted DNA molecule on the mica substrate.

From the results obtained one can conclude that while it was possible to obtain clear images of supercoiled DNA molecules the conditions under which such images can be routinely obtained are not easily defined.

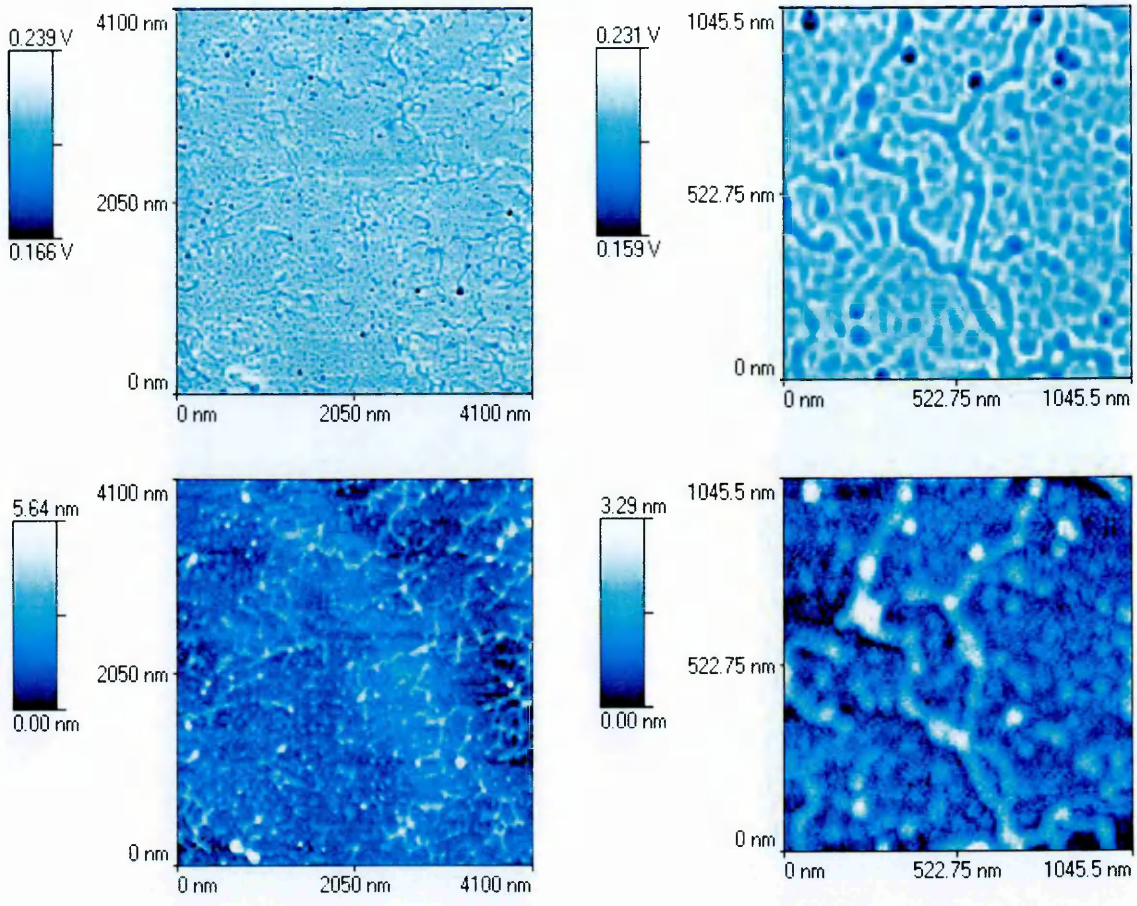

Figure 8-12. DNA network on the mica surface.

Chapter 9

Electron irradiation of dry DNA films

The main aim of these experiments was to try to reproduce the pioneering results obtained by Boudaïffa (Boudaiffa et al., 2002; Boudaiffa et al., 2000b) as well as to test a new experimental setup that was prepared at Aarhus University, Denmark, for solid state spectroscopy, for its compatibility with DNA irradiation experiments. A trochoidal electron monochromator was used as the electron source. This allowed studying DNA induced damage using electrons with energies between a 1 eV and 10 eV with a resolution of 200 meV. This source can deliver electron currents of up to 50 nA or more. Apart from the irradiation studies it is possible to use the setup to measure the transmission of DNA films at various energies of the incident electron beam.

9.1 Sample preparation and irradiation

Plasmid DNA pBR322 samples were prepared according to the protocol discussed in Chapter 4 and eluted into UHP water of pH 8.0, adjusted with 1 M NaOH solution. Six stocks of plasmid solution of well defined concentrations and purity were used in the experiments (see Table 9-1):

Table 9-1. Plasmid concentration and purity of samples used in electron irradiation experiments.

	ρ [ng/μl]	$A_{260/280}$
H1	134.75	1.833
H2	170.75	1.861
H3	112.5	1.857
H4	174.25	1.874
H5	184.25	1.847
H6	186.25	1.863

Prior to irradiation samples were removed from the freezer, defrosted and deposited in the centre of tantalum discs (of 1.5 cm diameter). In some cases some water was added to dilute the sample before placing it on the disc.

Once irradiated samples were eluted from the tantalum discs with 10 μl of pure water and mixed with loading buffer. For each sample that underwent irradiation, a control sample was prepared at the same time, which experienced exactly the same procedures as the irradiated sample, but was not exposed to the electron beam in the chamber during the irradiation (see Figure 9-1). Hence, it was possible to estimate the level of damage arising from the preparation and deposition procedure and substract it from the damage obtained by irradiation.

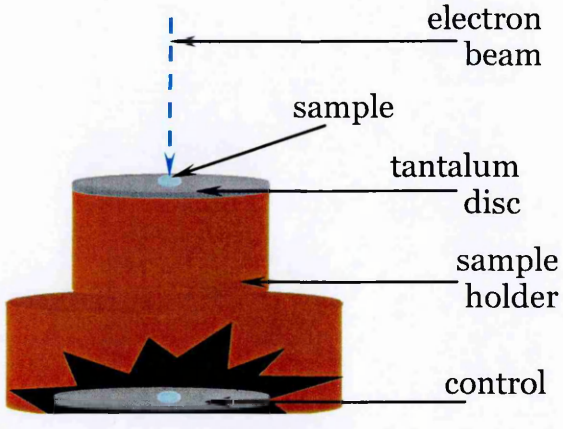

Figure 9-1. Position of the control sample in the sample holder.

A high yield of the supercoiled molecules was of great importance in the performed experiments, therefore various drying techniques were tested to establish conditions in which the damage introduced prior to irradiation was minimal. All of them seem to have a different influence on the quality of the sample prior to irradiation (for amounts of supercoiled, relaxed and linear DNA in the sample before irradiation please see Figure 9-2). Drying techniques are described in Table 9-2.

From these results it was clear that much less damage prior to irradiation was obtained for samples that were not cooled under vacuum, but just gently pumped on with the diaphragm pump. The time the sample spent under vacuum in these cases did not seem to have a great influence on the final quality of the sample.

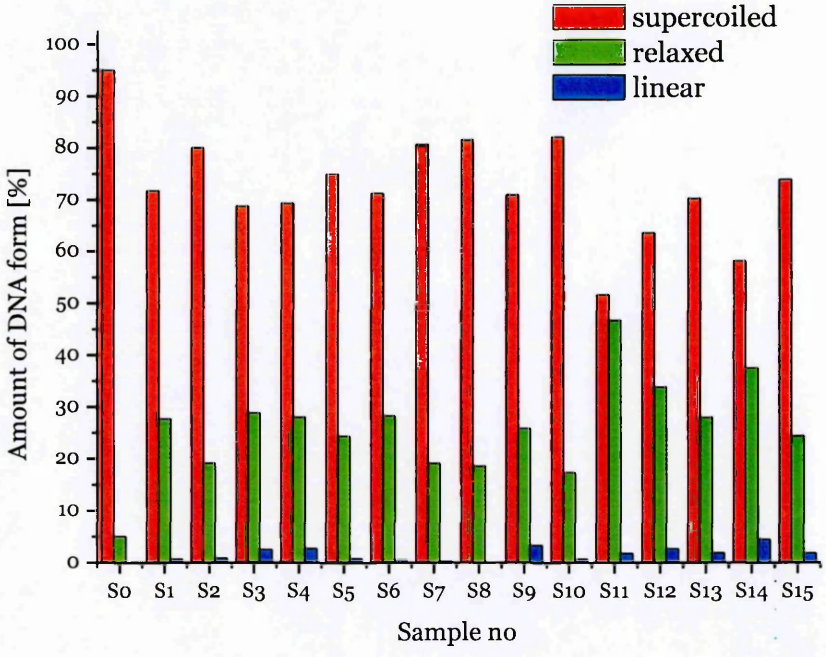

Figure 9-2. Strand breaks created by various drying techniques measured on the background samples; S0 is a fresh sample prepared from the stock solution neither dried nor treated with vacuum.

Fifteen samples were irradiated, each with different preparation conditions regarding volume, amount of plasmid, drying procedure, energy of the electrons, the time the sample spend under vacuum conditions and time of overall irradiation. The conditions for each sample, S, and their treatment are presented in Table 9-2.

A scan over the whole electron energy range was taken prior to irradiation and immediately afterwards to determine the contact potential of the electron beam (see Figure 9-3). Since charge builds up on the surface during irradiation, the contact potential and thus electron beam energy changes during irradiation period. In case of the first 11 samples a couple of scans were performed over the whole energy range (0-10 eV) both before the exposure and during the experiment as it

Table 9-2. Parameters of the sample treatments.

Treatment / Sample	Volume of the sample deposited on the tantalum disc [μl]	Amount of DNA deposited on the tantalum disc [ng]	Drying procedure	Electron energy [eV]	Time the sample spent under vacuum [min]	Irradiation time [min]	Sample's spot size [mm in diameter]
S1	8	1078	Cooled while pumping with diaphragm pump only for 1 h 20 min; left under UHV overnight	10	840	90	4
S2	8	1078	No cooling; pumped on with diaphragm pump for 1h and irradiated straight away	10	180	90	4
S3	8	1366	No cooling; pumped on with diaphragm pump overnight	10	450	300	4
S4	8	1366	No cooling; pumped on with diaphragm pump overnight; placed in the fridge before irradiation	10	150	60	4
S5	4	341.5	No cooling; pumped on with diaphragm pump overnight; spot size increased by diluting sample	4.6	180	60	4
S6	4	341.5	No cooling; pumped on with diaphragm pump overnight; placed in the fridge before irradiation; spot size increased by diluting sample	10	225	60	4
S7	6	225	No cooling; pumped on with diaphragm pump overnight; spot size increased by diluting sample	5	200	70	4
S8	6	225	No cooling; pumped on with diaphragm pump overnight; no awaiting time in the fridge; spot size increased by diluting sample	1	400	60	4
S9	10	1742.5	No cooling; pumped on with diaphragm pump for 105 min and 2 h on turbo pump	10	150	65	6
S10	10	1742.5	No cooling; pumped on with diaphragm pump for 105 min and 2 h on turbo pump; no awaiting time in the fridge	10	900	653	6
S11	10	1482.5	Sample cooled in desiccator on aluminium block chilled previously with liquid nitrogen while pumped on with diaphragm pump overnight	10	255	60	8
S12	5	741.25	Sample cooled in desiccator on aluminium block chilled previously with liquid nitrogen while pumped on with diaphragm pump overnight	10	120	1	4
S13	5	741.25	Sample cooled in desiccator on aluminium block chilled previously with liquid nitrogen while pumped on with diaphragm pump overnight	10	1020	60	4
S14	10	1862.5	Sample cooled in desiccator on aluminium block chilled previously with liquid nitrogen while pumped on with diaphragm pump for 9 h	10	600	663	8
S15	10	1862.5	No cooling; sample pumped on with turbo pump overnight	10	120	1	8

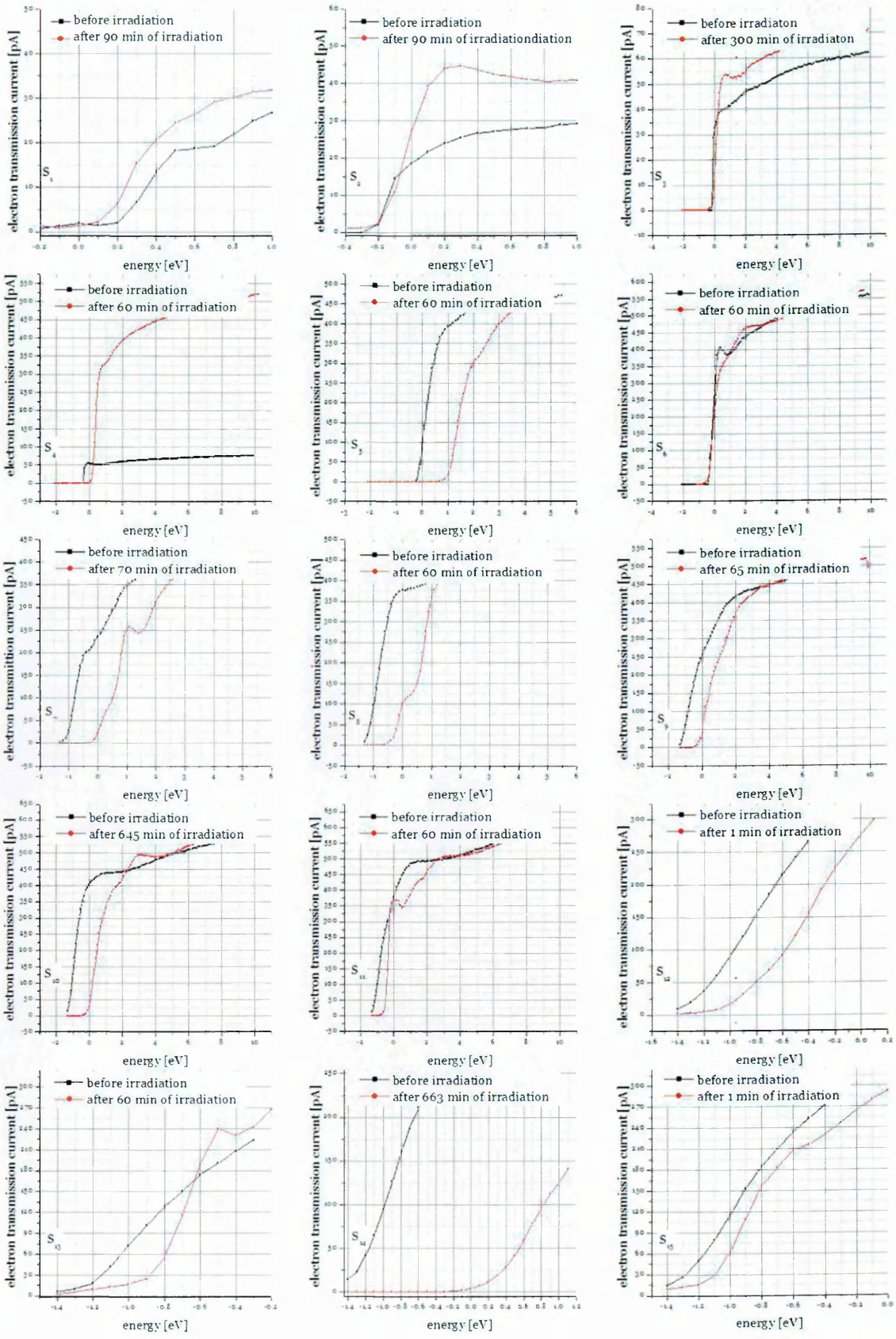

Figure 9-3. Transmission scans for all the samples before and after irradiation.

was important to determine, how the beam behaves through the irradiation. For the last 4 samples just 2 scans (before and after irradiation) were performed; scans

were stopped as soon as it was possible to determine the contact potential to avoid possible overirradiation as well as a charge build-up that might result in later electron beam repulsion from the sample surface and damage prohibition.

9.2 Analysis of the results

After irradiation 2 μl of each collected sample were mixed with 2 μl of loading buffer and placed on 1.4 % SeaKem LE agarose (Cambrex) gel. Electrophoresis (Wide Mini-Sub Cell GT system from Bio-Rad was used) was run at 35 V for 14 h in presence of 1 x TBE buffer. After electrophoresis, all the gels were stained with 1 x SYBRGreenI (Sigma-Aldrich) solution in 1 x TBE buffer for 30 min and de-stained in 1 x TBE buffer for 10 min. Fluorescent images of stained gels were taken with a GeneFlash gel imager.

The photographs were later analysed with ImageJ software to quantify the amount of DNA in each band, so the amount of single and double strand breaks as well as supercoiled DNA loss could be determined.

As the sample on the gel represents the whole population that was placed on the disc and just a fraction of it was irradiated (as the diameter of the electron beam was smaller than the diameter of the sample), after background abstraction, the relative change corresponds only to the amount of molecules that were irradiated, $N_{irradiated}$:

$$N_{irradiated} = N_{total} \cdot \left(\frac{a}{d}\right)^2 \qquad (9\text{-}1)$$

where N_{total} is the total number of molecules in the sample, a is the electron beam diameter and d is the diameter of the dried sample.

9.2.1 Single and double strand breaks – effective cross sections for interactions with 10 eV electrons

The ultimate aim of these experiments was to determine the effective cross sections for single (σ_{SSB}) and double (σ_{DSB}) strand breaks induced by electrons and to compare them with those published previously (Boudaiffa et al., 2002). Therefore the same way for method for evaluating these cross sections was used (see Appendix G for details). As discussed in Chapter 1 (section 1.6.2), resonant structure was observed at electron energies around 10 eV (Boudaiffa et al., 2000a), thus we focused on investigating DNA damage induced at 10 eV. An effective cross section, σ_X, was defined through the appearance of different plasmid DNA forms upon irradiation: For an electron current density of energy E, targeting a sample area A, over a period of time t, the number of breaks N_x can be written as

$$N_x = N_{irradiated} \cdot \sigma_X \cdot J \cdot t \qquad (9\text{-}2)$$

where X denotes S (supercoiled DNA loss), *SSB* or *DSB*.

Contrary to electron–molecule interactions in the gas phase, in the case of dry DNA films the cross section is considered effective for a given energy, density and average thickness of investigated film.

There are a several possible pathways for the formation of relaxed, linear DNA and DNA short fragments (multiple strand breaks). Figure 9-4 illustrates possible ways for transitions between all the forms that can appear upon irradiation.

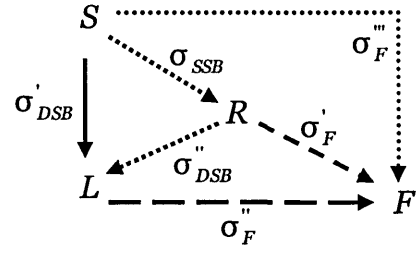

Figure 9-4. Schematic change of supercoiled (*S*) DNA into other forms: relaxed (*R*), linear (*L*) and short fragments (*F*). σ indicates a cross section for certain transition.

The effective cross section for supercoiled DNA loss, σ_S, is defined as

$$\sigma_S = \sigma'_{DSB} + \sigma_{SSB} \tag{9-3}$$

At low energies the probability for formation of small DNA fragments is negligible (also no DNA 'smears' were seen on the gel below the supercoiled DNA band level and the recovery from the support was close to 100 %), such events can be ignored in later discussion ($\sigma'_F, \sigma''_F, \sigma'''_F = 0$).

It is also possible to describe supercoiled DNA disappearance, *S*, and formation of other DNA forms (relaxed, *R*, and linear, *L*) with time via the following system of equations, employing the effective cross sections (Boudaiffa et al., 2002):

$$\begin{aligned}
\frac{dS(t)}{dt} &= -(\sigma'_{DSB} + \sigma_{SSB}) \cdot J \cdot S(t) \\
\frac{dR(t)}{dt} &= \sigma_{SSB} \cdot J \cdot S(t) - \sigma''_{DSB} \cdot J \cdot R(t) \\
\frac{dL(t)}{dt} &= \sigma'_{DSB} \cdot J \cdot S(t) + \sigma''_{DSB} \cdot J \cdot R(t) - \sigma''_F \cdot J \cdot L(t)
\end{aligned} \tag{9-4}$$

Solutions of these time evolutions are given by (see Appendix H for calculations)

$$\begin{aligned}
S(t) &= S_0 e^{-(\sigma'_{DSB} + \sigma_{SSB})J \cdot t} \\
R(t) &= R_0 e^{-\sigma''_{DSB} \cdot J \cdot t} + R'(e^{-(\sigma'_{DSB} + \sigma_{SSB})J \cdot t} - e^{-\sigma''_{DSB} \cdot J \cdot t}) \\
L(t) &= L_0 e^{-\sigma''_F \cdot J \cdot t} + L'(e^{-(\sigma'_{DSB} + \sigma_{SSB})J \cdot t} - e^{-\sigma''_F \cdot J \cdot t}) + L''(e^{-\sigma''_{DSB} \cdot J \cdot t} - e^{-\sigma''_F \cdot J \cdot t}) \\
F(t) &= 1 - S(t) - R(t) - L(t)
\end{aligned} \tag{9-5}$$

with:

$$R' = \frac{\sigma_{SSB} S_0}{\sigma''_{DSB} - \sigma'_{DSB} - \sigma_{SSB}}$$

$$L' = \frac{\sigma'_{DSB} S_0 + \sigma''_{DSB} R'}{\sigma''_F - \sigma'_{DSB} - \sigma_{SSB}}$$

$$L'' = \frac{\sigma''_{DSB}(R_0 - R')}{\sigma''_F - \sigma''_{DSB}}$$

As mentioned above, due to the lack of visible fragmentation, both *F(t)* and σ''_F can be considerer to be zero. Therefore, equations (9-5) can be rewritten as

$$
\begin{aligned}
S(t) &= S_0 e^{-(\sigma'_{DSB}+\sigma_{SSB})J\cdot t} \\
R(t) &= R_0 e^{-\sigma''_{DSB}\cdot J\cdot t} + R'(e^{-(\sigma'_{DSB}+\sigma_{SSB})J\cdot t} - e^{-\sigma''_{DSB}\cdot J\cdot t}) \\
L(t) &= L_0 e^{-\sigma''_{DSB}\cdot J\cdot t} + L'(e^{-(\sigma'_{DSB}+\sigma_{SSB})J\cdot t} - 1) + L''(e^{-\sigma''_{DSB}\cdot J\cdot t} - 1)
\end{aligned}
\qquad (9\text{-}6)
$$

with

$$
R' = \frac{\sigma_{SSB} S_0}{\sigma''_{DSB} - \sigma'_{DSB} - \sigma_{SSB}}
$$

$$
L' = \frac{\sigma'_{DSB} S_0 + \sigma''_{DSB} R'}{-\sigma'_{DSB} - \sigma_{SSB}}
$$

$$
L'' = -(R_0 - R')
$$

Being able to measure σ_S and σ_{SSB} directly from the agarose gel, using relation (9-2) it was possible to calculate σ'_{DSB}. From equations (9-6) it was possible to determine the value of σ''_{DSB} to be

$$
\sigma''_{DSB} = \sigma_S - \frac{\sigma_{SSB}\cdot S_0}{R_0} \qquad (9\text{-}7)
$$

Since electrons can only penetrate the sample to a certain depth, additional corrections to equations system (9-6) need to be taken into account. This modification employs an electron penetration depth, h, and the DNA film thickness, H, as follows:

$$
C_{corrected}(t) = \frac{h\cdot C(t) + (H-h)\cdot C_0}{H} \qquad (9\text{-}8)
$$

where C is S, R or L.

Measurements that would allow a direct experimental determination of value of the penetration depth were not performed in the present experiment but using the ImageJ program, it was possible to estimate both the surface area of a single plasmid molecule as well as its height. The surface area of a single plasmid molecule, A_{pBR322}, was estimated to be about $27\cdot10^3$ nm^2 ± 2 % (see Figure 9-5) and its height around 3 nm (picture not shown). From this it was possible to calculate

how many molecules are present in a single layer of a diameter of d, N_d, assuming that molecules in the monolayer are tightly packed:

$$N_d = \frac{\pi \cdot d^2}{A_{pBR322}} \tag{9-9}$$

One can now estimate how many monolayers, n_l, a sample of a total number of molecules N_{total} had to have, namely

$$n_l = \frac{N_{total}}{N_d} \tag{9-10}$$

Knowing that the height of one supercoiled molecule on a surface in a dry film is approximately 3 nm, it is possible to establish the thickness of the whole sample (H, in [nm]) as

$$H = n_l \cdot 3 \tag{9-11}$$

with the assumption that an average layer thickness equals a thickness of a single molecule.

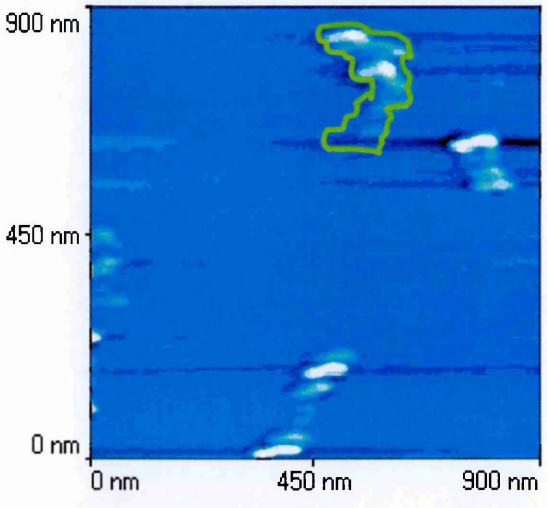

Figure 9-5. Example of AFM phase shift image of supercoiled plasmid pBR322 dry film on mica surface. Green line indicates the surface area of a sample molecule that was measured to be approx. 27091 nm²

Substituting (9-8), (9-9) and (9-11) into (9-6) makes it possible to compare the results obtained experimentally for samples irradiated at 10 eV against these published previously (Boudaiffa et al., 2002), from where the experimentally determined value of penetration depth, h = 12 nm, was taken.

Table 9-3. Cross sections for plasmid DNA transformations.

sample	Not corrected for the penetration depth, h				Corrected for the penetration depth, h				
	σ_S [cm²]	σ_{SSB} [cm²]	σ_{DSB} [cm²]	σ'_{DSB} [cm²]	σ_S [cm²]	σ_{SSB} [cm²]	σ_{DSB} [cm²]	σ'_{DSB} [cm²]	σ''_{DSB} [cm²]
published						**$(2.6\pm0.3)\cdot10^{-15}$**		**$(8\pm3)\cdot10^{-16}$**	**$<4\cdot10^{-17}$**
S1	$2.27\cdot10^{-16}$	$1.34\cdot10^{-16}$	$9.28\cdot10^{-17}$	$1.20\cdot10^{-16}$	$1.80\cdot10^{-18}$	$1.07\cdot10^{-18}$	$7.37\cdot10^{-19}$	$7.37\cdot10^{-19}$	$9.56\cdot10^{-19}$
S2	$1.41\cdot10^{-16}$	$5.60\cdot10^{-17}$	$8.55\cdot10^{-17}$	$9.28\cdot10^{-17}$	$1.12\cdot10^{-18}$	$4.44\cdot10^{-19}$	$6.79\cdot10^{-19}$	$6.77\cdot10^{-19}$	$7.37\cdot10^{-19}$
S3	$7.13\cdot10^{-17}$	$2.99\cdot10^{-17}$	$4.13\cdot10^{-17}$	$-9.18\cdot10^{-20}$	$4.47\cdot10^{-19}$	$1.87\cdot10^{-19}$	$2.59\cdot10^{-19}$	$2.59\cdot10^{-19}$	$-5.75\cdot10^{-22}$
S4	$4.68\cdot10^{-17}$	$2.36\cdot10^{-17}$	$2.33\cdot10^{-17}$	$1.15\cdot10^{-17}$	$2.93\cdot10^{-19}$	$1.48\cdot10^{-19}$	$1.46\cdot10^{-19}$	$1.46\cdot10^{-19}$	$7.21\cdot10^{-20}$
S6	$3.45\cdot10^{-17}$	$-1.57\cdot10^{-17}$	$5.02\cdot10^{-17}$	$-7.40\cdot10^{-17}$	$8.65\cdot10^{-19}$	$-3.93\cdot10^{-19}$	$1.26\cdot10^{-18}$	$1.26\cdot10^{-18}$	$-1.86\cdot10^{-18}$
S9	$6.76\cdot10^{-17}$	$5.28\cdot10^{-17}$	$1.48\cdot10^{-17}$	$7.69\cdot10^{-17}$	$7.47\cdot10^{-19}$	$5.83\cdot10^{-19}$	$1.64\cdot10^{-19}$	$1.64\cdot10^{-19}$	$8.50\cdot10^{-19}$
S10	$-2.97\cdot10^{-18}$	$-2.90\cdot10^{-18}$	$-6.98\cdot10^{-20}$	$-1.07\cdot10^{-17}$	$-3.28\cdot10^{-20}$	$-3.20\cdot10^{-20}$	$-7.71\cdot10^{-22}$	$-7.71\cdot10^{-22}$	$-1.19\cdot10^{-19}$
S11	$2.71\cdot10^{-16}$	$2.49\cdot10^{-16}$	$2.13\cdot10^{-17}$	$5.09\cdot10^{-18}$	$6.25\cdot10^{-18}$	$5.76\cdot10^{-18}$	$4.92\cdot10^{-19}$	$4.92\cdot10^{-19}$	$1.18\cdot10^{-19}$
S12	$2.79\cdot10^{-15}$	$2.30\cdot10^{-15}$	$4.94\cdot10^{-16}$	$4.88\cdot10^{-16}$	$3.22\cdot10^{-17}$	$2.66\cdot10^{-17}$	$5.71\cdot10^{-18}$	$5.63\cdot10^{-18}$	$1.77\cdot10^{-17}$
S13	$1.09\cdot10^{-17}$	$8.50\cdot10^{-18}$	$2.37\cdot10^{-18}$	$2.42\cdot10^{-18}$	$1.26\cdot10^{-19}$	$9.81\cdot10^{-20}$	$2.74\cdot10^{-20}$	$2.79\cdot10^{-20}$	$1.20\cdot10^{-19}$
S14	$2.53\cdot10^{-18}$	$-6.92\cdot10^{-19}$	$3.22\cdot10^{-18}$	$3.22\cdot10^{-18}$	$4.65\cdot10^{-20}$	$-1.27\cdot10^{-20}$	$5.92\cdot10^{-20}$	$5.92\cdot10^{-20}$	$-6.62\cdot10^{-20}$
S15	$7.25\cdot10^{-15}$	$5.39\cdot10^{-15}$	$1.87\cdot10^{-15}$	$1.86\cdot10^{-15}$	$1.33\cdot10^{-16}$	$9.91\cdot10^{-17}$	$3.44\cdot10^{-17}$	$3.42\cdot10^{-17}$	$1.67\cdot10^{-16}$

Table 9-3 shows results obtained for the cross sections, both with and without corrections for the penetration depth. On average the following values for 10 eV were obtained: σ'_{DSB} = 2.24·10^{-16} cm^2, σ_{SSB} = 6.86·10^{-16} cm^2, σ''_{DSB} = 9.05·10^{-16} cm^2 and σ'_{DSB} = 3.64·10^{-18} cm^2, σ_{SSB} = 1.11·10^{-17} cm^2, σ''_{DSB} = 1.55·10^{-17} cm^2 for penetration depth correction.

On average the values obtained are three orders of magnitude smaller than those of Boudaïffa when corrections made for the penetration depth. It can be seen that various preparation techniques of DNA film and irradiation fluxes and times had strong influence on the values obtained. Only the value for σ''_{DSB} agrees within the experimental error.

9.2.2 Number of breaks per incident electron

It was also interesting to establish, how many molecules underwent a conformational change per single electron delivered at particular energy, N_z, so it would be possible to compare our data against the literature ones (Boudaiffa et al., 2000a). For that purpose the following expression was used

$$N_z = \frac{(C_z - C_{oz}) \cdot \rho \cdot V \cdot N_{pBR322} \cdot q_e}{100 \cdot I \cdot t} \qquad (9\text{-}12)$$

where z denote either S (supercoiled), SSB (open circular form) or DSB (linear form), C_z is a fraction of form of interest after irradiation [%], C_{oz} is a fraction of form of interest before irradiation [%], ρ is sample concentration [g/μl], V is the volume used for the experiments [μl], N_{pBR322} for number of pBR322 molecules in 1g = 2.1·10^{11}, a and d is the diameter of electron beam and sample area, respectively, (both in [mm]), q_e is unit charge = 1.602·10^{-19} C, I is an electron current [A] and t indicates the irradiation time [s].

Boudaïffa obtained the following results for loss of supercoiled DNA, SSB and DSB formation per incident electron (Table 9-5)

Table 9-4. Values obtained by for electron irradiation experiments (X denotes no damage)

sample	E [eV]	N_S [molecules/ incident electron]	N_{SSB} [molecules/ incident electron]	N_{DSB} [molecules/ incident electron]	Number of layers, n	h-corrected N_S [molecules/ incident electron]	h-corrected N_{SSB} [molecules/ incident electron]	h-corrected N_{DSB} [molecules/ incident electron]	D [Gy]	I [nA]
S1	10	$1.06 \cdot 10^{-04}$	$6.24 \cdot 10^{-05}$	$4.32 \cdot 10^{-05}$	504	$8.38 \cdot 10^{-07}$	$4.95 \cdot 10^{-07}$	$3.43 \cdot 10^{-07}$	0.20	4
S2	10	$6.56 \cdot 10^{-05}$	$2.60 \cdot 10^{-05}$	$3.98 \cdot 10^{-05}$	504	$5.21 \cdot 10^{-07}$	$2.07 \cdot 10^{-07}$	$3.16 \cdot 10^{-07}$	0.26	5.25
S3	10	$4.20 \cdot 10^{-05}$	$1.76 \cdot 10^{-05}$	$2.43 \cdot 10^{-05}$	638	$2.63 \cdot 10^{-07}$	$1.10 \cdot 10^{-07}$	$1.53 \cdot 10^{-07}$	0.84	6.4
S4	10	$2.76 \cdot 10^{-05}$	$1.39 \cdot 10^{-05}$	$1.37 \cdot 10^{-05}$	638	$1.73 \cdot 10^{-07}$	$8.70 \cdot 10^{-08}$	$8.60 \cdot 10^{-08}$	1.32	50
S5	4.6	$5.36 \cdot 10^{-06}$	$4.06 \cdot 10^{-06}$	$1.29 \cdot 10^{-06}$	160	$1.34 \cdot 10^{-07}$	$1.02 \cdot 10^{-07}$	$3.23 \cdot 10^{-08}$	2.08	43
S6	10	$5.09 \cdot 10^{-06}$	$-2.31 \cdot 10^{-06}$	$7.39 \cdot 10^{-06}$	160	$1.27 \cdot 10^{-07}$	$-5.80 \cdot 10^{-08}$	$1.85 \cdot 10^{-07}$	5.60	53
S7	5	$5.74 \cdot 10^{-06}$	$3.81 \cdot 10^{-06}$	$1.93 \cdot 10^{-06}$	105.	$2.18 \cdot 10^{-07}$	$1.45 \cdot 10^{-07}$	$7.36 \cdot 10^{-08}$	3.56	38
S8	1	$1.78 \cdot 10^{-06}$	$1.78 \cdot 10^{-06}$	X	105.	$6.77 \cdot 10^{-08}$	$6.77 \cdot 10^{-08}$	X	0.56	35
S9	10	$2.26 \cdot 10^{-05}$	$1.76 \cdot 10^{-05}$	$4.95 \cdot 10^{-06}$	362	$2.50 \cdot 10^{-07}$	$1.95 \cdot 10^{-07}$	$5.47 \cdot 10^{-08}$	1.05	47
S10	10	$-9.91 \cdot 10^{-07}$	$-9.68 \cdot 10^{-07}$	$-2.33 \cdot 10^{-08}$	362	$-1.10 \cdot 10^{-08}$	$-1.07 \cdot 10^{-08}$	$-2.58 \cdot 10^{-10}$	11.92	53
S11	10	$4.33 \cdot 10^{-05}$	$3.99 \cdot 10^{-05}$	$3.41 \cdot 10^{-06}$	173	$9.99 \cdot 10^{-07}$	$9.21 \cdot 10^{-07}$	$7.87 \cdot 10^{-08}$	1.33	55
S12	10	$8.93 \cdot 10^{-04}$	$7.37 \cdot 10^{-04}$	$1.58 \cdot 10^{-04}$	346	$1.03 \cdot 10^{-05}$	$8.51 \cdot 10^{-06}$	$1.82 \cdot 10^{-06}$	0.05	60
S13	10	$3.49 \cdot 10^{-06}$	$2.72 \cdot 10^{-06}$	$7.58 \cdot 10^{-07}$	346	$4.03 \cdot 10^{-08}$	$3.14 \cdot 10^{-08}$	$8.75 \cdot 10^{-09}$	2.43	50
S14	10	$5.08 \cdot 10^{-07}$	$-1.39 \cdot 10^{-07}$	$6.47 \cdot 10^{-07}$	218	$9.34 \cdot 10^{-09}$	$-2.55 \cdot 10^{-09}$	$1.19 \cdot 10^{-08}$	10.25	48
S15	10	$1.46 \cdot 10^{-03}$	$1.08 \cdot 10^{-03}$	$3.76 \cdot 10^{-04}$	218	$2.68 \cdot 10^{-05}$	$1.99 \cdot 10^{-05}$	$6.91 \cdot 10^{-06}$	0.01	43
Average for 10 eV	10	$2.22 \cdot 10^{-04}$	$1.66 \cdot 10^{-04}$	$5.60 \cdot 10^{-05}$	372	$3.36 \cdot 10^{-06}$	$2.53 \cdot 10^{-06}$	$8.31 \cdot 10^{-07}$	2.94	39.6

Table 9-5. Values for measured quantum yields of loss of supercoiled DNA, SSB and DSB formation obtained by Boudaiffa *et al.*

Electron energy	N_S [molecules/ incident electron]	N_{SSB} [molecules/ incident electron]	N_{DSB} [molecules/ incident electron]
5 eV	$2 \cdot 10^{-4}$	$2 \cdot 10^{-4}$	0
10 eV	$9 \cdot 10^{-4}$	$7 \cdot 10^{-4}$	$2 \cdot 10^{-4}$

The obtained results are presented in Table 9-4. It can be seen that the average value obtained for irradiations carried at 10 eV agrees with the result of Boudaïffa within the order of the magnitude, although smaller number of DSBs was obtained. However when the correction for penetration depth was applied, calculated values decreased significantly. Values obtained for 5 eV were much smaller in both cases than the published ones with and without the *h* correction.

9.2.3 Dose dependence

It was also possible to determine the irradiation dose, *D*, that was delivered to the sample by (see Appendix I)

$$D[\mathrm{Gy}] = \frac{t \cdot E \cdot I}{M} \tag{9-13}$$

where *E* is the electron's energy [eV] and *M* is sample's mass [kg]. The results for all samples are shown in Table 9-4. It was interesting to plot the loss of supercoiled DNA, SSB and DSB formation against the dose of 10 eV electrons (Figure 9-6). Data for loss of supercoiled DNA presented in Figure 9-6 was fitted with high accuracy using an exponential decay model. Such fit indicates that the dose response curves for the electron irradiations should be similar to those obtained for photon irradiations, described in Chapter 5.

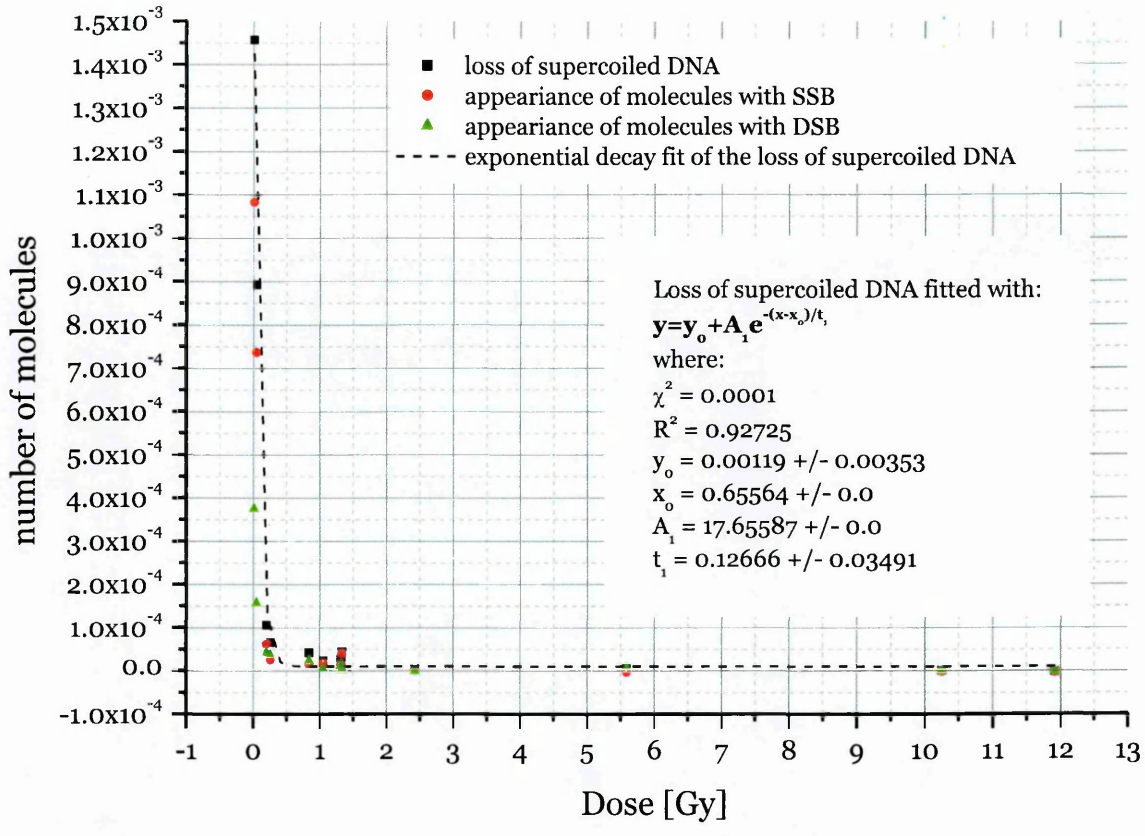

Figure 9-6. Dose response curve for plasmid DNA irradiated with electrons of energy of 10 eV.

9.3 Discussion and conclusions

The main aim of these experiments was to compare our experiments with previous ones by Boudaïffa *et al.* and to establish techniques for sample handling and data analysis in electron irradiation experiments.

Several parameters influenced the results we obtained. First of all, the definition of the beam size and its position led to a fairly large uncertainty (about 100 %) in the value of the beam diameter. Therefore the sample diameter had to be enlarged to ensure electrons targeted only the DNA molecules only and there is no loss of current due to the beam striking an empty tantalum disc. That of course introduces a fairly large error in the analysis as we had to correct for the small surface that

was irradiated, whereas we could only collect the whole deposited sample – both the irradiated and non irradiated parts.

Another issue that needs to be addressed is that the sample drying techniques used did not ensure a uniform plasmid distribution over the sample surface. The concern was that during water evaporation the plasmid distribution was denser at the edge, creating a ring, and thinner in the middle, where the electron beam was focused. That would influence the assumption we made of the amount of molecules in the irradiated spot to be directly proportional to the squared ratio of the beam and sample diameters.

As the sample was placed on the discs just by pipetting the solution straight onto the surface, it was not possible to ensure that the sample will be perfectly round and in the middle every single time.

Looking at the results qualitatively one notices that the values obtained differ significantly in each sample set. This shows the influence the preparation technique has on the levels of damage.

First of all, the problem of drying should be addressed as it was clear that in case of the samples experiencing the smallest damage were these prepared by freezing /vacuum treatment, also the damage after irradiation seemed to be lower. This of course can be corrected for in the background abstraction step; nonetheless, some changes that will be classified as DSB could have been, in fact, SSB, that occurred close enough to the place that was damaged preceding irradiation. More damage was observed in samples that were not overexposed to radiation by full range energy scans (samples S12-S15). Samples that were irradiated for a long time did not have the high levels of damage expected. Such a phenomenon might be a result of a charge build-up on the sample surface that would have caused further screening of the irradiated material by repulsing the electron beam.

The penetration depth of the incident electrons was also not taken into account in the measurements performed and no measurements were done to determine this value. To compare the new data to that previously published, a value that was found in the cited literature was used.

The average values for cross sections obtained differ significantly from those of Boudaïffa being an order of magnitude lower if calculated directly and three orders of magnitude lower if the corrections are made for the penetration depth. The value for the direct DSB formation from the supercoiled DNA is in our case the smallest and the ones that quantify the single events have relatively high values (both in case of direct analysis and in case of correction for the penetration depth). Such behaviour could not be influenced by the experimental error and would support the theory that the DSB are a product of two separate SSB events rather than a single electron strike.

The same order of magnitude difference was obtained in the case of quantification of numbers of strand breaks and loss of supercoiled molecules per single incident electron. Contrary to the published data the damage at 10 eV was around 100 times greater than the one at 5 eV. Comparing our results to those of Boudaïffa, we also obtained more SSB per incident electron that DSB. Also the ratios of SSB to DSB in both cases are around 3-3.5. Although Table 9-4 shows values corrected for the penetration depth of the electrons, it is rather certain that the published results that were used for comparision with the data presented in ths work were not corrected for it.

If the dose-response curve is considered one can easily notice that the damage obtained for small doses was greater than in case of high dose exposures. As in case of irradiations of samples in aqueous solutions the damage rate at the beginning of irradiation is high and decreases with time as the molecules are being damaged. It can be seen as in higher doses (above 1 Gy) there is an excess amount

of electrons comparing to the amount of plasmid that can be damaged. It would therefore be interesting to check for the influence of the dose delivery rate on the induced damage. There are two things that need to be taken into account, namely the very low dose samples did not have full energy scans performed on them, as well as the charge build-up during such a short period of time was noticeably smaller (see the shifts of the irradiation curves on Figure 9-3). It is believed that the excess amount of electrons increases on the sample surface enough to screen from the beam within first few minutes of irradiation and therefore such high yields of damage were acquired.

Chapter 10

Summary, conclusions and future work

10.1 Summary and conclusions

The work presented in this thesis confirmed that DNA damage may be induced by both VUV light (Folkard et al., 2002) and electron irradiation (Boudaiffa et al 2000) at energies below the ionisation potential of any of its constituent molecules. Enhanced damage was observed using 170 nm irradiation and may be explained by optical excitation leading to dissociation of water embedded within the plasmid helix forming hydroxyl (OH) radical which subsequently cause chemical damage to the plasmid DNA. It was shown that, although very low, there is some damage induced by photons of the wavelength of 190 nm. Photons of this wavelength do not interact with water molecules and thus the damage must arise from direct photon-DNA interactions.

Loss of supercoiled DNA and the production of both SSBs and DSBs was measured as a function of applied dose for a wide variety of experimental conditions. The rate of loss of supercoiled DNA under VUV irradiation was found to decay exponentially as a function of the radiation dose applied.

Since these were the first experiments on DNA damage performed by the Open University group it was necessary to develop a comprehensive set of protocols for both plasmid preparation and analysis. Full details are presented in this thesis, establishing a detailed protocol for plasmid DNA preparation. Optimisation of the conditions for bacteria growth made it possible to obtain large quantities of very pure (not contaminated by proteins and RNA) plasmid DNA (usually between 90 % and 95 % of supercoiled form) that could be used for irradiation studies.

Similarly protocols were developed for DNA damage analysis using gel electrophoresis. In addition some experiments were performed to explore the use of an atomic force microscope for imaging the DNA molecules. From these experiments it was concluded that it should be possible to image even single stranded DNA. In principle, it should be also possible to see the DNA breaks, however it was not possible to establish a repeatable protocol for DNA imaging with the AFM model available at The Open University.

A new method for labelling and thus quantifying single strand breaks was established, based on the ELISA assay. The new method allows an accurate analysis of small quantities of DNA and measured additional strand breaks that could not be seen via gel electrophoresis. It was also shown that with this new method uncertainties associated with the measurement can be reduced and thus the cross section values calculated on the basis of damage determined with the assay method are expected to be more accurate.

10.2 Future work

As for the future work it would be recommended to continue the irradiation studies. Higher accuracy of the average data points should be achieved by repeating each irradiation five or more times. It would be recommended to obtain the dose-response curves for irradiations with photons of 170 nm wavelength at the apparatus that was build at the Open University and compare it with the data obtained from the irradiations carried at the synchrotron source.

Since the work presented in this thesis was the first by the Open University group and remains one of the few investigations being pursued internationally there are many more experiments that can and should be developed. Employing the atomic force microscope for damage analysis will allow direct imaging of the lesions either by investigating the changes in DNA conformation of by attaching protein-based

probes to the specific lesions formed. It will also be possible to perform a statistical analysis of the length of product fragments induced by different types of irradiation and look for multiple strand breaks in a single plasmid. The ELISA assay method should be more widely adopted and utilised to quantify cross sections for different types of radiation. Experiments at even lower photon (> 200 nm) and electron energies (< 1 eV) should be developed to determine threshold for SSB formation and the role of resonance formation. Experiments with other types of radiation including positrons, anions and cations may be performed as all are or may be adopted in new types of radiotherapy.

Another set of experiments carried out, but not shown in this thesis, investigated synthesis of lesion-specific probes, which should allow us to label apurination sites formed via aldehyde site recognition (so-called aldehyde reactive probe, ARP) or formed by ketone site recognition (so-called biotinylated cysteine probe). The use of these probes should allow a better determination of the different types of lesions that can be formed upon low energy radiation and by the secondary species produced by ionising radiation

Sed fugit interea fugit irreparabile tempus

Virgil

Appendices

Appendix A

Plasmid DNA purification procedure (from "Qiaprep miniprep handbook"):

1. Resuspend pelleted bacterial cells in 250 µl Buffer P1 and transfer to a microcentrifuge tube.

Ensure that RNase A has been added to Buffer P1. No cell clumps should be visible after resuspension of the pellet. If LyseBlue reagent has been added to Buffer P1, vigorously shake the buffer bottle to ensure LyseBlue particles are completely dissolved. The bacteria should be resuspended completely by vortexing or pipetting up and down until no cell clumps remain.

2. Add 250 µl Buffer P2 and mix thoroughly by inverting the tube 4–6 times.

Mix gently by inverting the tube. Do not vortex, as this will result in shearing of genomic DNA. If necessary, continue inverting the tube until the solution becomes viscous and slightly clear. Do not allow the lysis reaction to proceed for more than 5 min. If LyseBlue has been added to Buffer P1 the cell suspension will turn blue after addition of Buffer P2. Mixing should result in a homogeneously colored suspension. If the suspension contains localized colorless regions or if brownish cell clumps are still visible, continue mixing the solution until a homogeneously colored suspension is achieved.

3. Add 350 µl Buffer N3 and mix immediately and thoroughly by inverting the tube 4–6 times.

To avoid localized precipitation, mix the solution thoroughly, immediately after addition of Buffer N3. Large culture volumes (e.g. ≥5 ml) may require inverting up

to 10 times. The solution should become cloudy. If LyseBlue reagent has been used, the suspension should be mixed until all trace of blue has gone and the suspension is colorless. A homogeneous colorless suspension indicates that the SDS has been effectively precipitated.

4. Centrifuge for 10 min at 13,000 rpm (~17,900 x g) in a table-top microcentrifuge.

A compact white pellet will form.

5. Apply the supernatants from step 4 to the QIAprep spin column by decanting or pipetting.

6. Centrifuge for 30–60 s. Discard the flow-through.

7. Recommended: Wash the QIAprep spin column by adding 0.5 ml Buffer PB and centrifuging for 30–60 s. Discard the flow-through.

This step is necessary to remove trace nuclease activity when using endA+ strains such as the JM series, HB101 and its derivatives, or any wild-type strain, which have high levels of nuclease activity or high carbohydrate content. Host strains such as XL-1 Blue and DH5α™ do not require this additional wash step.

8. Wash QIAprep spin column by adding 0.75 ml Buffer PE and centrifuging for 30–60 s.

9. Discard the flow-through, and centrifuge for an additional 1 min to remove residual wash buffer.

Important: Residual wash buffer will not be completely removed unless the flow-through is discarded before this additional centrifugation. Residual ethanol from Buffer PE may inhibit subsequent enzymatic reactions.

10. Place the QIAprep column in a clean 1.5 ml microcentrifuge tube. To elute DNA, add 50 µl Buffer EB (10 mM Tris·Cl, pH 8.5) or water to the center of each QIAprep spin column, let stand for 1 min, and centrifuge for 1 min.

Appendix B

The irradiation dose, D, equals the energy, E_{abs} [J], delivered to a body of a total mass M [kg]

$$D = \frac{E_{abs}}{M} [\text{Gy}]$$

In case of photon irradiation E_{abs} can be expressed as

$$E_{abs} = \frac{h \cdot c}{\lambda} \cdot n_{ph}$$

where:

h – Planck's constant = $6.662 \cdot 10^{-34}$ J·s,

c – speed of light = 299792458 m·s^{-1},

λ – wavelength [m],

n_{ph} – number of photons.

The current read from the electrometer depends on the number of electrons, n_{el}, emitted in the photocathode in one second, [sec], upon irradiation

$$I_{el} = \frac{q_e \cdot n_{el}}{[\text{sec}]}$$

where

q_e – electron charge = $1.602 \cdot 10^{-19}$ C.

The quantum efficiency, Q_E, of the photodiode provides a relationship between the number of electrons, n_{el}, emitted inside the photocathode per one incident photon,

$n_{ph} = 1$

$$n_{ph} = \frac{n_{el}}{Q_E}$$

In this way the current that results from the electron motion can be converted to photocurrent that depends on the number of incident photons and the number of photons can be derived as

$$I_{el} = \frac{q_e \cdot n_{ph} \cdot Q_E}{[\text{sec}]} \rightarrow n_{ph} = \frac{I_{el} \cdot \Delta S \cdot [\text{sec}]}{q_e \cdot Q_E \cdot s_{det}}$$

($\Delta S/s_{det}$ factor comes from the calibration from the active surface of the detector, s_{det}, onto the surface area of the sample, ΔS)

This allows us to express the dose as a function of known parameters

$$D = \frac{h \cdot c}{\lambda \cdot M} \cdot \frac{I_{el} \cdot \Delta S \cdot [\text{sec}]}{q_e \cdot Q_E \cdot s_{\text{det}}}$$

and the absorbed dose as

$$D_{absorbed} = \frac{D}{[\text{sec}]} = \frac{h \cdot c \cdot I_{el} \cdot \Delta S}{\lambda \cdot M \cdot q_e \cdot Q_E \cdot s_{\text{det}}}$$

From this the time needed for sample irradiation to reach the desired dose can be derived as

$$[\text{sec}] = \frac{D \cdot \lambda \cdot M \cdot q_e \cdot Q_E \cdot s_{\text{det}}}{h \cdot c \cdot I_{el} \cdot \Delta S}$$

Appendix C

An effective cross section for a lesion formation, σ_X, was defined through the appearance of different plasmid DNA forms upon irradiation: For a photon current density J of energy E (that corresponds to their wavelength λ), targeting a sample area ΔS, over a period of time t, the number of lesions, N_X, can be written as:

$$N_X = N_{ox} \cdot \sigma_x \cdot J \cdot t$$

where

N_{oX} is the initial amount of lesions in the sample prior to irradiation;

X can be either the loss of supercoiled DNA, S, or SSB or DSB formation.

As the photon current density can be written as the amount of photons ΔQ that cross the sample surface ΔS over the time t, the cross section can be given by

$$\sigma_X = \frac{N_X}{N_{oX}} \cdot \frac{\Delta S}{\Delta Q}$$

To obtain the number of photons striking the sample, the definition of detector's quantum efficiency, Q_E, needs to be used

$$Q_E = \frac{n_{el}}{n_{ph}},$$

where n_{el} is the number of the electrons that n_{ph} photons are converted into at a certain wavelength at a detector of a surface s_{det}. Such can be obtained knowing that the electron current measured on the detector, I_{el}, equals

$$I_{el} = \frac{n_{el} \cdot q_e}{[\text{sec}]},$$

where q_e is a unit charge of the electron. Knowing that the current is being integrated over 1 sec period of time, the total amount of electrons striking the sample during irradiation will be obtained when multiplied by the irradiation time, T_{irr}.

As the surface area of the detector, s_{det}, is smaller then ΔS, the amount of photons needs to be calibrated over the area of the whole sample, I_{sam}, as

$$n_{ph} = \frac{\Delta Q \cdot s_{det}}{\Delta S}$$

hence

$$\Delta Q = \frac{I_{el} \cdot \Delta S \cdot T_{irr}}{Q_E \cdot q_e \cdot s_{det}}$$

and

$$\sigma_X(\lambda) = \frac{N_X}{N_{oX}} \cdot \frac{s_{\text{det}} \cdot Q_E \cdot q_e}{I_{el} \cdot T_{irr}}$$

Appendix D

The total cross section for the loss of the supercoiled DNA is given as

$$\sigma_{TS} = \int_{D_o}^{D_f} \sigma_S^E(\lambda, D)\mathrm{d}D = P_1 \cdot \int_{D_o}^{D_f} \frac{N_S(D)}{D}\mathrm{d}D,$$

where

$$P_1 = \frac{h \cdot c \cdot \Delta S}{\lambda \cdot M \cdot N_{oS}}$$

and

D_o – starting dose [Gy],

D_f – final dose [Gy]

$N_S(D)$ – function describing loss of supercoiled form with the dose, D, obtained from the data modelling.

The supercoiled form is expressed by an exponential decay of the form

$$\sigma_S^E(\lambda) = P_1 \frac{P_2 \cdot e^{-P_3 \cdot D} + P_4}{D}$$

was chosen.

$$\sigma_{TS} = \int_{D_o}^{D_f} \sigma_S^E(\lambda, D)\mathrm{d}D = P_1 \int_{D_o}^{D_f} \frac{P_2 \cdot e^{-P_3 \cdot D} + P_4}{D}\mathrm{d}D = P_1 P_2 \int_{D_o}^{D_f} \frac{e^{-P_3 \cdot D}}{D}\mathrm{d}D + P_1 P_4 \int_{D_o}^{D_f} \frac{1}{D}\mathrm{d}D$$

The solution of the first integral is called an exponential integral and possesses an explicit form as the Puiseaux series

$$\int \frac{e^{-P_3 D}}{D}\mathrm{d}D = Ei(-P_3 D) = \gamma + \ln\left|-P_3 D\right| + \frac{(-P_3 D)}{1 \cdot 1!} + \frac{(-P_3 D)^2}{2 \cdot 2!} + \frac{(-P_3 D)^3}{3 \cdot 3!} + \ldots$$

Therefore, the total cross section for loss of supercoiled form can be expressed as

$$\sigma_{TS} = \int_{D_o}^{D_f} \sigma_S^E(\lambda, D)\mathrm{d}D \cong$$

$$\cong P_1 \left\{ P_2 \left[\ln\left(\frac{D_f}{D_o}\right) - P_3(D_f - D_o) + \frac{P_3^2}{4}(D_f^2 - D_o^2) - \frac{P_3^3}{18}(D_f^3 - D_o^3) \right] + P_4 \ln\left(\frac{D_f}{D_o}\right) \right\}$$

Appendix E

An effective cross section for a SSB formation, σ_{SSB}, was defined through the appearance of different plasmid DNA forms upon irradiation: For a photon current density J of energy E (that corresponds to their wavelength λ), targeting a sample area ΔS, over a period of time t, the number of breaks N_{SSB} can be written as

$$N_{SSB} = N_{oSSB} \cdot \sigma_{SSB} \cdot J \cdot t$$

where

N_{oSSB} is the initial amount of SSB in the sample prior to irradiation.

As the photon current density can be written as the amount of photons ΔQ that cross the sample surface ΔS over the time t, the cross section can be given by

$$\sigma_{SSB} = \frac{N_{SSB}}{N_{oSSB}} \cdot \frac{\Delta S}{\Delta Q}$$

To obtain the number of photons striking the sample, the definition of detector's quantum efficiency, Q_E, needs to be used

$$Q_E = \frac{N_{\bar{e}}}{Q_d},$$

where $N_{\bar{e}}$ is the number of the electrons that Q_d photons are converted into at a certain wavelength at a detector of a surface s_{det}. This can be obtained knowing that the electron current measured on the detector, I_{read}, equals

$$I_{read} = \frac{N_{\bar{e}} \cdot q_e}{[\text{sec}]},$$

where q_e is a unit charge of the electron. Knowing that the current is being integrated over 1 sec period of time, the total amount of electrons striking the sample during irradiation will be obtained when multiplied by the irradiation time, T_{irr}.

Since the surface area of the detector, s_{det}, is smaller then ΔS, the amount of photons needs to be calibrated over the area of the whole sample, I_{sam}, as

$$Q_d = \frac{\Delta Q \cdot s_{det}}{\Delta S}$$

so

$$\Delta Q = \frac{I_{read} \cdot \Delta S \cdot T_{irr}}{Q_E \cdot q_e \cdot s_{det}}$$

and

$$\sigma_{SSB}(\lambda) = \frac{N_{SSB}}{N_{0SSB}} \cdot \frac{s_{det} \cdot Q_E \cdot q_e}{I_{read} \cdot T_{irr}}$$

Appendix F

Plasmid DNA purification from enzymatic reactions (from "MinElute Handbook"):

1. Add 300 µl of Buffer ERC to the enzymatic reaction and mix. The maximum volume of enzymatic reaction that can be processed per MinElute column is 100 µl. If the enzymatic reaction is in a volume of <20 µl, adjust the volume to 20 µl. If the enzymatic reaction exceeds 100 µl, split your reaction, add 300 µl of Buffer ERC to each aliquot of the split reaction and use the appropriate number of MinElute columns.

2. Check that the color of the mixture is yellow (similar to Buffer ERC without the enzymatic reaction). If the color of the mixture is orange or violet, add 10 µl of 3 M sodium acetate, pH 5.0, and mix. The color of the mixture will turn to yellow.

3. Place a MinElute column in a 2 ml collection tube in a suitable rack.

4. To bind DNA, apply the sample to the MinElute column and centrifuge for 1 min. To obtain maximal recovery, transfer all traces of sample to the spin column.

5. Discard the flow-through and place the MinElute column back into the same tube.

6. To wash, add 750 µl Buffer PE to the MinElute column and centrifuge for 1 min.

7. Discard the flow-through and place the MinElute column back in the same tube. Centrifuge the column for an additional 1 min at maximum speed.

IMPORTANT: Residual ethanol from Buffer PE will not be completely removed unless the flow-through is discarded before this additional centrifugation.

8. Place the MinElute column in a clean 1.5 ml microcentrifuge tube.

9. To elute DNA, add 10 µl Buffer EB (10 mM Tris·Cl, pH 8.5) or H2O to the center of the membrane, let the column stand for 1 min, and then centrifuge for 1 min.

IMPORTANT: Ensure that the elution buffer is dispensed directly onto the membrane for complete elution of bound DNA. The average volume of eluate is 9 µl from 10 µl elution buffer. Elution efficiency is dependent on pH. The maximum elution efficiency is achieved between pH 7.0 and 8.5. When using water, make sure that the pH value is within this range, and store DNA at –20°C as DNA may degrade in the absence of a buffering agent. The purified DNA can also be eluted in TE (10 mM Tris·Cl, 1 mM EDTA, pH 8.0), but the EDTA may inhibit subsequent enzymatic reactions.

Appendix G

It was necessary to recalculate the equation system (9-4) in Chapter 9 since solutions shown in the paper (Boudaiffa et al., 2002) included some editorial errors

$$\frac{dS(t)}{dt} = -(\sigma'_{DSB} + \sigma_{SSB}) \cdot J \cdot S(t) \quad \text{(a)}$$

$$\frac{dR(t)}{dt} = \sigma_{SSB} \cdot J \cdot S(t) - \sigma''_{DSB} \cdot J \cdot R(t) \quad \text{(b)} \qquad (9\text{-}4)$$

$$\frac{dL(t)}{dt} = \sigma'_{DSB} \cdot J \cdot S(t) + \sigma''_{DSB} \cdot J \cdot R(t) - \sigma''_{F} \cdot J \cdot L(t) \quad \text{(c)}$$

Solution of the equation (9-4)(a) is pretty straight forward and results (assuming the boundary condition to be $R(t=0)=R_0$) as:

$$S(t) = S_0 e^{-(\sigma'_{DSB} + \sigma_{SSB})J \cdot t}$$

To solve the problem (9-4)(b), equation was written in the form of differential non-homogenous equation that can be expressed as a function that depends on the same variable, namely:

$$\frac{dR(t)}{dt} + \sigma''_{DSB} \cdot J \cdot R(t) = \sigma_{SSB} \cdot J \cdot S(t) = \sigma_{SSB} \cdot J \cdot S_0 e^{-(\sigma'_{DSB} + \sigma_{SSB})J \cdot t}$$

The left hand side of the equation can be treated as a homogenous differential equation and therefore can be written as:

$$\frac{dr(t)}{dt} + \sigma''_{DSB} \cdot J \cdot r(t) = 0$$

The solution of the above equation is a general solution of problem (9-4)(b) is

$$r(t) = c_1 \cdot e^{-\sigma''_{DSB} \cdot J \cdot t}$$

where c_1 is an integration constant.

The solution of a non-homogenous differential equation is a sum of the general solution and one particular case that fulfils the equation.

To find the particular solution, the method of varying the integration constant was used. The particular solution should be in the form of the general solution and fulfil the following condition

$$\frac{dC_1}{dt} \cdot e^{-\sigma''_{DSB} \cdot J \cdot t} = \sigma_{SSB} \cdot J \cdot S_0 e^{-(\sigma'_{DSB} + \sigma_{SSB})J \cdot t}$$

hence

$$C_1 = \frac{\sigma_{SSB} \cdot S_0}{\sigma''_{DSB} - \sigma'_{DSB} - \sigma_{SSB}} e^{-(\sigma'_{ISB} + \sigma_{SSB})J \cdot t}$$

From the boundary condition $R(t=0)=R_0$ C_1 can be determine to be

$$C_1 = R_0 - \frac{\sigma_{SSB} \cdot S_0}{\sigma''_{DSB} - \sigma'_{DSB} - \sigma_{SSB}}$$

and the solution of the primary non-homogenous equation is

$$R(t) = R_0 \cdot e^{-\sigma''_{ISB} \cdot J \cdot t} - \frac{\sigma_{SSB} \cdot S_0}{\sigma''_{DSB} - \sigma'_{DSB} - \sigma_{SSB}} (e^{-\sigma''_{ISB} \cdot J \cdot t} - e^{-(\sigma'_{ISB} + \sigma_{SSB})J \cdot t})$$

The same manner will be used to solve equation (9-4)(c). The general solution of the problem expresses as:

$$l(t) = c_2 \cdot e^{-\sigma'_F \cdot J \cdot t}$$

By varying the integration constant and using the boundary condition $L(t=0)=L_0$ the solution of the non-homogenous equation is given as

$$L(t) = L_0 e^{-\sigma''_F \cdot J \cdot t} + \frac{\sigma'_{DSB} S_0 + \sigma''_{DSB} R'}{\sigma''_F - \sigma'_{DSB} - \sigma_{SSB}} (e^{-(\sigma'_{DSB} + \sigma_{SSB})J \cdot t} - e^{-\sigma''_F \cdot J \cdot t}) + \\ + \frac{\sigma''_{DSB}(R_0 - R')}{\sigma''_F - \sigma''_{DSB}} (e^{-\sigma''_{DSB} \cdot J \cdot t} - e^{-\sigma''_F \cdot J \cdot t})$$

Consequently, (9-5) can be presented as:

$$\begin{aligned} S(t) &= S_0 e^{-(\sigma'_{ISB} + \sigma_{SSB})J \cdot t} \\ R(t) &= R_0 e^{-\sigma''_{ISB} \cdot J \cdot t} + R'(e^{-(\sigma'_{ISB} + \sigma_{SSB})J \cdot t} - e^{-\sigma''_{ISB} \cdot J \cdot t}) \\ L(t) &= L_0 e^{-\sigma''_F \cdot J \cdot t} + L'(e^{-(\sigma'_{ISB} + \sigma_{SSB})J \cdot t} - e^{-\sigma''_F \cdot J \cdot t}) + L''(e^{-\sigma''_{ISB} \cdot J \cdot t} - e^{-\sigma''_F \cdot J \cdot t}) \\ F(t) &= 1 - S(t) - R(t) - L(t) \end{aligned} \qquad (9\text{-}5)$$

with:

$$R' = \frac{\sigma_{SSB} S_0}{\sigma''_{DSB} - \sigma'_{DSB} - \sigma_{SSB}}$$

$$L' = \frac{\sigma'_{DSB} S_0 + \sigma''_{DSB} R'}{\sigma''_F - \sigma'_{DSB} - \sigma_{SSB}}$$

$$L'' = \frac{\sigma''_{DSB}(R_0 - R')}{\sigma''_F - \sigma''_{DSB}}$$

Appendix H

As mentioned in the Chapter 9, due to the lack of visible fragmentation, both F(t) and $\sigma_F^{''}$ can be considered to be equal 0. Therefore, equations (9-5) can be presented in a following manner:

$$S(t) = S_0 e^{-(\sigma_{DSB}^{'}+\sigma_{SSB})J\cdot t} \quad \text{(a)}$$
$$R(t) = R_0 e^{-\sigma_{DSB}^{*}\cdot J\cdot t} + R'(e^{-(\sigma_{DSB}^{'}+\sigma_{SSB})J\cdot t} + e^{-\sigma_{DSB}^{*}\cdot J\cdot t}) \quad \text{(b)} \qquad (9\text{-}6)$$
$$L(t) = L_0 + L'(e^{-(\sigma_{DSB}^{'}+\sigma_{SSB})J\cdot t} - 1) + L''(e^{-\sigma_{DSB}^{*}\cdot J\cdot t} - 1) \quad \text{(c)}$$

with

$$R' = \frac{\sigma_{SSB} S_0}{\sigma_{DSB}^{''} - \sigma_{DSB}^{'} - \sigma_{SSB}}$$
$$L' = \frac{\sigma_{DSB}^{'} S_0 + \sigma_{DSB}^{''} R'}{-\sigma_{DSB}^{'} - \sigma_{SSB}}$$
$$L'' = -(R_0 - R')$$

Since we can measure σ_S and σ_{SSB} directly from the gel electrophoresis by employing relation (9-2) it was possible to calculate $\sigma_{DSB}^{''}$ from equations (9-6). To determine the value, equations (9-6)(a) and (9-6)(b) were used. From (9-6)(b) it was possible to determine the relationship between $e^{-\sigma_{DSB}^{*}\cdot J\cdot t}$ and $\sigma_{DSB}^{''}$ to be:

$$e^{-\sigma_{DSB}^{*}\cdot J\cdot t} = \frac{R - \dfrac{\sigma_{SSB}\cdot S}{\sigma_{DSB}^{''} - \sigma_{DSB}^{'} - \sigma_{SSB}}}{R_0 + \dfrac{\sigma_{SSB}\cdot S_0}{\sigma_{DSB}^{''} - \sigma_{DSB}^{'} - \sigma_{SSB}}}$$

Next, it is possible to subsidise in (9-6)(c) all terms containing $e^{-\sigma_{DSB}^{*}\cdot J\cdot t}$. After rearranging all terms in the new equation obtained that way, one can easily obtain that:

$$\left\{\frac{L - L_0 - L'(\gamma - 1)}{R' - R_0} - \frac{R - R_0 - R'(\delta - 1)}{R' + R_0}\right\}[R_0 + R'] = 0$$

where:

$$\gamma = e^{-\sigma_S \cdot J \cdot t}$$

$$\delta = \frac{S}{S_0}$$

from there, two conditions for σ''_{DSB} can be obtained

either

$$\frac{L - L_0 - L'(\gamma - 1)}{R' - R_0} - \frac{R - R_0 - R'(\delta - 1)}{R' + R_0} = 0$$

or

$$R_0 + R' = 0$$

The first condition results only in negative values for σ''_{DSB}, therefore, the second one was used to determine values of σ''_{DSB} to be

$$\sigma''_{DSB} = \sigma_S - \frac{\sigma_{SSB} \cdot S_0}{R_0} \tag{9-7}$$

Appendix I

The irradiation dose, D [Gy], equals the energy, E_{abs} [J], delivered to a body of a total mass M [kg]

$$D = \frac{E_{abs}}{M}$$

In case of electron irradiation E_{abs} can be expressed as:

$$E_{abs} = E_{el} \cdot n_{el}$$

where:

E_{el} – energy of the electrons [J];

n_{el} – number of electrons.

The electron current, I_{el}, depends on the number of electrons, n_{el}, that reached the detector in one second, [sec], during irradiation

$$I_{el} = \frac{q_e \cdot n_{el}}{[\text{sec}]}$$

where:

q_e – electron charge = $1.602 \cdot 10^{-19}$ C,

and can be obtained from the intensity I_{meas} that can be measured on the detector as:

$$I_{el} = \frac{I_{meas} \cdot S_{sample}}{S_{\det}}$$

Where:

S_{sample} – surface of the sample;

S_{det} – diameter of the beam detected/surface of the detector.

In this way the current that results from the electron motion can be converted to photocurrent that depends on the number of incident photons and the number of photons can be derived as

$$E_{abs} = \frac{E_{el} \cdot I_{meas} \cdot S_{sample} \cdot [\text{sec}]}{q_e \cdot S_{\det}}$$

This allows to express the dose with the known parameters

$$D = \frac{E_{el} \cdot I_{meas} \cdot S_{sample} \cdot [\text{sec}]}{M \cdot q_e \cdot S_{\det}}$$

If all electrons reached the sample surface, the dose can be expressed as

$$D = \frac{\tilde{E} \cdot I_{el} \cdot t}{M}$$

where $\tilde{E}$ is the electrons energy in [eV] and t is irradiation time in [sec].

References

Abdoul-Carime, H., and L. Sanche. 2002. Fragmentation of short single DNA strands by 1-30 eV electrons: dependence on base identity and sequence. *International Journal of Radiation Biology*. 78:89-99.

Achey, P., and H. Duryea. 1974. Production of DNA strand breaks by hydroxyl radical. *International Journal of Radiation Biology*. 251:595-601.

Akita, S., H. Nishijima, Y. Nakayama, F. Tokumasu, and K. Takeyasu. 1999. Carbon nanotube tips for a scanning probe microscope: their fabrication and properties. *Journal of Physics D-Applied Physics*. 32:1044-1048.

Amati, P. 1970. Chloramphenicol - Effect on DNA Synthesis During Phage Development in Escherichia-Coli. *Science*. 168:1226-&

Anselmetti, D., J. Fritz, B. Smith, and X. Fernandez-Busquets. 2000. Single Molecule DNA Biophysics with Atomic Force Microscopy. *Single Molecules*. 1:53-58.

Argaman, M., R. Golan, N.H. Thomson, and H.G. Hansma. 1997. Phase imaging of moving DNA molecules and DNA molecules replicated in the atomic force microscope. *Nucleic Acids Research*. 25:4379-4384.

Barrios, R., P. Skurski, and J. Simons. 2002. Mechanism for damage to DNA by low-energy electrons. *Journal of Physical Chemistry B*. 106:7991-7994.

Berge, T., N.S. Jenkins, R.B. Hopkirk, M.J. Waring, J.M. Edwardson, and R.M. Henderson. 2002. Structural perturbations in DNA caused by bis-intercalation of ditercalinium visualised by atomic force microscopy. *Nucleic Acids Research*. 30:2980-2986.

Binnig, G., C.F. Quate, and C. Gerber. 1986. Atomic Force Microscope. *Physical Review Letters*. 56:930 - 933.

Bonura, T., and K.C. Smith. 1976. Involvement of indirect effects in cell killing and DNA double-strand breakage in gamma-irradiated Escherichia coli K-12. *International Journal of Radiation Biology*. 29:293-296.

Boudaiffa, B., P. Cloutier, D. Hunting, M.A. Huels, and L. Sanche. 2000a. Resonant formation of DNA strand breaks by low-energy (3 to 20 eV) electrons. *Science*. 287:1658-1660.

Boudaiffa, B., P. Cloutier, D. Hunting, M.A. Huels, and L. Sanche. 2002. Cross sections for low-energy (10-50 eV) electron damage to DNA. *Radiation Research*. 157:227-234.

Boudaiffa, B., D. Hunting, P. Cloutier, M.A. Huels, and L. Sanche. 2000b. Induction of single- and double-strand breaks in plasmid DNA by 100-1500 eV electrons. *International Journal of Radiation Biology*. 76:1209-1221.

Boullard, A., and P.U. Giacomoni. 1988. Effect of Uv Irradiation at Defined Wavelengths on the Tertiary Structure of Double-Stranded Covalently Closed Circular DNA. *Journal of Photochemistry and Photobiology B-Biology*. 2:491-501.

Bunch, J.S., T.N. Rhodin, and P.L. McEuen. 2004. Noncontact-AFM imaging of molecular surfaces using single-wall carbon nanotube technology. *Nanotechnology*. 15:S76-S78.

Caron, L., and L. Sanche. 2004. Diffraction in resonant electron scattering from helical macromolecules: A- and B-type DNA. *Physical Review A*. 70.

Caron, L., and L. Sanche. 2005. Diffraction in resonant electron scattering from helical macromolecules: Effects of the DNA backbone. *Physical Review A*. 72.

Caron, L., and L. Sanche. 2006. Temporary electron localization and scattering in disordered single strands of DNA. *Physical Review A*. 73.

Caron, L.G., and L. Sanche. 2003. Low-energy electron diffraction and resonances in DNA and other helical macromolecules. *Physical Review Letters*. 91.

Chen, J., K.L. Jin, M.Z. Chen, W. Pei, K. Kawaguchi, D.A. Greenberg, and R.P. Simon. 1997. Early detection of DNA strand breaks in the brain after transient focal ischemia: Implications for the role of DNA damage in apoptosis and neuronal cell death. *Journal of Neurochemistry*. 69:232-245.

Clewell, D.B. 1972. Nature of Col E1 Plasmid Replication in Escherichia-Coli in Presence of Chloramphenicol. *Journal of Bacteriology*. 110:667-&.

Clewell, D.B., and D.R. Helinski. 1969. Supercoiled Circular DNA-Protein Complex in Escherichia Coli - Purification and Induced Conversion to an Open Circular DNA Form. *Proceedings of the National Academy of Sciences of the United States of America*. 62:1159-&.

Clewell, D.B., and D.R. Helinski. 1970. Properties of a Supercoiled Deoxyribonucleic Acid-Protein Relaxation Complex and Strand Specificity of Relaxation Event. *Biochemistry*. 9:4428-&.

Clewell, D.B., and D.R. Helinski. 1972. Effect of Growth Conditions on Formation of Relaxation Complex of Supercoiled Cole1 Deoxyribonucleic Acid and Protein in Escherichia-Coli. *Journal of Bacteriology*. 110:1135-&.

Csaki, A., R. Moller, W. Straube, J.M. Kohler, and W. Fritzsche. 2001. DNA monolayer on gold substrates characterized by nanoparticle labeling and scanning force microscopy. *Nucleic Acids Research*. 29:art. no.-e81.

Davies, E., K.S. Teng, R.S. Conlan, and S.P. Wilks. 2005. Ultra-high resolution imaging of DNA and nucleosomes using non-contact atomic force microscopy. *Febs Letters*. 579:1702-1706.

Donoghue, D.J., and P.A. Sharp. 1978. Replication of Colicin E1 Plasmid DNA Invivo Requires No Plasmid-Encoded Proteins. *Journal of Bacteriology*. 133:1287-1294.

Falk, M. 1964. Ultraviolet Spectra of Native + Denatured Deoxyribonucleic Acid. *Journal of the American Chemical Society*. 86:1226-&.

Feng, X.Z., R. Bash, P. Balagurumoorthy, D. Lohr, R.E. Harrington, and S.M. Lindsay. 2000. Conformational transition in DNA on a cold surface. *Nucleic Acids Research*. 28:593-596.

Folkard, M., K.M. Prise, B. Brocklehurst, and B.D. Michael. 1999. DNA damage induction in dry and hydrated DNA by synchrotron radiation. *Journal of Physics B-Atomic Molecular and Optical Physics*. 32:2753-2761.

Folkard, M., K.M. Prise, C.J. Turner, and B.D. Michael. 2002. The production of single strand and double strand breaks in DNA in aqueous solution by vacuum UV photons below 10 eV. *Radiation Protection Dosimetry*. 99:147-149.

Folkard, M., K.M. Prise, B. Vojnovic, B. Brocklehurst, and B.D. Michael. 2000. Critical energies for ssb and dsb induction in plasmid DNA by vacuum-UV photons: an arrangement for irradiating dry or hydrated DNA with monochromatic photons. *International Journal of Radiation Biology*. 76:763-771.

Fotiadis, D., S. Scheuring, S.A. Muller, A. Engel, and D.J. Muller. 2002. Imaging and manipulation of biological structures with the AFM. *Micron*. 33:385-397.

Frenkel, L., and H. Bremer. 1986. Increased Amplification of Plasmids Pbr322 and Pbr327 by Low Concentrations of Chloramphenicol. *DNA-a Journal of Molecular & Cellular Biology*. 5:539-544.

Garcia, R., and A. San Paulo. 1999. Attractive and repulsive tip-sample interaction regimes in tapping-mode atomic force microscopy. *Physical Review B*. 60:4961-4967.

Garcia, R., J. Tamayo, M. Calleja, and F. Garcia. 1998. Phase contrast in tapping-mode scanning force microscopy. *Applied Physics a-Materials Science & Processing*. 66:S309-S312.

Hansma, H.G. 2001. Surface biology of DNA by atomic force microscopy. *Annual Review of Physical Chemistry*. 52:71-92.

Hansma, H.G., R.L. Sinsheimer, M.Q. Li, and P.K. Hansma. 1992. Atomic Force Microscopy of Single-Stranded and Double-Stranded DNA. *Nucleic Acids Research*. 20:3585-3590.

Harrison, K.L., N. Fairhurst, B.C. Challis, and D.E.G. Shuker. 1997. Synthesis, characterization, and immunochemical detection of O-6-(carboxymethyl)-2'-deoxyguanosine: A DNA adduct formed by nitrosated glycine derivatives. *Chemical Research in Toxicology*. 10:652-659.

Hendee, W.R., G.S. Ibbott, and E.G. Hendee. 2005. Radiation therapy Physics. John Wiley and Sons, New Jersey. 450 pp.

Hieda, K. 1994. DNA-Damage Induced by Vacuum and Soft-X-Ray Photons from Synchrotron-Radiation. *International Journal of Radiation Biology*. 66:561-567.

Hieda, K., K. Suzuki, T. Hirono, M. Suzuki, and Y. Furusawa. 1994. Single-Strand and Double-Strand Breaks in Pbr322 DNA by Vacuum-UV from 8.3 to 20.7 Ev. *Journal of Radiation Research*. 35:104-111.

Honda, S., I. Sugita, K. Miki, and I. Saito. 2004. The semi-quantitative comparison of oxidative stress mediated DNA single and double strand breaks using terminal deoxynucleotidyl transferase mediated end labeling combined with a slot blot technique. *Free Radical Research*. 38:481-485.

Huels, M.A., B. Boudaiffa, P. Cloutier, D. Hunting, and L. Sanche. 2003. Single, double, and multiple double strand breaks induced in DNA by 3-100 eV electrons. *Journal of the American Chemical Society*. 125:4467-4477.

Hunniford, C.A., D.J. Timson, R.J.H. Davies, and R.W. McCullough. 2007. Damage to plasmid DNA induced by low energy carbon ions. *Physics in Medicine and Biology*. 13:3729.

Inagaki, T., R.N. Hamm, E.T. Arakawa, and L.R. Painter. 1974. Optical and Dielectric Properties of DNA in Extreme Ultraviolet. *Journal of Chemical Physics*. 61:4246-4250.

Ito, T. 1992. The effects of vacuum-UV radiation (50-190nm) on microorganisms and DNA. *Adv. Space Res.* 4:(4)249-(4)253.

Ito, T., and M. Saito. 1988. Degradation of Oligonucleotides by Vacuum-Uv Radiation in Solid - Roles of the Phosphate Group and Bases. *Photochemistry and Photobiology*. 48:567-572.

Ito, T., M. Saito, and T. Taniguchi. 1987. A Survey of Photoproducts of an Irradiated Oligodeoxynucleotide by Monochromatic Photons with the Energy Ranged from 6.5 to 22.5 Ev. *Photochemistry and Photobiology*. 46:979-984.

Jackson, S.F., B.R. Wentzell, D.R. McCalla, and K.B. Freeman. 1977. Chloramphenicol Damages Bacterial DNA. *Biochemical and Biophysical Research Communications*. 78:151-157.

Klinov, D.V., E.V. Dubrovin, and I.V. Yaminsky. 2003. Substrate for scanning probe microscopy of DNA: HOPG versus mica. *Physics of Low-Dimensional Structures*. 3-4:119-124.

Lark, K.G. 1973. Initiation and Termination of Bacterial Deoxyribonucleic Acid Replication in Low Concentrations of Chloramphenicol. *Journal of Bacteriology*. 113:1066-1069.

Li, X.F., M.D. Sevilla, and L. Sanche. 2003. Density functional theory studies of electron interaction with DNA: Can zero eV electrons induce strand breaks? *Journal of the American Chemical Society*. 125:13668-13669.

Linchao, S., and H. Bremer. 1986a. Effect of Rela Function on the Replication of Plasmid Pbr322 in Escherichia-Coli. *Molecular & General Genetics*. 203:150-153.

Linchao, S., and H. Bremer. 1986b. Effect of the Bacterial-Growth Rate on Replication Control of Plasmid Pbr322 in Escherichia-Coli. *Molecular & General Genetics*. 203:143-149.

Lu, J.H., H.K. Li, H.J. An, G.H. Wang, Y. Wang, M.Q. Li, Y. Zhang, and J. Hu. 2004. Positioning isolation and biochemical analysis of single DNA molecules based on nanomanipulation and single-molecule PCR. *Journal of the American Chemical Society*. 126:11136-11137.

Lysetska, M., A. Knoll, D. Boehringer, T. Hey, G. Krauss, and G. Krausch. 2002. UV light-damaged DNA and its interaction with human replication protein A: an atomic force microscopy study. *Nucleic Acids Research*. 30:2686-2691.

Lyubchenko, Y., L. Shlyakhtenko, R. Harrington, P. Oden, and S. Lindsay. 1993. Atomic Force Microscopy of Long DNA - Imaging in Air and under Water. *Proceedings of the National Academy of Sciences of the United States of America*. 90:2137-2140.

Lyubchenko, Y.L., and L.S. Shlyakhtenko. 1997. Visualization of supercoiled DNA with atomic force microscopy in situ. *Proceedings of the National Academy of Sciences of the United States of America*. 94:496-501.

Martin, F., P.D. Burrow, Z.L. Cai, P. Cloutier, D. Hunting, and L. Sanche. 2004. DNA strand breaks induced by 0-4 eV electrons: The role of shape resonances. *Physical Review Letters*. 93.

Matsunaga, T., K. Hieda, and O. Nikaido. 1991. Wavelength Dependent Formation of Thymine Dimers and (6-4)Photoproducts in DNA by Monochromatic

Ultraviolet-Light Ranging from 150 to 365 Nm. *Photochemistry and Photobiology*. 54:403-410.

McMaster, T.J., M. Berry, A.P. Corfield, and M.J. Miles. 1999. Atomic force microscopy of the submolecular architecture of hydrated ocular mucins. *Biophysical Journal*. 77:533-541.

Michael, B.D., K.M. Prise, M. Folkard, B. Vojnovic, B. Brocklehurst, I.H. Munro, and A. Hopkirk. 1994. Action Spectra for Single-Strand and Double-Strand Break Induction in Plasmid DNA - Studies Using Synchrotron-Radiation. *International Journal of Radiation Biology*. 66:569-572.

Mota, R., R. Parafita, A. Giuliani, M.J. Hubin-Franskin, J.M.C. Lourenco, G. Garcia, S.V. Hoffmann, N.J. Mason, P.A. Ribeiro, M. Raposo, and P. Limao-Vieira. 2005. Water VUV electronic state spectroscopy by synchrotron radiation. *Chemical Physics Letters*. 416:152-159.

Mozejko, P., and L. Sanche. 2003. Cross section calculations for electron scattering from DNA and RNA bases. *Radiation and Environmental Biophysics*. 42:201-211.

Mozejko, P., and L. Sanche. 2005. Cross sections for electron scattering from selected components of DNA and RNA. *Radiation Physics and Chemistry*. 73:77-84.

Muller, D.J., M. Amrein, and A. Engel. 1997. Adsorption of biological molecules to a solid support for scanning probe microscopy. *Journal of Structural Biology*. 119:172-188.

Murakami, M., H. Hirokawa, and I. Hayata. 2000. Analysis of radiation damage of DNA by atomic force microscopy in comparison with agarose gel electrophoresis studies. *Journal of Biochemical and Biophysical Methods*. 44:31-40.

Norgard, M.V., K. Emigholz, and J.J. Monahan. 1979. Increased Amplification of Pbr322 Plasmid Deoxyribonucleic-Acid in Escherichia-Coli K-12 Strain-Rr1 and Strain-Chi-1776 Grown in the Presence of High-Concentrations of Nucleoside. *Journal of Bacteriology*. 138:270-272.

Onoa, G.B., G. Cervantes, V. Moreno, and M.J. Prieto. 1998. Study of the interaction of DNA with cisplatin and other Pd(II) and Pt(II) complexes by atomic force microscopy. *Nucleic Acids Research*. 26:1473-1480.

Oppenheim, A. 1981. Separation of Closed Circular DNA from Linear DNA by Electrophoresis in 2 Dimensions in Agarose Gels. *Nucleic Acids Research*. 9:6805-6812.

Pan, X., P. Cloutier, D. Hunting, and L. Sanche. 2003. Dissociative electron attachment to DNA. *Physical Review Letters*. 90.

Pan, X., and L. Sanche. 2005. Mechanism and site of attack for direct damage to DNA by low-energy electrons. *Physical Review Letters*. 94.

Pan, X., and L. Sanche. 2006. Dissociative electron attachment to DNA basic constituents: The phosphate group. *Chemical Physics Letters*. 421:404-408.

Pang, D., B.L. Berman, S. Chasovskikh, J.E. Rodgers, and A. Dritschilo. 1998. Investigation of neutron-induced damage in DNA by atomic force microscopy: Experimental evidence of clustered DNA lesions. *Radiation Research*. 150:612-618.

Pang, D., G. Popescu, J. Rodgers, B. Berman, and A. Dritschilo. 1996. Atomic force microscopy investigation of radiation-induced DNA double strand breaks. *Scanning Microscopy*. 10:1109-1110.

Podesta, A., L. Imperadori, W. Colnaghi, L. Finzi, P. Milani, and D. Dunlap. 2004. Atomic force microscopy study of DNA deposited on poly L-ornithine-coated mica. *Journal of Microscopy-Oxford*. 215:236-240.

Pope, L.H., M.C. Davies, C.A. Laughton, C.J. Roberts, S.J.B. Tendler, and P.M. Williams. 2000. Atomic force microscopy studies of intercalation-induced changes in plasmid DNA tertiary structure. *Journal of Microscopy-Oxford.* 199:68-78.

Prise, K.M., M. Folkard, B.D. Michael, B. Vojnovic, B. Brocklehurst, A. Hopkirk, and I.H. Munro. 2000. Critical energies for SSB and DSB induction in plasmid DNA by low-energy photons: action spectra for strand-break induction in plasmid DNA irradiated in vacuum. *International Journal of Radiation Biology.* 76:881-890.

Ray, S.G., S.S. Daube, and R. Naaman. 2005. On the capturing of low-energy electrons by DNA. *Proceedings of the National Academy of Sciences of the United States of America.* 102:15-19.

Rippe, K., N. Mucke, and J. Langowski. 1997. Molecules in Motion: Imaging DNA with the Scanning Force Microscope in Aqueous Solutions. *Bioforum International.* 1:42-44.

Rydberg, B. 1984. DNA strand breaks induced by low-energy heavy ions. *International Journal of Radiation Biology.* 47:57-61.

Sambrook, J., and D.W. Russell. 2001. Molecular Cloning. A laboratory manual. Cold Spring Harbor laboratory Press, New York.

Santos, N.C., and M. Castanho. 2004. An overview of the biophysical applications of atomic force microscopy. *Biophysical Chemistry.* 107:133-149.

Siddiqi, M.A., and E. Bothe. 1987. Single-Strand and Double-Strand Break Formation in DNA Irradiated in Aqueous-Solution - Dependence on Dose and Oh Radical Scavenger Concentration. *Radiation Research.* 112:449-463.

Smith, G.N., and C.S. Worrel. 1950. The Decomposition of Chloromycetin (Chloramphenicol) by Microorganisms. *Archives of Biochemistry*. 28:232-241.

Smith, G.N., and C.S. Worrel. 1953. Reduction of Chloromycetin and Related Compounds by Escherichia-Coli. *Journal of Bacteriology*. 65:313-317.

Sontag, W., and H. Dertinger. 1975. Energy-Requirements for Damaging DNA-Molecules .3. Mechanisms of Inactivation of Bacteriophage Phi-X 174 DNA by Vacuum Ultraviolet-Radiation. *International Journal of Radiation Biology*. 27:543-552.

Sontag, W., and K.F. Weibezahn. 1975. Absorption of DNA in Region of Vacuum-UV (3-25 Ev). *Radiation and Environmental Biophysics*. 12:169-174.

Tamayo, J., and R. Garcia. 1997. Effects of elastic and inelastic interactions on phase contrast images in tapping-mode scanning force microscopy. *Applied Physics Letters*. 71:2394-2396.

Utsuno, K., M. Tsuboi, S. Katsumata, and T. Iwamoto. 2001. Viewing of complex molecules of ethidium bromide and plasmid DNA in solution by atomic force microscopy. *Chemical & Pharmaceutical Bulletin*. 49:413-417.

van Noort, S.J.T., K.O. van der Werf, A.P.M. Eker, C. Wyman, B.G. de Grooth, N.F. van Hulst, and J. Greve. 1998. Direct visualization of dynamic protein-DNA interactions with a dedicated atomic force microscope. *Biophysical Journal*. 74:2840-2849.

Wang, H.D., R. Bash, J.G. Yodh, G.L. Hager, D. Lohr, and S.M. Lindsay. 2002. Glutaraldehyde modified mica: A new surface for atomic force microscopy of chromatin. *Biophysical Journal*. 83:3619-3625.

Watson, J.D., and F.H.C. Crick. 1953. Molecular Structure of Nucleic Acids - a Structure for Deoxyribose Nucleic Acid. *Nature*. 171:737-738.

Watson, N. 1988. A New Revision of the Sequence of Plasmid-Pbr322. *Gene.* 70:399-403.

Wehner, J., and G. Horneck. 1995. Effects of Vacuum UV and UVC Radiation on Dry Escherichia-Coli Plasmid Puc19 .1. Inactivation, Lacz(-) Mutation-Induction and Strand Breaks. *Journal of Photochemistry and Photobiology B-Biology.* 28:77-85.

Wisseman, C.L., J.E. Smadel, F.E. Hahn, and H.E. Hopps. 1954. Mode of Action of Chloramphenicol .1. Action of Chloramphenicol on Assimilation of Ammonia and on Synthesis of Proteins and Nucleic Acids in Escherichia-Coli. *Journal of Bacteriology.* 67:662-673.

Wright, M., and I. Revenko. 2004. Veeco.

Yang, W.S., O. Auciello, J.E. Butler, W. Cai, J.A. Carlisle, J. Gerbi, D.M. Gruen, T. Knickerbocker, T.L. Lasseter, J.N. Russell, L.M. Smith, and R.J. Hamers. 2002. DNA-modified nanocrystalline diamond thin-films as stable, biologically active substrates. *Nature Materials.* 1:253-257.

Yang, W.S., J.E. Butler, J.N. Russell, and R.J. Hamers. 2004. Interfacial electrical properties of DNA-modified diamond thin films: Intrinsic response and hybridization-induced field effects. *Langmuir.* 20:6778-6787.

Yokoya, A., R. Watanabe, and T. Hara. 1999. Single- and double-strand breaks in solid pBR322 DNA induced by ultrasoft X-rays at photon energies of 388, 435 and 573 eV. *Journal of Radiation Research.* 40:145-158.

Yoshida, K., M. Yoshimoto, K. Sasaki, T. Ohnishi, T. Ushiki, J. Hitomi, S. Yamamoto, and M. Sigeno. 1998. Fabrication of a new substrate for atomic force microscopic observation of DNA molecules from an ultrasmooth sapphire plate. *Biophysical Journal.* 74:1654-1657.

Zalar, A., D. Tepfer, S.r.V. Hoffmann, J.M. Kenney, and S. Leach. 2007. Directed exospermia: I. Biological modes of resistance to UV light are implied

through absorption spectroscopy of DNA and potential UV screens. *International Journal of Astrobiology*. 6:229-240.

Zheng, Y., P. Cloutier, D.J. Hunting, L. Sanche, and J.R. Wagner. 2005. Chemical basis of DNA sugar-phosphate cleavage by low-energy electrons. *Journal of the American Chemical Society*. 127:16592-16598.

Zheng, Y., J.R. Wagner, and L. Sanche. 2006. DNA damage induced by low-energy electrons: Electron transfer and diffraction. *Physical Review Letters*. 96.

Zlatanova, J., and S.H. Leuba. 2002. Stretching and imaging single DNA molecules and chromatin. *Journal of Muscle Research and Cell Motility*. 23:377-395.

Spectroscopic studies of biogenic gases and particulates from the terrestrial troposphere

Elizabeth Drage

Department of Physics and Astronomy

The Open University

February 25, 2008